Chemistry and Kinematics in Low-Mass Star-Forming Regions

Anna Punanova

München 2017

Chemistry and Kinematics in Low-Mass Star-Forming Regions

Anna Punanova

Dissertation
an der Fakultät für Physik
der Ludwig–Maximilians–Universität
München

vorgelegt von
Anna Punanova
aus Ilyinsko-Podomskoye, Russland

München, den 9 August 2017

Erstgutachter: Prof. Dr. Paola Caselli
Zweitgutachter: Prof. Dr. Andreas Burkert
Tag der mündlichen Prüfung: 25 September 2017

Contents

List of Figures

List of Tables

Zusammenfassung

Die vorliegende Arbeit untersucht die frühesten Phasen der Sternentstehung in unterschiedlichen Umgebungen. Hierfür beobachte ich deuterierte Moleküle und messe den Deuteriumsanteil, d.h. das Verhältnis zwischen der Säulendichte eines deuterierten Moleküls, z.B. N_2D^+ und DCO^+, und der Säulendichte des undeuterierten Moleküls, N_2H^+ und $H^{13}CO^+$. In pre-stellaren Kernen, d.h. kurz vor der Bildung des Protosterns, nimmt der Deuteriumsanteil zu. Deuterierte Moleküle stellen daher ein wichtiges diagnostisches Hilfsmittel dar, um Eigenschaften wie die physikalisch-chemische Struktur und die Kinematik von dichtem und kaltem Gas, wie man es es während der ersten Phasen der Sternentstehung in Molekülwolken findet, zu untersuchen.

In dieser Doktorarbeit lege ich den Fokus auf zwei nahegelegene massearme Sternentstehungsregionen: Die Schlangenträger Molekülwolke und die ruhigere Taurus Molekülwolke. Dieses Projekt basiert auf drei wissenschaftlichen Veröffentlichungen, in welchen die Chemie, Kinematik sowie die Substruktur dichter Kerner diskutiert werden.

Im ersten Kapitel untersuche ich die Deuteriumfraktionierung in den dichten Kernen von L1688 in der Schlangenträger Molekülwolke, eine der nahegelegensten ($\sim 120\,\mathrm{pc}$) Sternentstehungsregionen. Ein hoher Deuteriumsanteil ist eines der Hauptmerkmale von pre-stellaren Kernen, d.h. den dichten Kernen, welche an der Schwelle zur Sternentstehung stehen. Ich analysiere die Abhängigkeit des Deuteriumanteils von verschiedenen physikalischen Bedingungen, wie zum Beispiel Gasdichte und -temperatur, Turbulenz und CO-Verarmung. Ich zeige, dass Regionen derselben Molekülwolke unterschiedliche dynamische, thermische und chemische Entwicklungen durchlaufen. Dies hat Konsequenzen für die derzeitige Sternentstehungseffizienz und die Eigenschaften zukünftiger Sternsysteme innerhalb dieser Molekülwolke.

Im zweiten Kapitel untersuche ich die Kinematik der dichten Kerne im L1495 Filament in der Taurus Molekülwolke. Interstellare Filamente sind weit verbreitete Strukturen in Molekülwolken und spielen eine wichtige Rolle im Sternentstehungsprozess. Ich verwende N_2H^+(1–0) und N_2D^+(2–1) Spektralinien für den Nachweis von Gas im Zentrum der dichten Kerne, wo CO und andere Moleküle bereits verarmt sind, $H^{13}CO^+$(1–0) und DCO^+(2–1) Spektrallinien für die Untersuchung der Kernhülle auf der Suche nach Verbindungen zwischen der Gasbewegung auf Kern- und Wolkenskala, sowie $C^{18}O$(1–0) Spektrallinien für die Untersuchung der Gaskinematik im gesamten Filament. Im Gegensatz zu den dichten L1688 Kernen im Schlangenträger zeigen die L1495 Kerne sehr ähnliche Eigenschaften: Unterschalllinienbreite, Zentralgeschwindigkeite, Geschwindigkeitsgradient sowie spezifis-

ches Drehmoment. Im Übergang von der Wolke zu den Kernen kann ich eine zunehmende Rotation der Kernhüllen nachweisen. Auf kleineren Skalen wird das Kernmaterial abgebremst, was einen Verlust an spezifischem Drehimpuls impliziert. Das Gasmaterial der Wolke bleibt von den rotierenden Kernen und Protosternen unbeeinflusst.

Im dritten Kapitel untersuche ich die Substruktur des prototypischen isolierten prestellaren Kerns L1544 in der Taurus Molekülwolke. Die verwendeten interferometrischen Beobachtungen zeigen Strukturen auf Skalen von 700 au. Der Kern zeigt eine starke Asymmetrie in der Methanolverteilung welche durch ein asymmetrisches UV-Strahlungsfeld hervorgerufen sein könnte.

In der vorliegenden Arbeit gebe ich zudem einen Ausblick auf zukünftige Arbeiten bezüglich der Entwicklung dichter Kerne. Als Teil dieser Arbeit habe ich eine Anzahl von Beobachtungsanträgen im sub-mm Wellenlängenbereich gestellt, von denen viele genehmigt und bereits beobachtet wurden. Diese Folgeprojekte untersuchen die Chemie von L1495 in Taurus, L1688 im Schlangenträger, und B5 in Perseus, sowie die Kinematik in L1688 und B5. Ich vergleiche den Deuteriumsanteil von Ionen (N_2D^+/ N_2H^+, DCO^+/ $H^{13}CO^+$) und neutralen Molekülen (NH_2D/ NH_3) sowohl im Kerninneren (N_2D^+/ N_2H^+) als auch in den Kernhüllen (DCO^+/ $H^{13}CO^+$). Ich untersuche die kleinmaßstäbliche Struktur ausgewählter Kerne mit interferometrischen Beobachtungen von Nachweismitteln für sehr dichtes Gas (NOEMA Beobachtungen von para-NH_2D von B213-10 in Taurus). Diese Beobachtungsdaten werden zusammen mit chemischen Modellen verwendet um die chemische Entwicklung von dichten Kernen zu enthüllen. Ein Vergleich der Ergebnisse von verschiedenen Gruppen von dichten Kernen eingebettet in Taurus, Perseus und Schlangenträger, wird es ermöglichen die Umgebungseffekte auf die dynamische und chemische Entwicklung von dichten Kernen und der damit verbundenen Sternentstehungsrate zu quantifizieren.

Abstract

This project studies the earliest stages of star formation in different environments by observing deuterated molecules and by measuring the deuterium fraction (i.e. the ratio between the column density of the species containing deuterium, in particular N_2D^+ and DCO^+, and the column density of the same species containing hydrogen, N_2H^+ and $H^{13}CO^+$). The deuterium fraction is known to increase in pre-stellar cores, just before the formation of a protostar, and deuterated molecules are used to trace the kinematics and properties of pre-stellar cores. Deuterated molecules are important diagnostic tools for understanding the physical/chemical structure and kinematics of dense and cold gas in molecular clouds, i.e. to study the first steps in the process of star formation.

In the PhD project, I focus my studies on two nearby low-mass star-forming regions: the Ophiuchus molecular cloud, the nearest cluster forming region, and the more quiescent Taurus molecular cloud. The project is based on three papers in which dense core chemistry and kinematics, as well as the substructure around pre-stellar cores, are discussed.

In the first chapter, I study the deuterium fractionation in the dense cores of the L1688 clump in the Ophiuchus molecular cloud, one of the closest ($\sim$120 pc) sites of star formation. A high deuterium fraction is one of the key features of pre-stellar cores, the dense cores on the verge of star formation. I study how the deuterium fraction depends on various physical conditions, such as gas density, temperature, turbulence, and depletion of CO. I show that regions of the same molecular cloud experience different dynamical, thermal, and chemical histories with consequences for the current star formation efficiency and characteristics of future stellar systems.

In the second chapter, I study the kinematics of dense cores in the L1495 filament in the Taurus molecular cloud. Interstellar filaments are common structures in molecular clouds and play an important role in the star-forming process. I use the N_2H^+(1–0) and N_2D^+(2–1) lines to trace the gas of the core centres where CO and other molecules are depleted, the $H^{13}CO^+$(1–0) and DCO^+(2–1) lines to trace the core envelopes to search for any connections between core-scale and cloud-scale kinematics, and $C^{18}O$(1–0) to reveal the kinematics of the filament gas. Unlike the L1688 cores in Ophiuchus, the L1495 cores show very similar properties – subsonic line widths, centroid velocities, velocity gradients, and specific angular momenta. I found that at the level of the cloud-core transition, the core's envelope is spinning up. At small scales the core material is slowing down implying a loss of specific angular momentum. The cloud material stays unaffected by the presence of rotating cores and protostars.

In the third chapter, I study the substructure around a prototypical pre-stellar core, L1544, which is one of the isolated cores in the Taurus molecular cloud. The interferometric observations used reveal the structures of ~700 au scale. The core shows a strong asymmetry in the distribution of methanol around the core. This asymmetry might be produced by asymmetric UV irradiation.

The project gives a prospective to future work on the evolution of dense cores. As a part of the project, a number of observational proposals were submitted to single dish submm telescopes and interferometers, for many of them the data already have been collected. These projects will continue the study of the evolution of dense cores, including their chemistry and kinematics. I will study the chemistry of the dense cores in L1495 (Taurus), L1688 (Ophiuchus), and B5 (Perseus), as well as the kinematics in L1688 and B5. I will compare the deuterium fractions of ions (N_2D^+/N_2H^+, $DCO^+/H^{13}CO^+$) and neutrals (NH_2D/NH_3), as well as that of core centres (N_2D^+/N_2H^+) and envelopes ($DCO^+/H^{13}CO^+$). I will study the small-scale structure of the selected cores with interferometric observations of high density tracers (NOEMA observations of *para*-NH_2D towards the B213-10 core in Taurus). These observational data will be used in tandem with chemical models to unveil the chemical evolution of dense cores on the verge of star formation. Comparing the results from the different sets of dense cores embedded in Taurus, Perseus, and Ophiuchus, will allow us to quantify the environmental effects on the dynamical and chemical evolution of dense cores and the related star formation rate.

Аннотация

Диссертационная работа посвещена изучению ранних стадий звездообразования в разных окружениях с помощью наблюдений дейтерированных молекул и измерения доли дейтерия в молекулах и ионах (т. е. отношения лучевой концентрации молекулы или иона, содержащих дейтерий, в частности N_2D^+ и DCO^+ к лучевой концентрации тех же молекулы или иона, содержащих водород, N_2H^+ и $H^{13}CO^+$). Известно, что доля дейтерия увеличивается в дозвездных ядрах непосредственно перед образованием протозвезды, а дейтерированные молекулы используются для изучения кинематики и физических свойств дозвездных ядер. Дейтерированные молекулы являются важными диагностическими инструментами для понимания физико-химической структуры и кинематики плотного холодного газа в молекулярных облаках, то есть для изучения первых стадий процесса звездообразования.

В диссертационной работе исследованы две близлежащие маломассивные области звездообразования: молекулярное облако в Змееносце, ближайшей области формирования звезд в скоплениях и более спокойное молекулярное облако в Тельце. Диссертация основана на трех работах, в которых изучаются химия и кинематика плотных ядер, а также оболочка дозвездного ядра L1544.

В первой главе изучено фракционирование дейтерия в плотных ядрах клампа L1688 в молекулярном облаке в Змееносце, одной из ближайших ($\sim$120 пк) областей звездообразования. Высокая доля дейтерия является одной из ключевых особенностей дозвездных ядер, плотных ядер на грани звездообразования. Исследуется, как доля дейтерия зависит от различных физических условий, таких как плотность газа, температура, турбулентность и уменьшение содержания CO в газе. Показано, что динамическая, тепловая и химическая эволюции разных областей одного и того же молекулярного облака могут отличаться, что влияет на эффективность текущего звездообразования и свойства будущих звездных систем.

Во второй главе изучена кинематика плотных ядер в филаменте L1495 в молекулярном облаке в Тельце. Межзвездные филаменты являются распространенными структурами в молекулярных облаках и играют важную роль в процессе звездообразования. Линии N_2H^+(1–0) и N_2D^+(2–1) используются для изучения газа центральных областей ядер, где содержание CO и других молекул в газе понижено, линии $H^{13}CO^+$(1–0) и DCO^+(2–1) – для изучения оболочек ядер и поиска связей между кинематикой уровня ядра и уровня родительского облака; и $C^{18}O$(1–0), чтобы выявить кинематику газа в филаменте. В отличие от ядер в L1688 в Змееносце, ядра в L1495 обладают очень близкими свойствами – уровнем турбулентности, центральными скоростями, градиентами скорости и удельными угловыми моментами. Обнаружено, что на уровне перехода от молекулярного облака к плотному ядру оболочка ядра ускоряет вращение. На малых масштабах газ в ядре замедляется, что означает потерю удельного углового момента. Наличие вращающихся ядер и протозвезд не влияет на кинематку газа в окружающем молекулярном облаке.

В третьей главе изучено распределение метанола в оболочке дозвездного ядра L1544, одного из изолированных ядер в молекулярном облаке Тельца. Используемые интерферометрические наблюдения позволяют увидеть структуры размером ∼700 ае. Распределение метанола вокруг L1544 сильно асимметрично. Асимметрию распределения метанола можно объяснить тем, что L1544 неравномерно облучается ультафиолетом.

Наблюдения на радиотелескопах и интерферометрах, полученные в ходе работы над диссертацией, будут использоваться в дальнейшей работе по изучению эволюции плотных ядер. Начатые наблюдательные проекты продолжат изучение эволюции плотных ядер, в том числе их химии и кинематики. Будет изучена химия плотных ядер в L1495 (в Тельце), L1688 (в Змееносце) и B5 (в Персее), а также кинематика в L1688 и B5. Полученные наблюдения позволят сравнить доли дейтерия ионов (N_2D^+/N_2H^+, $DCO^+/H^{13}CO^+$) и молекул (NH_2D/NH_3), а также центральных областей (N_2D^+/N_2H^+) и оболочек ($DCO^+/H^{13}CO^+$) плотных ядер. Будет изучена мелкомасштабная структура выбранных ядер с помощью интерферометрических наблюдений трейсеров плотного газа (наблюдения на интерферометре NOEMA линии *para*-NH_2D(1,1) в ядре B213-10 в Тельце). Эти наблюдательные данные вместе с химическими моделями будут использоваться для реконструкции химической эволюции плотных ядер на пороге звездообразования. Сравнение результатов, полученных для плотных ядер в разных молекулярных облаках (в Тельце, Персее и Змееносце), позволит количественно оценить влияние окружения на динамическую и химическую эволюцию плотных ядер и соответствующую скорость звездообразования.

Introduction

Low-mass star formation

Stars are formed in molecular clouds (MC) out of dust and gas. Molecular clouds are self-gravitating structures with sizes of a few tens of parsecs (e.g. Cambrésy 1999), densities of $>10^3$ cm^{-3}, temperatures of $\sim$10 K, and lifetimes of a few millions of years (e.g. Stahler & Palla 2005; Bergin & Tafalla 2007, for review). The instabilities caused by external or internal effects (like supernovae explosions, stellar feedback) initiate the clouds' fragmentation. Hierarchical fragmentation leads to the formation of dense cores which collapse to form stars or dissipate. Figure 1 schematically shows the modern view of the low-mass star formation process. A dense core (pre-stellar core) starts to collapse, the infalling material forms an accretion disk and a class 0 young stellar object (YSO), also referred as a protostar, in the centre, with outgoing jets, and a vast envelope around it. With evolution, the envelope grows thinner as the material is accreted onto the protostar, the accretion disk becomes denser and thinner, and the jets grow stronger. The class II YSO is a classic T Tau star (a pre-main sequence star) and the class III YSO is an evolved T Tau star. On the way from a dense core to a main-sequence star, the infalling material looses its specific angular momentum by 6 to 7 orders of magnitude (e.g. Belloche 2013). Over time, the rest of the envelope is blown away and the protostar continues to contract until the nuclear fusion of hydrogen starts and the object becomes a zero age star.

Some of the closest sites of star formation to the Sun are the molecular clouds projected onto the constellations of Ophiuchus, Taurus, Auriga, Perseus. The molecular clouds show a diversity in mass, density, and rate of star formation. In this thesis I discuss the objects from two molecular clouds: the Ophiuchus molecular cloud, a site of active star formation with a higher level of turbulence and a higher average gas density; and the Taurus molecular cloud, with less dense and more quiescent gas, and a lower rate of star formation.

The latest sub-millimetre observations of nearby star-forming regions with the *Herschel Space Observatory* show that molecular clouds are often structured in interstellar filaments, so they play an important role in the star-forming process (e.g. Men'shchikov et al. 2010; André et al. 2014). The filaments host chains of dense cores (e.g. Hacar et al. 2013; Könyves et al. 2014). To study a typical process of star formation one needs to study the dense cores embedded within filaments.

The aim of this project is to study the environmental effects on the evolution of dense cores, including pre-stellar cores, the earliest stages of star formation. The environmental

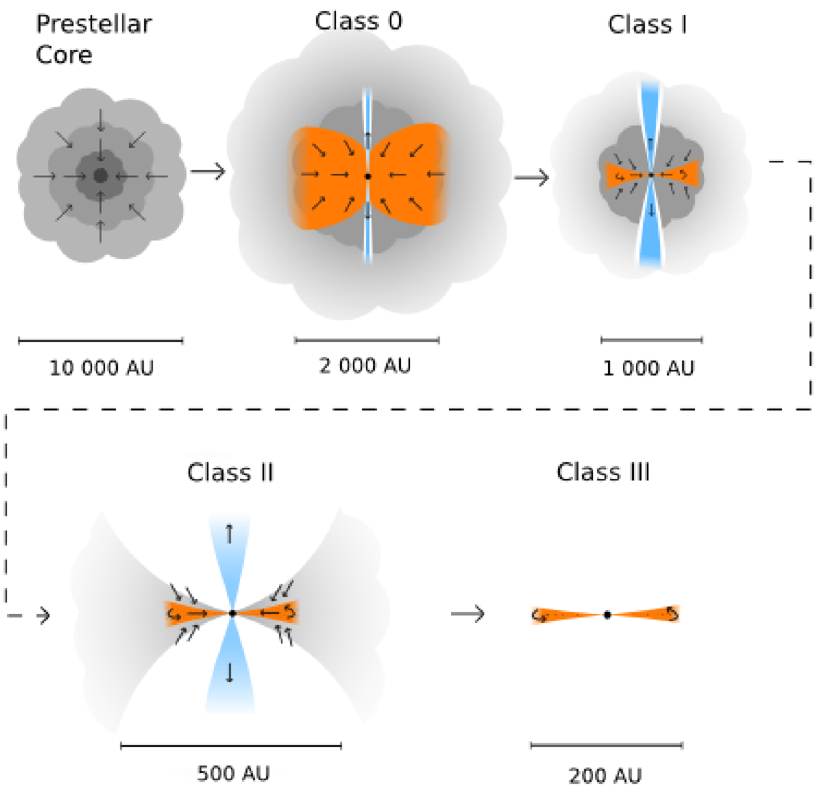

Figure 1: The scematic view of the current understanding of the star formation process. The picture is adapted from Magnus Vilhelm Persson's web page `http://vilhelm.nu/water.php`.

effects are important to understand the initial conditions of the star formation process. By studying the diverse regions I compare the environmental effects on the gas chemistry and kinematics.

Dense cores

The term dense core is a common name for cores at different evolutionary stages. They are classified as starless, pre-stellar, and protostellar cores. In this work, I call dense cores with no embedded protostar and no signs of contraction starless cores; dense cores with no embedded protostar but signs of starting gravitational collapse pre-stellar cores; and dense cores with an embedded protostar protostellar cores. From the observational point of view, at the stage of detection of a core with sub-millimetre observations of dust continuum emission or molecular line emission (which are usually used for cores detection) there is no difference between the three stages. Deep analysis is needed to confirm that a core is at the pre-stellar stage which is the stage of the most interest of this work as it represents the initial conditions of the star formation process.

Pre-stellar cores are dense (10^4–10^7 cm^{-3}), cold ($\sim$10 K), and quiescent (thermal pressure dominates over turbulent motions; e.g. Benson & Myers 1989; Fuller & Myers 1992; Lada et al. 2008; Caselli et al. 2008) self-gravitating structures (Ward-Thompson et al. 1999; Keto & Caselli 2008). Pre-stellar cores are characterised by high deuterium fractions (Crapsi et al. 2005; Emprechtinger et al. 2009; Friesen et al. 2013; Fontani et al. 2014; Punanova et al. 2016). The deuterium fraction is the ratio between the column density of the species containing deuterium, for example, N_2D^+ and DCO^+, and the column density of the same species containing hydrogen, N_2H^+ and $H^{13}CO^+$.

Chemical fractionation

The physical conditions within a dense core change with radius. From the edges to the centre the gas becomes colder and denser, turbulence dissipates, and the level of ultraviolet (UV) irradiation decreases. The changes in the physical conditions causes chemical fractionation (see Fig. 2). In the outskirts of cores and in the surrounding cloud, where the visual extinction is low ($A_v < 2^m$), the gas is chemically younger. At higher densities less UV radiation reaches the gas, such that various molecules and molecular ions, such as H_2O, CO, OH, simple carbon chains, HCO^+, form in the gas phase (dust grains can also play a small role in their formation). Most of carbon is locked in CO. At $A_v > 4^m$ and densities $> 10^4$ cm^{-3} the molecules, beginning with H_2O and CO, start to freeze onto the dust grain surfaces and form ice mantles (e.g. Bergin & Tafalla 2007). More complex molecules, like methanol, can then start to form on dust grains (e.g. Tielens & Hagen 1982). In reactions of atomic nitrogen with OH and CH, and the products of these reactions, NO and CN, in the gas phase, N-bearing species, N_2 and products of N_2 – N_2H^+ and NH_3, and their deuterated isotopologues, are formed (Hily-Blant et al. 2010). I will hereafter refer to the shell with densities between 10^4 cm^{-3} and 10^6 cm^{-3} as a neutral depletion zone.

The H_3^+ ion plays an important role in the formation of hydrogen-bearing ions like HCO^+ and N_2H^+. H_3^+ is formed via the following reactions:

$$H_2 + \text{cosmic ray proton} \rightarrow H_2^+, \tag{1}$$

$$H_2^+ + H_2 \rightarrow H_3^+ + H, \tag{2}$$

(Herbst & Klemperer 1973). In a molecular cloud, where hydrogen is mostly in molecular form and the cosmic ray ionization rate is mostly constant, the abundance of H_3^+ is constant and does not vary with depth within a dense core. In the depletion zone, the deuterated isotopologues of H_3^+ enhance their abundances (e.g. Parise et al. 2011). H_2D^+, which starts deuterated chemistry, is formed in the deuteron-proton exchange reaction:

$$H_3^+ + HD \rightleftharpoons H_2D^+ + H_2 + 230\text{ K}, \tag{3}$$

(Watson 1976; Millar et al. 1989). At the low temperatures of dense cores this reaction only goes left to right. Depending on its nuclear spin symmetry, H_2 molecule can take *ortho* (with parallel spins) and *para* (with antiparallel spins) forms. Being more energetic than *para*-H_2, *ortho*-H_2 could drive the reaction backwards, but in cold and dense gas, the abundance of *ortho*-H_2 is only a small fraction ($\simeq 10^{-4}$) of the *para*-H_2 abundance (e.g. Sipilä et al. 2013). CO and other neutrals, which could efficiently destroy H_3^+, are mainly frozen onto dust grain surfaces (e.g. Caselli et al. 1999; Bacmann et al. 2002). H_2D^+ can then cede a deuteron to abundant species such as CO and N_2, producing DCO^+ and N_2D^+:

$$H_3^+ + A \rightarrow AH^+ + H_2, \tag{4}$$

where A can be any of CO, N_2, and other neutral species (Herbst & Klemperer 1973). In the case of H_2D^+:

$$H_2D^+ + N_2 \rightarrow N_2D^+ + H_2, \tag{5}$$

or

$$H_2D^+ + N_2 \rightarrow N_2H^+ + HD, \tag{6}$$

(Dalgarno & Lepp 1984). Thus, deuterium fractionation increases in cold and dense regions, making deuterated molecules a powerful tool to study the initial conditions of star formation, including the ionisation fraction (Caselli et al. 2002c), which is crucial for the evolution of magnetised clouds (Bailey & Basu 2012).

The level of CO depletion can be estimated with the CO depletion factor, the ratio of the initial CO abundance to the CO abundance observed in the gas phase. The gas phase abundance of CO, the second most abundant molecule after H_2 in molecular clouds, plays a primary role in determining the abundance of any deuterated species, as CO (as well as other abundant neutral species) destroys H_3^+ and H_2D^+. The CO depletion factor also traces the physical conditions in the gas, such as the density, temperature, and UV irradiation.

The deuterium fraction observed in dense cores varies between 0.01 and 1, and the CO depletion factor typically lies between 1 and 30 (see e.g. Crapsi et al. 2005; Emprechtinger et al. 2009). Crapsi et al. (2005), in their study of starless cores in different star-forming regions (the Ophiuchus, Taurus and Aquila molecular clouds), derive an empirical relation between deuterium fraction and CO depletion factor, with the deuterium fraction increasing with increasing CO depletion factor. This positive correlation between deuterium fraction and CO depletion factor was confirmed with observations of a large sample (>100) of cores in the Taurus, Ophiuchus, and Perseus molecular clouds (Caselli et al. 2002c, 2008; Emprechtinger et al. 2009; Friesen et al. 2013; Punanova et al. 2016). The correlation was shown to be a natural result of chemical evolution in cold dark clouds in several theoretical works (e.g. Caselli et al. 2008; Kong et al. 2015; Harju et al. 2017).

At densities higher than a few 10^6 cm^{-3} most species are frozen onto the dust grains; only simple ions like H_2D^+ and D_2H^+ stay in the gas phase.

Gas tracers

The main instrument to study molecular clouds is sub-millimetre observations of dust continuum emission and spectral lines of different interstellar species. To measure the

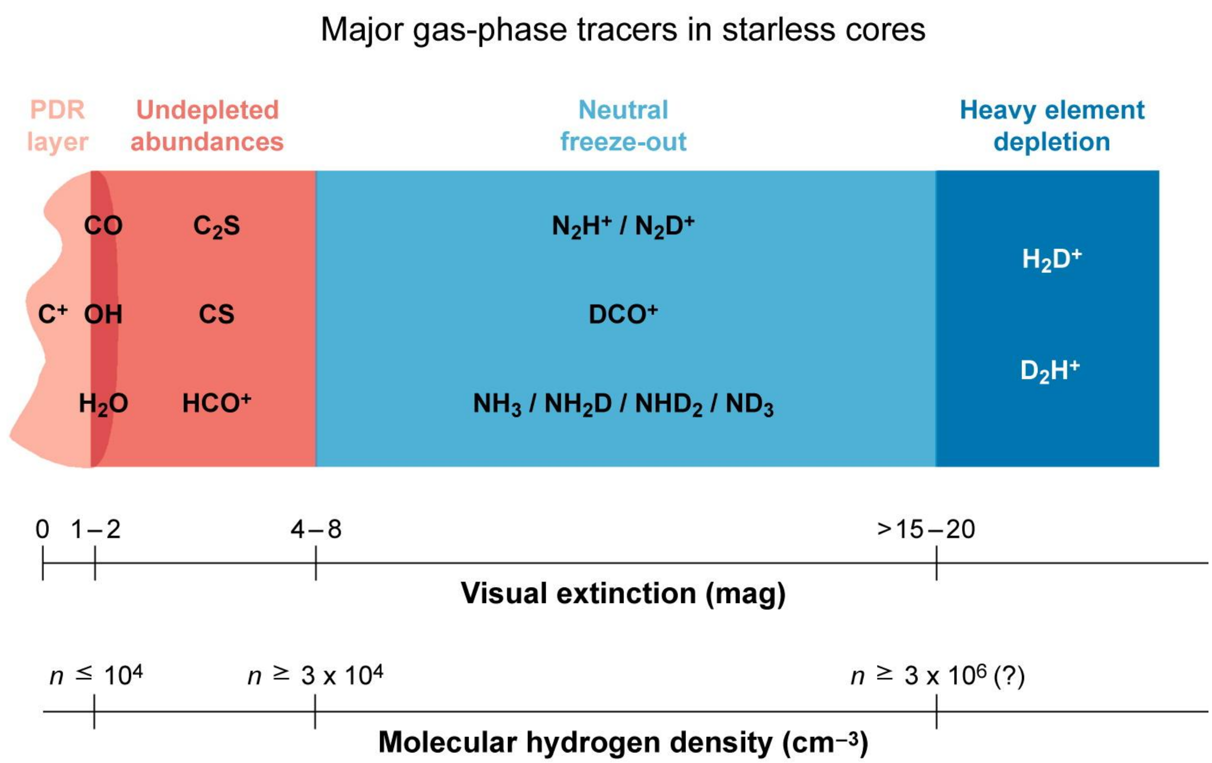

Figure 2: Schematic summary of the major gas-phase tracers in dense cores as a function of depth and density. The extinction and density scales are approximate. The temperature is assumed to be low (< 15 K) where $A_v > 2^m$. The picture is adapted from Bergin & Tafalla (2007).

total molecular hydrogen column density, needed to calculate molecular abundances, dust continuum emission between 0.25–1.3 mm is often used. Numerous surveys of such dust emission are presented in the literature, including some based on *Herschel* observations (e.g. André et al. 2010; Palmeirim et al. 2013; Marsh et al. 2014; Pattle et al. 2015). To measure the column densities of molecular species and to trace the gas kinematics, the emission lines of their rotational and inversional transitions are observed.

The chemical fractionation of dense cores means that different various species trace different parts of the cores. While carbon-bearing species are abundant in the outer layers of the cores and depleted in the deeper parts, nitrogen-bearing species appear in the evolved gas and stay in the gas phase up to densities of 10^6 cm^{-3} (Crapsi et al. 2005, 2007). Deuterated species trace denser gas than their hydrogenated analogues due to deuterium fractionation. Rare isotopologues, being less abundant than main isotopologues (for instance $H^{13}CO^+$ and $HC^{18}O^+$ compared to HCO^+), serve to test the optical depth of the lines. Rotational transitions of higher levels typically excited at higher densities (n_{crit}). For example, N_2H^+(1–0) has critical density $\sim 10^5$ cm^{-3} and N_2H^+(3–2) has $n_{crit} \simeq 2\times10^6$ cm^{-3}. This means that higher transitions trace higher densities and thus deeper areas of the dense cores.

Hyperfine splitting of transition levels produce hyperfine structure (hfs) of the spectral lines. If the line is not saturated and the hyperfine components are well separated, the hfs helps to define the centroid velocity and optical depth of the line with high accuracy, thereby improving the determination of the kinematics of the gas and the column densities of the observed species.

In this work, I use $C^{17}O$ and $C^{18}O$ to trace the molecular cloud gas; $H^{13}CO^+$, $HC^{18}O^+$, DCO^+, $D^{13}CO^+$, and CH_3OH to trace the core envelopes; and N_2H^+ and N_2D^+ to trace the central parts of the cores (including the neutral depletion zone).

Thesis overview

In the PhD project, I focus my studies on two nearby low-mass star-forming regions: the Ophiuchus molecular cloud, the nearest cluster forming region, and the more quiescent Taurus molecular cloud. The project is based on three papers in which dense core chemistry and kinematics, as well as the substructure around pre-stellar cores, are discussed.

Chapter 1 presents a study of deuterium fractionation in 33 dense cores in the L1688 clump in the Ophiuchus molecular cloud. The selection contains both starless and protostellar cores. I study how deuterium fraction depends on various physical conditions, such as gas density, temperature, turbulence, and depletion of CO. I show that regions of the same molecular cloud experience different dynamical, thermal, and chemical histories with consequences for the current star formation efficiency and characteristics of future stellar systems.

Chapter 2 presents a study of the kinematics of 13 dense cores in the L1495 filament in the Taurus molecular cloud. I use the N_2H^+(1–0) and N_2D^+(2–1) lines to trace the gas of the core centres, the $H^{13}CO^+$(1–0) and DCO^+(2–1) lines to trace the core envelopes to search for any connections between core-scale and cloud-scale kinematics, and the $C^{18}O$(1–0) line to reveal the kinematics of the filament gas. Unlike the L1688 cores in Ophiuchus, the L1495 cores show very similar properties – subsonic line widths, centroid velocities, velocity gradients, and specific angular momenta. I find that at the level of the cloud-core transition, the core's envelope is spinning up. At small scales the core material is slowing down implying a loss of specific angular momentum. The cloud material stays unaffected by the presence of rotating cores and protostars.

Chapter 3 presents a study of the substructure around a prototypical pre-stellar core, L1544, which is one of the isolated cores in the Taurus molecular cloud. The interferometric observations used reveal the structures of $\sim$700 au scale. The core shows a strong asymmetry in the distribution of methanol around the core. This asymmetry might be produced by asymmetric UV irradiation.

In **Chapter 4** I give the general conclusions of the thesis and show the prospects of started work on the evolution of dense cores. I describe the observational projects done with single dish sub-mm telescopes and interferometers, for which the data already have been collected. These projects will continue the study of the evolution of dense cores, including their chemistry and kinematics.

Chapter 1

Deuterium fractionation in the Ophiuchus molecular cloud

This chapter is based on the paper Punanova, A., Caselli, P., Pon, A., Belloche, A., and André, Ph., A&A 587, A118, 2016.

Abstract

Context. In cold ($T < 25\,$K) and dense ($n_H > 10^4\,$cm^{-3}) interstellar clouds, molecules like CO are significantly frozen onto dust grain surfaces. Deuterium fractionation is known to be very efficient in these conditions as CO limits the abundance of H_3^+, the starting point of deuterium chemistry. In particular, N_2D^+ is an excellent tracer of dense and cold gas in star-forming regions.

Aims. We measure the deuterium fraction, R_D, and the CO-depletion factor, f_d, towards a number of starless and protostellar cores in the L1688 region of the Ophiuchus molecular cloud complex and search for variations based upon environmental differences across L1688. The kinematic properties of the dense gas traced by the N_2H^+ and N_2D^+ (1–0) lines are also discussed.

Methods. R_D has been measured via observations of the J = 1–0 transition of N_2H^+ and N_2D^+ towards 33 dense cores in different regions of L1688. f_d estimates have been done using $C^{17}O$(1–0) and 850 μm dust continuum emission from the SCUBA survey. All line observations were carried out with the IRAM 30 m antenna.

Results. The dense cores show large ($\simeq$2–40%) deuterium fractions, with significant variations between the sub-regions of L1688. The CO-depletion factor also varies from one region to another (between $\simeq$1 and 7). Two different correlations are found between deuterium fraction and CO-depletion factor: cores in regions A, B2, and I show increasing R_D with increasing f_d, similar to previous studies of deuterium fraction in pre-stellar cores; cores in regions B1, B1B2, C, E, F, and H show a steeper R_D–f_d correlation, with large deuterium fractions occurring in fairly quiescent gas with relatively low CO freeze-out factors. These are probably recently formed, centrally concentrated starless cores which have not yet started the contraction phase towards protostellar formation. We also find

that the deuterium fraction is affected by the amount of turbulence, dust temperature, and distance from heating sources in all regions of L1688, although no clear trend is found.

Conclusions. The deuterium fraction and amount of CO freeze-out are sensitive to environmental conditions and their variations across L1688 show that regions of the same molecular cloud experience different dynamical, thermal and chemical histories, with consequences for the current star formation efficiency and the characteristics of future stellar systems. The large pressures present in L1688 may induce the formation of small dense starless cores, unresolved with our beam, where the $\mathrm{R_D}$–f_d relation appears to deviate from that expected from chemical models. We predict that high angular resolution observations will reconcile observations with theory.

1.1 Introduction

The first stages of the star formation process are dense starless and self-gravitating cores, i.e. the so-called pre-stellar cores (Ward-Thompson et al. 1999; Crapsi et al. 2005). Pre-stellar cores in nearby star-forming regions are typically cold ($\sim$10 K), dense (10^4–10^7 cm^{-3}), and quiescent (thermal pressure dominates over turbulent motions; e.g. Benson & Myers 1989; Fuller & Myers 1992; Lada et al. 2008; Keto & Caselli 2008).

Chemical differentiation takes place in pre-stellar cores (see e.g. Bergin & Tafalla 2007; di Francesco et al. 2007; Caselli 2011, for reviews). While CO is the second most abundant molecule in the interstellar medium, it tends to freeze onto dust grains in the dense, cold conditions at the centres of pre-stellar cores (e.g. Caselli et al. 1999; Bacmann et al. 2002). The level of CO depletion is usually measured as $f_d = X_{ref}(\mathrm{CO})/N(\mathrm{CO}) \cdot N(\mathrm{H_2})$, where $X_{ref}(\mathrm{CO})$ is the reference value of the CO fractional abundance, typically between 1 and 2 $\times\ 10^{-4}$ (e.g. Frerking et al. 1982; Lacy et al. 1994). The typical value of the CO-depletion factor in pre-stellar cores is 5–20 (Crapsi et al. 2005; Christie et al. 2012).

In such cold and dense gas, deuterated species are preferentially formed (e.g. Caselli & Ceccarelli 2012). $\mathrm{H_2D^+}$ is responsible for the enhancement of the deuterium fraction in most molecular species and is formed by the deuteron-proton exchange reaction $\mathrm{H_3^+ + HD \rightleftharpoons H_2D^+ + H_2} + 230$ K (Millar et al. 1989). The deuteron-proton exchange reaction is exothermic and does not proceed from right to left at temperatures lower than 30 K and if most of the $\mathrm{H_2}$ molecules are in para form (e.g. Pagani et al. 1992). $\mathrm{H_2D^+}$ then reacts with other species to form deuterated ions via $\mathrm{H_2D^+ + A \rightarrow AD^+ + H_2}$, where A can be any of CO, $\mathrm{N_2}$, and other neutral species (Herbst & Klemperer 1973; Dalgarno & Lepp 1984). When CO and other abundant neutral species, which destroy $\mathrm{H_3^+}$ and $\mathrm{H_2D^+}$, are severely frozen onto dust grain surfaces, the deuterium fraction becomes significant. For example, the deuterium fraction in pre-stellar cores is 5–50%, while the elemental abundance of deuterium is $\sim 1.5 \times 10^{-5}$ with respect to hydrogen atoms within 1 kpc of the Sun (Linsky et al. 2006; Caselli 2011).

In particular, the deuterium fraction of $\mathrm{N_2H^+}$ has been used to identify the earliest phases of star-formation, as the $\mathrm{N_2H^+}$ deuterium fraction peaks at the pre-stellar phase and towards the youngest protostars (Crapsi et al. 2005; Emprechtinger et al. 2009; Friesen et al. 2013; Fontani et al. 2014). The deuterium fraction in N_2H^+ is usually given as $R_D = N(N_2D^+)/N(N_2H^+)$, where $N(i)$ is the column density of species i.

L1688 is a nearby, 119±6 pc distant (Lombardi et al. 2008) low-mass star-forming region within the Ophiuchus Molecular Cloud Complex. The multiple star- forming regions within L1688 contain more than 60 dense cores and 200 young stellar objects in different evolutionary stages (Motte et al. 1998; André et al. 2007; Simpson et al. 2008; Pattle et al. 2015; Dunham et al. 2015). L1688 is divided into 10 regions (A–I; see Fig. 1.1) with different environmental properties. For instance, while the gas temperature is relatively constant within each region, it varies significantly from one region to another (≃10–17 K; Friesen et al. 2009).

The deuterium fraction across the entirety of L1688 has not been systematically studied yet. For only a few regions has the deuterium fraction been measured, for example, the B2 region has an average $R_D \sim 3\%$ (Friesen et al. 2010). CO-depletion across the whole of Ophiuchus has been found to be relatively low compared to the other Gould Belt star-forming regions, with an average value less than 10 (Gurney et al. 2008; Christie et al. 2012).

In this paper, we present observations of N_2D^+(1–0), N_2D^+(2–1), N_2H^+(1–0), $C^{17}O$(1–0), and $C^{17}O$(2–1) towards 40 cores to measure the deuterium fraction and CO depletion factor across the entire L1688 region. In Section 2, details regarding the observations are presented. Section 3 describes the results of hyperfine structure fitting as well as deuterium fraction and CO-depletion calculations. In Section 4, we discuss the results and their relation to possible environmental effects. The conclusions are given in Section 5.

1.2 Observations and data reduction

Figure 1.1 shows the L1688 region mapped in 850 μm dust continuum emission (Di Francesco et al. 2008). 40 dense cores, revealed by Motte et al. (1998) with 1.3 mm dust emission mapping, were selected for observation with the IRAM 30 m telescope and are shown with filled blue squares. The names and positions of the cores are given in Table A.1. We note that the majority of the dense cores are starless with the exception of: VLA1623, well known class 0 source (see e.g. André et al. 1993); E-MM3, YSO with an edge-on circumstellar disk (Brandner et al. 2000); B1-MM4, B1B2-MM2, B2-MM8, B2-MM10 where the protostar position does not coincide with the millimetre dust peak from Motte et al. (1998) but it is within half beam of our N_2D^+(1–0) observations. Figure 1.1 also shows the positions of young stellar objects (YSOs) embedded in the cloud as open circles (Motte et al. 1998; Simpson et al. 2008; Dunham et al. 2015). The molecular line observations were performed with the IRAM 30 m telescope in June 1998, July 2000, and December 2004. The following transitions were observed: N_2D^+(1–0), N_2D^+(2–1), N_2D^+(3–2), N_2H^+(1–0), N_2H^+(3–2), $C^{17}O$(1–0), and $C^{17}O$(2–1). The observations were obtained with the AB receiver and the VESPA backend. Typical system temperatures for the (1–0) transition observations were 100–200 K for N_2H^+–N_2D^+ and 200–360 K for the $C^{17}O$ line. The spectral resolution for the N_2H^+, N_2D^+, and $C^{17}O$ (1–0) lines varied

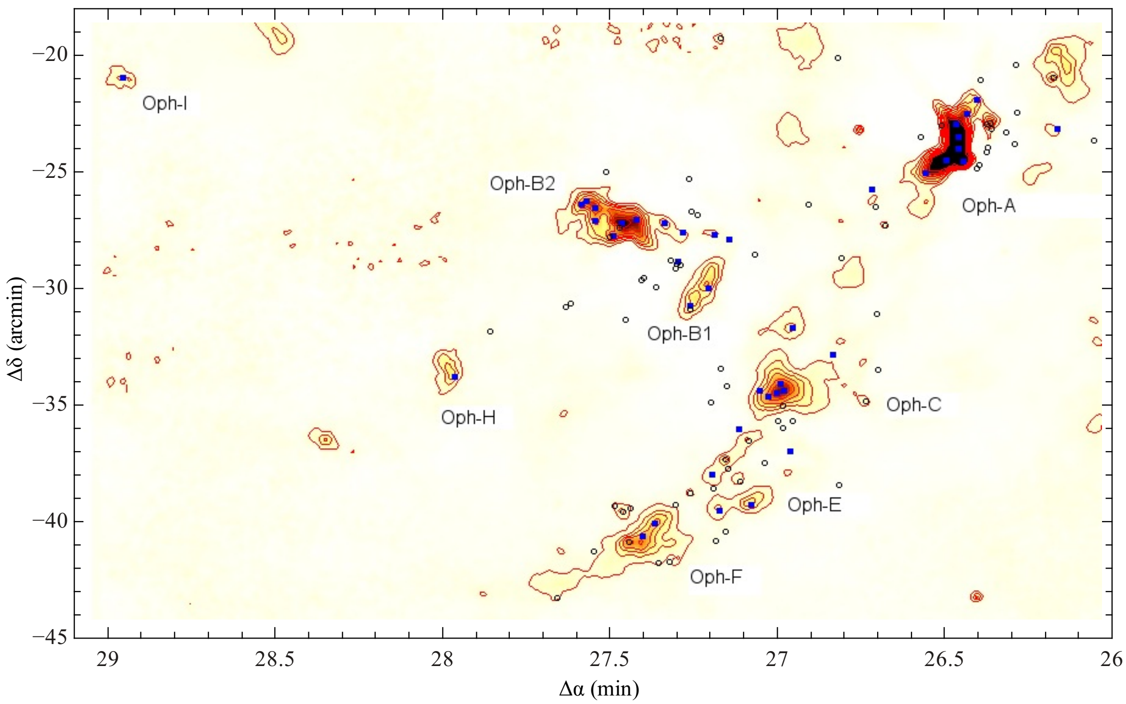

Figure 1.1: 850 μm continuum emission of the L1688 region mapped by the Submillimetre Common-User Bolometer Array (SCUBA, Di Francesco et al. 2008), the beam size is 22.″9. Contour levels go from 0.2 Jy beam^{-1} in steps of 0.2 Jy beam^{-1} (3σ). The dense cores studied here are marked by filled blue squares and young stellar objects by open circles. The (0,0) offsets correspond to the J2000 equatorial position $\alpha = 16^{\rm h}00^{\rm m}00^{\rm s}$, $\delta = -24°00'00''$. The fits file used to produce this map is available at http://www.cadc-ccda.hia-iha.nrc-cnrc.gc.ca/data/pub/JCMTSL/scuba_F_850umemi, file name scuba_F_353d1_16d8_850um.emi.fits.

from 6.5 to 40 kHz and the angular resolutions were 22, 32.1, and 26.6 arc seconds for $C^{17}O(1\text{–}0)$, $N_2D^+(1\text{–}0)$, and $N_2H^+(1\text{–}0)$, respectively (see Table 1.1). The spectra were taken using the position switching (datasets 051-00 and 188-97) and frequency switching (dataset 066-04, with a frequency throw of 7.8 MHz) modes. In Table 1.1, the dates of the observing runs are given and each run denoted with a dataset number. Part of $N_2H^+(1\text{–}0)$ spectra from datasets 051-00 and 188-97 are already presented in André et al. (2007).

The data reduction was performed with the CLASS package[1]. For each source, there were several spectra of the same line. These spectra have been adjusted to have the same central frequency and summed together to improve the sensitivity. The integration time for different lines and objects varies from 4 to 30 minutes. The intensity scale was converted to the main-beam temperature scale according to the beam efficiency values given in Table 1.1.

The $N_2D^+(1\text{–}0)$, $N_2D^+(2\text{–}1)$, $N_2H^+(1\text{–}0)$, $C^{17}O(1\text{–}0)$, and $C^{17}O(2\text{–}1)$ lines have hyperfine splitting with 15, 40, 15, 3, and 9 components respectively. As such, the spectra were analysed using the standard CLASS hyperfine structure (hfs) fitting method. The routine computes line profiles, with the assumptions of Gaussian velocity distribution and equal excitation temperatures for all hyperfine components. The rest frequencies of the main components, the velocity offsets and the relative intensities of the hyperfine components of the lines were taken from Frerking & Langer (1981), Pagani et al. (2009) and Dore, L. (private communication). The $N_2D^+(3\text{–}2)$ and $N_2H^+(3\text{–}2)$ spectra have very poor baselines and reconstruction of the signal is not possible, so these data are not considered hereafter in the paper.

All spectra were initially fit assuming one velocity component. The hfs fitting routine returns both the rms of the baseline and the region with the spectral line. In case the rms of the spectral line region was greater than the rms of the baseline by a factor of 1.5, we redid the fit with an additional velocity component. This was repeated until the two rms agreed within a factor of 1.5. The largest number of velocity components needed was three.

[1] Continuum and Line Analysis Single-Dish Software http://www.iram.fr/IRAMFR/GILDAS

Table 1.1: Observation parameters.

Species	Frequency[a] (GHz)	F_{eff}	B^{f}_{eff}	HPBW ($''$)	Δv^{g}_{res} (km s^{-1})	rms in T_{mb} (K)	T_{sys} (K)	Dates	Dataset[h]
N_2H^+(1–0)	93.1737637[b]	0.95	0.76	26.5	0.021	0.121	155–176	16.08.2004	066-04
N_2H^+(1–0)	93.1737637	0.92	0.78	26.5	0.063	0.089	114–205	11–16.07.2000	051-00
N_2H^+(1–0)	93.1737637	0.92	0.73	26.5	0.063	0.174	173–216	26–28.06.1998	188-97
N_2H^+(3–2)	279.511832[b]	0.87	0.46	8.8	0.021		652–2739	12–13.08.2004	066-04
N_2D^+(1–0)	77.1096162[b]	0.95	0.76	32.1	0.025	0.103	167–216	12–17.08.2004	066-04
N_2D^+(2–1)	154.2171805[c]	0.94	0.64	16.3	0.013	0.225	203–627	12–15.08.2004	066-04
N_2D^+(3–2)	231.3219119[c]	0.90	0.52	10.8	0.025		244–710	16.08.2004	066-04
$C^{17}O$(1–0)	112.358988[d]	0.95	0.78	22.0	0.017	0.218	243–320	16.08.2004	066-04
$C^{17}O$(1–0)	112.358988	0.92	0.78	22.0	0.052	0.143	184–289	12.07.2000	051-00
$C^{17}O$(1–0)	112.358988	0.92	0.73	22.0	0.052	0.180	265–359	29–30.06.1998	188-97
$C^{17}O$(2–1)	224.714370[e]	0.85	0.53	11.0	0.532	0.626	629–1366	13-16.07.2000	051-00
$C^{17}O$(2–1)	224.714370	0.90	0.42	11.0	0.052	0.977	995-1800	29–30.06.1998	188-97

[a] Frequency of the main hyperfine component; [b] from Pagani et al. (2009); [c] from Pagani et al. (2009) and Dore, L., private communication; [d] from Frerking & Langer (1981); [e] from SPLATALOGUE database http://www.cv.nrao.edu/php/splat/; [f] B_{eff} values are available at the 30 m antenna efficiencies web-page https://www.iram.fr/IRAMFR/ARN/aug05/node6.html; [g] Δv_{res} is the velocity resolution; [h] dataset name is the ID of the corresponding IRAM 30 m project.

1.3 Results

1.3.1 Spectra

The spectra of the N_2D^+(1–0), N_2H^+(1–0), and $C^{17}O$(1–0) lines are shown in Fig. 1.2. The N_2H^+(1–0), $C^{17}O$(1–0), and $C^{17}O$(2–1) emission was detected towards all 40 observed cores. N_2D^+(1–0) emission was detected towards 23 out of 33 observed cores and N_2D^+(2–1) emission was detected towards 25 out of 32 observed cores, with the A-MM4 core only having (2–1) detection. As the aim of the study is the measurement of deuterium fractions and their comparison to CO-depletion factors, we focus on the (1–0) transitions for the remainder of the paper, since they have the most similar beam sizes and excitation conditions. Towards five cores (B1-MM3, B1-MM4, B2-MM2, B2-MM8, and F-MM2), the N_2H^+(1–0) line shows two velocity components. The $C^{17}O$(1–0) line towards all of the objects in regions C (except C-Ne and C-MM3) and E and one in A (SM1N) shows two or three velocity components. The $N_2D^+(1-0)$ line shows two velocity components towards one core, B1-MM4. The results of the hfs fits are given in Tables A.2–A.6.

The centroid velocities, V_{LSR}, are determined from the hfs fitting and vary across L1688 from 3.3 to 4.6 km s^{-1} with a velocity generally increasing from region A to F. Figure 1.3 shows the centroid velocities for the N_2H^+(1–0), N_2D^+(1–0), and $C^{17}O$(1–0) lines. If two velocity components are detected in N_2H^+(1–0) and N_2D^+(1–0) (e.g. towards B1-MM4), both components are plotted in the left panel of Fig. 1.3. If only N_2H^+(1–0) shows two components we instead plot an average of the two components if the single N_2D^+(1–0) line component appears to be a blend of multiple component (cores B2-MM2, B2-MM8, and F-MM2), and we plot just the velocity of the closest N_2H^+(1–0) component if the N_2D^+(1–0) component does not appear to be blended, with the second N_2D^+(1–0) component presumably not being detected above the noise level (core B1-MM3). The three cases are illustrated in Fig. 1.4. However, only a small fraction of the points (4/25) shown in Fig. 1.3 are for locations with different numbers of components detected in the two different tracers. For the right panel of Fig. 1.3, we plot each N_2H^+(1–0) component against the closest $C^{17}O$(1–0) component.

For 80% of the cores, the V_{LSR} of the N_2H^+(1–0) and N_2D^+(1–0) lines are within 0.05 km s^{-1} of each other. The largest centroid velocity difference is only 0.21 km s^{-1}. The $C^{17}O$(1–0) and N_2H^+(1–0) V_{LSR} can differ significantly with discrepancies up to 1 km s^{-1}. 51% of the cores have velocities that differ by over 0.1 km s^{-1}. This suggests that N_2H^+(1–0) and N_2D^+(1–0) trace roughly the same gas while $C^{17}O$(1–0) likely traces more extended gas, as expected considering the widespread distribution of CO in molecular clouds and its freeze-out in dense cold regions.

The line widths (full width at half maximum, FWHM, hereinafter Δv) of N_2H^+, N_2D^+, and $C^{17}O$ (1–0) are shown in Fig. 1.5. As before, when N_2H^+ and N_2D^+ show two velocity components, we plot them separately (B1-MM4). In the case where two velocity components are present in N_2H^+ and only one is seen in N_2D^+, we either take the Δv of N_2H^+ of the component with the closest V_{LSR}, if it appears that one component of N_2D^+ is missing due to the noise level (B1-MM3), or we take $\Delta v = \Delta v_1/2 + \Delta v_2/2 + |V_{LSR1} - V_{LSR2}|$ if the

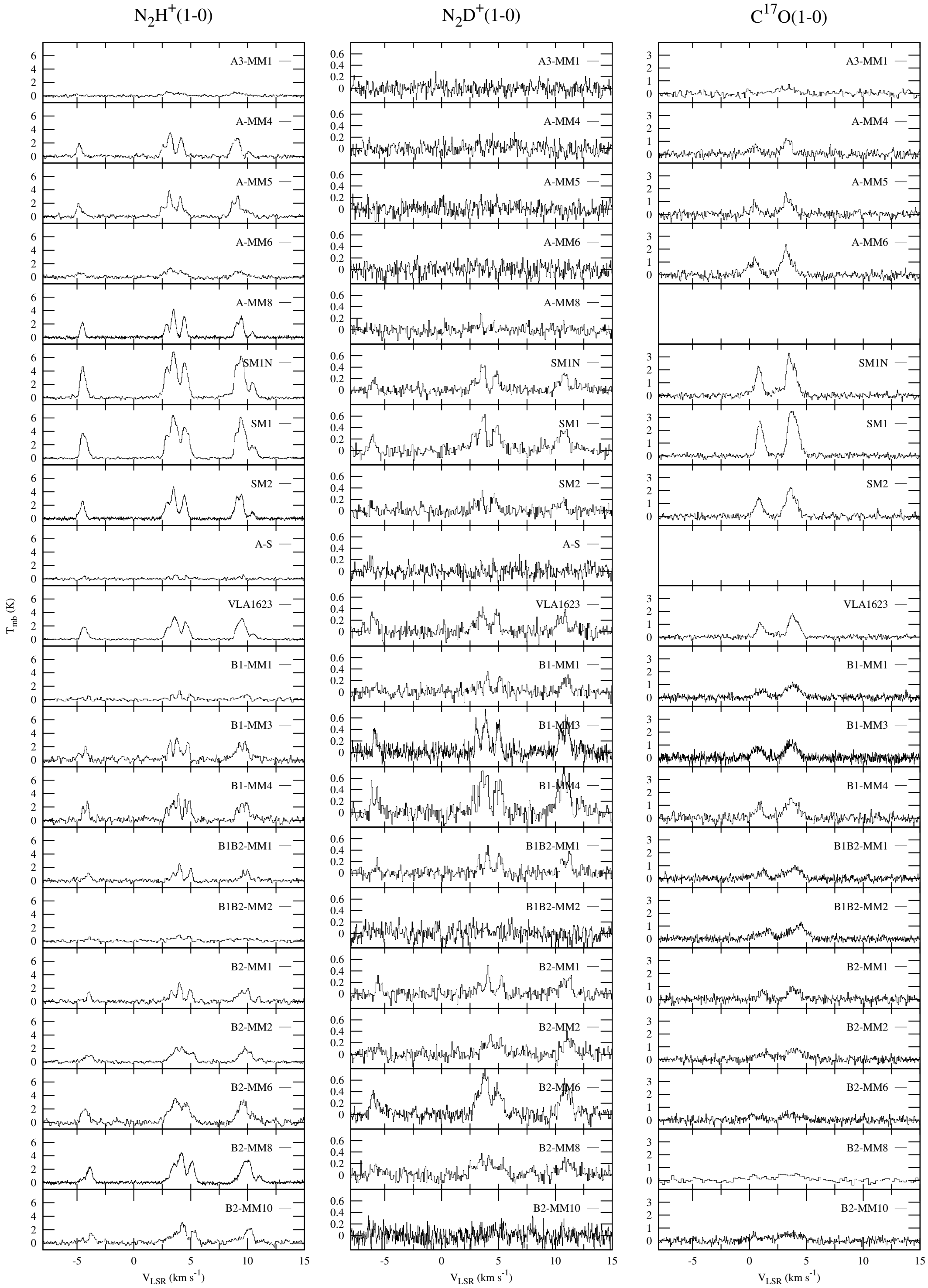

Figure 1.2: N_2H^+(1-0), N_2D^+(1-0), and $C^{17}O$(1–0) spectra towards the observed dense cores, labeled in each panel.

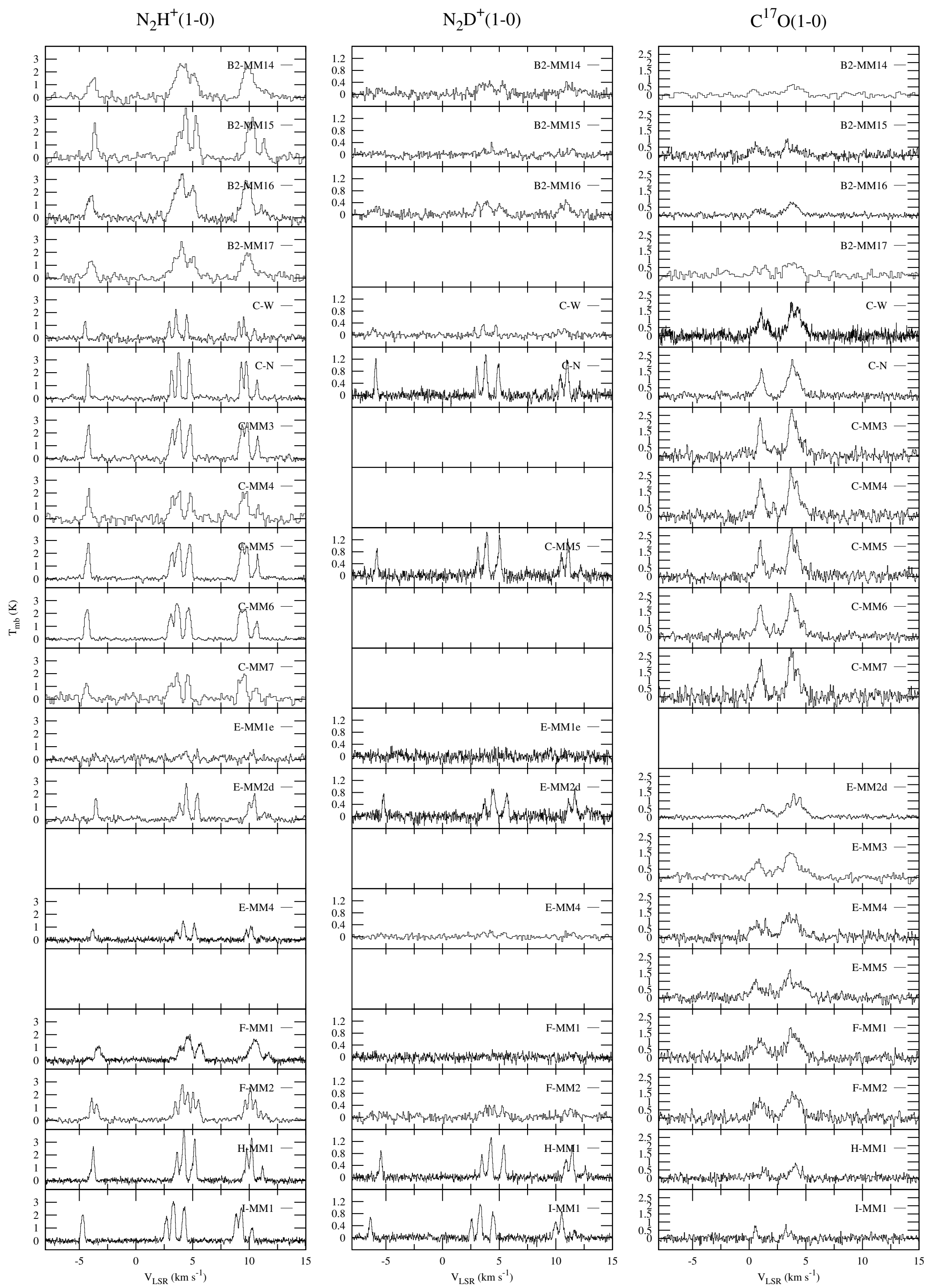

Figure 1.2: continued

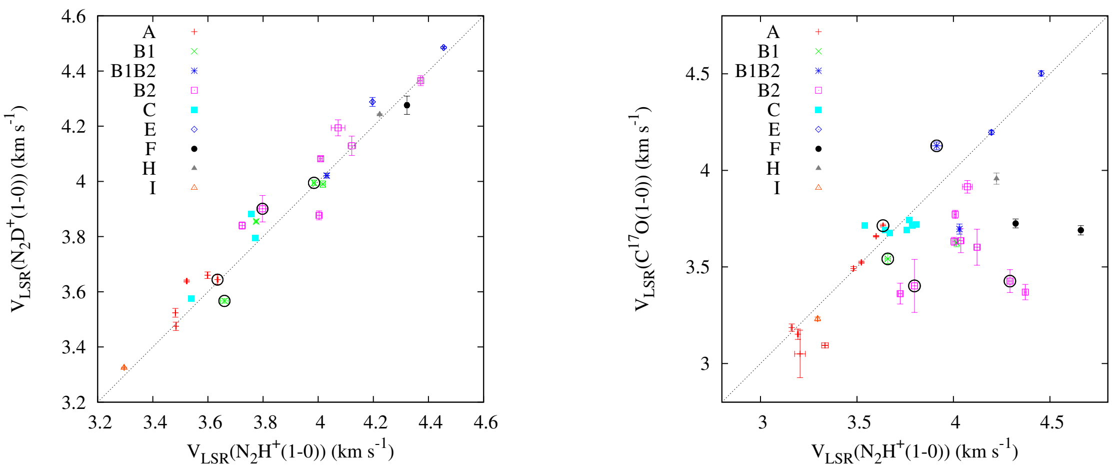

Figure 1.3: V_{LSR} of N_2D^+(1–0) on the left panel and $C^{17}O$(1–0) on the right panel as a function of the V_{LSR} of the N_2H^+(1–0) line. Black dotted lines are the lines of equal V_{LSR}. The protostellar cores are marked with black open circles.

.

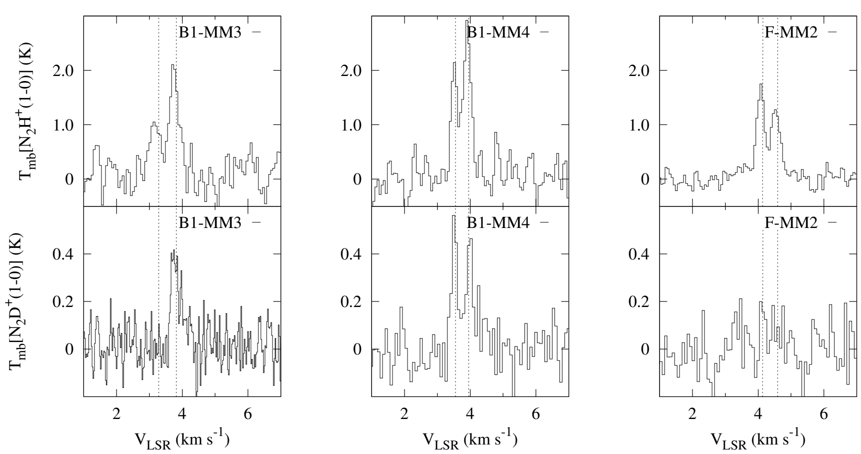

Figure 1.4: Isolated hyperfine components of N_2H^+ and N_2D^+ (1–0) towards cores where two velocity components are found. The spectra are centred at the frequency of the isolated component. The dotted lines show the centroid velocities of the N_2H^+(1–0) components.

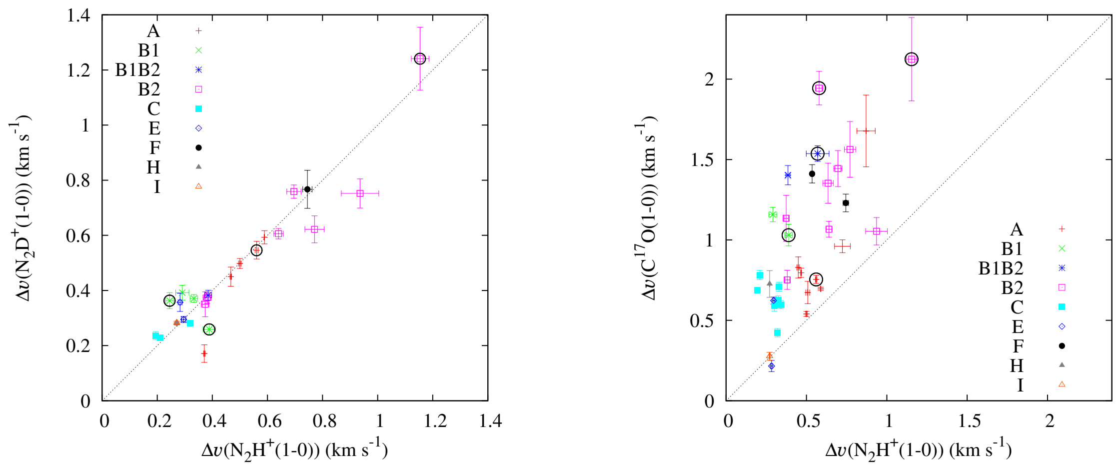

Figure 1.5: Line widths, Δv, of N_2D^+(1–0) on the left panel and $C^{17}O$(1–0) on the right panel in comparison with Δv of N_2H^+(1–0). Black dotted lines are the lines of equal Δv. Different colors show different parts of the cloud. The protostellar cores are marked with black open circles.

N_2D^+ line appears to be a blend of two components (B2-MM2, B2-MM8, F-MM2). The three cases are shown in Fig. 1.4. For the comparison of the N_2H^+ and $C^{17}O$ line widths, we took the Δv of the component having the closest V_{LSR}.

The N_2H^+ and N_2D^+ (1–0) line widths range from 0.2 to 0.7 km s^{-1}, except for the blended N_2D^+ line at B2-MM8 (1.2 km s^{-1}, see left panel of Fig. 1.5). While the line widths of the N_2H^+ and N_2D^+ (1–0) lines are similar for most of the cores, 84% of the cores are within 0.1 km s^{-1} of each other, the $C^{17}O$(1–0) line widths are overall larger than those of N_2H^+(1–0). The median width difference is 0.38 km s^{-1} and the median line width ratio is 1.9. Similar to what was found with the line centroids, this suggests that the N_2H^+ and N_2D^+ trace the same gas, while $C^{17}O$ traces different, in particular more turbulent, gas.

1.3.2 Non-thermal motions

Figure 1.6 presents the ratio of non-thermal components $\Delta v_{\rm NT}$ of the N_2D^+(1-0), N_2H^+(1-0), and $C^{17}O$(1-0) lines and thermal line widths of a mean particle, $\Delta v_{\rm T}$. The non-thermal components are derived from the observed line widths Δv_{obs} via:

$$\Delta v_{\rm NT}^2 = \Delta v_{obs}^2 - 8\ln(2)\frac{kT_k}{m_{obs}}, \tag{1.1}$$

where k is Boltzmann's constant, T_k is the kinetic temperature, and m_{obs} is the mass of the observed molecule (Myers et al. 1991). To measure the non-thermal component, we use the kinetic temperature determined by Friesen et al. (2009) from ammonia observations. For those cores which were not observed in Friesen et al. (2009), we use dust temperatures

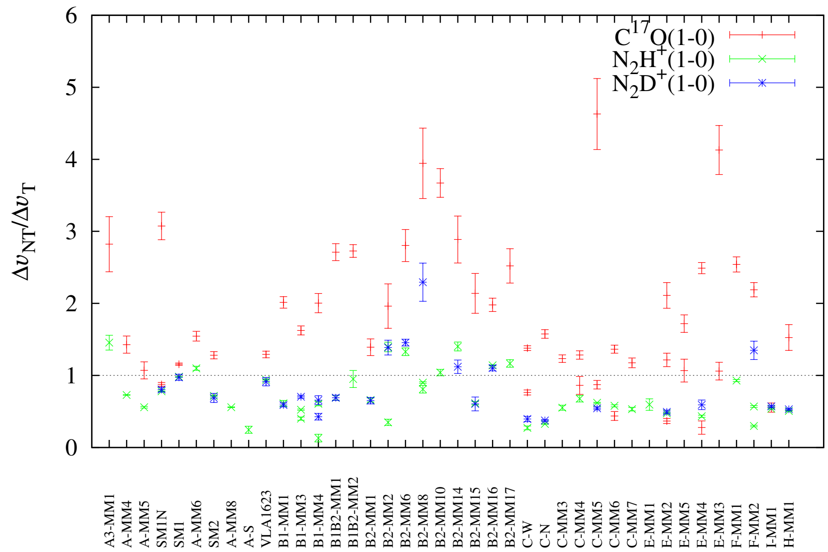

Figure 1.6: Ratio of non-thermal components to thermal components of the N_2D^+(1–0), N_2H^+(1–0), and $C^{17}O$(1–0) lines. The dashed line shows the ratio equal to 1.

determined by Pattle et al. (2015), assuming that the dust and gas temperatures are equivalent (assumption valid at volume densities above 10^4 cm^{-3}; Goldsmith 2001). For most of the cores where both the gas and dust temperatures have been measured, the two values are indeed similar, with the only exception being the B2 region, where the dust temperature is a few degrees lower than the gas temperature. This may be due to the effect of protostellar feedback, where shocks produced by outflows entraining the dense gas can heat the gas but not the dust (e.g. Draine 1980). For the I-MM1 core neither dust nor gas temperatures have ever been estimated, so we adopt 11 K, the same as H-MM1, as these two cores have similar characteristics, both being relatively isolated and far away from the main source of irradiation and heating (see Section 1.4.5). The kinetic temperatures for all cores are given in Table A.7.

For typical temperatures of 10–20 K across L1688, the thermal line widths, Δv_T, for a mean particle with mass 2.33 amu are 0.44–0.63 km s^{-1}. The majority of $C^{17}O$(1–0) lines are supersonic (78%) while most of N_2H^+(1–0) and N_2D^+(1–0) lines are subsonic (80% and 75%). The non-thermal to thermal line width ratio can be as high as 1.5 for N_2H^+(1–0), 2.5 for N_2D^+(1–0), and as high as 5 for $C^{17}O$(1–0). The most turbulent region is Oph-B2 and the most quiescent regions are Oph-B1, C, E, H, and I. Oph-A contains turbulent as well as relatively quiescent cores. For most cores, N_2D^+(1–0) and N_2H^+(1–0) have similar non-thermal components and are narrower than the $C^{17}O$(1–0) line.

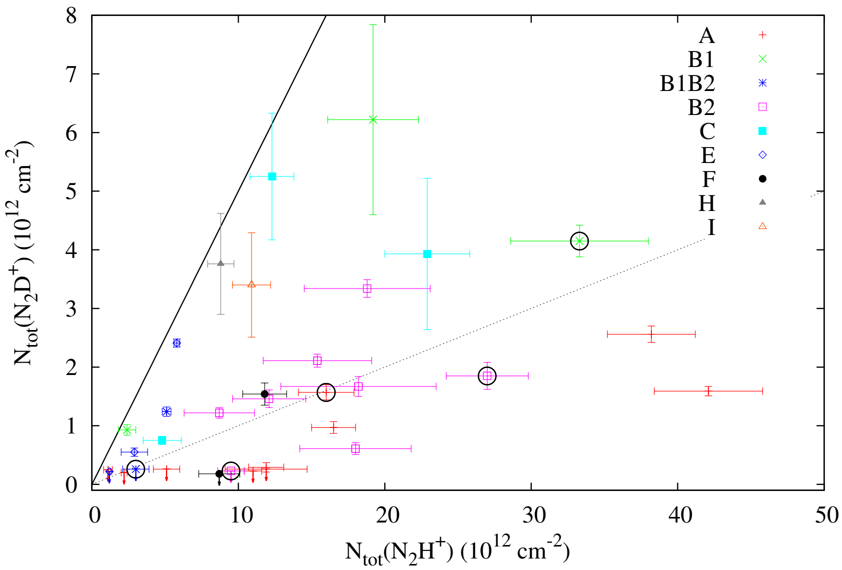

Figure 1.7: Column densities of N_2D^+ and N_2H^+ with lines of constant deuterium fraction (R_D). The black line shows R_D=0.5 and the dotted line shows R_D=0.1. The protostellar cores are depicted with black open circles.

1.3.3 Column densities and deuterium fractions

The hfs fits provide values needed to measure the excitation temperature (T_{ex}) and its error. These values are: the total optical depth, i.e. the sum of the optical depths of the various hyperfine components (τ), the quantity labelled $T_{ant} \times \tau$ (see below), the full width at half maximum of the line (FWHM, Δv), and the centroid velocity relative to the local standard of rest (V_{LSR}). In case of optically thick lines, $T_{ant} \times \tau$ is the total optical depth times the difference between the Rayleigh-Jeans equivalent excitation and background temperatures, while for optically thin lines it is the main beam temperature (T_{mb}). The T_{ex} can be calculated as

$$T_{ex} = \frac{h\nu}{k} \left[\ln \left(\frac{h\nu/k}{(T_{ant} \times \tau)/\tau + J_\nu(T_{bg})} + 1 \right) \right]^{-1}, \tag{1.2}$$

where h is the Planck constant, k is the Boltzmann constant, ν is the frequency of the observed transition, T_{bg} is the cosmic background temperature (2.7 K), $J_\nu(T_{bg})$ is the equivalent Rayleigh-Jeans background temperature, and $J_\nu(T)$ is the function

$$J_\nu(T) = \frac{h\nu/k}{\exp(h\nu/kT) - 1}. \tag{1.3}$$

The calculated excitation temperature depends on the value of τ. In the case of weak lines or low S/N, τ can not be determined properly and the error of τ ($\Delta\tau$) will be high. In all cases where $\tau/\Delta\tau \leq 3$, we consider the lines to be optically thin and fix

$\tau = 0.1$ (the minimum opacity value) in CLASS. In this case of optically thin conditions, for $N_2H^+(1-0)$, the excitation temperature value is assumed to be the average T_{ex} found for optically thick $N_2H^+(1-0)$ lines, while for $N_2D^+(1-0)$ we adopt the (measured or assumed) $N_2H^+(1-0)$ excitation temperature towards the same dense core.

For optically thick transitions, the column density (N_{tot}) is given by:

$$N_{tot} = \frac{8\pi^{3/2}\Delta v}{2\sqrt{\ln 2}\lambda^3 A_{ul}} \frac{g_l}{g_u} \frac{\tau}{1-\exp(-h\nu/kT_{ex})} \frac{Q_{rot}}{g_l \exp(-E_l/kT_{ex})}, \tag{1.4}$$

where λ is the wavelength of the observed transition, A_{ul} is the Einstein coefficient of the $u \rightarrow l$ transition, g_l and g_u are the statistical weights of the lower and upper levels, Q_{rot} is the partition function and E_l is the energy of the lower level (Caselli et al. 2002c). For linear rotors, g_l and g_u are determined by $g_J = 2J + 1$, where J is the rotational quantum number. The partition function of linear molecules (such as N_2H^+ and CO) is given by

$$Q_{rot} = \sum_{J=0}^{\infty} (2J+1) \exp(-E_J/kT), \tag{1.5}$$

where $E_J = J(J+1)hB$, and B is the rotational constant. For rotational transitions with hyperfine structure, τ refers to the total optical depth (given by the sum of the peak optical depths of all the hyperfine components) and Δv to the intrinsic line width. The error on N_{tot} is given by propagating the errors on Δv, τ and T_{ex} in equation 1.4.

For optically thin lines

$$N_{tot} = \frac{8\pi W}{\lambda^3 A_{ul}} \frac{g_l}{g_u} \frac{1}{J_\nu(T_{ex}) - J_\nu(T_{bg})} \frac{1}{1-\exp(-h\nu/kT_{ex})} \frac{Q_{rot}}{g_l \exp(-E_l/kT_{ex})}, \tag{1.6}$$

where W is the integrated intensity of the line:

$$W = \frac{\sqrt{\pi}\Delta v T_{mb}}{2\sqrt{\ln 2}}, \tag{1.7}$$

for a Gaussian line (Caselli et al. 2002c).

In case of non-detection of N_2D^+, upper limits on the N_2D^+ column density have been derived based on the 3σ uncertainty ($3\,\sigma_W$) of the integrated intensity, with:

$$\sigma_W = rms \times \sqrt{N_{ch}} \times \Delta v_{res}, \tag{1.8}$$

where N_{ch} is the mean number of channels covering the velocity range of all the detected lines and Δv_{res} is the velocity resolution.

The column densities of N_2H^+, N_2D^+, and $C^{17}O$ are given in Tables A.2–A.6. The N_2D^+ column densities derived from the (1–0) transition in most cores are larger than those derived from the (2–1) transition on average by only 10%. $C^{17}O$ column densities calculated with (1–0) lines in most cores are smaller than the ones calculated with (2–1) lines (see section 1.3.4 for details). Figure 1.7 shows the column densities of N_2H^+ and N_2D^+. Where multiple components are detected, we plot the sum of the column densities.

The deuterium fraction is defined as the ratio of column densities,

$$R_D = N_{tot}(N_2D^+)/N_{tot}(N_2H^+), \tag{1.9}$$

and it has been measured for all cores where the N_2D^+(1–0) line is detected. To calculate the deuterium fraction for cores where two velocity components are detected, we take the sum of the column densities derived from the two components. L1688 overall exhibits high levels of deuterium fractions with a large spread of values between different cores (R_D = 2–43 %; see Fig. 1.8). Such a high level of deuteration (over 20 %) was previously found towards other dense cores in different star-forming regions (e.g. Crapsi et al. 2005; Pagani et al. 2007; Emprechtinger et al. 2009; Fontani et al. 2011; Miettinen et al. 2012; Friesen et al. 2013; Fontani et al. 2014). The deuterium fraction across the B2 region was previously studied by Friesen et al. (2010), who found slightly lower deuterium fractions (1–10%) than in the present work (3–18%). The column densities of N_2D^+ (0.5–6$\times10^{11}$ cm^{-2}) and N_2H^+ (4–10$\times10^{12}$ cm^{-2}) they obtain are also smaller than those found in this work (6–33$\times10^{11}$ and 9–27$\times10^{12}$ cm^{-2}). This difference could be due to different transitions used to calculate column densities, while using similar excitation temperatures derived from the N_2H^+(1–0) line. Friesen et al. (2010) used N_2D^+(3–2) and N_2H^+(4–3) lines with 11″ and 13″ HBPW while we use the (1–0) transition for both species (32″ and 27″). The factor of 2 difference in deuterium fraction could arise also from not coincident dense core coordinates.

1.3.4 CO-depletion factor

In cold, dense, quiescent gas, CO freezes out onto dust grains and the level of this depletion is commonly expressed as a CO-depletion factor, f_d, calculated as:

$$f_d = \frac{X_{ref}(\mathrm{CO})}{X(\mathrm{CO})}, \tag{1.10}$$

where X_{ref}(CO) is the reference abundance and X(CO) is the observed abundance.

The reference abundance of CO in the local ISM has been found to be between 1 and 2×10^{-4} (Wannier 1980; Frerking et al. 1982; Lacy et al. 1994). We use $X_{ref}(C^{16}O) = 2\times10^{-4}$ (Frerking et al. 1982), $X(C^{18}O)/X(C^{17}O) = 4.11$ (Wouterloot et al. 2005), and $X(C^{16}O)/X(C^{18}O) = 560$ (Wilson & Rood 1994) such that:

$$X(\mathrm{C^{16}O}) = \frac{N_{tot}(\mathrm{C^{17}O}) \times 4.11 \times 560}{N(\mathrm{H_2})}. \tag{1.11}$$

To calculate the f_d in case of multiple velocity components, we consider the sum of the column densities of the individual components (as $N(H_2)$ is derived from the millimetre dust continuum emission, which does not contain kinematic information). Since millimetre

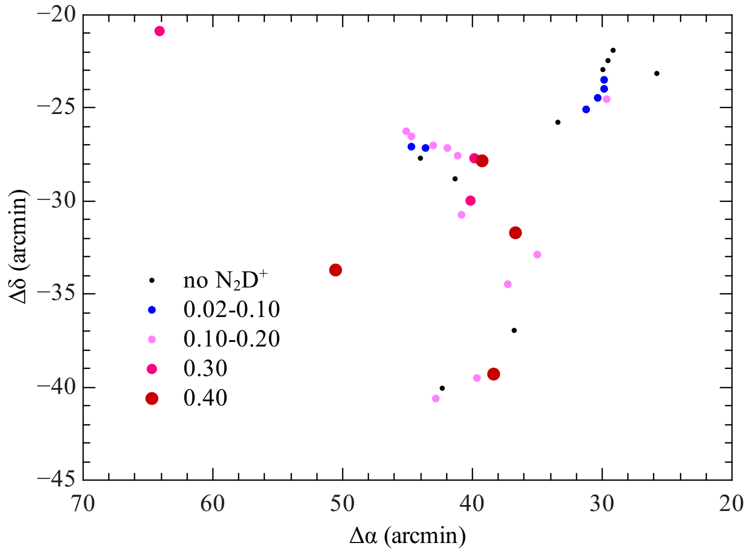

Figure 1.8: Deuterium fraction across L1688. The black points show the cores with no N_2D^+(1–0) detection. The coordinate offsets correspond to the J2000 equatorial position $\alpha = 16^{\rm h}24^{\rm m}16^{\rm s}$, $\delta = -24°00'00''$.

dust continuum emission is generally optically thin, the molecular hydrogen column density can be derived from the continuum flux density:

$$N(\mathrm{H_2}) = \frac{S_\lambda}{\Omega\,\mu_{\mathrm{H_2}}\,m_\mathrm{H}\,\kappa_\lambda\,B_\lambda(T_{dust})}; \tag{1.12}$$

where S_λ is the flux in a single beam, Ω is the main beam solid angle, $\mu_{\mathrm{H_2}} = 2.8$ is the mean molecular weight per H_2 molecule (Kauffmann et al. 2008), m_H is the mass of atomic hydrogen, κ_λ is the dust opacity per unit mass column density at a given wavelength ($\kappa_{850\mu m}$=0.01 cm^2 g^{-1}; Johnstone et al. 2000) and $B_\lambda(T_{dust})$ is the Planck function for a dust temperature T_{dust} (Motte et al. 1998).

The 850 μm dust continuum emission flux measurements from the SCUBA survey (with the beam size of the convolved map of 22″.9, Di Francesco et al. 2008) have been used to calculate $N(\mathrm{H_2})$, adopting the dust temperature from Pattle et al. (2015) when available and the gas temperature from Friesen et al. (2009) in the other cases. For those cores not studied in the above mentioned papers, the dust temperature estimated by Motte et al. (1998) has been adopted. For Oph-I, where no dust or gas temperature has been measured, we assumed 11 K, the same as in Oph-H, as Oph-I has similar characteristics to Oph-H, as already mentioned. The dust temperatures for all cores are given in Table A.7.

The depletion factor of CO is generally quite low in L1688, ranging from 0.2 to 2 in the B1, B1B2, C, E, and F regions, and from to 0.7 to 7.3 in the A, B2, H, and I regions. This result is consistent with previous large scale (e.g. Christie et al. 2012) and small scale (e.g. Bacmann et al. 2002; Gurney et al. 2008) studies. However, larger CO depletion factors are found for the A region compared to the work of Gurney et al. (2008): 1 to 6 instead of 1.5 to 4.5. This small discrepancy could be due to slightly different pointings or from the use of different CO isotopologues and transitions. In particular, we note that our $C^{17}O(2–1)$ observations tend to produce column densities larger than $N_{tot}(C^{17}O(1–0))$ by an average factor of 1.5 in Oph-A and 1.1 in B1, B1B2, B2, C, E, and F regions (and thus depletion factors would be lower by 1.5 and 1.1), suggesting that temperature and density gradients along the line of sight may be present, slightly affecting the derived depletion factor depending on the CO transition used. To calculate column densities of $C^{17}O$, LTE is assumed, with the kinetic temperature equal to the dust temperature.

Christie et al. (2012) suggest that the low depletion factor of L1688 could be due to an unusual dust grain size distribution with a population of very large dust grains and very small spinning dust grains which reduces the surface area available for freeze-out. However, L1688 is a complex region, with active star formation and externally irradiated. Below, we discuss possible causes of the general low CO depletion factors and the significant variation in R_D and f_d found across L1688.

1.4 Discussion

1.4.1 Deuterium fraction

This work has found a large range of deuterium fractions across L1688, from a minimum of 2% to a maximum of 43%. Previous studies of deuterium fraction did not show such a big spread: for example, 5–25% in Taurus (Crapsi et al. 2005), 1–10% in Ophiuchus B (Friesen et al. 2010), and 3–25% in Perseus (Emprechtinger et al. 2009; Friesen et al. 2013). The large values of deuterium fractions found towards some of the cores in L1688 in our more extensive survey may indicate the presence of centrally concentrated pre-stellar cores on the verge of star formation. The Ophiuchus Molecular Cloud is known to be denser on average than other nearby star-forming regions (e.g. Lada et al. 2013). The higher average densities, together with the generally higher molecular cloud temperatures (Pattle et al. 2015; Liseau et al. 2015), imply larger pressures which may accelerate the formation of denser cores and the rate of star formation (e.g. Kennicutt & Evans 2012) compared to the other nearby molecular cloud complexes. It is interesting to note that these high R_D values are found towards E-MM2d, C-Ne, I-MM1, H-MM1, B1-MM1, B1-MM3, B1B2-MM1 which do not prominently appear in the 850 μm map and they are all relatively isolated structures (I and H) or in between bright sub-millimetre clumps (E, C-N, B1, B1B2). They are probably recently formed cold and dense structures on the verge of star formation.

1.4.2 Deuterium fraction and CO depletion

Deuterium fraction and CO-depletion factor are expected to correlate, because CO is one of the main destruction partners of H_3^+ and its deuterated forms (Dalgarno & Lepp 1984).

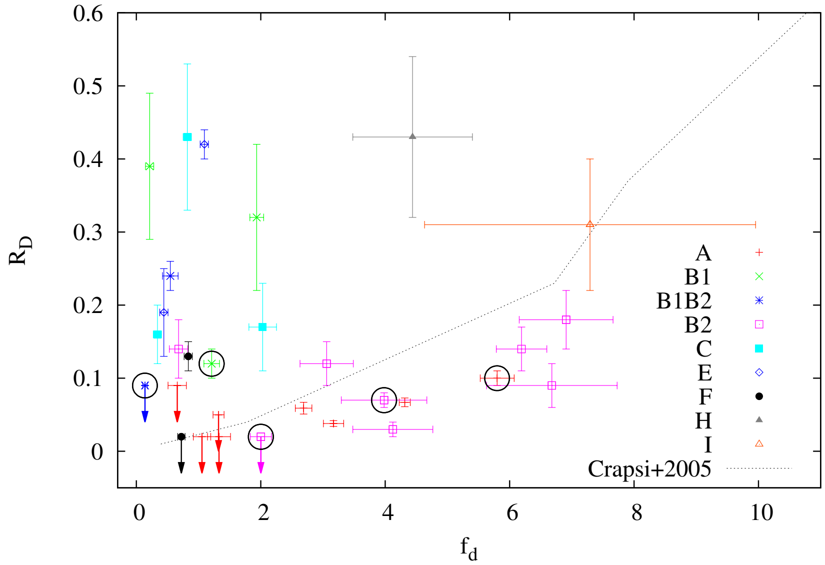

Figure 1.9: Deuterium fraction as a function of CO-depletion factor. The protostellar cores are depicted with black open circles.

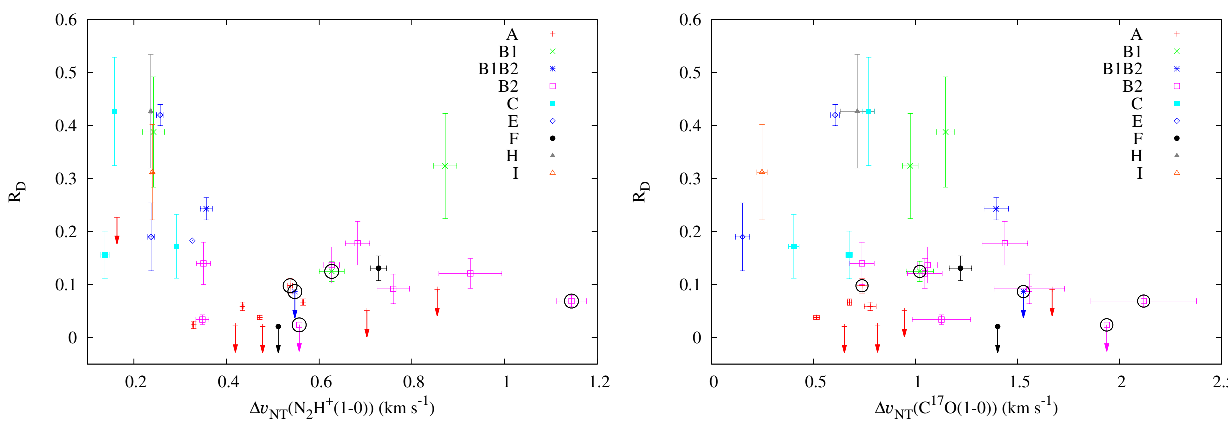

Figure 1.10: Deuterium fraction as a function of the nonthermal component of the N_2H^+(1–0) line width (left) and the $C^{17}O$(1–0) line width (right). The protostellar cores are depicted with black open circles.

This correlation has been presented in several theoretical works (Crapsi et al. 2005; Caselli et al. 2008; Kong et al. 2015) and confirmed with observations (Crapsi et al. 2005; Emprechtinger et al. 2009; Friesen et al. 2013). Figure 1.9 shows the deuterium fraction as a function of CO-depletion factor in L1688. The dotted curve in the figure shows the prediction from simple modelling by Crapsi et al. (2005), shifted to take into account the different reference CO abundance adopted here. The first thing to note is that f_d values go below 1, which suggests that our adopted X_{ref}(CO) has been underestimated by a factor of a few (2–3, considering the lowest f_d value in Table A.7); or the dust opacity, κ, which depends on the evolutionary stage and the properties of dust grains (see Henning et al. 1995) has been overestimated by a factor of 1.5–2, or the dust temperature has been overestimated by a few (1–3) K. However, to allow comparison with recent literature work (where X_{ref}(CO) = 2×10^{-4}, see e.g. Hernandez et al. 2011; Fontani et al. 2012), and considering the factor of 2 uncertainty associated with X_{ref}(CO) (see also Miotello et al. 2014), we did not modify X_{ref}(CO), warning the reader that the calculated f_d values may be underestimated by a factor of a few. The important message here is to see if previously found trends are reproduced and/or if L1688 hosts dense cores with a larger variety of chemical/physical properties than found in other nearby star-forming regions.

From Fig. 1.9, it is evident that two classes of cores are present in L1688. One group includes the A, B2, and I cores, which show a correlation between R_D and f_d similar to that found by Crapsi et al. (2005). The other group contains the B1, B1B2, C, E, F, and H cores, which completely deviate from the Crapsi et al. (2005) correlation. This latter group of cores shows R_D =12–43% and f_d =0.2–4.4. From the parameter space exploration of Caselli et al. (2008) and Kong et al. (2015), large values of R_D ($>$ 0.02) cannot be achieved in standard conditions if little CO freeze-out is present *in the same gas traced by* N_2D^+. How to reconcile theory with observations? One possibility is that the dense and cold regions responsible for the bright N_2D^+ lines have sizes smaller than the IRAM-30m beam at 3mm. In this case, the CO-depleted zone would be too diluted to be clearly detected within the larger scale CO-emitting region. Indeed, 2 of 6 cores with $R_D > 20\%$ and $f_d < 4.4$ (B1-MM3 and B1B2-MM1) have estimated sizes 1300–1800 AU, less then 2640 AU corresponding to 22″ at 120 pc, one unresolved (B1-MM1) (Motte et al. 1998), one (H-MM1) has no size estimate (outside of the mapped area in Motte et al. 1998). Higher angular resolution observations of dust continuum and molecular lines are needed to prove this point.

1.4.3 Deuterium fraction and non-thermal motions

To understand further the characteristics of the highly deuterated, but CO-rich cores in Fig. 1.9, we plot the deuterium fraction as a function of non-thermal line width of N_2H^+(1–0) and $C^{17}O$(1–0) in Fig. 1.10. This figure shows that these cores preferentially occupy the left area of the panels, indicating that on average they have narrower $C^{17}O$(1–0) and especially N_2H^+(1–0) lines. Thus, the highly deuterated cores are overall more quiescent than the rest of the sample, in agreement with their relatively isolated nature and maybe smaller size, as mentioned in the previous section. Please also note that these are the cores

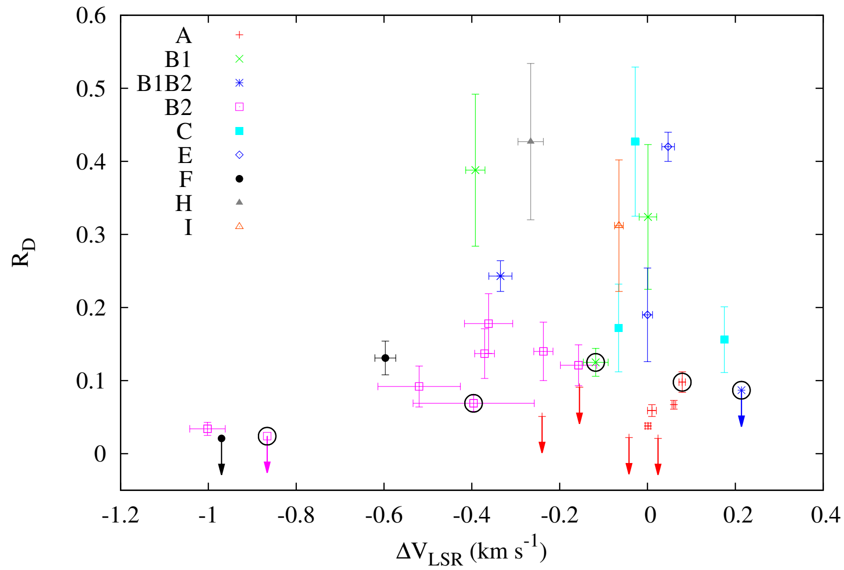

Figure 1.11: Deuterium fraction as a function of the difference between the central velocities of the $C^{17}O$(1–0) and N_2H^+(1–0) lines ΔV_{LSR}. The protostellar cores are depicted with black open circles.

with relatively small differences between $C^{17}O$(1–0) and N_2H^+(1–0) LSR velocities (see Fig. 1.11), again suggesting quiescent conditions. The rest of the sample displays broader line-widths, suggestive of faster internal motions (in case of gravitational contraction) or external stirring, e.g. due to proximity to active sites of star formation. Indeed, relatively large N_2H^+(1–0) line widths have been found by Crapsi et al. (2005) towards some of the most evolved starless cores in their sample (L1544 and L429; see their Fig. 6). Line widths tend to increase towards the centre of L1544 (Caselli et al. 2002b) because of contraction motions. The quiescent and highly deuterated cores found in L1688 may then represent an earlier evolutionary stage, compared to L1544 and other contracting pre-stellar cores, where the core has just started to become centrally concentrated but contraction has not started yet (or it has not affected scales large enough to be detected with the current single-dish observations). High angular resolution observations are needed to investigate this conclusion.

1.4.4 R_D and f_d versus molecular hydrogen column density and temperature

The measured R_D and f_d values are plotted as a function of molecular hydrogen column density, $N(H_2)$, and dust temperature, T_{dust}, in Fig. 1.12. No correlation is found for R_D vs $N(H_2)$, while f_d appears to increase with $N(H_2)$ with different slopes depending on the region. In particular, f_d is increasing faster with $N(H_2)$ in the B2 region compared to the A and C regions. For the other regions, it is hard to see any trend, probably because of the

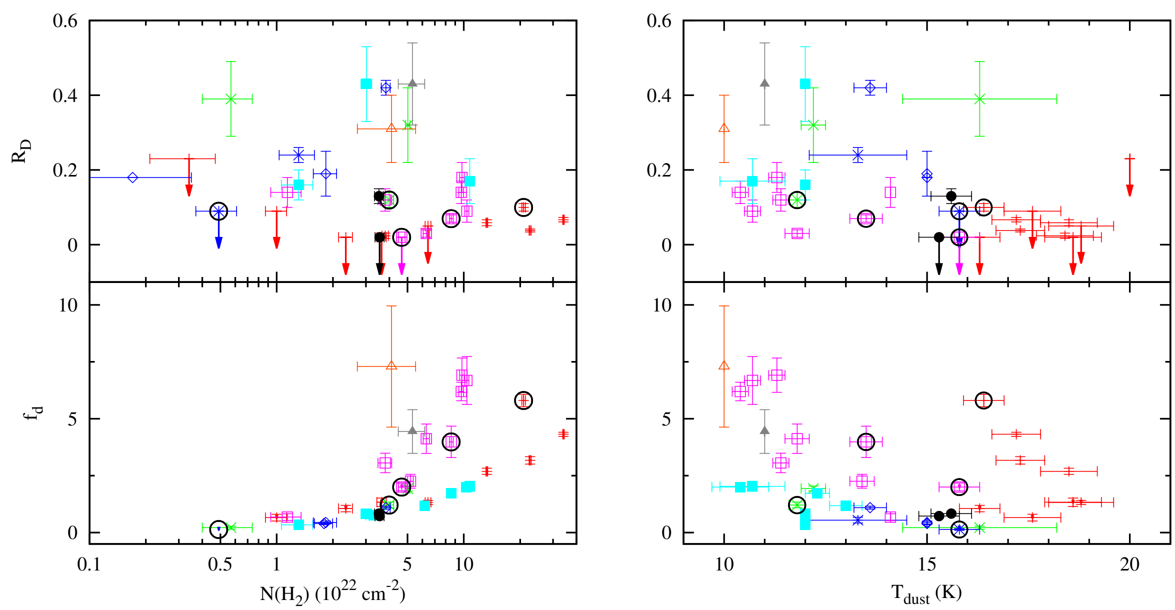

Figure 1.12: Left upper panel: deuterium fraction depending on the molecular hydrogen column density, N(H_2). Right upper panel: deuterium fraction as a function of dust temperature taken from Pattle et al. (2015); Friesen et al. (2009) and Motte et al. (1998). Left lower panel: CO-depletion factor versus the molecular hydrogen column density. Right panel: CO-depletion factor as a function of dust temperature. The protostellar cores are depicted with black open circles, the color coding is given in Fig. 1.11.

more limited range of N(H_2) values detected. One possible cause of the different slopes in the f_d – N(H_2) correlations is the different amount of external heating due to the proximity of Oph-A to HD 147889 (see next section and Fig. 1.13). This extra illumination maintains the dust grains in region A at a higher temperature compared to the other L1688 regions (see also Liseau et al. 2015), so that larger column/volume densities are needed to reach dust temperatures low enough (<25 K) to allow CO molecules to freeze-out onto the dust grains. The C region which rather follow the same trend as the A region is the next close to HD 147889 after the A region (see Fig. 1.13) and probably also illuminated by the star, although it's temperature ($\leq$ 15 K) and column density ($\leq 10^{22}$ cm^{-2}) are as low as in the other regions.

The difference in dust temperatures among the various regions in L1688 is also causing the scatter plot in the right panels of Fig. 1.12. Here we note that the different amount of external illumination impinging the different L1688 regions causes the well-known f_d vs $T_{\rm dust}$ correlation (e.g. Kramer et al. 1999) to disappear. Oph-A is the only region in L1688 with dust temperatures larger than 15 K and significant CO freeze-out. Oph-B2 displays a sharp drop of f_d with increasing $T_{\rm dust}$, as expected given the exponential dependence on $T_{\rm dust}$ of the CO evaporation rate (see e.g. Hasegawa et al. 1992).

The deuterium fraction is also expected (and has been measured) to drop with dust temperatures above about 15-20 K (.e.g. Emprechtinger et al. 2009; Caselli et al. 2008; Kong et al. 2015). However, this trend is not observed in L1688, as shown in the top left panel of Fig. 1.12. Once again, the non-uniform conditions among the various regions (in particular the amount of external illumination, gas volume density etc.) make it difficult to see a well defined pattern. Even within the same regions, we do not notice any trend, which may be caused by dust temperatures (mainly derived from Herschel data) not being representative of the cold regions within which the deuterium fractionation is taking place. More detailed and higher resolution data are needed to explore this possibility.

1.4.5 Distance to heating sources

It is well-known that star formation in L1688 is affected by the OB-association Sco OB 2 (Pattle et al. 2015), which is located ~145 pc from the Sun (de Zeeuw et al. 1999), i. e. ~25 pc behind L1688. Sco OB 2 is a moving group of more than 120 stars, mostly of B and A spectral types. It occupies an area of about 15° diameter on the sky (de Zeeuw et al. 1999). We looked for a correlation between R_D, f_d, the distance to nearby stars (ρ Oph, HD 147889, V 2246 Oph, Oph S1) and the closest YSOs (see Fig. 1.13). ρ Oph is a multiple system of B2IV–B2V spectral type stars; it is a member of the Sco OB 2 association, located to the North of L1688, and is the most distant from L1688 among the four nearby stars. The cores in Oph-A, the nearest region to ρ Oph, show a tentative correlation between the CO-depletion factor and the projected angular distance D to the ρ Oph system, with f_d increasing with D (see Fig. 1.14). The cores in the others sub-regions do not show any correlation.

The other three stars are pre-main sequence or very young stars related to the Ophiuchus star-forming region. Oph S1 is a B4-K8 type binary star with a T-Tauri star being the fainter component (Gagné et al. 2004) to the East of the A region; V 2246 Oph is a Herbig Ae/Be star on the West side of the A region; and HD 147889 is a young B2 star on the West side of L1688 (e.g. van den Ancker et al. 1997; Liseau et al. 1999). In all regions of L1688, f_d does not show any correlation with the distance to the brightest young and PMS stars of L1688.

The A region contains more YSOs than other regions and is the closest to the external heating sources. Oph-A has the smallest values of R_D and the highest values of f_d in L1688. Relatively low deuteration could be due to this proximity to nearby irradiating sources, while the large f_d values may be due to the fact that this region is also the densest one in L1688, thus probably harbouring the densest cores. Here, the dust temperatures are probably low enough (< 25 K) to allow molecular freeze-out to proceed at a higher rate due to the larger gas-dust collision rates (because of the overall larger densities), but not large enough to promote deuterium fractionation, likely because of an increase of the ortho-to-para H_2 ratio in warmer environments (see e.g. Flower et al. 2006). An alternative to the low values of R_D found in Oph-A could be that N_2D^+ cores are compact and small compared to our beam, while N_2H^+ is extended and abundant due to the large average densities (see e.g. Friesen et al. 2014; Liseau et al. 2015), as also found in Infrared Dark Clouds where massive stars and star clusters form (Henshaw et al. 2014). Indeed, Friesen et al. (2014) detected compact (a few hundred AU in size) dust continuum condensation and ortho-H_2D^+ emission towards one of the cores embedded in Oph-A. However, we note that the line widths of N_2H^+(1–0) and N_2D^+(1–0) lines are the same within the errors (see Fig. 1.5), so this alternative scenario may be harder to justify. Again, higher angular resolution observations of N_2D^+ are needed to disentangle between these two scenarios.

No correlation between R_D and distance to any heating source (embedded or external) was found, although the largest R_D values are found at projected distances larger than 50 arcsec from embedded YSOs and greater than 20 arcsec from HD 147889 (these are the already discussed large R_D - low f_d relatively isolated cores, which we discussed in section 1.4.2). Moreover, the region closest to ρ Oph and V 2246 Oph, the sub-region Oph-A, has the lowest deuterium fractions.

Friesen et al. (2010) studied the deuterium fraction in the B2 region and found a correlation between R_D and distance to the nearest protostar. The deuterium fraction we measure in this region (0–18%, median ~12%) is systematically higher than that found by Friesen et al. (2010) (0–10%, mostly < 4%). According to our study, there is no correlation between R_D and the distance to the closest YSO (see Fig. 1.13 right upper panel). This difference in the results of the studies (R_D — YSO correlation) can be due to the fewer cores studied by us in this particular region (9 cores instead of full mapping of the B2 region as done by Friesen et al. 2010).

1.5 Conclusions

This paper presents single point observations of the ground state transitions of N_2H^+, N_2D^+, and $C^{17}O$ towards prestellar cores in L1688. We measure the deuterium fraction,

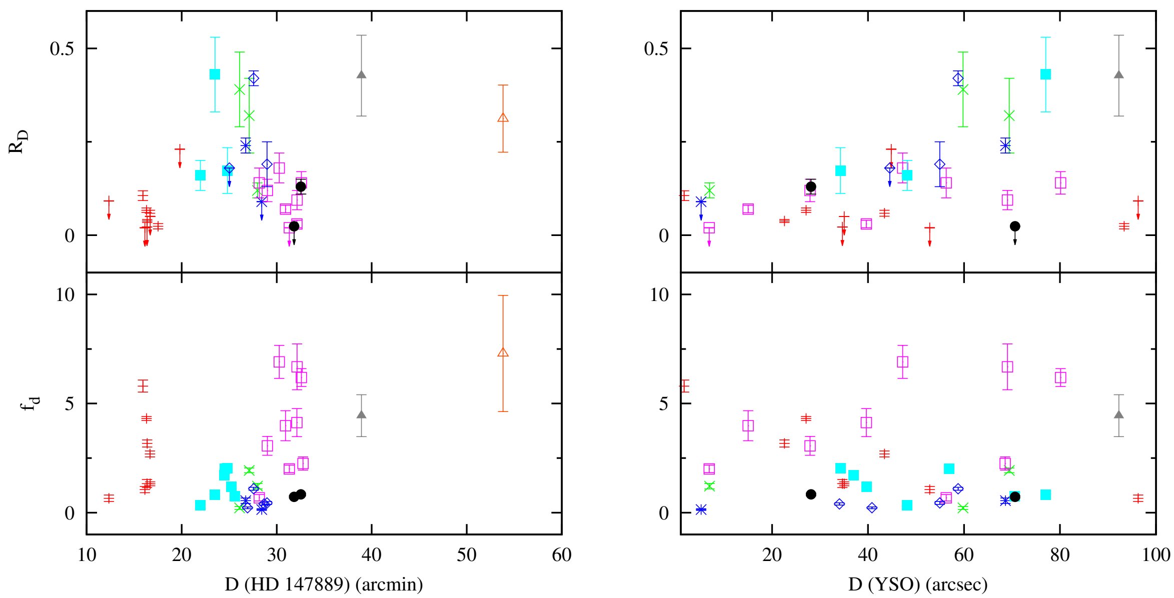

Figure 1.13: Left upper panel: deuterium fraction depending on the angular distance to HD 147889. Right upper panel: deuterium fraction as a function of the angular distance to the closest YSO. The positions of YSOs were taken from Motte et al. (1998); Simpson et al. (2008) and Dunham et al. (2015). Left lower panel: CO-depletion factor depending on the angular distance to HD 147889. Right lower panel: CO-depletion factor depending on the angular distance to the closest YSO. The color coding is given in Fig. 1.11.

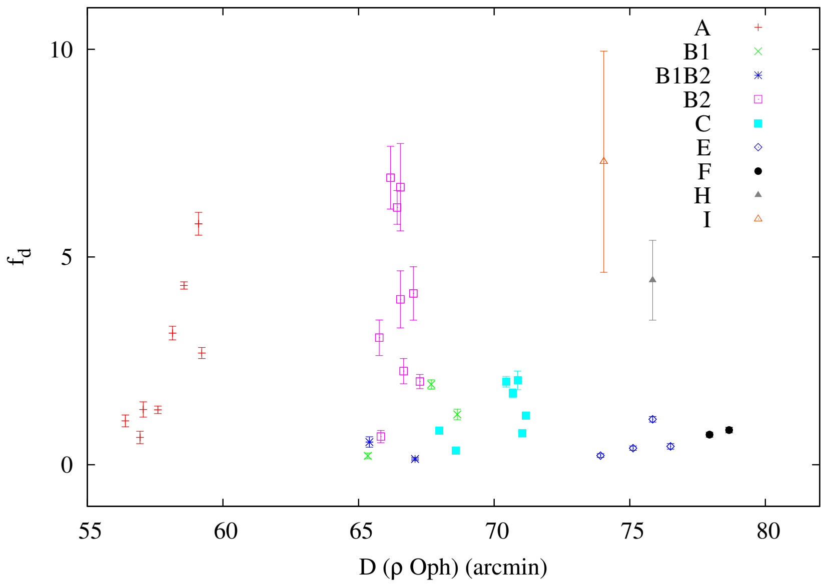

Figure 1.14: CO-depletion factor as a function of angular distance to the ρ Oph system.

R_D, and CO-depletion factor, f_d, and study the correlation between these two parameters as well as with physical parameters varying across the cloud, such as dust temperature, molecular hydrogen column density, level of turbulence, projected distance to stellar sources which externally irradiate the cloud and embedded sources which can internally stir and shock the gas. The following conclusions have been reached:

1. The L1688 cores show a large spread of deuterium fractions, 2–43% and moderate CO depletion factors (up to 7, although the reference value of the CO fractional abundance adopted here, 2×10^{-4}, may be underestimated by a factor of 2–3 or the dust opacity value used in the work, 0.01 cm^2 g^{-1} may be overestimated by a factor of 1.5–2).

2. The largest R_D values are found towards (B1, B1B2, C, E, H, I) dense cores which present relatively quiescent (subsonic) motions as measured from the width of the high density tracer lines; thus, they are probably in an evolutionary stage just preceding the contraction towards protostellar birth, as found in other more evolved pre-stellar cores such as L1544 in Taurus (Caselli et al. 2002b). These highly deuterated cores are also relatively isolated (they are typically found in between strong sub-millimetre dust continuum emission and far away from embedded protostars) and the CO freeze-out is low, in contrast with chemical model predictions. This dichotomy (large R_D and low f_d) can be understood if the deuterated gas is confined in a region smaller than the beam size, so that the CO-depleted region is too small to be revealed with observations of the widespread $C^{17}O(1–0)$ emitting gas. Higher angular resolution observations are needed to confirm this statement.

3. Except for this sub-group of highly deuterated cores, widths are generally supersonic in $C^{17}O(1–0)$ (78%) and subsonic in $N_2H^+(1–0)$ and $N_2D^+(1–0)$ (75% and 80%). The B2 region stands out here with supersonic widths in all tracers in the majority of cores. This is probably a combination of internal systematic motions (e.g. contraction) and external stirring (turbulence, interaction with outflows driven by embedded protostars).

4. The correlation between R_D and f_d already found in other studies of starless cores is maintained for a sub-group of cores (those in A, B2, and I, when plotted together). The highly deuterated cores show a significantly steeper rise of R_D with f_d, suggesting that the CO observations are not sensitive to the CO-depleted zone, as mentioned above.

5. The densest region in L1688, Oph-A, hosts dense cores with significant amount of CO freeze-out (f_d close to 7) but no corresponding large R_D values. This can be explained if the gas and dust temperatures are low enough (<25 K) to allow CO freeze-out but high enough to significantly increase the ortho-to-para ratio compared to cooler regions. Alternatively, the N_2D^+ cores may be small and diluted within our beam, whereas the N_2H^+ is abundant all across the region as a consequence of the large average densities.

6. The nearby ρ Oph star in the Sco OB2 association appears to affect the amount of CO freeze-out in Oph-A cores, as f_d increases with projected distance to this star. No other regions appear to be chemically affected by their proximity to external stars or embedded young stellar objects, except for the B2 region, where f_d decreases with increasing dust temperature.

7. Our observations hint at the present of compact starless cores (smaller than those found towards less dense and cooler molecular cloud complexes, such as Taurus) with large deuterium fractions (12–43%) and small CO depletion factors (0.2–4.4). These cores have relatively low temperatures compared to their surroundings, so that they do not appear as clear structures in dust continuum emission maps at 850 μm. Their compact nature may be a consequence of the overall higher densities and temperatures across L1688 compared to other nearby star-forming regions. High angular resolution observations are needed to test these predictions.

Chapter 2

Kinematics of dense gas in the L1495 filament

This chapter is based on the paper Punanova, A., Caselli, P., Pineda, J. E., Pon, A., Tafalla, M., Hacar, A., Bizzocchi, L., submitted to A&A 11 of May 2017.

Abstract

Context. Nitrogen bearing species, such as NH_3, N_2H^+, and their deuterated isotopologues, show enhanced abundances in CO-depleted gas, and thus are perfect tracers of dense and cold gas in star-forming regions. The Taurus molecular cloud contains the long L1495 filament providing an excellent opportunity to study the process of star formation in filamentary environments.

Aims. We study the kinematics of the dense gas of starless and protostellar cores traced by the N_2D^+(2–1), N_2H^+(1–0), DCO^+(2–1), and $H^{13}CO^+$(1–0) transitions along the L1495 filament and the kinematic links between the cores and the surrounding molecular cloud.

Methods. We measure velocity dispersions, local and total velocity gradients and estimate the specific angular momenta of 13 dense cores in the four transitions using the on-the-fly observations with the IRAM 30 m antenna. To study a possible connection to the filament gas, we use the fit results of the $C^{18}O$(1–0) survey performed by Hacar et al. (2013).

Results. The velocity dispersions of all studied cores are mostly subsonic in all four transitions, with similar and almost constant dispersion across the cores in N_2D^+(2–1) and N_2H^+(1–0). A small fraction of the DCO^+(2–1) and $H^{13}CO^+$(1–0) lines show transonic dispersion and exhibit a general increase in velocity dispersion with line intensity. All cores have velocity gradients (0.6–6.1 km s^{-1} pc^{-1}), typical of dense cores in low-mass star-forming regions. All cores show similar velocity patterns in the different transitions, simple in isolated starless cores, and complex in protostellar cores and starless cores close to young stellar objects where the gas motions can be affected by outflows. The large-scale velocity field traced by $C^{18}O$(1–0) does not show any perturbation due to protostellar feedback and does not mimic the local variations seen in the other four tracers. The

local velocity gradient is usually perpendicular to the core major axis. Specific angular momentum J/M varies in a range $(0.6–21.0)\times10^{20}$ cm^2 s^{-1} which is similar to the results previously obtained for dense cores. J/M measured in N_2D^+(2–1) is systematically lower than J/M measured in DCO^+(2–1) and $H^{13}CO^+$(1–0).

Conclusions. All cores show similar properties along the 10 pc-long filament. N_2D^+(2–1) shows the most centrally concentrated structure, followed by N_2H^+(1–0), DCO^+(2–1), and $H^{13}CO^+$(1–0). The non-thermal contribution to the velocity dispersion increases from higher to lower density tracers. The change of magnitude and direction of the total velocity gradients depending on the tracer used indicates that internal motions change at different depths within the cloud. N_2D^+ and N_2H^+ show smaller gradients than the lower density tracers DCO^+ and $H^{13}CO^+$, implying a loss of specific angular momentum at small scales. At the level of cloud-core transition, the core's external envelope traced by DCO^+ and $H^{13}CO^+$ is spinning up. $C^{18}O$ traces the cloud material and stays unaffected by the presence of rotating cores. The decrease in specific angular momentum towards the centres of the cores shows the importance of local magnetic fields to the small scale dynamics of the cores. The random distributions of angles between the total velocity gradient and large scale magnetic field suggests that the magnetic fields may become apparent only in the high density gas within dense cores.

2.1 Introduction

Recent submillimetre studies of the nearest star-forming clouds with the *Herschel Space Observatory* show that interstellar filaments are common structures in molecular clouds and play an important role in the star-forming process (e.g. Men'shchikov et al. 2010; André et al. 2014). The filaments host chains of dense cores (e.g. Hacar et al. 2013; Könyves et al. 2014); some of the cores are pre-stellar – on the verge of star formation. Pre-stellar cores are cold (∼10 K), dense (10^4–10^7 cm^{-3}), and quiescent (thermal pressure dominates turbulent motions; e.g. Benson & Myers 1989; Fuller & Myers 1992; Lada et al. 2008; Caselli et al. 2008) self-gravitating structures (Ward-Thompson et al. 1999; Keto & Caselli 2008), characterised by high deuterium fractions (>10%, Crapsi et al. 2005). Pre-stellar cores represent the initial conditions in the process of star formation, thus their study is crucial to understand how stars and stellar systems form.

The target of our study, L1495 (Lynds 1962), is an extended filamentary structure in the Taurus molecular cloud, a nearby (140 pc distance, Elias 1978), relatively quiescent, low-mass star-forming region. The selected filament contains 39 dense cores revealed in ammonia by Seo et al. (2015) including 19 dense cores previously detected in N_2H^+(1–0) emission (Hacar et al. 2013) (see Fig. 2.1) at different stages of star formation. Tens of starless cores are detected there via continuum emission by the *Herschel*, and about fifty low-mass protostars in different evolutionary stages were observed with *Spitzer* (see the survey by Rebull et al. 2010). L1495 is a very well studied region, with its physical properties and structure determined by several large observational studies. This includes its gas kinetic temperature (Seo et al. 2015); dust extinction (Schmalzl et al. 2010); low

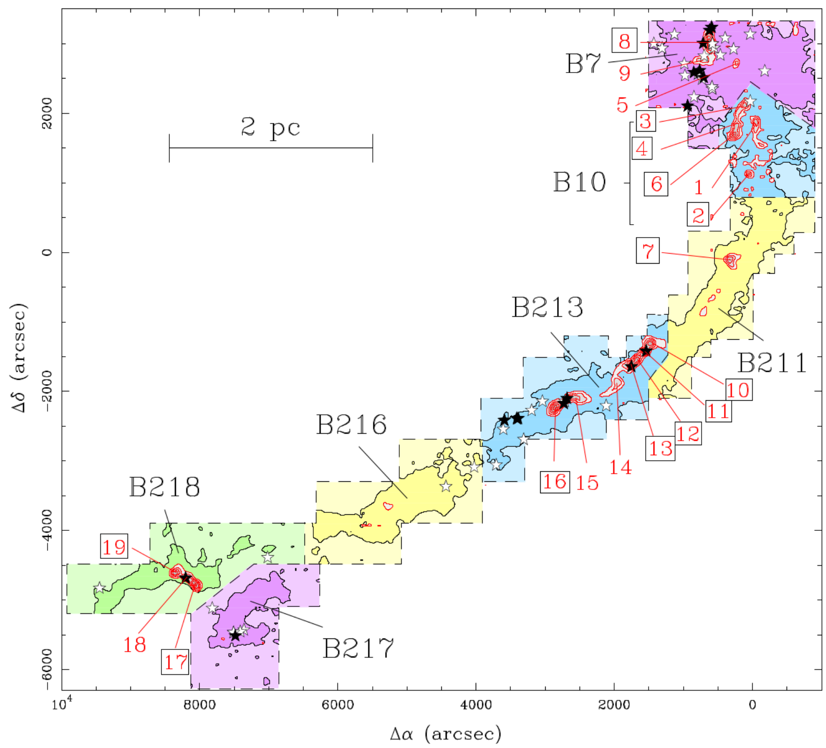

Figure 2.1: Schematic view of the selected L1495 filament within the Taurus Molecular Cloud Complex (adapted from Hacar et al. 2013). The offsets refer to the centre at $\alpha = 4^h17^m47.1^s$, $\delta = +27°37'18''$ (J2000). The black solid line represents the lowest $C^{18}O(1–0)$ contour (0.5 K km s^{-1}). The red lines represent the $N_2H^+(1–0)$ emission (first contour and contour interval are 0.5 K km s^{-1}), which traces the dense cores. The $C^{18}O(1–0)$ and $N_2H^+(1–0)$ data are from Hacar et al. (2013). The red labels identify the cores found by Hacar et al. (2013), and black squares around the labels show the cores studied in this work. The stars correspond to young stellar objects from the survey of Rebull et al. (2010). Solid symbols represent the youngest objects (Class I and Flat), and open symbols represent evolved objects (Class II and III).

density gas distribution, as traced by $H^{13}CO^+$ (Onishi et al. 2002) and $C^{18}O$ (Hacar et al. 2013); and dense gas distribution and dense cores locations, as traced by N_2H^+ (Hacar et al. 2013; Tafalla & Hacar 2015) and NH_3 (Seo et al. 2015). Thus, L1495 is an excellent place to test theories of dense core formation within filaments.

Hacar et al. (2013) mapped the whole filament in $C^{18}O$(1–0), SO(3–2), and N_2H^+(1–0) using the FCRAO antenna. They found that the filament is not a uniform structure and consists of many fibers. The fibers are elongated structures mostly aligned with the axis of the large-scale filament, with typical lengths of 0.5 pc, coherent velocity fields, and internal velocity dispersions close to the sound speed. The fibers were revealed in the low density gas tracer $C^{18}O$(1–0) kinematically. Their distribution resembles the small scale structure seen in dust continuum emission (e.g. André et al. 2014). Some of the CO fibers contain dense cores revealed by the high density tracer N_2H^+(1–0). Hacar et al. (2013) conclude that fragmentation in the L1495 complex proceeded in a hierarchical manner, from cloud to subregions (bundles) to fibers and then to individual dense cores. In the following study, Tafalla & Hacar (2015) found that the cores tend to cluster in linear groups (chains). Hacar et al. (2013) and Seo et al. (2015) note that some parts of the filament are young (B211 and B216) and others (B213 and B7) are more evolved and actively star-forming. The gas temperature they derived from NH_3 is low, 8–15 K with a median value of 9.5 K, with less evolved (B10, B211, and B216) regions only having a median temperature 0.5 K less than more evolved (B7, B213, B218) regions. They found that the gas kinetic temperature decreases towards dense core centres. With NH_3, which traces less dense gas than N_2H^+, Seo et al. (2015) found 39 ammonia peaks including those 19 found by Hacar et al. (2013). Onishi et al. (2002) presented a large survey of $H^{13}CO^+$(1–0) observed towards $C^{18}O$ emission peaks in L1495.

The previous studies of the gas kinematics in L1495 were focused on the large-scale structure, the filament as a whole and its subregions. Here we focus on the kinematics within the dense gas of the cores traced by N_2H^+ and N_2D^+, and the kinematics of the surrounding core envelope traced by $H^{13}CO^+$ and DCO^+ to study the gas that connects the cores to their host cloud.

The best tracers of the dense gas kinematics are N-bearing species. In dense (> a few $\times 10^4$ cm^{-3}) and cold (T$\simeq$10 K) regions, CO, CS, and other C-bearing species are highly frozen onto dust grains (Caselli et al. 1999; Tafalla et al. 2006; Bizzocchi et al. 2014). Nitrogen-bearing species such as N_2H^+ and NH_3 and their deuterated isotopologues stay in the gas phase up to densities of 10^6 cm^{-3} (Crapsi et al. 2005, 2007) and become good tracers of dense gas (see also Tafalla et al. 2004). N_2H^+ rotational transitions have higher critical densities ($n_{crit} \geq 10^5$ cm^{-3}) than the inversion transitions of NH_3 ($n_{crit} \sim 10^3$ cm^{-3}) and thus N_2H^+ traces dense gas better then NH_3. Deuterated species also increase their abundance towards the central regions of cores because of the enhanced formation rate of deuterated forms of H_3^+, for example, H_2D^+ (the precursor of deuterated species, such as DCO^+, N_2D^+, and deuterated ammonia), in zones where CO is mostly frozen onto dust grains (e.g. Dalgarno & Lepp 1984; Caselli et al. 2003). To study the kinematics of the gas in the central parts of the cores, we choose the N_2D^+(2–1) transition (n_{crit} =

Table 2.1: The observed cores. The names (numbers) of the cores are given following Hacar et al. (2013). The given coordinates are the central positions of the cores from Hacar et al. (2013). The protostellar cores are indicated with asterisks (*).

Core	α_{J2000} ($^{h\ m\ s}$)	δ_{J2000} ($^{\circ\ \prime\ \prime\prime}$)
2	04 17 50	27 56 07
3	04 17 56	28 12 23
4	04 18 04	28 08 14
6	04 18 06	28 05 41
7	04 18 10	27 35 29
8	04 18 34	28 27 37
10	04 19 37	27 15 48
11*	04 19 44	27 13 36
12	04 19 52	27 11 42
13*	04 19 59	27 10 30
16	04 21 21	27 00 09
17	04 27 54	26 17 50
19	04 28 14	26 20 34

2.5×10^6 cm^{-3}, calculated using the data[1] from the LAMDA database, Schöier et al. 2005), and the N_2H^+(1–0) line to connect to the work of Hacar et al. (2013), who also mapped N_2H^+(1–0), and also to study the deuterium fraction across the cores, which will be presented in a subsequent study (Punanova et al., in prep.). HCO^+ follows CO and thus it depletes in the centres of dense cores (e.g. Pon et al. 2009); therefore, HCO^+ is a good tracer of core envelopes. To study the kinematics of the core surroundings and provide a connection between the kinematics of the cores and that of the cloud, we choose the $H^{13}CO^+$(1–0) and DCO^+(2–1) transitions. This will also enable a future study of the deuterium fraction of the cores and core envelopes (Punanova et al., in prep.).

This paper presents observations of N_2D^+(2–1), N_2H^+(1–0), DCO^+(2–1), and $H^{13}CO^+$(1–0) towards 13 dense cores to study the kinematics of the dense gas along the L1495 filament. In Section 2.2, the details of the observations are presented. Section 2.3 describes the data reduction procedure. Section 2.4 presents the results of the hyperfine structure fitting and velocity gradients and specific angular momenta calculations. In Section 2.5 we discuss the results and connections between core-scale and cloud-scale kinematics. The conclusions are given in Section 2.6.

2.2 Observations

[1]http://home.strw.leidenuniv.nl/ moldata/datafiles/n2h+@xpol.dat

Table 2.2: Observation parameters.

Transition	Frequency^{a} (GHz)	F_{eff}	B^{h}_{eff}	HPBW ($''$)	Δv^{i}_{res} (km s^{-1})	rms in T_{mb} (K)	T_{sys} (K)	Mode^{j}	Dates
N_2H^+(1–0)	93.1737637^{b}	0.95	0.80	26.5	0.063	0.075–0.140	155–176	OTF	09–14.07.2014
N_2D^+(2–1)	154.2171805^{c}	0.93	0.72	16.3	0.038	0.040–0.100	203–627	OTF	09–14.07.2014
$H^{13}CO^+$(1–0)	86.7542884^{d}	0.95	0.81	28.5	0.068	0.110–0.190	102–129	OTF	02–08.12.2014
						0.140–0.190	122–126	OTF	03–04.06.2015
DCO^+(2–1)	144.0772804^{e}	0.93	0.73	17.2	0.041	0.150–0.250	115–155	OTF	02–08.12.2014
						0.310–0.500	198–220	OTF	03–04.06.2015
$HC^{18}O^+$(1–0)	85.1622231^{f}	0.95	0.81	28.5	0.069	0.026–0.039	96–105	SP	08.12.2014
						0.020–0.038	99–109	SP	04.06.2015
$D^{13}CO^+$(2–1)	141.4651331^{g}	0.93	0.74	17.5	0.041	0.028–0.039	90–96	SP	08.12.2014
						0.029–0.059	142–164	SP	04.06.2015

Notes. [(a)] Frequency of the main hyperfine component; [(b)] from Pagani et al. (2009); [(c)] from Pagani et al. (2009) and Dore, L., private communication; [(d)] from Schmid-Burgk et al. (2004); [(e)] from Caselli & Dore (2005); [(f)] from Schmid-Burgk et al. (2004); [(g)] from Caselli & Dore (2005); [(h)] B_{eff} and F_{eff} values are available at the 30 m antenna efficiencies web-page http://www.iram.es/IRAMES/mainWiki/Iram30mEfficiencies; [(i)] Δv_{res} is the velocity resolution; [(j)] Observational mode: OTF is an on-the-fly map, SP is a single-pointing on-off observation towards the DCO^+(2–1) emission peak.

We mapped 13 out of 19 dense cores of the L1495 filamentary structure (see Fig. 2.1 and Table 2.1) in N_2D^+(2–1) at 154.2 GHz, N_2H^+(1–0) at 93.2 GHz, DCO^+(2–1) at 144.1 GHz, and $H^{13}CO^+$(1–0) at 86.8 GHz with the IRAM 30 m telescope (IRAM projects 032-14 and 156-14). The $D^{13}CO^+$(2–1) at 141.5 GHz and $HC^{18}O^+$(1–0) at 85.2 GHz lines were observed towards the DCO^+(2–1) emission peaks of 9 cores. The observations were performed on 09–14 July, 02–08 December 2014 and 04 June 2015 under acceptable weather conditions, pwv=1–9 mm. The on-the-fly maps and single pointing observations were obtained with the EMIR 090 (3 mm band) and EMIR 150 (2 mm band) heterodyne receivers[2] in position switching mode, and the VESPA backend. The spectral resolution was 20 kHz, the corresponding velocity resolutions were $\simeq$0.07 for the 3 mm band and $\simeq$0.04 km s^{-1} for the 2 mm. The beam sizes were $\simeq$28″ for the 3 mm band and $\simeq$17″ for the 2 mm. The system temperatures were 90–627 K depending on the lines. The exact line frequencies, beam efficiencies, beam sizes, spectral resolutions and sensitivities are given in Table 2.2. Sky calibrations were obtained every 10–15 minutes. Reference positions were chosen individually for each core to make sure that the positions were free of N_2H^+(1–0) emission, using the Hacar et al. (2013) maps. The reference position for core 4 was contaminated with N_2H^+(1–0) emission, thus it is not analysed in the paper. Pointing was checked by observing QSO B0316+413, QSO B0415+379, Uranus, and Venus every 2 hours and focus was checked by observing Uranus and Venus every 6 hours.

To connect core-scale and cloud-scale kinematics, we used the fit results of the $C^{18}O$(1–0) observations by Hacar et al. (2013) convolved to 60″, performed with the 14 m FCRAO telescope.

2.3 Data reduction and analysis with Pyspeckit

The data reduction up to the stage of convolved spectral data cubes was performed with the CLASS package[3]. The intensity scale was converted to the main-beam temperature scale according to the beam efficiency values given in Kramer et al. (2013) (see Table 2.2 for details). The N_2H^+(1–0) maps were convolved to a resolution of 27.8″ with 9″ pixel size. The N_2D^+(2–1) maps were convolved to the resolution of the N_2H^+(1–0) with the same grid spacing to improve the sensitivity for a fair comparison of the kinematics traced by these transitions. The $H^{13}CO^+$(1–0) and DCO^+(2–1) maps were convolved to resolutions of 29.9″ and 18″, with pixel sizes of 9″ and 6″, respectively. The rms across the maps in T_{mb} scale is 0.075–0.14 K, 0.04–0.10 K, 0.11–0.21 K, and 0.15–0.50 K for the N_2H^+(1–0), N_2D^+(2–1), $H^{13}CO^+$(1–0), and DCO^+(2–1), respectively. Each map has a different sensitivity (see Table B.3 for details). The undersampled edges of the maps are not used for the analysis. Each data cube contains spectra of one transition towards one core. Some cores lie close to each other so we also produced combined data cubes (cores 4 and 6 and the chain of cores 10–13, see for example, Fig. 2.1 and B.8). Another dataset with all maps convolved to the biggest beam (29.9″) and Nyquist sampling was produced to compare

[2]http://www.iram.es/IRAMES/mainWiki/EmirforAstronomers

[3]Continuum and Line Analysis Single-Dish Software http://www.iram.fr/IRAMFR/GILDAS

local and total velocity gradients across the cores seen in different species (see Sect. 2.4.5 for details). The rms in T_{mb} scale across the maps smoothed to 29.9″ is in the ranges 0.065–0.12 K, 0.04–0.085 K, 0.11–0.21 K, and 0.05–0.15 K for the N_2H^+(1–0), N_2D^+(2–1), $H^{13}CO^+$(1–0), and DCO^+(2–1), respectively (see Table B.4 for details).

The spectral analysis was performed with the Pyspeckit module of Python (Ginsburg & Mirocha 2011). The N_2H^+(1–0), N_2D^+(2–1), $H^{13}CO^+$(1–0), and DCO^+(2–1) lines have hyperfine splitting with 15, 40, 6, and 6 components, respectively. Thus we performed hyperfine structure (hfs) fitting using the standard routines of Pyspeckit. The routine computes line profiles with the assumptions of Gaussian velocity distributions and equal excitation temperatures for all hyperfine components. It varies four parameters (excitation temperature T_{ex}, optical depth τ, central velocity of the main hyperfine component V_{LSR}, and velocity dispersion σ) and finds the best fit with the Levenberg-Marquardt non-linear regression algorithm. The rest frequencies of the main components, the velocity offsets, and the relative intensities of the hyperfine components were taken from Pagani et al. (2009), Schmid-Burgk et al. (2004), Caselli & Dore (2005), and Dore L. (priv. comm.). For the spectra of each transition towards the N_2H^+(1–0) emission peak of core 2, the results of Pyspeckit hfs fitting procedure were compared to the results of the CLASS hfs fitting method. The results agree within the errors. We first fitted Gaussians to the $H^{13}CO^+$(1–0) and DCO^+(2–1) lines and compared the results to the hfs fit results. We found that the hyperfine structure significantly affects the line profile and should be taken into account to provide accurate line widths (see Appendix B.1.1 for details).

The general data fitting procedure went as follows. First each spectrum in one data cube (one core, one species) was fitted two times assuming 1) unconstrained τ (all four parameters T_{ex}, τ, V_{LSR} and σ were free) and 2) constrained τ (τ was fixed at 0.1, which makes the fit close to the assumption that the line is optically thin; the other three parameters were free). Second, the final results data cube was produced by combining the results of the τ-constrained and τ-unconstrained fits. If $\tau/\Delta\tau \geq 3$, where $\Delta\tau$ is the optical depth uncertainty, the results of the τ-unconstrained fit were written to the final result data cube. If $\tau/\Delta\tau < 3$, the τ-constrained fit was chosen and written to the final result data cube. The $\tau/\Delta\tau$ test was done for each pixel. The combined results data cube was written to the final fits file after masking poor data. For the integrated intensity maps, we use all data except the undersampled edges of the maps. The excitation temperature and the optical depth have been measured only for those spectra with a high signal-to-noise ratio (SNR): $I > 5 \cdot rms \cdot \sqrt{N_{ch}} \cdot \Delta v_{res}$, where I is the integrated intensity, N_{ch} is the number of channels in the line, and Δv_{res} is the velocity resolution. For N_{ch}, we take all channels in the ranges: 2–12, -4–16, 5–10, and 5–10 km s^{-1} for N_2D^+(2–1), N_2H^+(1–0), and DCO^+(2–1) and $H^{13}CO^+$(1–0), respectively. These ranges define the emission above one $rms \cdot \sqrt{N_{ch}} \cdot \Delta v_{res}$ over spectrum averaged over the whole mapped area. For the central velocity and velocity dispersion maps we used the signal-to-noise mask and a mask based on velocity dispersion: the minimum line width must be larger than the thermal line width (σ_T) for a temperature of 5 K (slightly below the minimum gas temperature in L1495 found by Seo et al. 2015), which is 0.04 km s^{-1} for the given species, and the line width must be defined with an accuracy better than 20% ($\sigma/\Delta\sigma > 5$). If the line is optically thick, the intrinsic line width is found by means of the hfs fit.

In $H^{13}CO^+$(1–0) the hyperfine components are blended and the τ-unconstrained fit is often too ambiguous. For the majority of the $H^{13}CO^+$ spectra, optical depth was defined with an uncertainty $\Delta\tau > \tau/3$, thus we used the τ-constrained fit (τ=0.1) to gauge the central velocities and the velocity dispersions. The N_2H^+(1–0) and $H^{13}CO^+$(1–0) spectra show the presence of a second component towards cores 3, 8, 13, and 16 (see Fig. 2.2 and B.5). When the second component is more than one line width away from the main line, it is assumed to represent an independent velocity component and is not considered in our analysis. When the second component is closer than one line width and blended with the main line so the fitting routine can not resolve them, we consider the two components as one line.

The DCO^+(2–1) spectra towards all of the observed cores show double or multiple peaked lines caused by either additional velocity components or self-absorption. The velocity dispersions produced by τ-constrained fits of self-absorbed or blended lines are overestimated, because the fit considers only one velocity component and the optical depth is assumed to be 0.1. We compared the velocity dispersion values obtained with the τ-constrained and τ-unconstrained fits where the optical depth is defined with $\tau > 3\Delta\tau$. We found that the τ-constrained fit produces a velocity dispersion 1–3.3 times larger than the τ-unconstrained fit, with an average dispersion 1.56 times larger. As such, the velocity dispersions derived from these fits should be considered as upper limits for our DCO^+ data. Thus, for all of the DCO^+ spectra we used the τ-constrained fit (τ=0.1) to define the velocity dispersion upper limits and the central velocities. Significant asymmetry of the DCO^+(2–1) line towards core 7 (see Fig. 2.2) produced a systematic difference of $\simeq$0.1 km s^{-1} in its centroid velocity compared to the other species.

2.4 Results

2.4.1 Distribution of gas emission

Figure 2.2 presents the spectra of all four species towards the N_2H^+(1–0) emission peak of each core. For core 4, where the reference position was contaminated with N_2H^+(1–0) emission, we present the spectra towards the N_2D^+(2–1) emission peak.

There are starless (2, 3, 4, 6, 7, 8, 10, 12, 16, 17 and 19) and protostellar (11 and 13) cores among the observed targets. The protostellar cores host class 0–I young stellar objects (YSOs). Two YSOs (class II and III) are close in projection to but not associated with core 8. Two cores (2 and 7) are isolated from other cores and YSOs, the other cores are clustered in chains with other starless and protostellar cores and YSOs (see Fig. 2.1). The integrated intensity maps are shown in Fig. B.8. All four species are detected towards all observed cores (with SNR$>$ 5) except for N_2D^+(2–1) towards core 3 (detected with SNR$\simeq$ 3).

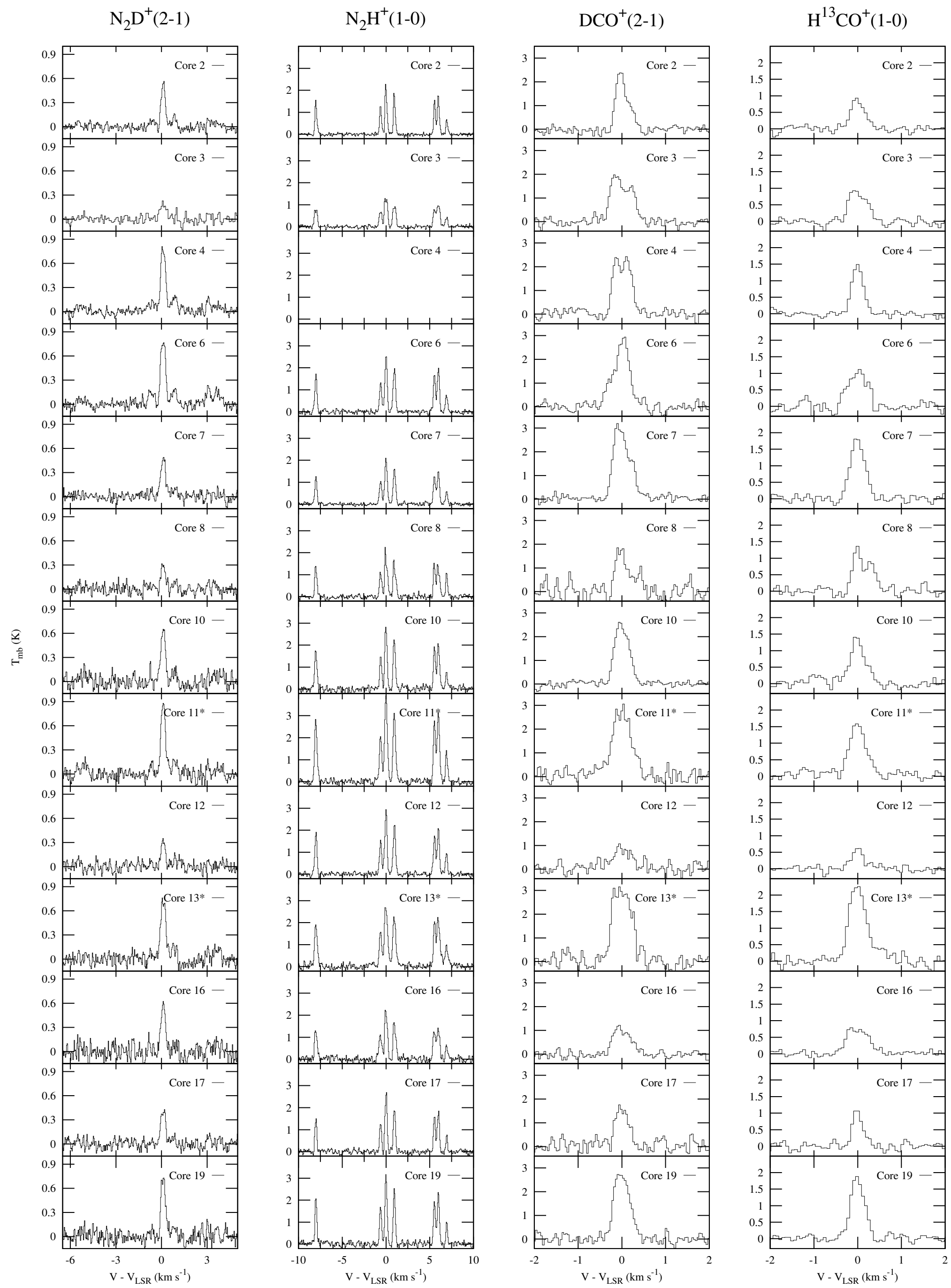

Figure 2.2: Spectra of all observed transitions towards the $N_2H^+(1–0)$ intensity peak for each core. For core 4, where the reference position was contaminated with $N_2H^+(1–0)$ emission, we present the spectra towards the $N_2D^+(2–1)$ emission peak. The cores with an asterisk (*) near the title contain protostars.

The N_2H^+(1–0) and N_2D^+(2–1) emission peaks usually match within one beam size (cores 2, 6, 7, 8, 10, 11, 13, 17, 19), however in cores 12 and 16 the peaks are offset by one or two beam widths (∼30–60″, see Fig. 2.3). Often the N_2H^+(1–0) and N_2D^+(2–1) emission areas have different shapes, with the N_2D^+(2–1) being more elongated (cores 6, 7, 12, 17) and compact. Emission peaks of N_2H^+(1–0) and N_2D^+(2–1) are associated with a position of a YSO towards the protostellar cores (11 and 13). One core (12) has two N_2D^+(2–1) emission peaks with the N_2H^+(1–0) emission peak in between (see cores 10–13 in Fig. B.8).

$H^{13}CO^+$(1–0) usually has several emission peaks within one core (3, 4, 6, 8, 10, 12, 17) and avoids the N_2D^+(2–1) emission peaks (2, 3, 4, 6, 10, 12, 16, 17), which is a sign of possible depletion. Towards the protostellar cores 11 and 13, $H^{13}CO^+$(1–0) and DCO^+(2–1) are centrally concentrated and their emission peaks are within a beam size to the YSOs. The DCO^+(2–1) emission follows the shape of the N_2D^+(2–1) emission, but it is more extended (4, 6, 7, 10, 11, 13, 16, 17) and in a few cases avoids N_2D^+(2–1) (2, 3, 8, 12) (see Fig. B.8).

Towards the cores 7, 11 and 13 all four species have very similar emission distribution and close peak positions.

2.4.2 Velocity dispersion

The velocity dispersions (σ) of all transitions are determined from the hfs fits. The maps of the velocity dispersions of the N_2D^+(2–1), N_2H^+(1–0), DCO^+(2–1), and $H^{13}CO^+$(1–0) lines are shown in Fig. B.9. The velocity dispersions of N_2D^+(2–1) range from 0.04 to 0.26 km s^{-1} with a median value of 0.10 and a median uncertainty of 0.01 km s^{-1}. σ of N_2H^+(1–0) ranges from 0.07 to 0.29 km s^{-1} with a median value of 0.12 and a median uncertainty of 0.003 km s^{-1}. σ of DCO^+(2–1) ranges from 0.05 to 0.30 km s^{-1} with a median value of 0.16 and a median uncertainty of 0.01 km s^{-1}. σ of $H^{13}CO^+$(1–0) ranges from 0.06 to 0.46 km s^{-1} with a median value of 0.16 and a median uncertainty of 0.02 km s^{-1}. Thus the velocity dispersion increases going from higher density gas tracers (N_2D^+ and N_2H^+) to lower density gas tracers (DCO^+ and $H^{13}CO^+$), as expected (Fuller & Myers 1992).

The velocity dispersion increases towards YSOs (cores 3, 8, 11, 12, 13, 17, 19, there is a protostellar core 18 between cores 17 and 19 see e.g. Fig. 2.1). Also, the velocity dispersion increases towards the centre of core 17, as seen in all four species, which may be a signature of contraction as found towards pre-stellar cores (Caselli et al. 2002b; Crapsi et al. 2005). Nevertheless, the line widths stay very narrow across the cores and are dominated by thermal motions (see Sect. 2.4.3 for details). The N_2D^+(2–1) velocity dispersions become large (compared to the thermal linewidth) only towards the protostar in core 13 and on the edges of cores 6, 7, and 19. The N_2H^+(1–0) velocity dispersions become large (compared to the thermal linewidth) only towards the protostars in cores 11 and 13, and on the edges of cores 6, 7, 8, and 16. The N_2H^+(1–0) and $H^{13}CO^+$(1–0) lines towards cores 3, 8, 13 and 16 also have hints of a second velocity component, not clearly resolved with our observations, which may increase the velocity dispersions towards those positions (see Sect. B.1.2 for details). A small fraction of the DCO^+(2–1) and $H^{13}CO^+$(1–0) spectra show a transonic

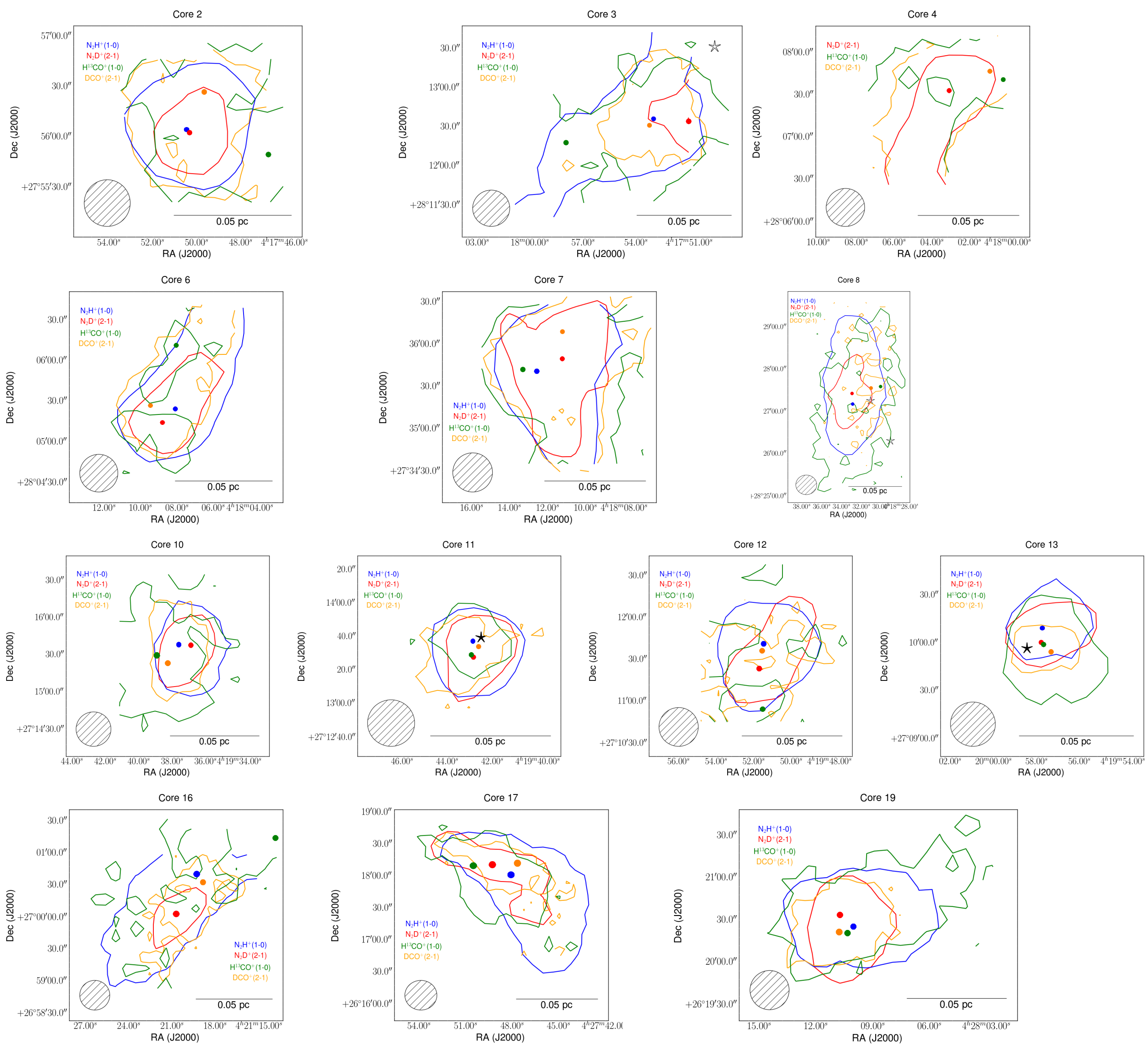

Figure 2.3: Integrated intensities of the N_2D^+(2–1), N_2H^+(1–0), DCO^+(2–1), and $H^{13}CO^+$(1–0) lines across the cores. The contours show 60% of the intensity peak, filled circles show the emission peaks. Stars show the positions of young stellar objects (YSOs) from Rebull et al. (2010): black stars are young, flat and class I objects, white stars are more evolved, class II and III objects. The 27.8″ beam size of N_2H^+(1–0) is shown in the bottom left of each panel.

velocity dispersions towards each core. The DCO^+(2–1) lines show asymmetric, double, or multiple peaked lines which are probably unresolved multiple velocity components towards all cores (see Sect. B.1.2 for details).

2.4.3 Non-thermal motions

Figure 2.4 shows the ratio of the non-thermal components σ_{NT} of the N_2D^+(2–1), N_2H^+(1–0), DCO^+(2–1), $H^{13}CO^+$(1–0), and $C^{18}O$(1–0) lines in each pixel of the maps and the thermal velocity dispersion of a mean particle, σ_T, as a function of core radius measured as a distance from the pixel to the N_2H^+(1–0) emission peak. The $C^{18}O$(1–0) velocity dispersions come from the fit results in Hacar et al. (2013). For the $C^{18}O$(1–0) plot, we take only the CO components whose V_{LSR} coincide with the V_{LSR} of the dense gas. The non-thermal components are derived from the observed velocity dispersion σ_{obs} via

$$\sigma_{NT}^2 = \sigma_{obs}^2 - \frac{kT_k}{m_{obs}}, \tag{2.1}$$

where k is Boltzmann's constant, T_k is the kinetic temperature, and m_{obs} is the mass of the observed molecule. The formula is adopted from Myers et al. (1991), taking into account that $\sigma^2 = \Delta v^2/(8\ln(2))$, where Δv is the full width at half maximum of the line, FWHM. To measure the non-thermal component, we use the kinetic temperature determined by Seo et al. (2015) from ammonia observations. We use the same temperature for all five lines, the temperature towards the N_2H^+(1–0) peak, for each core. The variations in the kinetic temperature across the mapped core areas are within 1–2 K, which produce an uncertainty of 6–12% in the σ_{NT}/σ_T ratio. Since the kinetic temperature of the gas in the studied cores usually increases towards their edges, we can expect the right hand sides of the distributions in Fig. 2.4 to shift down by 6–12%.

The thermal velocity dispersions σ_T for a mean particle with mass 2.33 amu are 0.17–0.21 km s^{-1} for typical temperatures of 8–12 K across the cores of L1495. The majority of all four high density tracers' lines are subsonic. However going from tracers of more dense gas to tracers of less dense gas, the fraction of transonic ($1 < \sigma_{NT}/\sigma_T < 2$) lines increases: 0.8% of the N_2D^+(2–1) lines, 2.6% of the N_2H^+(1–0) lines, 19% of the DCO^+(2–1) lines, and 24% of the $H^{13}CO^+$(1–0) lines are transonic, while 67% of the $C^{18}O$(1–0) lines show transonic or supersonic line widths. The median σ_{NT}/σ_T ratio also increases from high to low density, being 0.49, 0.58, 0.84, 0.81, and 1.16 for N_2D^+(2–1), N_2H^+(1–0), DCO^+(2–1), $H^{13}CO^+$(1–0), and $C^{18}O$(1–0), respectively. The maximum non-thermal to thermal velocity dispersion ratio is 1.4 for N_2D^+(2–1), 1.5 for N_2H^+(1–0), 1.6 for DCO^+(2–1), 2.4 for $H^{13}CO^+$(1–0), and 3.9 for $C^{18}O$(1–0). The ratio slightly decreases with radius for N_2D^+(2–1) and DCO^+(2–1), but stays relatively constant for N_2H^+(1–0) and $H^{13}CO^+$(1–0). The highest density in the points distribution occupies the same σ_{NT}/σ_T range in the N_2H^+ and N_2D^+ plots (0.4–0.6), and another zone for $H^{13}CO^+$ and DCO^+ (0.65–0.85). Nevertheless, with possibly overestimated velocity dispersions of N_2H^+(1–0) and $H^{13}CO^+$(1–0) and to a greater extent DCO^+(2–1), the lines stay subsonic and split between more narrow N_2D^+/N_2H^+ with 0.5 σ_T and less narrow $DCO^+/H^{13}CO^+$ with 0.8 σ_T.

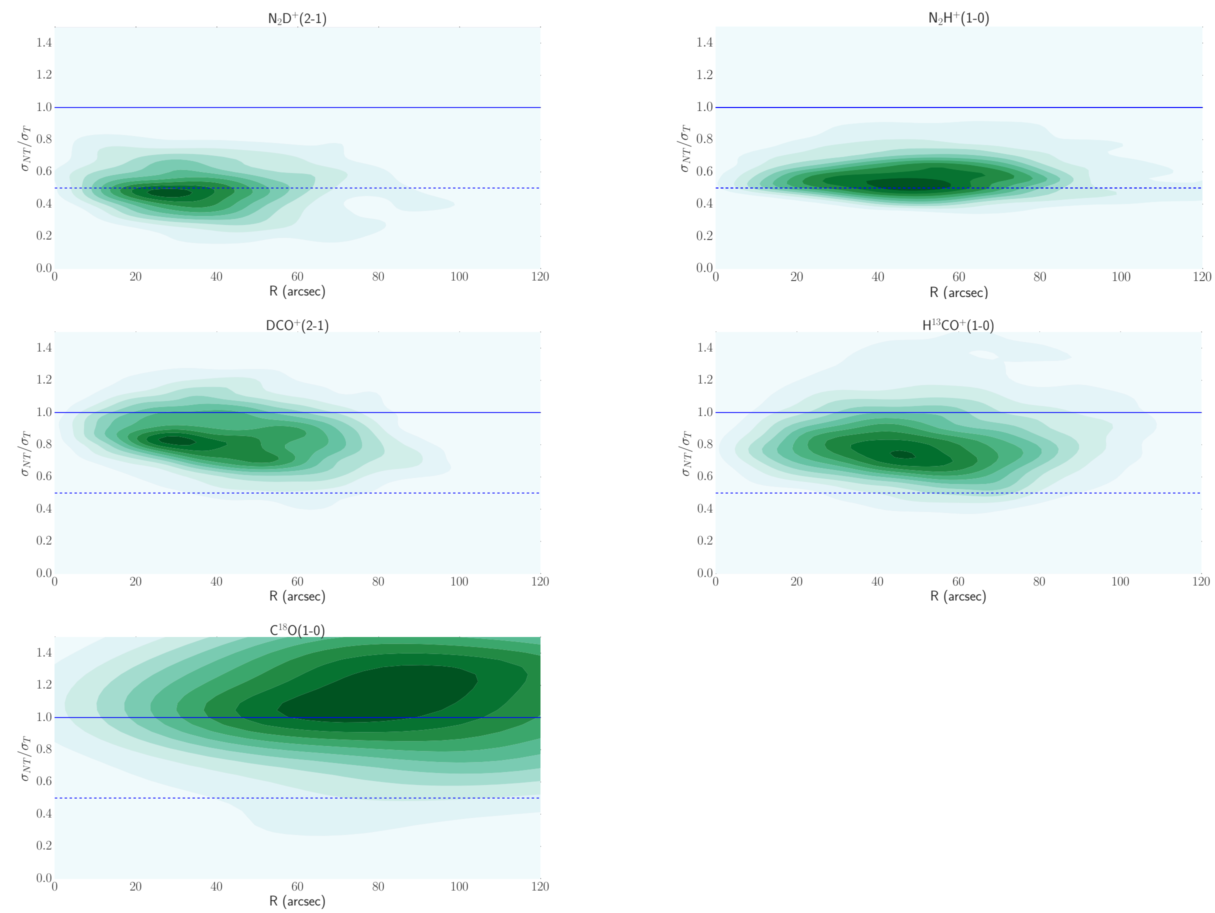

Figure 2.4: Ratio of non-thermal components of N_2D^+(2–1), N_2H^+(1–0), DCO^+(2–1), $H^{13}CO^+$(1–0), and $C^{18}O$(1–0) to the thermal line width of a mean particle as a function of radius (distance from the N_2H^+(1–0) intensity peak) for all cores. The solid and dashed blue lines show the ratios equal to 1 and 0.5. The colourscale represents the density of the points.

2.4.4 Velocity field: V_{LSR} and velocity gradients

The centroid velocities V_{LSR} of all the transitions are determined from the hfs fits. The maps of the centroid velocities of the N_2D^+(2–1), N_2H^+(1–0), DCO^+(2–1), and $H^{13}CO^+$(1–0) lines across the cores are presented in Fig. B.10. The range of the V_{LSR} seen in all lines (6.3–7.6 km s^{-1}) is narrower than the velocity range seen across the entire filament in NH_3 (5.0–7.2 km s^{-1}, Seo et al. 2015) and $C^{18}O$ (4.5–7.5 km s^{-1}, Hacar et al. 2013), which trace both dense and diffuse gas. The velocity fields traced by the four lines are usually similar within one core. The dense gas in core 13, which hosts the class 0 protostar IRAS 04166+2706 (Santiago-García et al. 2009), has a peculiar velocity field in that the different species have significantly different velocity field morphologies. It is probably affected by the outflow of the protostar.

Figure 2.5 presents velocity profiles along the fiber directions defined in Hacar et al. (2013), from core 19 in the south-east to core 8 in the north-west. Some cores (3, 7, 8, 10, 17, and 19) are located next to the places where the fibers change their directions. Core 2 is not associated with any fiber, such that we use a -45° position angle measured from the north to east for the filament direction there. The velocity changes both along and across the fibers. Figure 2.5 shows that the N_2D^+(2–1) velocity is less spread than that of N_2H^+(1–0) and the other lines towards cores 6, 8, 10, 11, 12, 13, and 16 (all observed cores in more evolved subregions B213 and B7, and core 6). Comparison of the velocity maps in Fig. B.10 shows that the smaller area of the N_2D^+(2–1) emission can not explain the difference. Here the densest gas is not participating in the flow of material along the fibers as seen in N_2H^+ and other tracers. The highest dispersions of the centroid velocities ($\simeq$0.6 km s^{-1}) appear at the protostellar cores (11 and 13) and cores close to a protostar (10, 12, 17, and 19).

The V_{LSR} of DCO^+(2–1) towards core 7 is systematically lower than that of other tracers. The DCO^+(2–1) line here is blended with a second velocity component and the V_{LSR} has a systematic shift because of the line asymmetry (see Fig. 2.2). The N_2D^+(2–1) velocity along the filament is systematically lower than that of N_2H^+ and the other species towards cores 6, 7, 8, 12, 17, and 19.

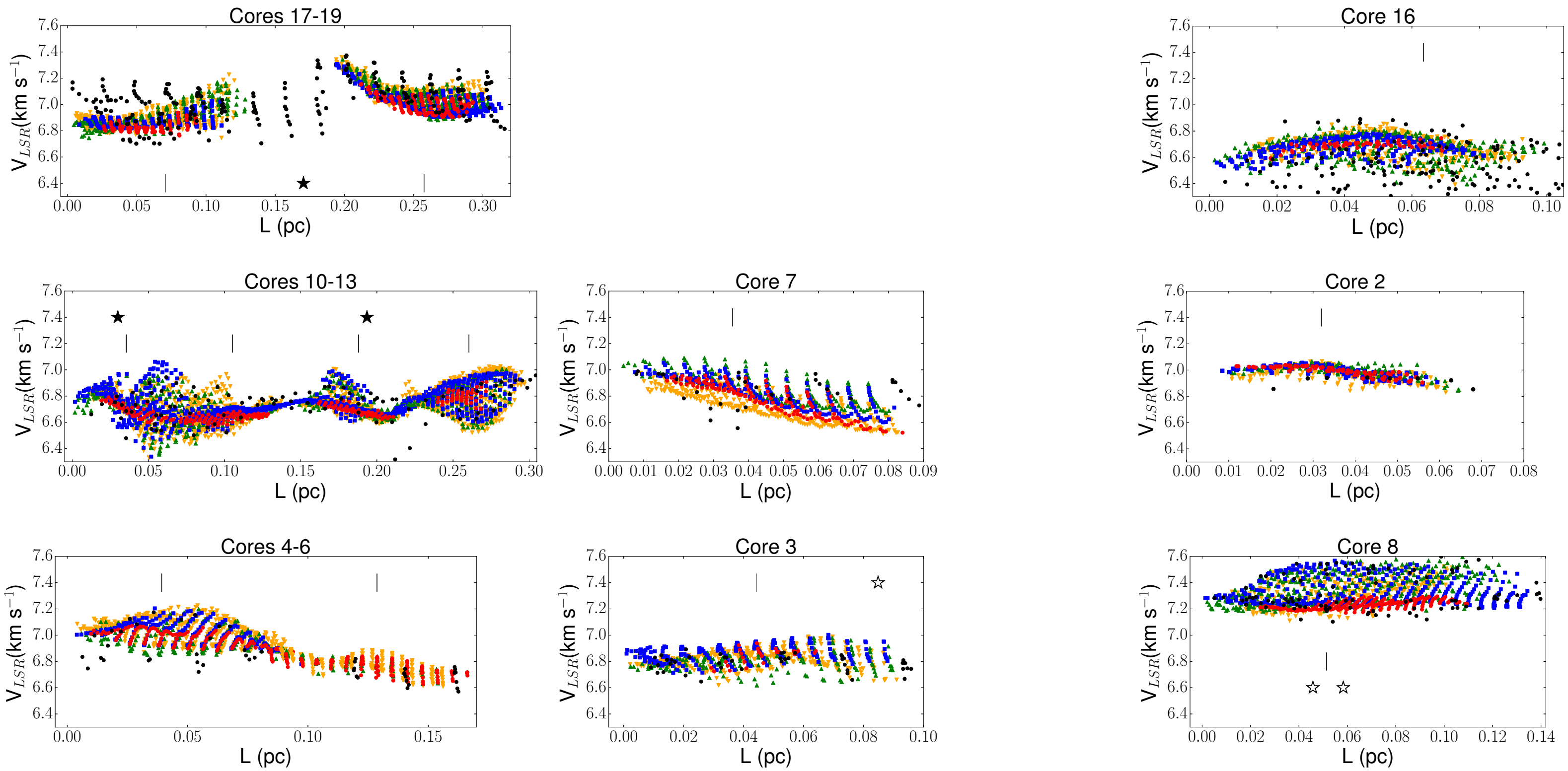

Figure 2.5: V_{LSR} along the filament direction (from core 19 in the south-east to core 8 in the north-west). The transitions are shown with colours: N_2D^+(2–1) – red circles, N_2H^+(1–0) – blue squares, DCO^+(2–1) – orange flipped triangles, $H^{13}CO^+$(1–0) – green triangles, and $C^{18}O$(1–0) – black circles. The vertical bars show the N_2H^+(1–0) emission peaks. Stars show the positions of YSOs from Rebull et al. (2010): black stars are flat and class I objects, white stars are class II and III objects.

2.4.5 Total gradients and specific angular momentum

Assuming that the cores are in solid body rotation, we estimate total and local velocity gradients across the cores following the method described in Goodman et al. (1993) for total gradients and applied for local gradients by Caselli et al. (2002a) (see Sect. 3.4.2 for local gradients). The results of the total velocity gradient calculation provide the average velocity across the core $< \mathrm{V_{LSR}} >$, the magnitude of the velocity gradient G, and the position angle θ_G. The total gradients are calculated using all available points weighted by $1/\Delta^2_{\mathrm{V_{LSR}}}$, where $\Delta_{\mathrm{V_{LSR}}}$ is the uncertainty of the central velocity. We also calculate the specific angular momentum as $J/M \equiv p\Omega R^2$, where $p = 0.4$ is a geometry factor appropriate for spheres, Ω is the angular velocity, derived from the velocity gradient analysis, R is the radius, with the assumption that $R = \sqrt{S/\pi}$, where S is the emitting area (see e.g. Phillips 1999) which is here the area of the velocity map.

Total gradients and specific angular momentum measured over all detected emission

At first, $< \mathrm{V_{LSR}} >$, G, θ_G, R and J/M are calculated for all emitting areas for each species (the numbers are given in Table B.5). The total gradients of the four species with their position angles are shown in Fig. B.11. One can expect that higher density tracers have smaller gradient values than lower density tracers, as the decrease in velocity gradient values should trace the loss of the corresponding specific angular momentum towards the small scales (Crapsi et al. 2007; Belloche 2013). That means that velocity gradients should increase in a sequence $\mathrm{N_2D^+} \rightarrow \mathrm{N_2H^+} \rightarrow \mathrm{DCO^+} \rightarrow \mathrm{H^{13}CO^+}$. Only core 19 obeys this sequence. Four cores (4, 6, 8, and 16) increase their gradients in a sequence $\mathrm{N_2D^+} \rightarrow \mathrm{N_2H^+} \rightarrow \mathrm{H^{13}CO^+} \rightarrow \mathrm{DCO^+}$ (although for core 4 there is no $\mathrm{N_2H^+}$ data and gradients of $\mathrm{DCO^+}$ and $\mathrm{H^{13}CO^+}$ differ within the uncertainties, by $\simeq$1%). Three cores (11, 12, and 13), belonging to one core chain, increase their gradients in a sequence $\mathrm{N_2H^+} \rightarrow \mathrm{N_2D^+} \rightarrow \mathrm{H^{13}CO^+} \rightarrow \mathrm{DCO^+}$. Core 17 has the sequence $\mathrm{N_2H^+} \rightarrow \mathrm{N_2D^+} \rightarrow \mathrm{DCO^+} \rightarrow \mathrm{H^{13}CO^+}$; core 10 has the sequence $\mathrm{N_2D^+} \rightarrow \mathrm{H^{13}CO^+} \rightarrow \mathrm{N_2H^+} \rightarrow \mathrm{DCO^+}$. Cores 2 and 3 have the sequence $\mathrm{H^{13}CO^+} \rightarrow \mathrm{DCO^+} \rightarrow \mathrm{N_2H^+} \rightarrow \mathrm{N_2D^+}$ (core 2 has equal $\mathrm{DCO^+}$ and $\mathrm{H^{13}CO^+}$ gradients, and core 3 has an unreliable detection of $\mathrm{N_2D^+}$ with SNR=3). Core 7 has the sequence $\mathrm{DCO^+} \rightarrow \mathrm{H^{13}CO^+} \rightarrow \mathrm{N_2H^+} \rightarrow \mathrm{N_2D^+}$. The differences between the gradient values are significant taking the errors into account. If we assume that $\mathrm{N_2H^+}$ and $\mathrm{N_2D^+}$ equally well trace the dense central part of a core, and $\mathrm{DCO^+}$ and $\mathrm{H^{13}CO^+}$ equally well trace the more diffuse envelope of a core, we have 10 out of 13 cores which follow the expectations about total gradient increase. There are three cores (2, 3, and 7) which show a total velocity gradient increase towards the denser gas (similar to L1544, Caselli et al. 2002b). Cores 2 and 7 are isolated starless cores, whereas core 3 has an evolved YSO nearby. Among them only core 7 shows a coherent velocity field and very likely is in solid body rotation.

Specific angular momentum varies in a range $(0.6\text{–}21.0)\times10^{20}$ cm^2 s^{-1} with a typical error of $(0.02\text{–}0.21)\times10^{20}$ cm^2 s^{-1} at core radii between 0.019–0.067 pc. It is similar to the results for other dense cores (J/M = $(6.2\text{–}30.9) \times 10^{20}$ cm^2 s^{-1} at radii 0.06–

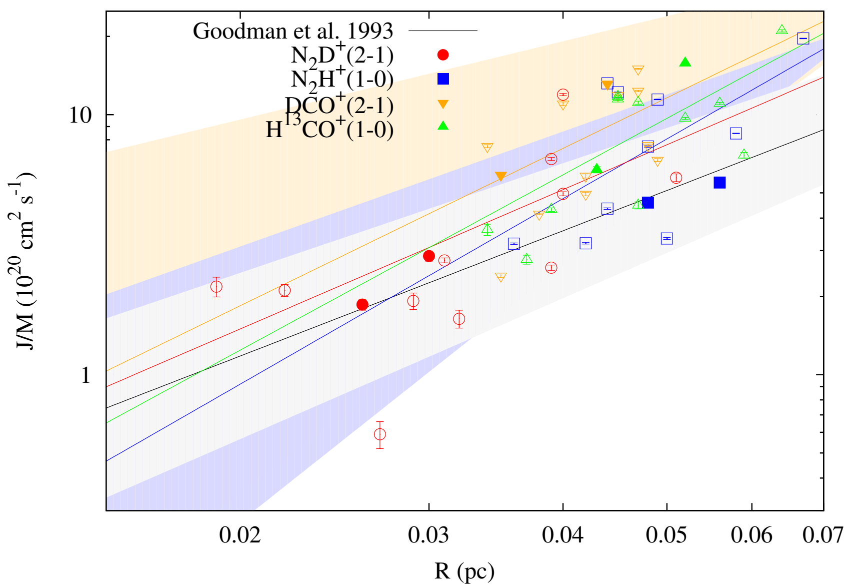

Figure 2.6: Specific angular momentum as a function of core radius, measured with different lines. Filled symbols show protostellar cores, open symbols show starless cores. The lines are the best fits of a power-law function aR^b calculated for each species (N_2H^+(1–0) – blue, N_2D^+(2–1) – red, $H^{13}CO^+$(1–0) – green, DCO^+(2–1) – orange), a and b values are given in the main text. The black line shows the relation found by Goodman et al. (1993). Thick light-colour strips represent the accuracies of the fits (N_2H^+(1–0) – light blue, DCO^+(2–1) – light orange, Goodman et al. (1993) – grey).

0.60 pc and J/M = (0.04–25.7) $\times 10^{20}$ cm^2 s^{-1} at radii 0.018–0.095 pc, Goodman et al. 1993; Caselli et al. 2002a, respectively). Figure 2.6 shows the correlation between specific angular momentum and radius of the core. For each species we find a best-fit power law correlation aR^b: for N_2D^+(2–1) $J/M = 10^{23\pm1}R^{1.8\pm0.8}$ cm^2 s^{-1}; for N_2H^+(1–0) $J/M = 10^{24\pm1}R^{2.4\pm0.9}$ cm^2 s^{-1}; for DCO^+(2–1) $J/M = 10^{24\pm1}R^{2.0\pm1.1}$ cm^2 s^{-1}; and for $H^{13}CO^+$(1–0) $J/M = 10^{24\pm1}R^{2.2\pm0.7}$ cm^2 s^{-1}. These numbers agree with those found by Goodman et al. (1993) with ammonia observations: $J/M = 10^{22.8\pm0.2}R^{1.6\pm0.2}$ cm^2 s^{-1}. We note that the radii used to calculate J/M here are larger than the radii at FWHM of emission. The significant difference between FWHM and equivalent radius of emission (see Fig. B.14) shows that the common approach to use FWHM as a size of a core may not be correct. All data used to calculate J/M have signal-to-noise ratio > 5 except for the N_2D^+ data for core 3 with SNR$\simeq$ 3.

Total gradients and specific angular momentum measured over the maps with uniform area and resolution

To compare the total velocity gradients for the four species on the same size scale, we convolve all maps to the spatial resolution of 29.9″, corresponding to the $H^{13}CO^+$(1–0) beam size, with Nyquist grid spacing, and use only the area where the emission in all four species is detected, which matches where N_2D^+(2–1) is detected, because it has the most compact emission. The results of the gradient calculations are given in Table B.6.

We compare the results for N_2D^+(2–1) with the results obtained with the other species in Fig. B.12. The average centroid velocity $< V_{LSR} >$ of N_2D^+(2–1) agrees with the $< V_{LSR} >$ of the other species within 1.5%, however for most of the cores the N_2D^+(2–1) velocity is systematically lower (see Fig. B.12, a). The total centroid velocity gradient G of N_2D^+(2–1) for the majority of cores is also lower than G measured with other species. The range of the total gradients seen in all species is 0.66–7.35 km s^{-1} pc^{-1} with the errors in a range 0.02–0.14 km s^{-1} pc^{-1}. The N_2D^+(2–1) line is most similar to the N_2H^+(1–0) line, with the maximum difference being 1.9 km s^{-1}pc^{-1} at core 8, and the median difference being 0.5 km s^{-1}pc^{-1}. The difference with $H^{13}CO^+$(1–0) and DCO^+(2–1) is more significant. The maximum difference between N_2D^+(2–1) and $H^{13}CO^+$(1–0) is 2.8 km s^{-1} pc^{-1} at core 16. The median difference is 1.1 km s^{-1} pc^{-1}. The maximum difference between N_2D^+(2–1) and DCO^+(2–1) is 3.8 km s^{-1} pc^{-1} at core 16. The median difference is 1.2 km s^{-1} pc^{-1}.

The directions of the gradients seen in different species are generally in better agreement. The typical errors of the determination of the position angle are 0.4–3.0°. The best agreement is between N_2D^+(2–1) and DCO^+(2–1); the biggest difference is 94° at core 16, and the median difference is 10°. The biggest difference between N_2D^+(2–1) and $H^{13}CO^+$(1–0) is 118° at core 16, and the median difference is 11°. The biggest difference between N_2D^+(2–1) and N_2H^+(1–0) is 68° at core 16, and the median difference is 12°. Thus, the median difference in the total gradient directions between the species is the same within the uncertainties.

The specific angular momentum varies in a range of (0.7–12.2)$\times 10^{20}$ cm^2 s^{-1} with a typical error of (0.02–0.31)$\times 10^{20}$ cm^2 s^{-1}. J/M measured in N_2D^+(2–1) agrees better with J/M measured in $N_2H^+(1\text{–}0)$ (median difference is 14%, maximum difference is 114% at core 8). J/M measured in $N_2D^+(2\text{–}1)$ is systematically lower than J/M measured in $H^{13}CO^+(1\text{–}0)$ and $DCO^+(2\text{–}1)$ (median differences with $N_2D^+(2\text{–}1)$ are 40 and 39%, maximum differences 425 and 578% at core 16) with the exception of core 7.

We also compare the results for $DCO^+(2\text{–}1)$ and $H^{13}CO^+(1\text{–}0)$ in Fig. B.13. The average centroid velocities of the two lines agree within 0.7%. The total centroid velocity gradient of the two species stays along the one-to-one correlation with no systematic difference. A median scatter of G is 0.9 km s^{-1} pc^{-1} and the maximum difference is 3.6 km s^{-1} pc^{-1} at core 3. The directions of the gradients of $DCO^+(2\text{–}1)$ and $H^{13}CO^+(1\text{–}0)$ are in good agreement, with the difference in position angle varying from 0.4–24° and having a median difference of 6°. The specific angular momentum of the two lines agrees within (0.03–2.2)$\times 10^{20}$ cm^2 s^{-1} with a maximum difference at core 8.

2.4.6 Local gradients

The local velocity gradients are presented in Fig. B.15 with black arrows, plotted over integrated intensity colour maps of the corresponding molecular transition along with red arrows which present local velocity gradients of $C^{18}O(1\text{–}0)$ calculated from the Hacar et al. (2013) fit results (a comparison with the $C^{18}O$ local velocity gradients is given in Sect. 2.5.2). The maps are convolved to a 29.9″ beam with Nyquist sampling. To calculate a gradient in a local position, we use all pixels closer than two pixel size distance, weighted according to their distance to the given position and their uncertainty of the central velocity:

$$W = \frac{1}{\Delta^2_{\mathrm{V_{LSR}}}} \cdot \exp\left\{-d^2 \Big/ \left[2\left(\frac{\theta_{Gauss}}{2.354}\right)^2\right]\right\}, \tag{2.2}$$

where W is the weight, $\Delta_{\mathrm{V_{LSR}}}$ is the uncertainty of the central velocity, d is the distance from the weighted pixel to the given position, and $\theta_{Gauss} = 2$ is the FWHM of the weighting function.

The majority of the cores are elongated (3, 6, 7, 8, 16, 17, and 19) along the filament axis and also stay in the elongated chains (3-4-6, 10-11-12-13, 15-16 with protostars in between, 17-18-19). Some cores (6, 7, and 17) are "bent". The directions of the velocity gradient is usually perpendicular to the core major axis (see cores 3, 6, 7, 8, 10, 12, 19). Cores 2, 4, and 16 increase their velocities towards the core centres, while core 17 shows velocities decreasing towards the core centre (the arrows shown in Fig. B.15 point towards higher $\mathrm{V_{LSR}}$). For a given core, the velocity fields of the different species are typically fairly similar.

There are, however, some variations from one species to the other, in particular towards the protostellar cores. Core 13 has the most complex velocity field with the $N_2H^+(1\text{–}0)$ data showing four different velocity gradient directions in various areas across the core. Only two of these gradients can be seen in the $N_2D^+(2\text{–}1)$ data due to the smaller detected extent of the $N_2D^+(2\text{–}1)$ emission. The significant change of the gradient direction on a small spatial scale, which is also present in core 11 and less prominent in cores 3, 8, and 12 is characteristic for a protostellar core, first revealed by Crapsi et al. (2004) towards another Taurus core, L1521F. This would imply that the last three cores known as starless may be relatively highly evolved. The difference between N_2D^+/N_2H^+ and $DCO^+/H^{13}CO^+$ can represent some differential gas motions between the core envelope and the central regions.

2.5 Discussion

2.5.1 Velocity dispersions

Pineda et al. (2010) define the coherent dense core as a region with nearly constant subsonic non-thermal motions. The linewidth distribution we see in the dense gas tracers, N_2D^+(2–1) and N_2H^+(1–0), shows constant subsonic ($\simeq \sigma_T/2$) non-thermal motions (see Fig. 2.4), with N_2D^+ having $\simeq$20% lower non-thermal components than N_2H^+, consistent with these observations tracing the coherent centres of dense cores in L1495.

Pineda et al. (2010) observed a sharp transition to coherence, where the line widths of NH_3(1,1) increased by a factor of at least two over a distance of less then 0.04 pc, which corresponds to their beam size. We do not see any reliable sign of the transition to coherence in any of the tracers that we have observed. One can explain this by the fact that the N_2D^+(2–1) line, which traces the high density gas, has a significantly higher critical density than the inversion transitions of NH_3. Thus, the N_2D^+ line intensity drops faster towards the edge of the core because the excitation temperature decreases more rapidly than the one of the NH_3 inversion line. Similarly, for most of the cores, the next highest density gas tracers, the N_2H^+(1–0) and DCO^+(2–1) lines (both having critical densities higher than that of NH_3(1,1)), are detected over larger areas and still do not show any sudden increase in line width, as seen in NH_3. Towards those cores where the emission strongly decreases away from the core centres (cores 6 and 17 for N_2H^+ and cores 8, 11, 13, 16, and 17 for DCO^+), the line widths at the edges do not increase significantly from the line widths towards the centre of the cores, or even decrease. However, even the NH_3 maps by Seo et al. (2015), which cover larger areas than our maps, still do not show a significant increase in the velocity dispersions towards the core edges.

We see however supersonic line widths in $H^{13}CO^+$, with the line widths reaching 2.4 σ_T in some places. Its transonic non-thermal motions lie mostly between 1 and 1.5 σ_T, consistent with the typical observed $C^{18}O$ non-thermal component (see Fig. 2.4). $H^{13}CO^+$ tends to be slightly (cores 2, 6, 8, 10) or significantly (cores 4, 12, 16) depleted towards the core centres and better traces the core envelopes compared to N_2D^+ and N_2H^+. The fact that the median velocity dispersions of N_2D^+(2–1) and the N_2H^+(1–0) are 1.3–1.6 times lower than the median velocity dispersions of DCO^+(2–1) and $H^{13}CO^+$(1–0) indicates that the velocity dispersion is indeed increasing outwards.

2.5.2 Connection to the filament scale

To search for a connection from the cores and their envelopes to the filament scale, we estimate local and total V_{LSR} gradients of the CO and compare the velocity field patterns and total gradients to the patterns seen in each species we observed. For the CO data we use the fit results of the $C^{18}O(1–0)$ mapping done by Hacar et al. (2013), which created maps convolved to a 60″ beam size. In their work, Hacar et al. (2013) found multiple velocity components of the $C^{18}O(1–0)$ line and revealed the fiber structure of the L1495 filament. They classify the fibers as "fertile", if they host dense cores and coincide with N_2H^+ emission, and "sterile" if they do not. For our study, we take only the $C^{18}O(1–0)$ components that have a V_{LSR} close to the V_{LSR} of our lines (6.3–7.6 km s^{-1}).

We show the maps of local velocity gradients in Fig. B.15. Here, black arrows represent the velocity gradients of $N_2D^+(2–1)$, $N_2H^+(1–0)$, $DCO^+(2–1)$, and $H^{13}CO^+(1–0)$ and red arrows represent the velocity gradients of $C^{18}O(1–0)$. For the majority of the cores, the $C^{18}O$ velocity gradient value G is lower than the G of the other lines. The velocity field of the dense gas is affected by protostars both in protostellar cores (11 and 13 as seen in all species) and cores sitting next to protostellar cores and YSOs (3, 8, 10, 12, 16, 17, and 19 as seen mostly in $H^{13}CO^+$, see Sect. 3.4.2). While the $C^{18}O$ velocity fields do not show the same level of complexity as that of the dense gas tracers, the velocity field of the $C^{18}O$ is by no means uniform and exhibits changes in direction in cores 3, 8, 10, 16, and 19.

In cores 3, 6, 12, and 19 the velocity pattern of $C^{18}O$ matches the patterns of the higher density tracers, with the agreement being better between $C^{18}O$, N_2H^+, and N_2D^+. In cores 4, 11, 13, and 17, $C^{18}O$ has uniform velocity patterns which match some velocity patterns seen in N_2H^+, DCO^+, and $H^{13}CO^+$. In the northern half of core 8 the velocity pattern of $C^{18}O$ matches the velocity patterns of N_2D^+, DCO^+, and $H^{13}CO^+$ (the velocity increases to the north-west) while in the southern half of the core the $C^{18}O$ velocity gradient is perpendicular to the gradients of the other species. Here, the dense gas tracers all increase in velocity towards the south-west, towards a YSO, whereas the CO velocity increases to the north-west. In core 16 the velocity of the high density tracers increases towards the core centre and the velocity of the $C^{18}O$ increases towards a position $\sim 1'$ to the north of the core, so the pattern looks similar but shifted, although this could be insignificant given the 60″ beam size of the $C^{18}O$ data. In core 2 the velocity of the high density tracers also increases towards the core centre and the velocity of the $C^{18}O$ uniformly increases towards the south-west of the core. Core 10 has curved velocity fields both in the $C^{18}O$ and high density tracers, although the $C^{18}O$ velocity field is roughly perpendicular to the velocity fields of the other tracers towards most locations. Core 7 has coherent velocity fields both in $C^{18}O$ and high density tracers (local gradients arrows almost parallel in $C^{18}O$ and divergent in the other species), oriented with an angle to each other which changes from 90° to 0°. In general, $C^{18}O$ show similar velocity patterns in the starless cores as high density tracers, with less complexity, and does not show any affect from embedded protostars in the protostellar cores, which makes the $C^{18}O$ velocity gradients almost perpendicular to those of the high density tracers.

The total gradients are shown in Fig. B.11. The difference between $C^{18}O$ and the higher density tracers is more significant in the overall gradient directions due to the additional complexity of the higher density tracers' velocity fields. Cores 4 and 6 show a good correlation between $C^{18}O$ and the other species, with the largest difference being the 8° separation between the $C^{18}O$ and $H^{13}CO^+$ gradients in core 6. Cores 3, 6, 7, 8, 10, 11, 12, 17, and 19 show directions for the gradient of $C^{18}O$ which differ less than 90° (20–83°) from that of the dense gas tracers. The $C^{18}O$ gradient differs by more than 90° from that of at least one dense gas tracer in cores 2, 13, and 16, although the total velocity gradient of $C^{18}O$ towards core 2 has a large error of 40° owing to the small number of data points. Core 13 has very complex velocity fields of the higher density tracers due to the strong affect of the embedded protostar. Core 16 has complex velocity patterns both in $C^{18}O$ and the higher density tracers which affect the total gradient. For the majority of the cores. The $C^{18}O$(1–0) velocity field coincides with the high density tracers' but does not show the variations near YSOs (cores 8, 11, 12, 13, 17, and 19) seen in high density tracers.

The value of the $C^{18}O$ total velocity gradient (0.3–3.3 km s pc^{-1} measured with a typical error of 0.03–0.17 km s pc^{-1}) is usually lower than that of the other species (0.6–6.1 km s pc^{-1} in cores 2, 3, 6, 7, 8, 10, 13, and 16) or lower than that of only DCO^+ and $H^{13}CO^+$ (cores 4, 11, 12, 17, and 19). This may mean that the denser material is spinning up in the process of core formation.

2.5.3 Velocity gradient and large-scale polarization

Caselli et al. (2002b) found that in another Taurus core, L1544, the directions of the total gradients observed in DCO^+(2–1) and N_2H^+(1–0) are similar to the direction of the magnetic field. In Fig. 2.7 we compare the total velocity gradients of our N_2D^+(2–1), N_2H^+(1–0), DCO^+(2–1), and $H^{13}CO^+$(1–0) maps and $C^{18}O$(1–0) from Hacar et al. (2013) with the polarization directions measured with optical (Heyer et al. 1987) and infrared (Goodman et al. 1992; Chapman et al. 2011) observations. The magnetic field is parallel to the polarization direction. Chapman et al. (2011) point out that where the filament turns sharply to the north (above core 7 or starting from the B10 subregion and farther up in Fig. 2.1), the magnetic field changes sharply from being perpendicular to the filament to being parallel to the filament.

To quantify the alignment of the total velocity gradients with the polarization directions, we plot the minimum angle between the corresponding position angles (see left panel of Fig. 2.8). In Fig. 2.8 the grey and cyan strips show the directions within 10° of being parallel or perpendicular to the magnetic field, respectively, because the typical uncertainty of the position angle difference is of the order of 10°. There is no big difference between the species in the alignment with the polarization directions.

We compare the alignment of the polarization directions with a random angle distribution (see right panel of Fig. 2.8). The alignment between the total velocity gradient and polarization directions is comparable to a random distribution: 27% of the gradient directions are parallel to the polarization directions and 14% of the random directions are parallel to the polarization directions; 13% of the gradient directions are perpendicular

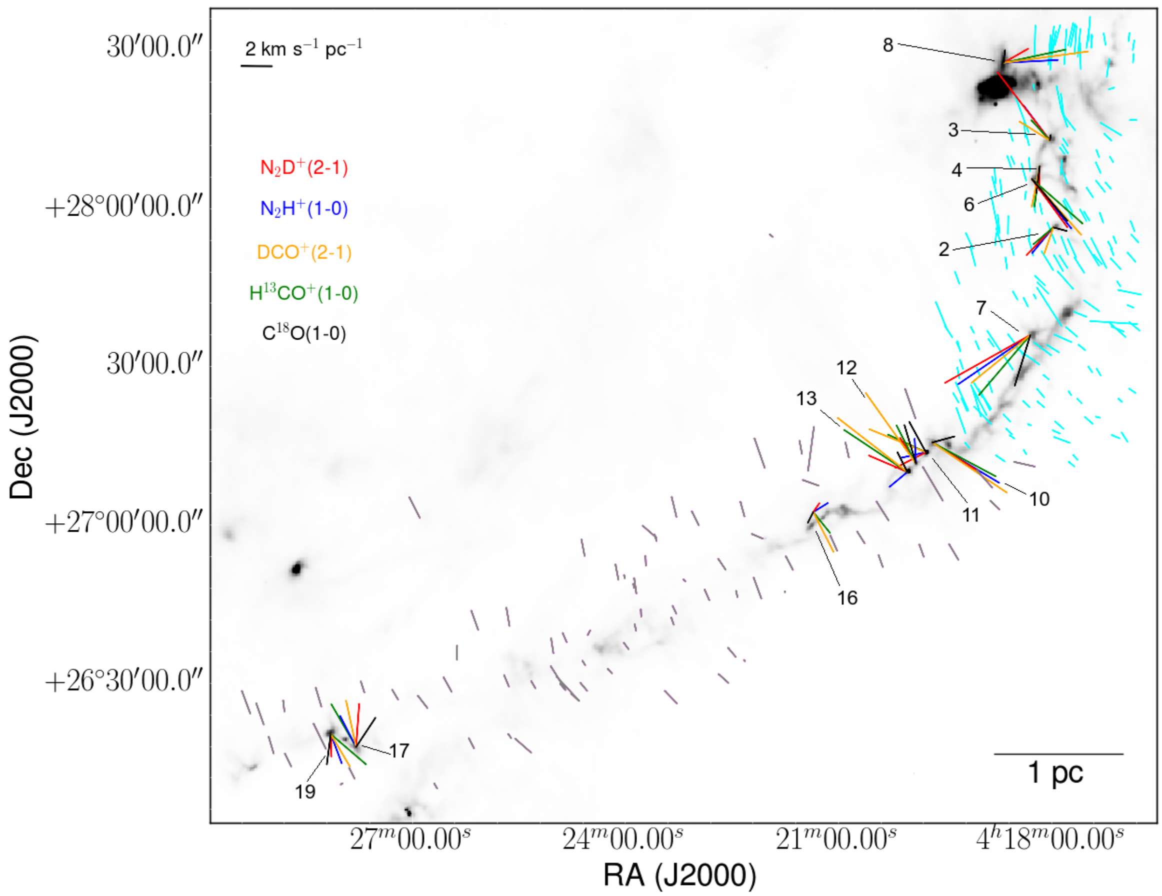

Figure 2.7: Polarization in L1495 measured with optical (Heyer et al. 1987) (grey segments) and infrared (Goodman et al. 1992; Chapman et al. 2011) observations (cyan segments) and total velocity gradients across the cores (N_2D^+ – red, N_2H^+ – blue, DCO^+ – orange, $H^{13}CO^+$ – green, and $C^{18}O$ – black). The colourscale shows the dust continuum emission at 500 μm obtained with *Herschel*/SPIRE (Palmeirim et al. 2013).

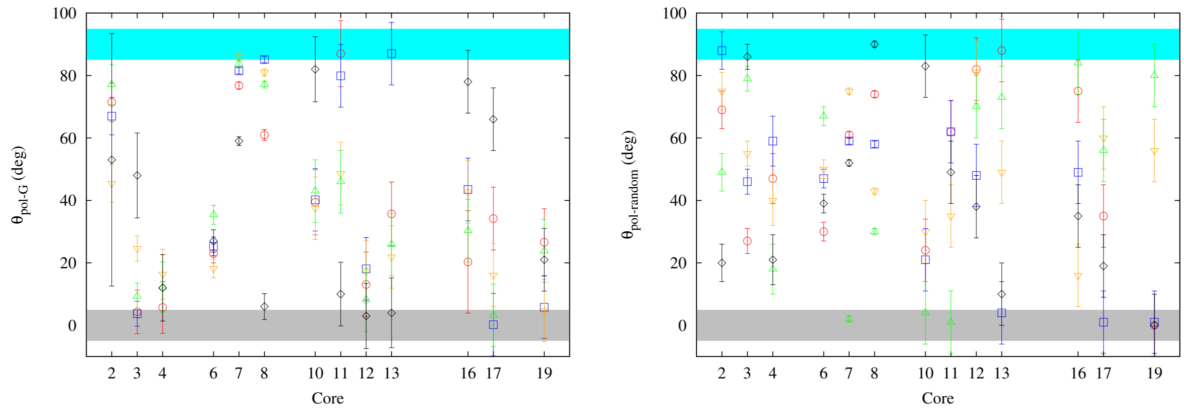

Figure 2.8: Left: difference between polarization angles θ_{pol} and position angles of the total gradients θ_G for each core (N_2D^+ – red circles, N_2H^+ – blue squares, DCO^+ – orange flipped triangles, $H^{13}CO^+$ – green triangles, and $C^{18}O$ – black diamonds). Right: difference between θ_{pol} and a set of random angles θ_{random} from 0 to 90°. Gray strip corresponds to parallel directions ±10°, cyan strip corresponds to perpendicular directions ±10°.

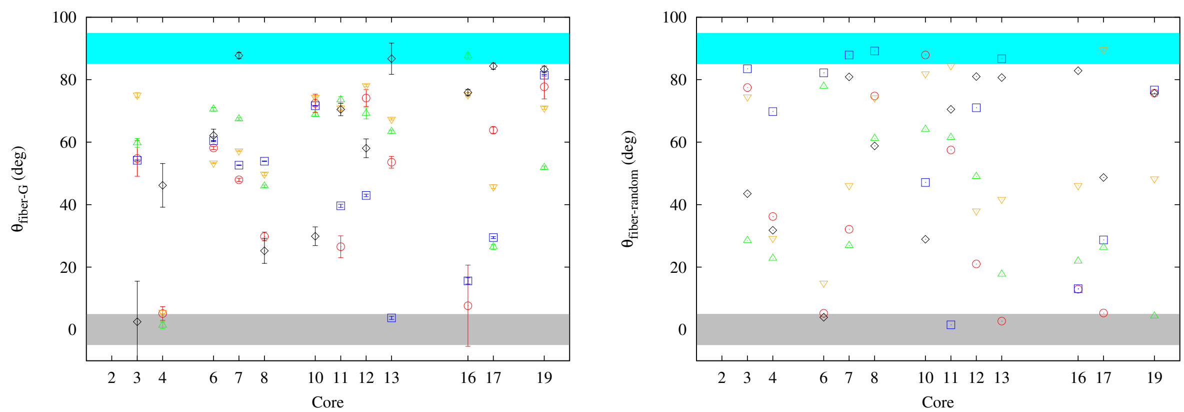

Figure 2.9: Left: difference between fiber position angles θ_{fiber} and position angles of the total gradients θ_G for each core (N_2D^+ – red circles, N_2H^+ – blue squares, DCO^+ – orange flipped triangles, $H^{13}CO^+$ – green triangles, and $C^{18}O$ – black diamonds). Right: difference between θ_{fiber} and a set of random angles θ_{random} from 0 to 90°. Gray strip corresponds to parallel directions ±10°, cyan strip corresponds to perpendicular directions ±10°.

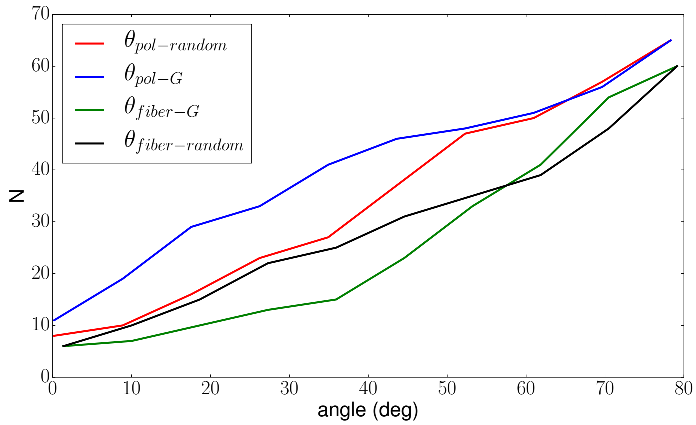

Figure 2.10: Cumulative distribution of angles between the random angles and polarization (red), the total gradients and polarization (blue), the total gradients and the fiber directions (green), and the random angles and the fiber directions (black).

to the polarization directions and 14% of the random directions are perpendicular to the polarization directions.

We also compare the gradient directions with the directions of the fibers which host the cores and test if the alignment is significant compared to a random distribution of the angles (see Fig. 2.9). The alignment between the total gradient directions and the fibers' directions is comparable to a random distribution: 10% of the gradient directions are parallel to the fibers' directions and 10% of the random directions are parallel to the fibers' directions; 7% of the gradient directions are perpendicular to the fibers' directions and 8% of the random directions are perpendicular to the fibers' directions. Figure 2.10 compares cumulative distributions of the angles between the total gradients, polarization, fiber directions, and random directions.

2.5.4 Dynamical state of the cores

Six out of 13 cores (6, 7, 8, 10, 12, and 19, all starless) show relatively coherent velocity fields consistent with solid body rotation. Five of the listed above cores show significantly lower total gradients in higher density tracers (N_2D^+ and N_2H^+) than in lower density tracers (DCO^+ and $H^{13}CO^+$) on a core scale, which implies that denser material is spinning down. This does not contradict to the fact that all four core tracers show higher total velocity gradients than $C^{18}O$. At the level of cloud–core transition, the core material, namely it's external envelope traced by DCO^+ and $H^{13}CO^+$ is spinning up. However within the core at higher densities the central material traced by N_2D^+ and N_2H^+ is spinning down probably because of magnetic breaking or gravitational torques, and/ or the transfer of angular momentum into the orbital motions of fragments if further material fragmentation takes place in the cores as explained by Belloche (2013). These five cores may be more evolved than the other cores not listed here except of core 17. Core 17 shows an increase in velocity dispersion towards the centre in all four transitions, which could be a sign of infall motions observed at later evolutionary stages instead of solid body rotation. Three starless cores (3, 8, and 12) show complex local velocity gradient patterns resembling those of protostellar cores, thus they may contain a very low luminosity object, as in the case of L1521F (Crapsi et al. 2004; Bourke et al. 2006).

Emission peaks of N_2H^+(1–0) and N_2D^+(2–1) are associated with the position of a YSO towards both protostellar cores, 11 and 13. This means that these YSOs are very young or very low luminosity, so that they have not yet affected the chemistry of their surrounding. One core (12) has two N_2D^+(2–1) emission peaks with the N_2H^+(1–0) emission peak in between (see Fig. B.8), which could be a sign of further core fragmentation or binary formation.

Four cores (6, 7, 12, and 17) show that the N_2D^+(2–1) emission is more elongated and compact than the emission from the other lines. For two cores, 6 and 12, the elongation is perpendicular to the magnetic field direction. This may mean that the N_2D^+ is tracing the higher density gas, which may be contracting along the magnetic field lines, thus producing the elongated structure.

2.6 Conclusions

This paper presents maps of four high density tracers, N_2D^+(2–1), N_2H^+(1–0), DCO^+(2–1), and $H^{13}CO^+$(1–0), towards 13 dense cores (starless and protostellar) along the L1495 filament. We use N_2D^+(2–1) and N_2H^+(1–0) as tracers of the core central regions, and DCO^+(2–1) and $H^{13}CO^+$(1–0) as tracers of the core envelope. We measure velocity dispersions, local and total velocity gradients, and specific angular momenta. We connect the core-scale kinematics traced by these high-density tracers to the filament-scale kinematics traced by the $C^{18}O$(1–0) observations presented in Hacar et al. (2013). We study the variations in the dense gas kinematics along the filament. Our main findings are:

1. All studied cores show similar kinematic properties along the 10 pc-long filament. They have close central velocities (6.3–7.6 km s^{-1}), similar velocity dispersions (mostly subsonic), same order of total velocity gradient magnitudes (0.6–6 km s pc^{-1}), same order of specific angular momentum magnitudes ($\sim$10^{20} cm^2 s^{-1}).

2. N_2D^+(2–1) shows the most centrally concentrated structure, followed by N_2H^+(1–0), DCO^+(2–1), and $H^{13}CO^+$(1–0).

3. The cores show very uniform velocity dispersions. The N_2D^+(2–1) and N_2H^+(1–0) lines are subsonic, close to 0.5 σ_T with thermal linewidth σ_T=0.17–0.21 km s^{-1}. The DCO^+(2–1) and $H^{13}CO^+$(1–0) lines are mostly subsonic, close to 0.8 σ_T, and partly transonic. The non-thermal contribution to the velocity dispersion increases from higher to lower density tracers. The median σ_{NT}/σ_T are 0.49, 0.58, 0.84, 0.81, and 1.16 for N_2D^+(2–1), N_2H^+(1–0), DCO^+(2–1), $H^{13}CO^+$(1–0), and $C^{18}O$(1–0),

respectively. The non-thermal contribution increases by $\simeq$20% from N_2D^+ to N_2H^+, and by $\simeq$40% from N_2H^+ to DCO^+ and $H^{13}CO^+$ and further to $C^{18}O$.

4. The total velocity gradients of the observed core tracers show a variety of directions and values. For 10 out of 13 cores the higher density tracers N_2D^+(2–1) and N_2H^+(1–0) show lower gradients than the lower density tracers DCO^+(2–1) and $H^{13}CO^+$(1–0), implying a loss of specific angular momentum at small scales due to magnetic breaking, gravitational torques, and/ or the transfer of angular momentum into the orbital motions of fragments, as theoretically expected (e.g. Belloche 2013). For the other 3 cores, the higher density tracers have higher gradients than the lower density tracers. The change of magnitude and direction of the total velocity gradients depending on the tracer indicates that internal motions change at different depths within the cloud.

5. The above point is strengthen by looking at local velocity gradients, which show complex patterns, especially in comparison with the velocity field traced by $C^{18}O$ (although with lower spatial resolution). Half of the cores (6 out of 13) show a velocity pattern consistent with solid body rotation. Some cores are elongated and "bent", their local velocity gradients remain perpendicular to the core axes even when the axes change their directions. The velocity fields are mainly similar in different high density tracers, however DCO^+(2–1) and $H^{13}CO^+$(1–0) show more local variations because they also trace some of the additional motions within the extended core envelope. The presence of a YSO at a distance less than 0.1 pc from a core locally affects the core's velocity field.

6. $C^{18}O$ traces the cloud material and stays unaffected by the presence of rotating cores: it's total velocity gradient is always lower than that of DCO^+ and $H^{13}CO^+$, the core envelope tracers; for the majority of the cores, the $C^{18}O$ velocity field coincides with that of the high density tracers, but does not show the variations near YSOs (cores 8, 11, 12, 13, 17, and 19) seen in the high density tracers, thus suggesting that the gas traced by $C^{18}O$ is not affected by protostellar feedback. At the level of cloud-core transition, the core's external envelope traced by DCO^+ and $H^{13}CO^+$ is spinning up.

7. The specific angular momenta of the cores vary in the range $(0.6\text{–}21.0)\times10^{20}$ cm^2 s^{-1}, consistent with previous observations of dense cores (Goodman et al. 1993; Caselli et al. 2002a). The specific angular momentum decreases at higher densities which shows the importance of local magnetic fields to the small scale dynamics of the cores.

8. The distributions of angles between the total velocity gradient and large scale magnetic field is consistent with being random as well as the distributions of angles between the velocity gradient and filament direction. This suggests that the magnetic fields may become apparent only in the high density gas within dense cores.

Chapter 3

SOLIS III: Methanol towards the pre-stellar core L1544

This chapter is based on the paper Punanova, A., Caselli, P., Feng, S., Chacón-Tanarro, A., Jiménez-Serra, I., Neri, R., Pon, A., Spezzano, S., Vastel, C., Vasyunin, A. I., Ceccarelli, C., and the SOLIS collaboration, to be submitted to ApJ.

Abstract

Context. Methanol is a precursor of many complex organic molecules (COMs), such as dimethyl ether and methyl formate. Understanding methanol chemistry is an important step forward in determining the dominant processes in the formation of other larger COMs. The observed abundances of methanol in the cold gas of pre-stellar cores is still not well explained by chemical models.

Aims. We study the distribution of methanol emission towards the methanol emission peak near the prototypical pre-stellar core L1544 to investigate the chemical and physical processes which lead to a local enhancement of methanol (CH_3OH). This work is part of the NOEMA large program SOLIS (Seeds of Life in Space).

Methods. We measure the distribution of emission, velocity dispersions, and local and total velocity gradients of three methanol lines observed with the NOEMA interferometer and the IRAM 30m antenna. We calculate the rotational temperature and the total column density of methanol and estimate the average methanol abundance. We use the molecular hydrogen column density previously measured with the dust continuum emission data from *Herschel*.

Results. The velocity dispersion changes across the observed region, with an increase towards the south-east, the same direction as the total velocity gradient. The lines stay subsonic. The centroid velocity shows a total gradient of $\simeq$7.2 km s^{-1} pc^{-1}. The rotational temperature increases towards the dust peak by $\simeq$4 K. The local velocity gradients show complex patterns which differ from a general gas motion towards the south-east.

Conclusions. The increase in line width on the edge of the core and the sharp change in direction of the velocity gradients may be caused by the accretion of external material

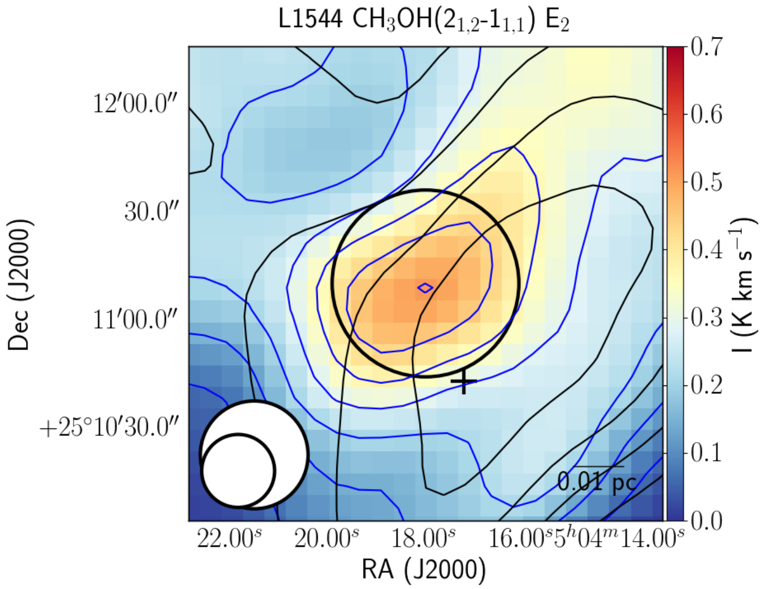

Figure 3.1: Methanol emission towards L1544 mapped with the IRAM 30m antenna (color scale and blue contours, Bizzocchi et al. 2014) and the 250 μm dust continuum emission mapped with *Herschel*/SPIRE (black contours, André et al. 2010). The blue contours of methanol start at 30% of the peak integrated intensity (0.509 K km s^{-1}) with a step of 10%. The black contours start at 60% of the peak dust emission (232.81 MJy sr^{-1}) with a step of 10%. The black circle shows the NOEMA primary beam. The *Herschel* and the 30m beams are shown in the bottom left (the larger beam is of *Herschel*, the smaller beam is of the 30 m). The 1.3 mm dust continuum emission peak (Ward-Thompson et al. 1999), considered as the core centre, is shown with the cross.

onto the core or the collision of two cores. However, the observed lines are excited at low energies and can not be used to test the temperature of the shock.

3.1 Introduction

Methanol is a key precursor for many organic and pre-biotic molecules found in regions of star- and planet formation (e.g. Herbst & van Dishoeck 2009). Methanol has been observed towards different types of sources, such as the molecular envelopes around low-mass and high-mass protostars (the so-called hot corinos and hot cores), and pre-stellar cores in low- and high- mass star-forming regions (e.g. Gibb et al. 2000; Schöier et al. 2002; Parise et al. 2004; Tafalla et al. 2006; Bizzocchi et al. 2014; Vastel et al. 2014; Jiménez-Serra et al. 2016). According to present models and experiments, methanol is formed on dust grains via the hydrogenation of CO (e.g. Tielens & Hagen 1982; Watanabe & Kouchi 2002) and released to the gas phase via thermal and/or non-thermal processes (Garrod & Herbst 2006; Vasyunin & Herbst 2013). It has been shown experimentally that the photodesorption of methanol is not effective, as it breaks the molecule into fragments (Cruz-Diaz et al. 2016; Bertin et al. 2016). In the cold ($\simeq$10 K) dense (10^4–10^7 cm^{-3}) gas of pre-stellar cores, the mechanisms of photo and thermal desorption are not effective; alternatively, reactive desorption is responsible for the release of methanol into the gas upon formation on icy mantles (e.g. Garrod et al. 2007; Vasyunin & Herbst 2013; Vasyunin et al. 2017).

L1544 is a prototypical pre-stellar core, being centrally concentrated (Ward-Thompson et al. 1999), with a central density of 2×10^6 cm^{-3}, having low central temperatures ranging from 5 to 11 K in the inner 10000 au (Crapsi et al. 2007) and undergoing a slow quasi-static contraction (Keto & Caselli 2010; Keto et al. 2015). It presents the chemical features of CO freeze-out and enhanced deuteration towards the centre (Caselli et al. 1999, 2002c; Vastel et al. 2006). L1544 also shows signs of chemical differentiation, with methanol residing away from the sharp H_2 column density drop (by an order of magnitude) towards the south-west of the core, where carbon chain molecules have their peaks (Spezzano et al. 2016, 2017).

In dense cores, gaseous methanol should preferentially be found in an intermediate-extinction shell around a central denser part, where CO has already formed and is partly frozen onto the dust grains so that methanol can form via hydrogenation. Methanol molecules more efficiently desorb upon formation onto CO-rich ices (Vasyunin et al. 2017). At the same time, the H_2 gas density is not very high ($\sim10^4$ cm^{-3}), so that species like methanol that are non-thermally ejected from grains can stay in the gas in appreciable amounts. At higher densities, the freeze-out rate of methanol overcomes its production rate, with a consequent drop in its gas phase abundance (Vasyunin et al. 2017).

Previous observations of methanol towards dense cores (L1498, L1517B; Oph-H-MM1 Tafalla et al. 2006, Harju et al. in prep.) reveal ring-like structures as expected. CH_3OH towards L1544 has also been found to have a ring-like distribution, with the peak being found towards the north-east (see Fig. 3.1), away from the low extinction regions (Bizzocchi et al. 2014; Spezzano et al. 2016). Many complex organic molecules (e.g. acetaldehyde, formic acid, dimethyl ether, methyl formate) have been detected towards L1544 (Vastel et al. 2014; Jiménez-Serra et al. 2016). At the location of the methanol peak of L1544, Jiménez-Serra et al. (2016) found enhanced abundances of O-bearing complex organic molecules (in particular CH_3CHO, $HCOOCH_3$, and CH_3OCH_3), likely related to methanol (also HCO, Spezzano et al. 2017), as well as CH_3O, a possible product of methanol photodissociation (Bertin et al. 2016; Cruz-Diaz et al. 2016) or, alternatively, a product of rapid gas-phase reactions between methanol and hydroxyl radical (OH) (Shannon et al. 2014).

We present interferometric observations of the methanol peak of L1544 with the aim of investigating the chemical and physical processes which lead to a local enhancement of methanol (CH_3OH). This work is a part of the NOEMA large program SOLIS (Seeds of Life in Space), aimed at studying the formation of complex organic molecules across all stages of star formation (Ceccarelli & Caselli et al. submt.). In section 3.2, the details of the observations are presented. In section 3.3, we describe the data reduction procedure and analysis of the spectra. Section 3.4 presents the results of the Gaussian fitting, velocity gradients, rotational temperatures and column density calculations. In section 3.5, we discuss the results and possible origins of the methanol-rich zone and give our conclusions. The summary of the paper is given in section 3.6.

3.2 Observations

Observations of the $(2_{1,2}–1_{1,1})$-E_2, $(2_{0,2}–1_{0,1})$-A^+, and $(2_{0,2}–1_{0,1})$-E_1 methanol lines at $\simeq$96.74 GHz towards the methanol emission peak near L1544 (α =05^{h}04^{m}18^s.0, δ = +25°11′10″, J2000, Bizzocchi et al. 2014) were carried out with the NOEMA interferometer (Northern Extended Millimetre Array) in C and D configurations on 21–23 and 30 July and 25–26 October 2015 under acceptable weather conditions (pwv=1–30 mm). The rest frequencies are given in Table 3.1. The primary beam size was 52″, the synthesised beam was 6.50×4.06″ at a position angle $\theta = -49.95°$. The data were obtained with the narrow band correlator with a spectral resolution of 39 kHz corresponding to a velocity resolution of 0.12 km s^{-1}. The system temperatures were 70–250 K. Sources 0234+285, MWC349, LKHA101, and 0507+179 were used as flux calibrators; 0507+179 was used as a phase/amplitude calibrator; and 3C454.3 and 3C84 were used as bandpass calibrators.

Simultaneously, the dimethyl ether ($CH_3OCH_3$$(5_{5,1}–4_{4,0})$-$EA$ at 95.85 GHz) and methyl formate (CH_3OCHO $(5_{4,1}–5_{3,3})$-E at 96.94 and $(17_{5,12}–17_{4,13})$-A at 97.20 GHz) lines were observed with the same spectral setup with the narrow band correlator but were not detected (the rms was 6 mJy beam^{-1} with the beam size of 5.7″×3.9″). Dust continuum emission observed with the wide band correlator WideX was also not detected down to an rms noise level of 0.026 mJy beam^{-1} with a beam size of 3.4″×2.4″. The SO$(2_3–1_2)$ line at 99.30 GHz and the CS(2–1) line at 97.98 GHz lines were detected in the WideX band with a spectral resolution of 1950 kHz or 5.6 and 6.0 km s^{-1} at the given frequencies. The peak intensities were ∼4.0 mJy beam^{-1} and ∼3.5 mJy beam^{-1} for CS and SO, and the rms was 0.7 mJy beam^{-1} with a beam size of 3.4″×2.4″. Because of their poor spectral resolution compared to the methanol lines, these data will not be discussed in this paper, which will focus on CH_3OH at its peak location in L1544.

To recover the emission from scales larger than 20″ we add zero spacing in the uv plane. We combined the IRAM 30 m observations of the methanol lines obtained by Bizzocchi et al. (2014) with our NOEMA data. The single dish observations were carried out in October 2013 under excellent weather conditions (pwv$\simeq$0.5 mm). The on-the-fly maps were obtained with the EMIR 090 (3 mm band) heterodyne receiver in frequency switching mode, with a frequency throw of 3.9 MHz, and the FTS backend with a spectral resolution of 50 kHz, corresponding to a velocity resolution of 0.15 km s^{-1} at the frequency of 96.74 GHz. The spatial resolution was 25.6″. The system temperature was $\simeq$90 K (for details see Bizzocchi et al. 2014).

Table 3.1: The observed methanol lines.

Transition	Frequency$^{(a)}$ (GHz)	$E_{up}/k^{(a)}$ (K)	$A^{(a)}$ (10^{-5} s^{-1})	$\simeq n_{crit}$ (10^5 cm^{-3})
$(2_{1,2}$–$1_{1,1})$-E_2	96.739362	12.53$^{(b)}$	0.2558	0.82
$(2_{0,2}$–$1_{0,1})$-A^+	96.741375	6.96	0.3408	1.09
$(2_{0,2}$–$1_{0,1})$-E_1	96.744550	20.08$^{(b)}$	0.3407	1.09

Notes. $^{(a)}$The frequencies, energies and Einstein coefficients are taken from Bizzocchi et al. (2014) following Xu & Lovas (1997) and Lees & Baker (1968). $^{(b)}$ Energy relative to the ground $0_{0,0}$, A rotational state.

3.3 Data reduction and analysis

3.3.1 Spectral data cubes

The calibration, imaging, and cleaning of the NOEMA data were performed with the CLIC and MAPPING packages of the GILDAS software[1]. The single dish data reduction up to the stage of convolved spectral data cubes was performed with the CLASS package of GILDAS. The comparison of the peak intensities of the methanol lines observed with the NOEMA and with the 30 m antenna shows that the interferometric observations recover 50–60% of the total flux. To recover the missing flux we merged the NOEMA and the 30 m data with a standard routine in the MAPPING package. The resulting data cubes have a velocity resolution of 0.15 km s^{-1}, the same as the single dish data. The rms of the resulting spectral data cubes is 0.003–0.009 Jy/beam.

3.3.2 Pyspeckit line analysis

The spectral analysis was performed with the Pyspeckit module of Python (Ginsburg & Mirocha 2011). The three methanol lines were fitted with a Gaussian. The routine varies three parameters (peak intensity, central velocity V_{LSR}, and velocity dispersion σ) and finds the best fit with the Levenberg-Marquardt non-linear regression algorithm. The fit results were written to the final data cubes after masking poor data. For the integrated intensity maps, we used all data within the primary beam. For the central velocity and velocity dispersion we used the data within the primary beam, with a velocity dispersion accuracy better than 20% ($\sigma/\Delta\sigma > 5$), and with a high signal-to-noise ratio (SNR): $I > 5 \cdot rms \cdot \sqrt{N_{ch}} \cdot \Delta v_{res}$, where I is the integrated intensity, N_{ch} is the number of channels in the line, and Δv_{ch} is the velocity resolution. For N_{ch} we take all channels in the range 6.1–8.0 km s^{-1}. This range defines the emission above one $rms \cdot \sqrt{N_{ch}} \cdot \Delta v_{res}$ over the spectrum averaged over the whole mapped area.

[1]The GILDAS software is developed at the IRAM and the Observatoire de Grenoble, and is available at http://www.iram.fr/IRAMFR/GILDAS

3.4 Results

3.4.1 Distribution of gas emission

Figure 3.2 shows the integrated intensities of the three methanol lines. The maps are centred at the methanol emission peak revealed with the IRAM 30 m observations (Bizzocchi et al. 2014). The dust emission peak at 1.3 mm from Ward-Thompson et al. (1999) (considered as the core centre), shown with a cross, is outside the primary beam area. Theoretical models predict that gas-phase methanol should be found in a shell around the densest parts of a core (e.g. Vasyunin et al. 2017) giving rise to a ring-like structure in observations (e.g. Tafalla et al. 2006, Harju et al. in prep.). Although methanol is distributed in a ring-like structure around the dust continuum peak of L1544 (see Bizzocchi et al. 2014), the ring is not uniform, with a clear maximum about 4000 au north-east of the dust peak position. The emission distribution revealed with interferometric observations matches the previous single-dish maps (Bizzocchi et al. 2014) and does not show any small-scale substructure. The asymmetric distribution of methanol could be related to the inhomogeneities in the distribution of cloud material around the dense core, with the southern part more exposed to the interstellar radiation field (Spezzano et al. 2016). Gas phase methanol preferentially traces the more shielded material around the dense core.

Figure 3.3 shows the integrated intensity of the E_2 methanol line before combining the NOEMA data with the zero-spacing data from the 30 m antenna. Here the extended methanol emission is missing and only the compact emission resolved by NOEMA is present. The methanol emission detected with NOEMA has an elongated structure on the northern side of the dense core, with a thickness of about 10″ (1400 au at the distance of 140 pc) and partly covering the extent of the mm dust emission, from the 3 $\sigma_{T_{mb}}$ up to the 12 $\sigma_{T_{mb}}$ contour.

3.4.2 Kinematics

Velocity dispersion

Figure 3.4 shows the velocity dispersions (σ) of the methanol lines. The velocity dispersions range from 0.11 to 0.26 km s^{-1} with a median value of 0.15 km s^{-1} and typical uncertainties of 0.003 km s^{-1} and 0.014 km s^{-1} for the bright lines (A^+ and E_2) and weak line (E_1). The line width increases towards the south-east in all three lines. The line widths of the A^+ line are on average larger than those of the E_2 line by 0.01 km s^{-1} (a factor of three larger than the uncertainty of the line width). This might be due to an optical depth effect.

The line widths towards the south-eastern part of the combined map (NOEMA and 30m) are significantly larger than the line widths observed with only the 30 m single dish telescope, by 0.05–0.10 km s^{-1}. This difference is not systematic; it decreases with distance from the location with the largest line width and becomes negligible in the northern part of the map. A detailed inspection of the spectra reveals the presence of a small-scale higher velocity part of the line in the south-eastern part of the core. NOEMA, being more

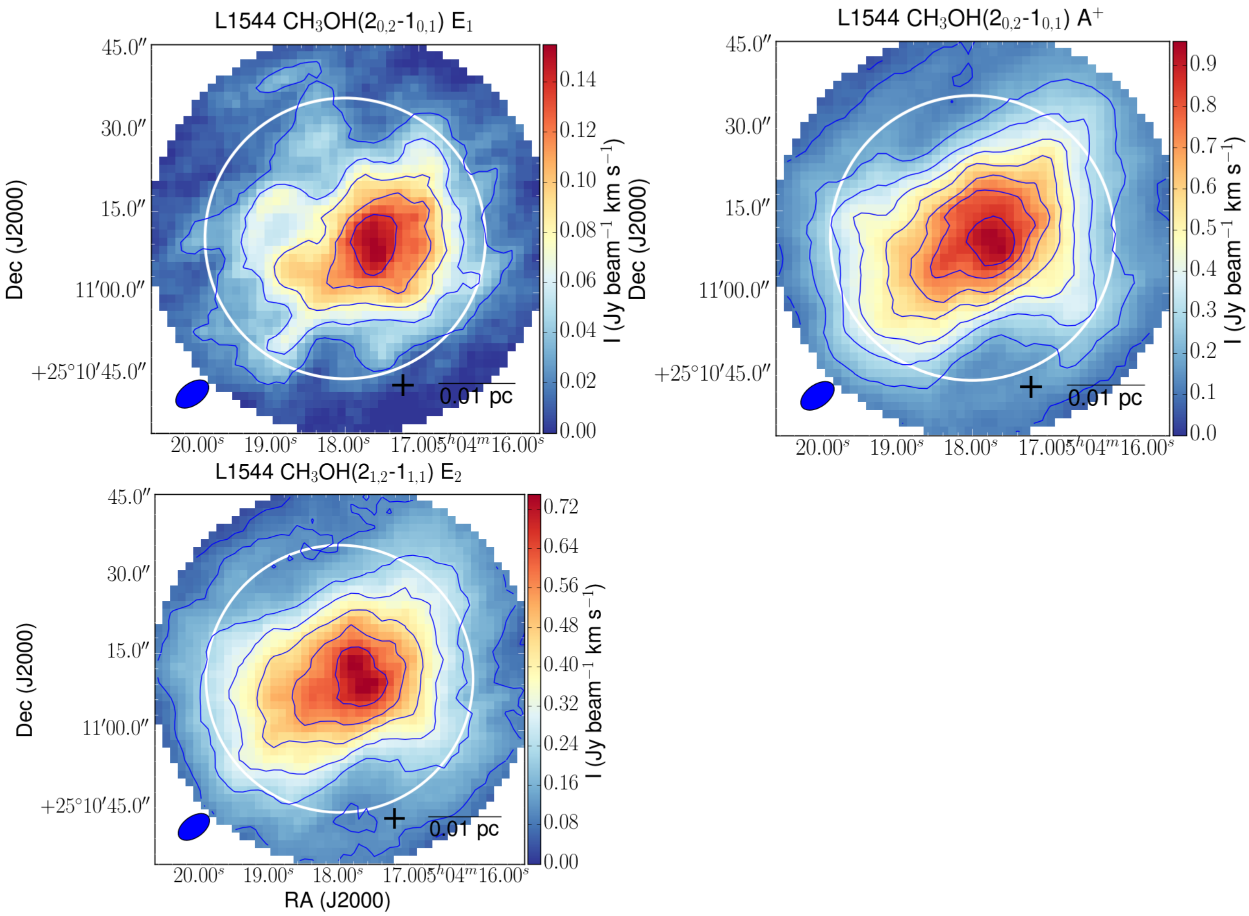

Figure 3.2: Integrated intensities of the methanol lines. The blue contours represent integrated intensity, and start at 3 $\sigma_{T_{mb}}$ with a step of 3 $\sigma_{T_{mb}}$ for the E_1 line (left), at 12 $\sigma_{T_{mb}}$ with a doubling step for the A^+ line (middle), and at 6 $\sigma_{T_{mb}}$ with a doubling step for the E_2 line (right). $3\sigma_{T_{mb}}$=0.027 Jy beam^{-1}. The white circle in the centre is the primary beam of NOEMA. The cross shows the dust emission peak (Ward-Thompson et al. 1999). The synthesized beam of NOEMA is shown in the bottom left corner.

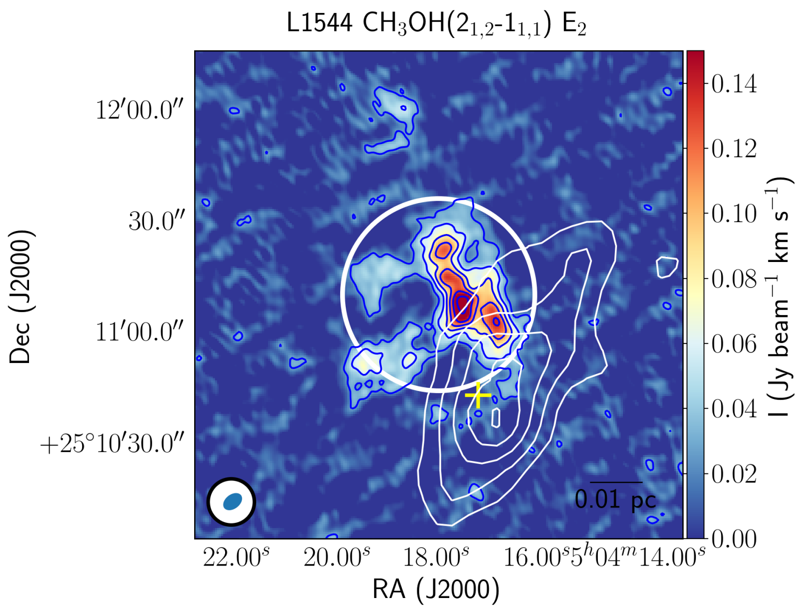

Figure 3.3: Integrated intensity of the E_2 line before combining with the single dish data. The blue contours start at 3 $\sigma_{T_{mb}}$ (0.027 Jy beam^{-1}) with a step of 3 $\sigma_{T_{mb}}$. The white contours represent the 1.2 mm dust continuum emission from NIKA (Chacón-Tanarro et al. 2017), which start at 3 $\sigma_{T_{mb}}$ (4.2 MJy sr^{-1}) and increase with a step of 3 $\sigma_{T_{mb}}$. The white circle in the centre is the primary beam of NOEMA for the methanol data. The yellow cross shows the dust emission peak (Ward-Thompson et al. 1999). The synthesized beam of NOEMA (blue) and the NIKA beam (white) are shown in the bottom left corner.

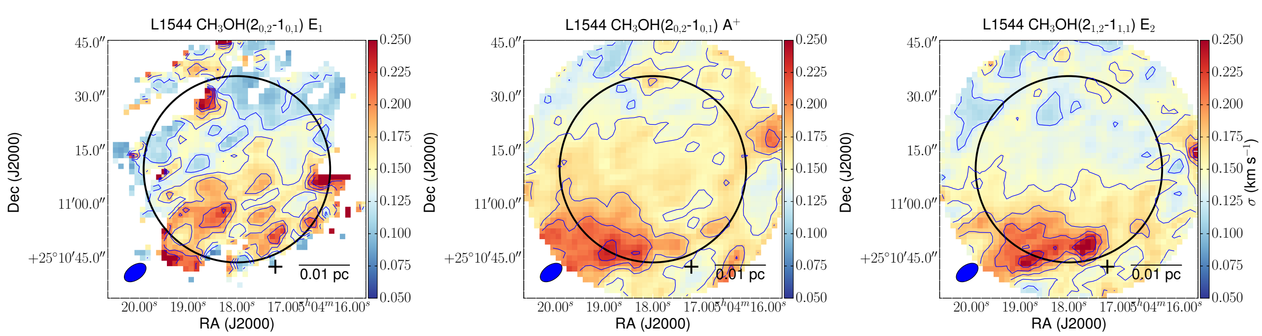

Figure 3.4: Velocity dispersions of the methanol lines. The blue contours show velocity dispersions of 0.125, 0.150, 0.175, 0.200, and 0.225 km s^{-1}. The circle shows the primary beam. The cross shows the dust peak position. The synthesized beam is shown in the bottom left corner.

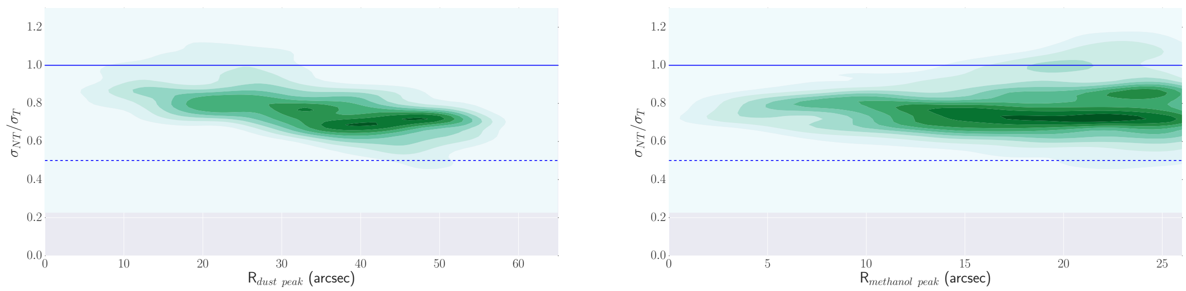

Figure 3.5: Ratio of non-thermal components of the three methanol lines to the thermal line width of a mean particle as a function of distance to the dust peak (left) and distance to the methanol intensity peak (right). The solid and dashed blue lines show the ratios equal to 1 and 0.5. The colorscale represents the density of the points. The gray areas do not contain any data points.

sensitive than the 30m antenna, reveals the weak component (but filters out the main component which comes from the large-scale emission). In the combined spectrum the main component is blended with the weak component, and the resulting line is broader and its centroid velocity is also larger than that observed with single dish. The high-velocity part of the line detected with NOEMA appears on the edge of the dense core.

Non-thermal motions

Figure 3.5 shows the ratio of the non-thermal components (σ_{NT}) of the three methanol lines in each pixel within the primary beam and the thermal velocity dispersion of a mean particle, σ_T, as a function of the distance to the dust peak (left panel) and the distance to the methanol peak (right panel). The non-thermal components are derived from the observed velocity dispersion (σ_{obs}) via

$$\sigma_{NT}^2 = \sigma_{obs}^2 - \frac{kT_k}{m_{obs}}, \tag{3.1}$$

where k is Boltzmann's constant, T_k is the kinetic temperature, and m_{obs} is the mass of the observed molecule. The formula is adopted from Myers et al. (1991), taking into account that $\sigma^2 = \Delta v^2/(8\ln(2))$, where Δv is the full width at half maximum of the line, FWHM. We assume that the kinetic temperature is 10 K as this is the temperature of the outer part of the core measured with ammonia by Crapsi et al. (2007). This 10 K temperature is also consistent with the methanol rotational temperatures we derive close to the dust peak, where the gas is close to local thermodynamic equilibrium (LTE) (see Sect. 3.4.3 for details).

The thermal velocity dispersion (σ_T) for a mean particle with mass 2.33 amu for a temperature of 10 K is 0.19 km s^{-1}. The ratio of the non-thermal component to the thermal velocity dispersion varies from 0.3 to 1.7, being 0.8 on average. The ratio decreases with distance from the dust peak from ∼0.9 to ∼0.7. The ratio stays constant with distance

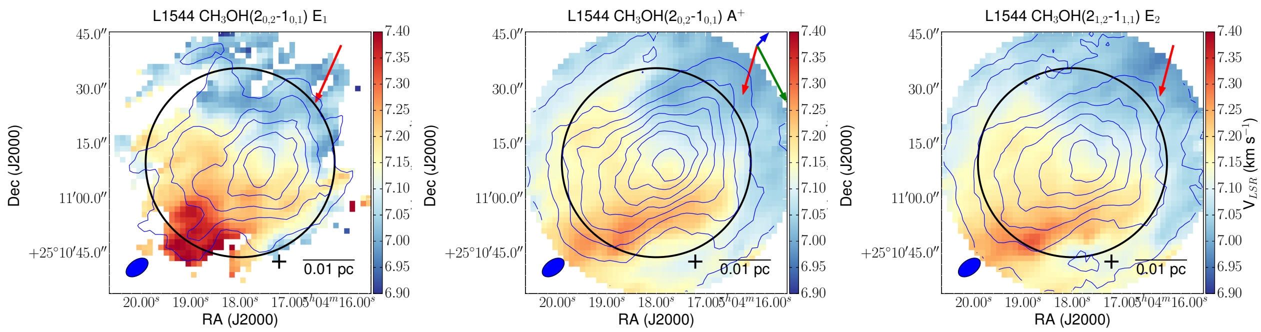

Figure 3.6: Centroid velocities of the methanol lines. The blue contours represent integrated intensity, and start at 3 $\sigma_{T_{mb}}$ with a step of 3 $\sigma_{T_{mb}}$ for the E_1 line (left), at 12 $\sigma_{T_{mb}}$ with a doublig step for the A^+ line (middle), and at 6 $\sigma_{T_{mb}}$ with a doubling step for the E_2 line (right). $3\sigma_{T_{mb}}$=0.027 Jy beam^{-1}. The red arrows show the total velocity gradients. The green and blue arrows in the central panel show the total velocity gradients of NH_3 and NH_2D measured over the core (Crapsi et al. 2007). The circle shows the primary beam. The cross shows the dust peak position. The synthesized beam is shown in the bottom left corner.

from the methanol peak with a local spot of σ_{NT}/σ_T=1 approximately 20$''$ away from the peak. This spot is the area on the south-east of the map, which has the largest line widths observed. Large line widths are also present towards the edge of the primary beam (which might be due to higher noise levels, see the bottom panel of Fig. 3.5). The majority of the lines (92%) are subsonic; the small fraction of transonic lines come from the south-east part of the map.

Velocity field

Figure 3.6 shows the centroid velocity (V_{LSR}) maps. The V_{LSR} varies in the range 6.9–7.3 km s^{-1}, consistent with previous single-dish observations (Spezzano et al. 2016). The interferometric observations reveal some substructure in the velocity field, which was not seen in the single-dish data: the velocity increases towards the south, south-east and east. The three lines show similar velocity patterns; the E_1 line shows higher velocities in the south-east, possibly because of higher uncertainties at the edge of the map, where the SNR of the weak E_1 line is low ($\simeq$5).

Total gradients

We estimate total and local velocity gradients across the methanol emission following the method described in Goodman et al. (1993) for total gradients and applied for local gradients by Caselli et al. (2002a) (see the description of local gradients below). The results of the total velocity gradient calculation provide the average velocity across the core $< V_{LSR} >$, the magnitude of the velocity gradient G, and the position angle θ_G. The total gradients are calculated using all available points weighted by $1/\Delta^2_{\mathrm{V_{LSR}}}$, where $\Delta_{\mathrm{V_{LSR}}}$ is the uncertainty of the central velocity.

We calculate the total gradients for all three lines. The total velocity gradients are 8.77±0.04, 7.10±0.01, and 7.24±0.01 km s^{-1} pc^{-1} at position angles 153.7°±0.3°, 162.13°±0.08°, and 163.76°±0.07° measured east of north for the E_1, A^+, and E_2 lines respectively. The total gradients are shown as red arrows in Fig. 3.6. We also compare them with the total velocity gradients of the high density tracers NH_3 and NH_2D (green and blue arrows in the central panel of Fig. 3.6), measured with interferometric data across the entire L1544 core (Crapsi et al. 2007). The gradient direction of methanol significantly differs from those of the dense core tracers (θ_G differ by ∼40° and ∼140° from those of NH_3 and NH_2D, and G differs by ∼7 km s^{-1} pc^{-1} from that of NH_2D) so we can conclude that the shell traced by methanol is not affected much by the dense core kinematics (see below a comparison of the local velocity gradients).

Local gradients

The local velocity gradients are presented in Fig. 3.7 with black arrows, plotted over integrated intensity colour maps, along with red arrows which present the total velocity gradients. To calculate a gradient in a local position, we use all pixels within 6″ (where 1 pixel is 1.5″ in size), weighted according to their distance to the given position and their uncertainty of the central velocity:

$$W = \frac{1}{\Delta^2_{\mathrm{V_{LSR}}}} \cdot \exp\left\{-d^2 / \left[2\left(\frac{\theta_{Gauss}}{2.354}\right)^2\right]\right\}, \tag{3.2}$$

where W is the weight, $\Delta_{\mathrm{V_{LSR}}}$ is the uncertainty of the central velocity, d is the distance from the weighted pixel to the given position, and $\theta_{Gauss} = 4$ pixels is the FWHM of the weighting function. The four-pixel radius is used to compensate for the oversampling of the map.

The velocity increases towards the south-east, as shown with the total velocity gradient direction. However, the velocity field is quite complex, and the local velocity gradients show significant variations across the observed area. The local velocity gradient values vary from ≃0.5 to 12 km s^{-1} pc^{-1}. Along with the general trend, also shown in Spezzano et al. (2016), there is a high velocity bar in the south of the mapped area and then a sharp decrease (local velocity gradients are ≃11 km s^{-1} pc^{-1}) of the centroid velocity further to the south, towards the dust peak (see Fig. 3.6 and 3.7). Another variation of the velocity pattern, a local increase towards a position in the north-east quadrant of the primary beam area, contributes to the general trend (as the position of the maximum velocity is in the south-east, see Fig. 3.6 and 3.7).

3.4.3 Rotational temperature

Using the spectra of the observed lines we calculate the rotational temperature T_{rot} and the total column density N_{tot} of methanol, assuming LTE and optically thin emission. With

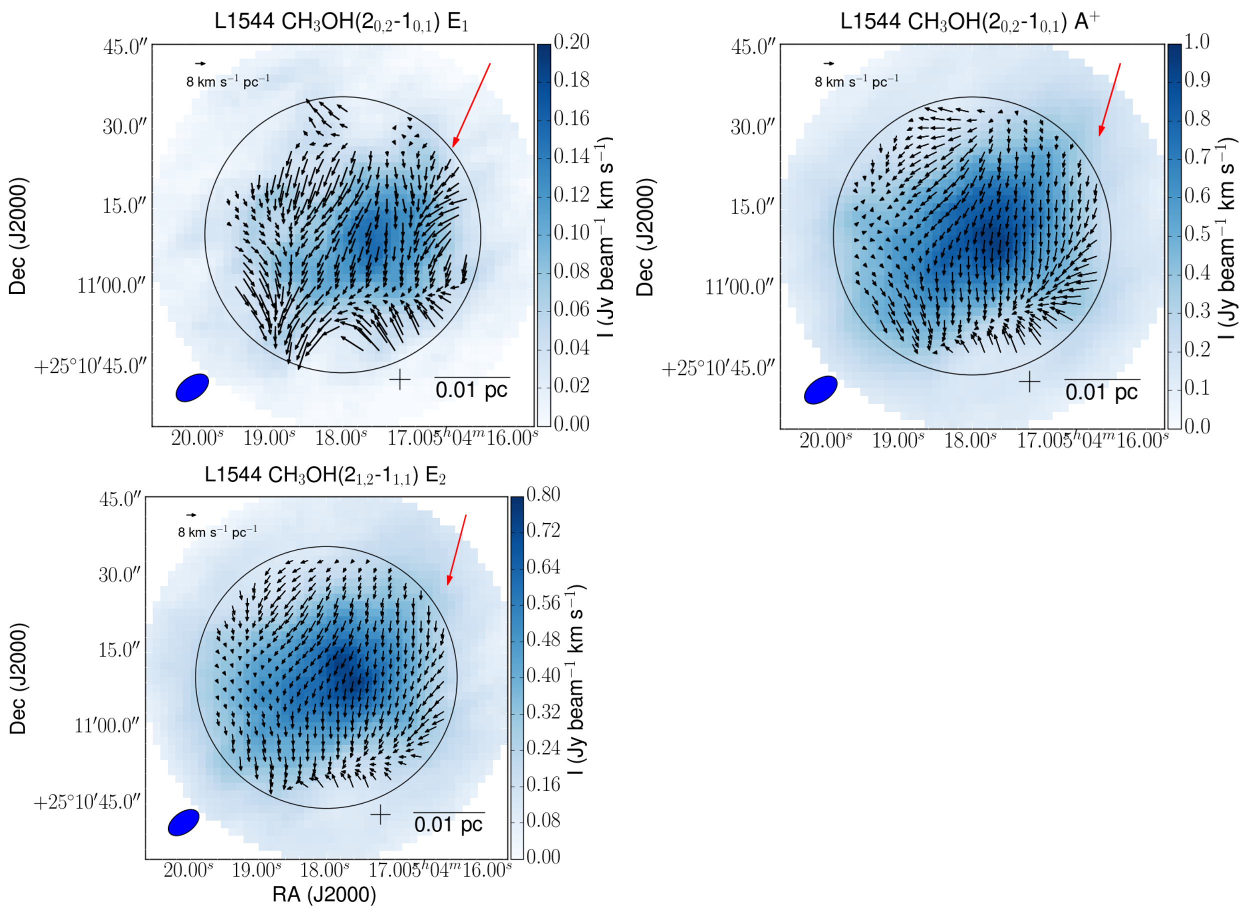

Figure 3.7: Local velocity gradients of the methanol lines for the E$_1$, A$^+$, and E$_2$ lines (top, middle, and bottom, respectively). The color scale shows integrated intensity. The black arrows show the local velocity gradients. The red arrows show the total velocity gradients (the scale of the total gradients are eight times larger than the scale of the local gradients). The circle shows the primary beam. The cross shows the dust peak position. The synthesized beam is shown in the bottom left corner.

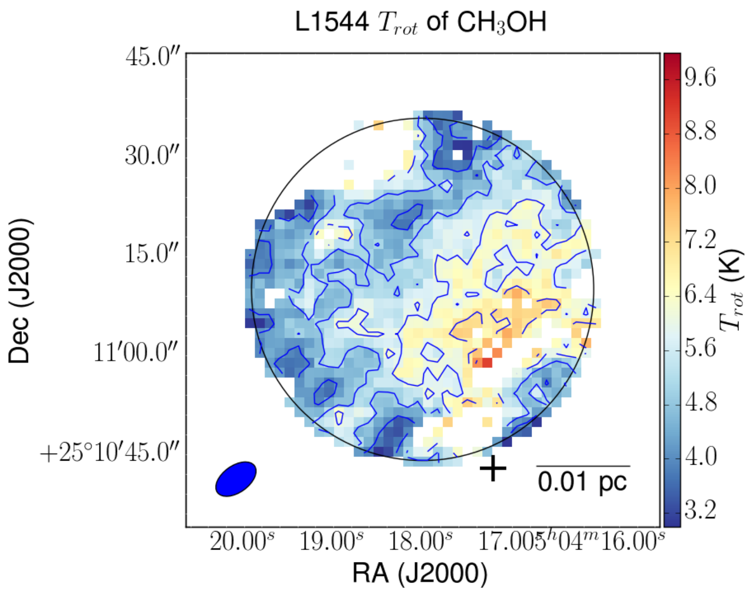

Figure 3.8: Rotational temperature of methanol. The blue contours show T_{rot} of 4, 5, 6, 7, and 8 K. The cross shows the dust peak position. The synthesized beam is shown in the bottom left corner.

the assumption of LTE, the population of all the energy levels can be described by a unique temperature, T_{rot}. With the assumption of optically thin emission, T_{rot} is defined as $-1/a$ from a linear fit $ax + b$ to a $\log(N_{up}/g_{up})$ versus E_{up} plot, where E_{up} is the energy of the upper level, expressed in K (given in Table 3.1). N_{up} is the column density of the upper level population, defined as

$$N_{up} = \frac{8\pi k W \nu^2}{A h c^3}, \tag{3.3}$$

where k is the Boltzmann constant, W is the integrated intensity of the line, ν is the frequency, A is the Einstein coefficient (given in Table 3.1), h is the Planck constant, and c is the speed of light (e.g. Goldsmith & Langer 1999).

Figure 3.8 shows the map of rotational temperature. We show only those values with an uncertainty ΔT_{rot} <2.5 K. The typical values for ΔT_{rot} are 1–2 K. T_{rot} varies from 3.0±0.8 K to 9±2 K, with an average T_{rot} of 5.3±1.0 K. The temperature increases towards the south-west and the dust peak. The rotational temperature increase is most likely a result of the gas density increasing towards the core centre, from a few 10^4 cm^{-3} in the north-eastern part of the observed area to a few 10^5 cm^{-3} in the south-western part (see e.g. the model of Keto & Caselli 2010), as the methanol lines have critical densities of $\simeq 10^5$ cm^{-3} and are thus likely to be subthermally excited. As the density increases towards the core centre, the energy level populations become closer to that expected from LTE and the rotational temperature becomes closer to the kinetic temperature of the gas.

Crapsi et al. (2007), derived ammonia rotational temperatures towards the core centre and found that the temperature increases from the centre outwards, from 5.5 to 10–13 K.

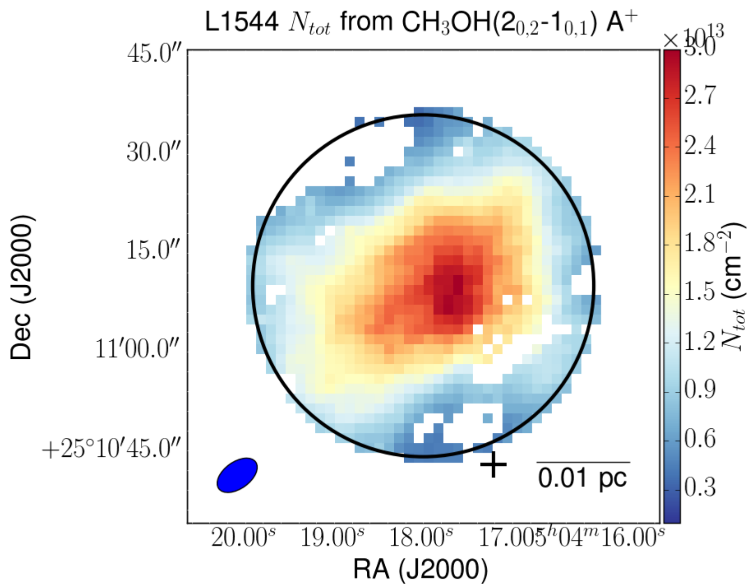

Figure 3.9: Total column densities of methanol measured with the A^+ line. The circle shows the primary beam. The cross shows the dust peak position. The synthesized beam is shown in the bottom left corner.

The ammonia map obtained with the VLA covers the ammonia emission area of $75'' \times 36''$ centred at the dust peak. The peak methanol rotational temperature of 9 ± 2 K is consistent with these ammonia derived temperatures, suggesting that the methanol is indeed close to being in LTE in the south-western part of the mapped region. The opposing directions of the methanol and ammonia temperature gradients further support the notion that the methanol gradient is only an excitation effect caused by changes in the gas density. In general, CH_3OH and NH_3 trace different material, as NH_3 (as well as other N-bearing molecules) remains in the gas phase at significantly higher volume densities compared to C-bearing molecules (e.g. Caselli et al. 1999; Hily-Blant et al. 2010; Bizzocchi et al. 2014), but CH_3OH and NH_3 overlap at densities between 10^4 and 10^5 cm^{-3}, where both CH_3OH and NH_3 are already formed and CH_3OH is still in the gas phase.

3.4.4 Column density and methanol abundance

We can define the total column density:

$$N_{tot} = \frac{N_{up} Q_{rot}}{g \exp(-E_{up}/kT)}, \tag{3.4}$$

where g is the statistical weight of the upper level ($g_J = 2J+1$, with J being the rotational quantum number), E_{up} is the energy of the upper level, k is the Boltzmann constant, T_{rot}

is used as the temperature T, and Q_{rot} is the rotational partition function defined as

$$Q_{rot} = 5.34 \cdot 10^6 \sqrt{\frac{T^3}{A \cdot B \cdot C}}, \tag{3.5}$$

following equation (3.69) in Gordy & Cook (1970), where A, B, and C are the rotational constants of the molecule in MHz. We use A = 127523.4 MHz, B = 24690.2 MHz, and C = 23759.7 MHz (Xu & Lovas 1997) for methanol.

Figure 3.9 shows the total column density map of methanol derived for the brightest line, A^+. The variation between N_{tot} defined with the different lines is within a factor of 3: $N_{tot}(E_2)/N_{tot}(E_1) = 2$, $N_{tot}(E_2)/N_{tot}(A^+) = 3$. The uncertainties of the total column densities ΔN_{tot} are high: 30–300%, 20–100%, and 20–300% for the E_1, A^+, and E_2 lines, respectively, so the differences between the total column densities defined with the different lines are within the errors. The average column densities are 2.2±0.9, 1.4±0.6, and 4.3±1.6 $\times 10^{13}$ cm^{-2} for the E_1, A^+, and E_2 lines, respectively. This result is consistent with that of Bizzocchi et al. (2014), who found (2.7±0.6)$\times 10^{13}$ cm^{-2}.

We use the H_2 column density, $N(H_2)$, to define the methanol abundance within the primary beam area. The molecular hydrogen column density map for L1544 was produced by Spezzano et al. (2016) using the dust continuum emission data from the three *Herschel*/SPIRE bands at 250 μm, 350 μm, and 500 μm. As the *Herschel* beam of 38″ is comparable with the NOEMA primary beam at 96.4 GHz (52″) we only can define an average abundance of methanol within the observed area.

With the average total column densities and average molecular hydrogen column density, $(1.90 \pm 0.47) \times 10^{22}$ cm^{-2}, the average methanol abundances

$$X(\mathrm{CH_3OH}) = N_{tot}(\mathrm{CH_3OH})/N(\mathrm{H_2}) \tag{3.6}$$

are 1.16±0.55, 0.74±0.36, and 2.26±1.01 $\times 10^{-9}$ for the E_1, A^+, and E_2 lines, respectively, consistent with 0.92$\times 10^{-9}$ defined byBizzocchi et al. (2014).

3.5 Discussion and conclusions

The single-dish observations of methanol towards L1544 (Bizzocchi et al. 2014) revealed a ring-like structure of emission with a strong peak on the north-east side of the core. The interferometric observations could have resolved any substructures on 6″ size scales present within this methanol peak. However, the bright methanol clump, as seen with NOEMA (spatial resolution ~700 au), shows a smooth elongated structure. The most compact methanol emission seen in the NOEMA-only data (see Fig. 3.3) is an elongated structure perpendicular to the core major axis.

The centroid velocities show variations across the mapped area, with an increase towards the south-east part and a higher velocity bar in the south part followed by a velocity drop towards the south.

The velocity dispersion increases towards the south-east of the map. The line widths towards the south-east part of the combined map (NOEMA and 30m) are significantly larger

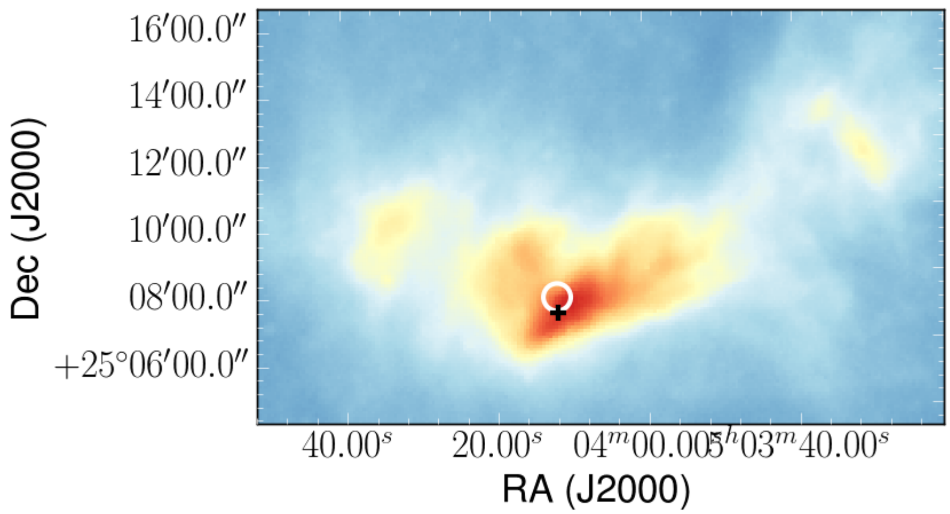

Figure 3.10: The 250 μm dust contimuum emission *Herschel*/SPIRE map towards the L1544 region (André et al. 2010). The white circle shows the NOEMA primary beam centered at the methanol peak. The black cross shows the 1.3 mm dust emission peak (Ward-Thompson et al. 1999).

than the line widths observed with only the 30 m single dish telescope, by 0.05–0.10 km s^{-1}. NOEMA reveals the presence of gas at small scales moving at slightly ($\simeq$0.1 km s^{-1}) higher velocities compared to the bulk motions in the methanol clump. The higher velocity gas is concentrated towards the edge of the dense core. This compact emission may be an interface region between the dense core and the accreting envelope material, where a low-velocity shock may be present due to accretion motions onto the dense core, as was shown in Pon et al. (2014). It also could be caused by a slow shock from a collision of two cores (L1544 and the less dense core on its north-east side, seen only in the *Herschel* maps, see Fig. 3.10). The currently available data, however, are not sufficient to conclusive identify the presence of a shock at this location. The observed transitions have low energies (see Tab. 3.1) and thus are not sensitive to high temperatures.

As shown in Bizzocchi et al. (2014) and Spezzano et al. (2016), the methanol distribution in L1544 is strongly asymmetric: the majority of the methanol is concentrated on the north-east of the core. Methanol appears to prefer locations screened by UV photons (which probably destroy CH_3OH Bertin et al. 2016; Cruz-Diaz et al. 2016) and where carbon atoms are mainly locked into CO molecules, which start to significantly freeze onto the dust grain mantles (Spezzano et al. 2016) at volume densities around a few $\times 10^4$ cm^{-3} (Caselli et al. 1999). In higher density regions, the CH_3OH freeze-out wins over reactive desorption. Following Vasyunin et al. (2017) (and discussion therein) reactive desorption on CO-rich ice is the most important mechanism for gas-phase methanol production.

The methanol rotational temperature map defined with the assumption of LTE and optically thin lines show a slight ($\simeq$4 K) temperature increase towards the denser parts of the core. This change in the rotational temperature is likely an effect of the volume density decrease with distance from the core centre. According to the Keto & Caselli (2008) model, the density changes from a few 10^5 cm^{-3} to $\sim 10^4$ cm^{-3} across the NOEMA methanol map, that is from a density close to the critical density of methanol (see Tab. 3.1), to a much lower density. In the dense part of the core, where the gas is close to LTE, the rotational temperature is expected to approach the kinetic temperature.

3.6 Summary

This paper presents high spatial resolution ($\sim$700 au) observations of the methanol emission peak towards the prototypical pre-stellar core L1544 (revealed by Bizzocchi et al. 2014). The bright methanol clump, as seen with NOEMA, shows a smooth shape with small-scale elongated structure perpendicular to the core axis. The increase in line width on the edge of the core and sharp change of the velocity gradients may be caused by the accretion of external material onto the core or by a collision of two cores. However, the observed lines are excited at low energies and can not be used to test the temperature of the shock. The asymmetry of methanol emission is likely caused by an irregular distribution of the core material and a lack of UV radiation at the methanol peak, as was suggested by Spezzano et al. (2016).

This work is a part of the NOEMA large program SOLIS (Seeds of Life in Space), aimed at studying the formation of complex organic molecules at all stages of star formation (Ceccarelli & Caselli et al., submt.).

Chapter 4

Conclusions and prospective work

4.1 Summary of the thesis

The thesis presented a study of the chemistry and kinematics of dense cores in two nearby low-mass star-forming regions, representing different environments: L1688, the site of clustered star formation in the Ophiuchus molecular cloud, and the L1495 filament and the isolated pre-stellar core L1544 in the more quiescent Taurus molecular cloud. The main results of the work are given below.

Deuterium fractionation in the Ophiuchus molecular cloud. I studied how the deuterium fraction in N_2H^+ depends on the physical conditions of the cloud. The 33 studied dense cores in L1688 show large ($\simeq$2–40%) deuterium fractions, with significant variations between the regions of the cloud. The CO-depletion factor also varies from one region to another (between $\simeq$1 and 7). Two different correlations are found between the deuterium fraction and the CO-depletion factor: one group of cores shows an increasing deuterium fraction with increasing CO depletion factor, similar to previous studies of deuterium fraction in pre-stellar cores; the other group of cores shows a steeper deuterium fraction – CO depletion factor correlation, with large deuterium fractions occurring in fairly quiescent gas with relatively low CO freeze-out factors. These are probably recently formed, centrally concentrated starless cores which have not yet started the contraction phase towards protostellar formation.

The deuterium fraction and amount of CO freeze-out are sensitive to environmental conditions and their variations across L1688 show that regions of the same molecular cloud experience different dynamical, thermal and chemical histories, with consequences for the current star formation efficiency and the characteristics of future stellar systems. The large pressures present in L1688 may induce the formation of small dense starless cores, unresolved with our beam, where the R_D–f_d relation appears to deviate from that expected from chemical models. I predict that high angular resolution observations will reconcile observations with theory. The observing proposal "Highly deuterated starless cores with low CO freeze out: a chemical puzzle" aimed at resolveing these small cores has been recently accepted by the ALMA (Atacama Large Millimetre Array) time allocation committee.

Kinematics of dense gas in the L1495 filament. I studied the kinematics of the dense gas of starless and protostellar cores along the L1495 filament and the kinematic links between the cores and the surrounding molecular cloud. I used N_2D^+(2–1) and N_2H^+(1–0) to trace the core centres, DCO^+(2–1) and $H^{13}CO^+$(1–0) to trace the core envelopes, and $C^{18}O$(1–0) from Hacar et al. (2013) to trace the cloud material. All cores show similar properties along the 10 pc-long filament. N_2D^+ shows the most centrally concentrated structure, followed by N_2H^+, DCO^+, and $H^{13}CO^+$. The non-thermal contribution to the velocity dispersion increases from higher to lower density tracers. The changes in magnitude and direction of the total velocity gradients between the different tracers indicate that internal motions change with depth within the cloud. N_2D^+ and N_2H^+ show smaller gradients than the lower density tracers DCO^+ and $H^{13}CO^+$, implying a loss of specific angular momentum at small scales. At the level of the cloud-core transition, the core's external envelope traced by DCO^+ and $H^{13}CO^+$ is spinning up. $C^{18}O$ traces the cloud material and stays unaffected by the presence of rotating cores. The decrease in specific angular momentum towards the centres of the cores shows the importance of local magnetic fields to the small scale dynamics of the cores. The random distributions of angles between the total velocity gradients and the large scale magnetic field suggests that the magnetic fields may only be dynamically important in the high density gas within dense cores. One core, B213-10, has been chosen for additional observation in order to study the gas kinematics at even smaller scales and to test if the specific angular momentum continues to decrese towards the core centre (see Section 4.2.3).

SOLIS III: Methanol towards the pre-stellar core L1544. We observed methanol towards the methanol emission peak near the prototypical pre-stellar core L1544, one of the isolated cores in the Taurus molecular cloud, with the high spatial resolution ($6\times4''$ or $\sim$700 au) of the NOEMA interferometer to study the substructure around the core and to understand what triggers methanol formation or/and its release into the gas phase. The asymmetric distribution of methanol around the core noticed in previous works (Bizzocchi et al. 2014; Spezzano et al. 2016, 2017) might be produced by asymmetric UV irradiation field caused by the irregular distribution of the cloud material, as suggested by Spezzano et al. (2016). The NOEMA observations revealed a high-velocity part of the line on the edge of the dense core, not detected with the single dish observations. This compact emission containing the high-velocity part of the line may be an interface region between the dense core and the accreting envelope material, where a low-velocity shock may be present due to accretion motions onto the dense core. The velocity dispersions of the methanol lines stay subsonic but increase towards the position of the possible low-velocity shock.

4.2 Ongoing and prospective work

The work presented in Chapters 1–3 is just the beginning of a deep, detailed study of the influence of environmental conditions on low-mass star formation. Multiple observing projects, not presented in the previous chapters, were also started in the past four years and will allow for the continued study of the chemical processes and kinematics in dense cores. These observations target the kinematics of cores in additional star-forming regions, the chemistry of cores on large scales, and the environmental effects on the evolution of cores. This section describes the started observing projects, for which all data are already obtained.

4.2.1 Kinematics of dense gas in L1688 and B5

In Chapter 2, I studied the kinematics of dense cores embedded in a filamentary structure, in a calm Taurus molecular cloud. I will do a similar study of dense cores in more active star-forming regions, L1688 in the Ophiuchus MC and B5 in the Perseus MC. With the IRAM 30 m antenna, I mapped the dense cores Oph-C-N, Oph-E-MM2, Oph-F, Oph-H-MM1, Oph-I-MM1, and B5, and obtained single pointing observations towards the cores Oph-H-MM2, Oph-I-MM2, and IC348 in $H^{13}CO^+$(1–0), DCO^+(2-1), N_2H^+(1–0), N_2D^+ (1–0), N_2D^+(2–1), and *para*-NH_2D(1,1) with high spectral resolution (20 kHz, corresponding to 0.04–0.07 km s^{-1} at the observed frequencies) to study the kinematics of the cores. I will also use the NH_3 maps obtained with the Green Bank ammonia survey (GAS, Friesen et al. 2017) to trace the kinematics of the clouds. The Perseus and Ophiuchus molecular clouds are more dense than the Taurus MC, so the ammonia inversional transitions are excited and observed towards Perseus and Ophiuchus in both dense cores and in the surrounding parent cloud. I will then compare the kinematics of the dense cores in active and more dense (Perseus and Ophiuchus) to that in calm and less dense (Taurus) star-forming regions. These observations will also be useful for comparing the significance of environmental effects on core formation and evolution between more and less active star-forming environments.

4.2.2 Deuterium fraction as a function of physical conditions

So far, most of the deuterium fractionation studies in nearby star-forming regions have focused on small maps of individual, preselected cores (Caselli et al. 2002c; Crapsi et al. 2005; Vastel et al. 2006; Parise et al. 2011; Harju et al. 2017) and single pointing observations of cores in individual star-forming region (Friesen et al. 2013; Punanova et al. 2016). I have shown that the typical characteristics of different sub-regions within one star-forming region can vary significantly (in L1688, Chapter 1) or stay almost constant (in L1495, Chapter 2). Thus, detailed studies of the deuterium fractionation, which would highlight and take into account the variations of physical conditions of the gas within a cloud and from one cloud to another, are needed. No large surveys of the deuterium fraction have been conducted in the vast majority of star-forming regions. The Friesen et al. (2010) study of the Oph-B2 region is one of the few projects that has studied the deuterium fraction on larger scales. To find links between physical conditions and chemistry, it is important to study the deuterium fraction on a larger scale.

With the data described in Chapter 2 and Section 4.2.1, I will study the distribution of deuterium fraction across the cores in the L1688 clump in Ophiuchus, in the L1495 filament in Taurus, and the B5 core in Perseus.

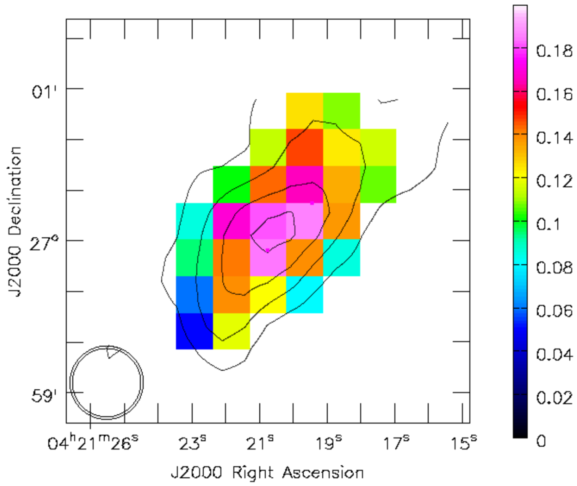

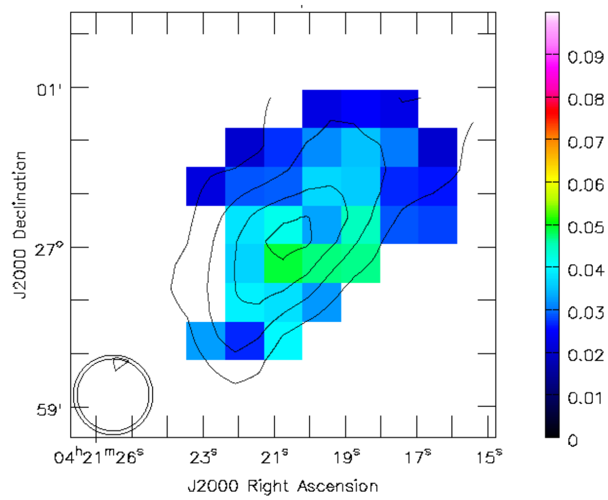

Figure 4.1: Maps of the deuterium fraction, $R_{\rm D}$, of N_2H^+ (left) and HCO^+ (right) towards core 16 in the L1495 filament. The contours show N_2D^+(2–1) emission (as the best tracer of the dense core), starting at the 5σ level of emission with a step of 5σ, where 5σ=0.5 K. The IRAM 30m beam sizes are shown in the bottom left corner, the 29.9″ beam of the $R_{\rm D}$ maps and the 27.8″ beam of the N_2D^+(2–1) map.

With this project, I will measure the deuterium fraction as a function of the physical properties of the gas, such as gas temperature (derived from André et al. 2007; Friesen et al. 2009; Pattle et al. 2015; Seo et al. 2015; Friesen et al. 2017); turbulent content, from line width measurements (André et al. 2007; Hacar et al. 2013; Punanova et al. 2016, Punanova et al., submt); CO freeze-out, using the CO data (Gurney et al. 2008; Nakamura et al. 2011; Hacar et al. 2013) and dust continuum data (Di Francesco et al. 2008; André et al. 2010; Pattle et al. 2015); kinematics of the dense gas, by measuring $V_{\rm LSR}$ variations in various tracers; and distance from young stellar objects, to determine the environmental effects on the chemistry of star-forming regions. These observations will also put stringent constraints on chemical models, thereby improving the determination of the cloud core ages and the diagnostic power of the deuterated species (e.g. Pagani et al. 2013; Sipilä et al. 2013; Kong et al. 2015). The chemical models of Sipilä et al. (2013, 2015, 2016) include spin chemistry (in particular the *ortho* and *para* forms of the H_2 and H_3^+ isotopologues) and will be used to investigate possible differences in the chemical evolution and ionisation fraction across the regions. Chemical ages can also be provided by spin state chemistry when physical parameters and the deuterium fraction are known (Pagani et al. 2013).

I will also study the difference between the deuterium fractionation of ions (N_2H^+/N_2D^+, DCO^+/HCO^+) and neutrals (NH_2D/NH_3), which will constrain available chemical models. So far a detailed study of the deuterium fraction in N_2H^+ and NH_3, with an attempt to explain the observed values with one model, has been done by Harju et al. (2017) for one core, Oph-H-MM1. Comparing the data from Taurus, Ophiuchus, and Perseus as well as comparing with the data already collected towards Oph-A and Oph-B2, will provide further clues on how cold gas evolves in different environments.

Figure 4.1 illusrates the difference between the deuterium fraction in the core centre and envelope of core 16 of the L1495 filament. It shows maps of the deuterium fraction in N_2H^+ (left) and HCO^+ (right). The deuterium fraction of N_2H^+ (which traces the core centre) is approximately a factor of 4 larger than that of HCO^+ (which traces the core envelope). Both maps also show an increase in the deuterium fractions from the edges of the core towards its centre.

4.2.3 Kinematics and a search for hierarchical structures within the B213-10 dense core

The earliest stages of dense core evolution in low-mass star formation are still not well understood. One of the main problems hindering our understanding of star formation is our poor knowledge of the mechanisms at work in reducing the specific angular momentum during the evolution from dense cores to stars (see e.g. Belloche 2013). In particular, the typical specific angular momentum of a dense core is 10^{21-22} cm^2 s^{-1} while that of a protoplanetary disk is only 10^{19-21} cm^2 s^{-1} (Belloche 2013).

In my study of the dense cores' kinematics in L1495 (see Chapter 2), I measured the specific angular momenta of the cores in different lines which trace both envelopes ($H^{13}CO^+$ and DCO^+) and the central parts of the cores (N_2H^+ and N_2D^+). I found that the material is slowing down at small scales, however the specific angular momenta only differ by less than an order of magnitude from tracer to tracer. Crapsi et al. (2007) in their study of the L1544 isolated pre-stellar core, within the Taurus molecular cloud, examined the difference in the velocity fields of the *para*-NH_2D(1,1) line, tracing the very central region of the core, and the NH_3 (1,1) and (2,2) lines, tracing a more extended region (close to that traced by N_2H^+), and also found a decrease in specific angular momentum towards smaller scales by an order of magnitude. (Crapsi et al. 2007) also detected a change in the direction of the velocity gradient between the different tracers, both of which are consistent with magnetic braking (e.g. Stahler & Palla 2005). The fact that the inner regions show kinematic properties different from those of the dense core and that the specific angular momentum of the central zone traced by *para*-NH_2D(1,1) is of the same order of magnitude as the angular momentum typical for protoplanetary disks, possibly means that the core is transitioning between a starless and protostellar state.

The 10 pc long L1495 filament was noticed first in Duvert et al. (1986) and interpreted as an interaction of at least two filaments. Hacar et al. (2013), with a $C^{18}O$(1–0) survey, identified 35 small filamentary structures in position-position-velocity space within the filament. From this filament-scale kinematics, they concluded that the cores in L1495 had formed via hierarchical fragmentation. That is, the cloud first fragmented into several one parsec sized regions and each of these regions then fragmented into velocity-coherent filaments. A small number of these filaments have produced 19 dense cores, seven of which are protostellar with an embedded YSO. The star-forming process is ongoing and we can now investigate if the hierarchical fragmentation process occurs at the dense core scale.

To study how the specific angular momentum changes from large to small scales and to determine if hierarchical fragmentation continues within individual cores, we probe the internal structure and kinematics of one of these cores. With the Northern Extended Millimeter Array (NOEMA) we observed the central part of core 10 in *para*-$NH_2D(1,1)$ emission to determine the internal structure and kinematics of the core on 560–4000 au scales. We will compare the kinematics of the internal part of the core traced by the *para*-$NH_2D(1,1)$ and the kinematics of the more extended gas traced by $N_2D^+(2–1)$ (described in Chapter 2). *Para*-$NH_2D(1,1)$ traces high density gas, with its critical density (8.85×10^6 cm^{-3} Machin & Roueff 2006) being about four times higher than that of $N_2D^+(2–1)$ (2.5×10^6 cm^{-3}, calculated using the data[1] from the LAMDA database, Schöier et al. 2005). We will also compare this core, in a region of clustered star formation, to the L1544 core, a prototypical example of an isolated core that is also in the Taurus MC.

Out of the 13 cores in L1495 studied in Chapter 2 we chose one to study the kinematics of the central ∼4000 au and search for substructures within the core. Many of the previously well-studied cores are in isolation: L1521F (Crapsi et al. 2004), L1544 (Caselli et al. 2002b,c; Crapsi et al. 2007), H-MM1 (Parise et al. 2011; Harju et al. 2017), and L1451 (Pineda et al. 2011). Most stars, however, are formed in groups or clusters (see e.g. Gomez et al. 1993, for the distribution of young stars in Taurus). To study a typical example of low-mass star formation, we chose core 10, sitting within a chain of dense cores (see e.g. Fig. 2.1). The core is not directly impacted by any outflows from the nearby protostars (Rebull et al. 2010; Wang et al. 2014), so that the kinematic information deduced from the observations will give us insights on the process of core accretion and evolution towards star formation. Core 10 is the most compact among the bright starless cores in L1495. Estimates of the core mass vary from 0.8 to 3.4 $M_\odot$ (Marsh et al. 2014) while the Jeans mass for this core (considering T=10 K and n=6.8×10^5 cm^{-3}, Marsh et al. 2014) is 0.36 $M_\odot$. This means that the core must still be fragmenting and we will be able to see the small-scale substructures and study their kinematics.

[1] http://home.strw.leidenuniv.nl/ moldata/datafiles/n2h+@xpol.dat

Appendix A

Hyperfine splitting fit results for L1688

In tables A.2–A.6, the quantity labelled $T_{ant} \times \tau$, is $\tau \times (J_\nu(T_{ex}) - J_\nu(T_{bg}))$ in the case of optically thick transition ($\tau > 0.1$) or the main beam temperature (T_{mb}) in the case that the line is optically thin (with an adopted value of $\tau = 0.1$). For the details, see section 1.3.3.

Table A.1: Dense core coordinates and dataset numbers.

Core	α_{J2000} ($^{h\ m\ s}$)	δ_{J2000} ($^{\circ\ \prime\ \prime\prime}$)	N_2H^+(1–0)	N_2D^+(1–0)	N_2D^+(2–1)	$C^{17}O$(1–0)	starless (s)/ protostellar (p)[a]
				Dataset			
A3-MM1	16:26:09.7	-24:23:06	188-97	066-04	066-04	188-97	s
A-MM4	16:26:24.1	-24:21:52	188-97	066-04	066-04	188-97	s
A-MM5	16:26:25.9	-24:22:27	188-97	066-04	066-04	188-97	s
VLA1623	16:26:26.5	-24:24:31	188-97	066-04	066-04	188-97	p
SM1N	16:26:27.3	-24:23:28	188-97	066-04	066-04	188-97	s
SM1	16:26:27.5	-24:23:56	188-97	066-04	066-04	188-97	s
A-MM6	16:26:27.9	-24:22:53	188-97	066-04	066-04	188-97	s
SM2	16:26:29.5	-24:24:27	066-04	066-04	066-04	188-97	s
A-MM8	16:26:33.4	-24:25:01	066-04	066-04	066-04	–	s
A-S	16:26:43.1	-24:25:42	188-97	066-04	066-04	–	s
B1-MM1	16:27:08.7	-24:27:50	051-00	066-04	066-04	066-04	s
B1-MM3	16:27:12.4	-24:29:58	188-97	066-04	066-04	066-04	s
B1-MM4	16:27:15.7	-24:30:42	188-97	066-04	066-04	188-97	p?
B1B2-MM1	16:27:11.3	-24:27:39	051-00	066-04	066-04	066-04	s
B1B2-MM2	16:27:18.0	-24:28:48	051-00	066-04	–	066-04	p?
B2-MM1	16:27:17.0	-24:27:32	051-00	066-04	066-04	066-04	s
B2-MM2	16:27:20.3	-24:27:08	051-00	066-04	066-04	066-04	s
B2-MM6	16:27:25.3	-24:27:00	188-97	066-04	066-04	066-04	s
B2-MM8	16:27:28.0	-24:27:07	066-04	066-04	066-04	188-97	p?
B2-MM10	16:27:29.6	-24:27:42	188-97	066-04	066-04	066-04	p?
B2-MM14	16:27:32.8	-24:26:29	051-00	066-04	066-04	051-00	s

Table A.1 continued on the next page

Given coordinates are the observed positions, the centres of the cores determined by Motte et al. (1998).
[a]In this paper, cores are considered protostellar if they host an YSO (VLA1623, E-MM3) or if the YSO is within a half beam from the millimetre dust peak coordinates of Motte et al. (1998) used for our N_2D^+(1–0) survey.
We label the latter cores with p? to indicate that the YSO is not coincident with the dust peak, so that it may have not formed within the core but it is sufficiently close to affect the core physical and chemical properties.

Table A.1 (continued)

Core	α_{J2000} ($^{h\ m\ s}$)	δ_{J2000} ($^{\circ\ \prime\ \prime\prime}$)	N_2H^+(1–0)	N_2D^+(1–0)	N_2D^+(2–1)	$C^{17}O$(1–0)	starless (s)/ protostellar (p)[a]
				Dataset			
B2-MM15	16:27:32.8	-24:27:03	051-00	066-04	066-04	066-04	s
B2-MM16	16:27:34.5	-24:26:12	188-97	066-04	066-04	051-00	s
B2-MM17	16:27:35.2	-24:26:21	051-00	–	–	051-00	s
C-We	16:26:50.0	-24:32:49	051-00	066-04	066-04	066-04	s
C-Ne	16:26:57.2	-24:31:39	051-00	066-04	066-04	051-00	s
C-MM3	16:26:58.9	-24:34:22	051-00	–	–	051-00	s
C-MM4	16:26:59.4	-24:34:02	051-00	–	–	051-00	s
C-MM5	16:27:00.1	-24:34:27	188-97	066-04	066-04	051-00	s
C-MM6	16:27:01.6	-24:34:37	051-00	–	–	051-00	s
C-MM7	16:27:03.3	-24:34:22	051-00	–	–	051-00	s
E-MM1e	16:26:57.7	-24:36:56	051-00	066-04	066-04	–	s
E-MM2d	16:27:04.9	-24:39:15	188-97	066-04	066-04	051-00	s
E-MM3	16:27:05.8	-24:37:09	–	–	–	188-97	p
E-MM4	16:27:10.6	-24:39:30	066-04	066-04	066-04	051-00	s
E-MM5	16:27:11.8	-24:37:57	–	–	–	188-97	s
F-MM1	16:27:22.1	-24:40:02	066-04	066-04	066-04	188-97	s
F-MM2	16:27:24.3	-24:40:35	188-97	066-04	066-04	188-97	s
H-MM1	16:27:58.3	-24:33:42	066-04	066-04	066-04	066-04	s
I-MM1	16:28:57.7	-24:20:48	066-04	066-04	066-04	066-04	s

Given coordinates are the observed positions, the centres of the cores determined by Motte et al. (1998).
[a]In this paper, cores are considered protostellar if they host an YSO (VLA1623, E-MM3) or if the YSO is within a half beam from the millimetre dust peak coordinates of Motte et al. (1998) used for our N_2D^+(1–0) survey. We label the latter cores with p? to indicate that the YSO is not coincident with the dust peak, so that it may have not formed within the core but it is sufficiently close to affect the core physical and chemical properties.

Table A.2: Results of hfs-fitting of N_2H^+(1–0), excitation temperature T_{ex} and total column density N_{tot} calculations.

Source	$T_{ant} \cdot \tau$ (K km s^{-1})	$V_{\rm LSR}$ (km s^{-1})	Δv (km s^{-1})	τ	rms T_{mb} (K)	T_{ex}^{a} (K)	N_{tot} (10^{13} cm^{-2})
A3-MM1	1.82 ± 0.12	3.205 ± 0.028	0.871 ± 0.057	0.1	0.097	7.3	0.22 ± 0.02
A-MM4	17.92 ± 0.83	3.194 ± 0.003	0.449 ± 0.008	2.3 ± 0.5	0.152	11.0 ± 4.6	1.19 ± 0.28
A-MM5	15.76 ± 0.78	3.162 ± 0.004	0.508 ± 0.012	0.1	0.254	7.3	1.10 ± 0.06
VLA1623A	20.79 ± 0.52	3.635 ± 0.002	0.561 ± 0.005	4.5 ± 0.3	0.105	7.7 ± 0.9	1.60 ± 0.19
SM1N	58.19 ± 1.27	3.523 ± 0.002	0.500 ± 0.005	8.2 ± 0.3	0.244	10.2 ± 0.8	4.21 ± 0.37
SM1	44.75 ± 0.11	3.599 ± 0.001	0.589 ± 0.001	6.2 ± 0.0	0.224	10.3 ± 0.1	3.82 ± 0.30
A-MM6	5.13 ± 0.88	3.334 ± 0.017	0.724 ± 0.049	0.1	0.157	7.3	0.51 ± 0.09
SM2	23.99 ± 0.35	3.482 ± 0.001	0.467 ± 0.003	3.1 ± 0.2	0.178	10.9 ± 1.1	1.65 ± 0.15
A-MM8	21.50 ± 0.36	3.484 ± 0.001	0.371 ± 0.003	2.7 ± 0.2	0.128	11.2 ± 1.5	1.19 ± 0.12
A-S	3.28 ± 0.76	3.672 ± 0.008	0.242 ± 0.024	0.1	0.110	7.3	0.11 ± 0.03
B1-MM1	6.10 ± 1.30	4.017 ± 0.009	0.291 ± 0.024	0.1	0.186	7.3	0.24 ± 0.06
B1-MM3	28.35 ± 1.83	3.183 ± 0.012	0.248 ± 0.016	0.1	0.273	7.3	0.97 ± 0.09
	20.72 ± 2.09	3.775 ± 0.006	0.333 ± 0.014	4.3 ± 1.3	0.273	7.9 ± 4.3	0.95 ± 0.30
B1-MM4	43.15 ± 3.11	3.660 ± 0.015	0.389 ± 0.023	25.3 ± 1.9	0.369	4.6 ± 0.6	2.87 ± 0.46
	13.62 ± 2.41	3.985 ± 0.006	0.245 ± 0.014	0.1	0.369	7.3	0.46 ± 0.09
B1B2-MM1	9.56 ± 0.57	4.031 ± 0.005	0.385 ± 0.013	0.1	0.192	7.3	0.51 ± 0.03
B1B2-MM2	3.84 ± 0.98	3.913 ± 0.026	0.570 ± 0.071	0.1	0.188	7.3	0.30 ± 0.09
B2-MM1	16.30 ± 1.55	4.009 ± 0.006	0.381 ± 0.015	4.8 ± 1.2	0.245	6.5 ± 2.8	0.87 ± 0.24
B2-MM2	9.33 ± 0.82	3.841 ± 0.023	0.628 ± 0.059	3.9 ± 0.9	0.121	5.4 ± 1.9	0.89 ± 0.25
	7.36 ± 0.94	4.303 ± 0.009	0.319 ± 0.023	0.1	0.121	7.3	0.32 ± 0.05
B2-MM6	19.64 ± 1.61	3.724 ± 0.010	0.696 ± 0.026	4.0 ± 0.8	0.303	8.0 ± 3.0	1.88 ± 0.43

Table A.2 continued on the next page

We find that the results differ slightly from André et al. (2007) because we used different criterion in the hfs fit. In particular, we assume $\tau = 0.1$ if $\tau/\Delta\tau < 3$, which affects the linewidth and intensity, while André et al. (2007) did not fix τ. Also, different hfs files were used, Caselli et al. (1995) by André et al. (2007) and Pagani et al. (2009) in this work. [(a)] In case when optical depth τ value was less than 3σ we did not calculate the excitation temperature with equation 1.2, but rather adopt the average of the excitation temperatures of the other cores.

Table A.2 (continued)

Source	$T_{ant} \cdot \tau$ (K km s^{-1})	$V_{\rm LSR}$ (km s^{-1})	Δv (km s^{-1})	τ	rms T_{mb} (K)	T^a_{ex} (K)	N_{tot} (10^{13} cm^{-2})
B2-MM8	7.89 ± 0.84	3.463 ± 0.017	0.460 ± 0.026	10.7 ± 1.7	0.138	3.6 ± 0.6	1.01 ± 0.22
	23.63 ± 0.43	4.133 ± 0.003	0.507 ± 0.006	3.8 ± 0.2	0.138	9.3 ± 1.0	1.69 ± 0.17
B2-MM10	11.85 ± 1.04	4.293 ± 0.010	0.579 ± 0.024	0.1	0.273	7.3	0.95 ± 0.09
B2-MM14	17.13 ± 1.78	4.122 ± 0.014	0.771 ± 0.035	3.7 ± 1.0	0.236	7.7 ± 3.8	1.82 ± 0.53
B2-MM15	34.75 ± 3.16	4.372 ± 0.006	0.374 ± 0.014	6.7 ± 1.3	0.270	8.3 ± 3.0	1.80 ± 0.38
B2-MM16	17.27 ± 1.14	4.003 ± 0.008	0.640 ± 0.017	3.0 ± 0.7	0.232	8.8 ± 3.6	1.54 ± 0.37
B2-MM17	15.50 ± 1.82	4.038 ± 0.013	0.635 ± 0.032	0.1	0.236	7.3	1.36 ± 0.17
C-We	16.50 ± 1.88	3.540 ± 0.003	0.195 ± 0.009	6.7 ± 1.7	0.182	5.4 ± 2.1	0.48 ± 0.13
C-Ne	41.94 ± 1.64	3.772 ± 0.001	0.210 ± 0.003	12.3 ± 0.7	0.155	6.5 ± 0.7	1.23 ± 0.15
C-MM3	36.01 ± 0.20	3.786 ± 0.003	0.325 ± 0.003	11.8 ± 0.2	0.196	6.1 ± 0.2	1.67 ± 0.19
C-MM4	34.24 ± 6.92	3.807 ± 0.010	0.341 ± 0.021	16.3 ± 4.4	0.277	5.1 ± 2.3	1.84 ± 0.56
C-MM5	48.70 ± 1.86	3.758 ± 0.002	0.320 ± 0.004	18.3 ± 0.9	0.179	5.7 ± 0.5	2.29 ± 0.29
C-MM6	42.64 ± 1.86	3.670 ± 0.001	0.330 ± 0.004	16.9 ± 1.0	0.118	5.5 ± 0.6	2.10 ± 0.28
C-MM7	35.74 ± 2.66	3.647 ± 0.012	0.300 ± 0.015	28.1 ± 1.6	0.242	4.2 ± 0.4	2.12 ± 0.33
E-MM1e	2.51 ± 0.20	4.396 ± 0.019	0.361 ± 0.028	0.1	0.181	7.3	0.12 ± 0.01
E-MM2d	14.40 ± 0.91	4.455 ± 0.003	0.296 ± 0.008	2.8 ± 0.7	0.148	8.2 ± 3.9	0.59 ± 0.17^b
E-MM3							
E-MM4	7.29 ± 0.42	4.197 ± 0.003	0.283 ± 0.007	2.2 ± 0.7	0.120	6.3 ± 3.0	0.29 ± 0.09
E-MM5							
F-MM1	11.02 ± 0.45	4.660 ± 0.004	0.535 ± 0.008	4.1 ± 0.5	0.143	5.7 ± 1.0	0.87 ± 0.14
F-MM2	20.95 ± 1.52	4.094 ± 0.003	0.238 ± 0.009	8.8 ± 1.2	0.147	5.4 ± 1.2	0.75 ± 0.14
	9.20 ± 0.74	4.550 ± 0.005	0.340 ± 0.013	0.1	0.147	7.3	0.43 ± 0.04
H-MM1	23.02 ± 0.47	4.223 ± 0.001	0.271 ± 0.002	3.7 ± 0.3	0.209	9.3 ± 1.2	0.88 ± 0.09

Table A.2 continued on the next page

We find that the results differ slightly from André et al. (2007) because we used different criterion in the hfs fit. In particular, we assume $\tau = 0.1$ if $\tau/\Delta\tau < 3$, which affects the linewidth and intensity, while André et al. (2007) did not fix τ. Also, different hfs files were used, Caselli et al. (1995) by André et al. (2007) and Pagani et al. (2009) in this work. $^{(a)}$ In case when optical depth τ value was less than 3σ we did not calculate the excitation temperature with equation 1.2, but rather adopt the average of the excitation temperatures of the other cores.

Table A.2 (continued)

Source	$T_{ant} \cdot \tau$ (K km s^{-1})	$V_{\rm LSR}$ (km s^{-1})	Δv (km s^{-1})	τ	rms T_{mb} (K)	T_{ex}^{a} (K)	N_{tot} (10^{13} cm^{-2})
I-MM1	28.57 ± 0.74	3.296 ± 0.001	0.271 ± 0.003	8.9 ± 0.4	0.142	6.3 ± 0.5	1.09 ± 0.13

We find that the results differ slightly from André et al. (2007) because we used different criterion in the hfs fit. In particular, we assume $\tau = 0.1$ if $\tau/\Delta\tau < 3$, which affects the linewidth and intensity, while André et al. (2007) did not fix τ. Also, different hfs files were used, Caselli et al. (1995) by André et al. (2007) and Pagani et al. (2009) in this work. $^{(a)}$ In case when optical depth τ value was less than 3σ we did not calculate the excitation temperature with equation 1.2, but rather adopt the average of the excitation temperatures of the other cores.

$^{(b)}$ N_{tot} calculated assuming the line is optically thick, produce large uncertainty which propagates to the $R_{\rm D}$ uncertainty so $R_{\rm D} < 2.5\ \Delta R_{\rm D}$. Thus, to measure $R_{\rm D}$ for E-MM2d, $N_{tot} = (0.58 \pm 0.02) \times 10^{13}\ cm^{-2}$ calculated assuming the line is optically thin ($\tau = 0.1$, T=7.3 K) used.

Table A.3: Results of hfs-fitting of N_2D^+(1–0)

Source	$T_{ant} \cdot \tau$ (K km s^{-1})	$V_{\rm LSR}$ (km s^{-1})	Δv (km s^{-1})	τ	rms T_{mb} (K)	T_{ex} (K)	N_{tot} (10^{12} cm^{-2})
A3-MM1					0.103	7.3	<0.20
A-MM4					0.120	11.0	<0.26
A-MM5					0.120	7.3	<0.23
VLA1623a	1.56 ± 0.09	3.644 ± 0.017	0.546 ± 0.032	0.1	0.114	7.7	1.57 ± 0.13
SM1N	1.62 ± 0.06	3.639 ± 0.004	0.498 ± 0.018	0.1	0.074	10.2	1.59 ± 0.08
SM1	2.18 ± 0.08	3.660 ± 0.012	0.593 ± 0.024	0.1	0.107	10.3	2.56 ± 0.14
A-MM6					0.136	7.3	<0.26
SM2	1.06 ± 0.07	3.524 ± 0.016	0.450 ± 0.035	0.1	0.088	10.9	0.97 ± 0.10
A-MM8	0.83 ± 0.15	3.475 ± 0.015	0.171 ± 0.032	0.1	0.063	11.2	0.29 ± 0.08
A-S					0.131	7.3	<0.25
B1-MM1	1.29 ± 0.08	3.990 ± 0.012	0.392 ± 0.027	0.1	0.087	7.3	0.93 ± 0.09
B1-MM3	4.71 ± 0.43	3.855 ± 0.006	0.371 ± 0.014	6.5 ± 1.3	0.090	3.5 ± 0.5	6.22 ± 1.62
B1-MM4	3.19 ± 0.17	3.567 ± 0.008	0.259 ± 0.019	0.1	0.115	4.6	1.81 ± 0.16
	2.94 ± 0.15	3.995 ± 0.010	0.363 ± 0.029	0.1	0.115	4.6	2.34 ± 0.22
B1B2-MM1	1.76 ± 0.08	4.021 ± 0.008	0.383 ± 0.018	0.1	0.086	7.3	1.24 ± 0.08
B1B2-MM2					0.135	7.3	<0.26
B2-MM1	1.77 ± 0.09	4.082 ± 0.008	0.374 ± 0.021	0.1	0.092	6.5	1.22 ± 0.09
B2-MM2	1.00 ± 0.07	4.194 ± 0.029	0.752 ± 0.053	0.1	0.100	5.4	1.46 ± 0.15
B2-MM6	2.38 ± 0.07	3.840 ± 0.013	0.759 ± 0.024	0.1	0.107	8.0	3.34 ± 0.15
B2-MM8	0.78 ± 0.06	3.901 ± 0.048	1.241 ± 0.114	0.1	0.104	9.3	1.85 ± 0.23
B2-MM10					0.119	7.3	<0.23
B2-MM14	1.46 ± 0.10	4.129 ± 0.035	0.622 ± 0.049	0.1	0.129	7.0	1.67 ± 0.17
B2-MM15	0.95 ± 0.10	4.365 ± 0.018	0.350 ± 0.045	0.1	0.101	7.3	0.61 ± 0.10
B2-MM16	1.85 ± 0.08	3.877 ± 0.016	0.606 ± 0.019	0.1	0.127	8.8	2.11 ± 0.11
B2-MM17							
C-We	1.63 ± 0.10	3.575 ± 0.007	0.236 ± 0.015	0.1	0.088	5.4	0.75 ± 0.07

Table A.3 continued on the next page

Table A.3 (continued)

Source	$T_{ant} \cdot \tau$ (K km s^{-1})	$V_{\rm LSR}$ (km s^{-1})	Δv (km s^{-1})	τ	rms T_{mb} (K)	T_{ex} (K)	N_{tot} (10^{12} cm^{-2})
C-N	10.07 ± 0.65	3.795 ± 0.002	0.228 ± 0.006	6.4 ± 0.9	0.127	4.4 ± 0.7	5.25 ± 1.08
C-MM3							
C-MM4							
C-MM5	7.42 ± 0.49	3.881 ± 0.003	0.282 ± 0.008	2.5 ± 0.8	0.127	5.9 ± 2.4	3.93 ± 1.29
C-MM6							
C-MM7							
E-MM1					0.113	7.3	<0.22
E-MM2d	5.91 ± 0.53	4.485 ± 0.004	0.295 ± 0.011	4.9 ± 1.2	0.115	4.0 ± 1.0	4.51 ± 1.30^{a}
E-MM3							
E-MM4	0.82 ± 0.07	4.288 ± 0.016	0.357 ± 0.033	0.1	0.081	6.3	0.55 ± 0.07
E-MM5							
F-MM1					0.087	5.7	<0.18
F-MM2	1.03 ± 0.09	4.276 ± 0.033	0.767 ± 0.069	0.1	0.121	5.4	1.54 ± 0.19
H-MM1	6.95 ± 0.30	4.243 ± 0.002	0.280 ± 0.005	2.7 ± 0.5	0.081	5.5 ± 1.4	3.76 ± 0.86
I-MM1	5.88 ± 0.31	3.325 ± 0.002	0.283 ± 0.006	2.8 ± 0.6	0.079	5.0 ± 1.4	3.40 ± 0.89

$^{(a)}$ N_{tot} calculated assuming the line is optically thick, produce large uncertainty which propagates to the $R_{\rm D}$ uncertainty so $R_{\rm D} < 2.5\ \Delta R_{\rm D}$. Thus, to measure $R_{\rm D}$ for E-MM2d, $N_{tot} = (2.41 \pm 0.07) \times 10^{12}\ cm^{-2}$ calculated assuming the line is optically thin ($\tau = 0.1$, T=7.3 K) used.

Table A.4: Results of hfs-fitting of N_2D^+(2–1)

Source	$T_{ant} \cdot \tau$ (K km s^{-1})	$V_{\rm LSR}$ (km s^{-1})	Δv (km s^{-1})	τ	rms T_{mb} (K)	T_{ex} (K)	N_{tot} (10^{12} cm^{-2})
A3-MM1					0.186	7.3	<0.22
A-MM4	1.10 ± 0.15	3.169 ± 0.019	0.303 ± 0.047	0.1	0.170	11.0	0.31 ± 0.06
A-MM5					0.275	7.3	<0.32
VLA1623A	4.13 ± 0.08	3.653 ± 0.006	0.549 ± 0.009	0.1	0.268	7.7	2.43 ± 0.06
SM1N	5.42 ± 0.25	3.627 ± 0.004	0.468 ± 0.011	1.2 ± 0.2	0.139	8.0 ± 3.3	2.64 ± 0.45
SM1	3.38 ± 0.37	3.754 ± 0.011	0.493 ± 0.028	1.6 ± 0.5	0.202	5.6 ± 3.9	2.54 ± 0.83
A-MM6					0.183	7.3	<0.22
SM2	2.74 ± 0.15	3.435 ± 0.008	0.311 ± 0.019	0.1	0.193	10.9	0.79 ± 0.06
A-MM8	1.42 ± 0.23	3.411 ± 0.035	0.383 ± 0.068	0.1	0.223	11.2	0.50 ± 0.12
A-S					0.178	7.3	<0.21
B1-MM1	1.84 ± 0.32	3.952 ± 0.023	0.298 ± 0.060	0.1	0.215	7.3	0.61 ± 0.16
B1-MM3	3.53 ± 0.29	3.747 ± 0.011	0.321 ± 0.032	0.1	0.365	7.9	1.19 ± 0.15
B1-MM4	1.85 ± 0.17	3.752 ± 0.036	0.702 ± 0.066	0.1	0.309	4.6	2.84 ± 0.37
B1B2-MM1	2.11 ± 0.27	3.978 ± 0.016	0.274 ± 0.041	0.1	0.310	7.3	0.65 ± 0.13
B1B2-MM2							
B2-MM1	3.23 ± 0.21	3.967 ± 0.010	0.286 ± 0.019	0.1	0.294	6.5	1.15 ± 0.11
B2-MM2	1.73 ± 0.14	4.072 ± 0.030	0.743 ± 0.070	0.1	0.192	5.4	2.06 ± 0.26
B2-MM6	3.90 ± 0.14	3.785 ± 0.013	0.735 ± 0.031	0.1	0.335	8.0	2.99 ± 0.17
B2-MM8	1.83 ± 0.14	4.160 ± 0.017	0.435 ± 0.036	0.1	0.253	9.3	0.77 ± 0.09
B2-MM10					0.326	7.3	<0.38
B2-MM14	3.97 ± 0.11	4.160 ± 0.006	0.426 ± 0.014	0.1	0.197	7.0	1.96 ± 0.08
B2-MM15	1.00 ± 0.14	4.305 ± 0.029	0.446 ± 0.076	0.1	0.107	7.3	0.50 ± 0.11
B2-MM16	4.59 ± 0.13	3.921 ± 0.008	0.611 ± 0.021	0.1	0.266	8.8	2.77 ± 0.13
B2-MM17							
C-W	1.40 ± 0.27	3.507 ± 0.018	0.239 ± 0.057	0.1	0.160	5.4	0.54 ± 0.17
C-N	12.80 ± 0.93	3.743 ± 0.004	0.175 ± 0.009	6.4 ± 0.7	0.235	5.4 ± 1.4	3.59 ± 0.46

Table A.4 continued on the next page

Table A.4 (continued)

Source	$T_{ant} \cdot \tau$ (K km s^{-1})	$V_{\rm LSR}$ (km s^{-1})	Δv (km s^{-1})	τ	rms T_{mb} (K)	T_{ex} (K)	N_{tot} (10^{12} cm^{-2})
C-MM3							
C-MM4							
C-MM5	7.83 ± 0.98	3.829 ± 0.006	0.222 ± 0.018	4.2 ± 0.9	0.270	5.2 ± 2.5	2.96 ± 0.67
C-MM6							
C-MM7							
E-MM1					0.222	7.3	<0.26
E-MM2D	12.07 ± 0.80	4.413 ± 0.004	0.232 ± 0.010	3.2 ± 0.4	0.247	7.3 ± 2.5	3.11 ± 0.43
E-MM3							
E-MM4	1.06 ± 0.20	4.187 ± 0.026	0.295 ± 0.061	0.1	0.168	6.3	0.41 ± 0.11
E-MM5							
F-MM1					0.230	5.7	<0.36
F-MM2	1.21 ± 0.10	4.244 ± 0.032	0.948 ± 0.100	0.1	0.197	5.4	1.83 ± 0.25
H-MM1	19.87 ± 0.74	4.208 ± 0.002	0.217 ± 0.005	4.4 ± 0.3	0.209	8.1 ± 1.4	4.44 ± 0.31
I-MM1	5.49 ± 0.55	3.242 ± 0.005	0.259 ± 0.015	2.0 ± 0.5	0.194	6.3 ± 3.9	1.84 ± 0.51

Table A.5: Results of hfs-fitting of $C^{17}O(1–0)$ and column density calculations

Source	$T_{ant} \cdot \tau$ (K km s^{-1})	$V_{\rm LSR}$ (km s^{-1})	Δv (km s^{-1})	τ	rms T_{mb} (K)	T_{ex} (K)	N_{tot} (10^{15} cm^{-2})
A3-MM1	0.61 ± 0.08	3.050 ± 0.123	1.678 ± 0.223	0.1	0.154	17.6	1.32 ± 0.24
A-MM4	1.88 ± 0.12	3.152 ± 0.027	0.829 ± 0.066	0.1	0.198	16.3	1.92 ± 0.20
A-MM5	2.65 ± 0.21	3.186 ± 0.019	0.673 ± 0.069	0.1	0.210	18.6	2.37 ± 0.30
VLA1623a	3.35 ± 0.09	3.714 ± 0.007	0.755 ± 0.025	0.1	0.114	16.4	3.13 ± 0.13
SM1N	5.98 ± 0.16	3.524 ± 0.006	0.540 ± 0.015	0.1	0.152	17.3	4.11 ± 0.16
	0.90 ± 0.10	3.096 ± 0.097	1.812 ± 0.111	0.1	0.152	17.3	2.09 ± 0.27
SM1	7.77 ± 0.09	3.659 ± 0.004	0.696 ± 0.010	0.1	0.134	17.2	6.86 ± 0.13
A-MM6	3.30 ± 0.11	3.094 ± 0.013	0.961 ± 0.040	0.1	0.209	18.8	4.24 ± 0.23
SM2	4.06 ± 0.12	3.492 ± 0.010	0.796 ± 0.029	0.1	0.159	18.5	4.28 ± 0.20
B1-MM1	1.60 ± 0.06	3.625 ± 0.020	1.158 ± 0.045	0.1	0.192	16.3	2.29 ± 0.12
B1-MM3	2.12 ± 0.07	3.480 ± 0.015	0.984 ± 0.038	0.1	0.202	16.4	2.58 ± 0.13
B1-MM4	2.61 ± 0.13	3.542 ± 0.024	1.030 ± 0.067	0.1	0.223	13.0	2.97 ± 0.25
B1B2-MM1	1.33 ± 0.05	3.696 ± 0.026	1.403 ± 0.060	0.1	0.204	13.3	2.09 ± 0.12
B1B2-MM2	1.65 ± 0.05	4.127 ± 0.020	1.537 ± 0.049	0.1	0.206	15.8	3.08 ± 0.13
B2-MM1	1.70 ± 0.11	3.772 ± 0.021	0.752 ± 0.060	0.1	0.268	14.1	1.46 ± 0.15
B2-MM2	0.97 ± 0.07	3.915 ± 0.033	1.054 ± 0.085	0.1	0.231	14.2	1.18 ± 0.13
B2-MM6	0.81 ± 0.06	3.362 ± 0.054	1.444 ± 0.112	0.1	0.246	13.2	1.30 ± 0.14
B2-MM8	0.79 ± 0.09	3.402 ± 0.137	2.124 ± 0.259	0.1	0.171	14.5	1.94 ± 0.33
B2-MM10	0.86 ± 0.05	3.427 ± 0.059	1.944 ± 0.104	0.1	0.231	14.0	1.90 ± 0.15
B2-MM14	0.84 ± 0.09	3.602 ± 0.093	1.563 ± 0.173	0.1	0.172	14.6	1.52 ± 0.24
B2-MM15	1.10 ± 0.10	3.370 ± 0.040	1.135 ± 0.143	0.1	0.235	13.9	1.42 ± 0.22
B2-MM16	1.24 ± 0.05	3.632 ± 0.021	1.067 ± 0.049	0.1	0.102	14.3	1.53 ± 0.09
B2-MM17	1.32 ± 0.12	3.636 ± 0.062	1.353 ± 0.125	0.1	0.180	14.3	2.06 ± 0.26
C-We	3.39 ± 0.06	3.715 ± 0.008	0.688 ± 0.016	0.1	0.217	12.0	2.50 ± 0.07
	2.07 ± 0.09	4.395 ± 0.010	0.398 ± 0.016	0.1	0.217	12.0	0.88 ± 0.05
C-Ne	3.82 ± 0.11	3.744 ± 0.009	0.782 ± 0.029	0.1	0.153	12.0	3.21 ± 0.15

Table A.5 continued on the next page

Table A.5 (continued)

Source	$T_{ant} \cdot \tau$ (K km s^{-1})	$V_{\rm LSR}$ (km s^{-1})	Δv (km s^{-1})	τ	rms T_{mb} (K)	T_{ex} (K)	N_{tot} (10^{15} cm^{-2})
C-MM3	6.37 ± 0.21	3.716 ± 0.009	0.626 ± 0.026	0.1	0.228	12.3	4.32 ± 0.23
C-MM4	6.10 ± 0.21	3.721 ± 0.009	0.598 ± 0.026	0.1	0.212	10.4	3.75 ± 0.21
	1.72 ± 0.21	4.911 ± 0.026	0.413 ± 0.056	0.1	0.212	10.4	0.73 ± 0.13
C-MM5	5.15 ± 0.26	3.692 ± 0.008	0.423 ± 0.026	0.1	0.227	10.7	2.26 ± 0.18
	1.05 ± 0.18	3.962 ± 0.114	2.140 ± 0.225	0.1	0.227	10.7	2.33 ± 0.46
C-MM6	5.07 ± 0.15	3.676 ± 0.008	0.709 ± 0.028	0.1	0.173	13.0	3.98 ± 0.20
	1.93 ± 0.18	4.855 ± 0.012	0.266 ± 0.031	0.1	0.173	13.0	0.57 ± 0.09
C-MM7	5.94 ± 0.28	3.691 ± 0.012	0.591 ± 0.033	0.1	0.307	12.0	3.77 ± 0.27
E-MM2d	1.27 ± 0.03	3.447 ± 0.016	1.128 ± 0.029	0.1	0.080	13.6	1.62 ± 0.05
	1.90 ± 0.07	3.930 ± 0.005	0.243 ± 0.009	0.1	0.080	13.6	0.52 ± 0.03
	1.29 ± 0.04	4.502 ± 0.014	0.623 ± 0.022	0.1	0.080	13.6	0.91 ± 0.04
E-MM3	1.02 ± 0.15	3.700 ± 0.099	2.261 ± 0.184	0.1	0.175	15.0	2.71 ± 0.46
	2.09 ± 0.20	3.477 ± 0.022	0.600 ± 0.066	0.1	0.175	15.0	1.48 ± 0.21
E-MM4	2.04 ± 0.04	3.427 ± 0.022	1.369 ± 0.042	0.1	0.108	15.0	3.30 ± 0.12
	1.16 ± 0.14	4.197 ± 0.011	0.216 ± 0.035	0.1	0.108	15.0	0.30 ± 0.06
E-MM5	2.42 ± 0.11	3.314 ± 0.023	0.952 ± 0.065	0.1	0.176	15.0	2.72 ± 0.22
	1.63 ± 0.16	4.549 ± 0.031	0.603 ± 0.083	0.1	0.176	15.0	1.16 ± 0.20
F-MM1	2.54 ± 0.09	3.690 ± 0.024	1.411 ± 0.057	0.1	0.217	15.3	4.27 ± 0.23
F-MM2	2.49 ± 0.10	3.725 ± 0.023	1.230 ± 0.055	0.1	0.206	15.6	3.68 ± 0.22
H-MM1	1.38 ± 0.12	3.957 ± 0.029	0.726 ± 0.083	0.1	0.213	11.0	1.04 ± 0.15
I-MM1	1.74 ± 0.13	3.231 ± 0.010	0.277 ± 0.025	0.1	0.206	10.0	0.49 ± 0.06

Table A.6: Results of hfs-fitting of $C^{17}O(2\text{–}1)$ and column density calculations

Source	$T_{ant} \cdot \tau$ (K km s^{-1})	$V_{\rm LSR}$ (km s^{-1})	Δv (km s^{-1})	τ	rms T_{mb} (K)	T_{ex} (K)	N_{tot} (10^{15} cm^{-2})
A3-MM1	3.94 ± 0.55	2.513 ± 0.051	0.702 ± 0.110	0.1	0.846	17.6	1.57 ± 0.33
A-MM4	6.85 ± 0.62	3.231 ± 0.034	0.682 ± 0.067	0.1	0.966	16.3	2.66 ± 0.36
	1.64 ± 0.79	5.071 ± 0.115	0.523 ± 0.289	0.1	0.966	16.3	0.49 ± 0.36
A-MM5	9.12 ± 0.70	3.208 ± 0.025	0.634 ± 0.052	0.1	1.068	18.6	3.29 ± 0.37
VLA1623a	9.53 ± 0.40	3.733 ± 0.017	0.820 ± 0.039	0.1	0.401	16.4	4.46 ± 0.28
SM1N	15.79 ± 0.47	3.496 ± 0.006	0.469 ± 0.018	0.1	0.308	17.3	4.21 ± 0.21
	4.53 ± 0.28	3.011 ± 0.050	1.834 ± 0.078	0.1	0.308	17.3	4.72 ± 0.35
SM1	35.26 ± 1.71	3.667 ± 0.006	0.638 ± 0.015	1.8 ± 0.2	0.572	17.2	7.95 ± 0.92
A-MM6	12.29 ± 0.54	3.038 ± 0.021	0.942 ± 0.046	0.1	0.966	18.8	6.60 ± 0.43
SM2	10.29 ± 0.67	3.322 ± 0.030	0.937 ± 0.045	0.1	0.699	18.5	5.49 ± 0.44
	8.54 ± 0.99	3.615 ± 0.015	0.274 ± 0.042	0.1	0.699	18.5	1.33 ± 0.26
A-MM8	7.62 ± 1.18	3.446 ± 0.034	0.414 ± 0.065	0.1	0.950	18.4	1.80 ± 0.40
B1-MM1	4.04 ± 0.43	3.611 ± 0.061	1.235 ± 0.155	0.1	0.516	16.3	2.84 ± 0.47
B1-MM4	5.65 ± 0.68	3.587 ± 0.063	0.969 ± 0.124	0.1	1.298	13.0	3.27 ± 0.57
B1B2-MM1	3.03 ± 0.30	3.633 ± 0.076	1.697 ± 0.199	0.1	0.476	13.3	3.04 ± 0.47
B1B2-MM2	3.34 ± 0.26	4.148 ± 0.063	1.931 ± 0.190	0.1	0.419	15.8	3.69 ± 0.46
B2-MM1	3.62 ± 0.39	3.826 ± 0.053	1.041 ± 0.125	0.1	0.430	14.1	2.20 ± 0.35
B2-MM2	1.88 ± 0.14	3.782 ± 0.047	1.072 ± 0.086	0.1	0.301	14.2	1.18 ± 0.13
B2-MM8	1.70 ± 0.21	3.380 ± 0.121	1.875 ± 0.248	0.1	0.416	14.5	1.84 ± 0.33
B2-MM14	1.90 ± 0.30	3.676 ± 0.137	1.632 ± 0.278	0.1	0.519	14.6	1.80 ± 0.42
B2-MM16	2.73 ± 0.14	3.662 ± 0.032	1.162 ± 0.065	0.1	0.181	14.3	1.85 ± 0.14
C-W	3.70 ± 0.33	3.698 ± 0.329	1.626 ± 0.167	0.1	0.531	12.0	3.71 ± 0.50
C-MM3	1.97 ± 0.24	3.906 ± 0.070	2.602 ± 0.231	0.1	0.259	12.3	3.12 ± 0.47
	5.31 ± 0.36	3.657 ± 0.014	0.500 ± 0.042	0.1	0.259	12.3	1.62 ± 0.18
C-MM4	8.91 ± 0.77	3.716 ± 0.030	0.765 ± 0.081	0.1	0.662	10.4	4.57 ± 0.62
C-MM5	5.31 ± 0.36	3.657 ± 0.014	0.499 ± 0.042	0.1	0.241	10.7	1.74 ± 0.19

Table A.6 continued on the next page

Table A.6 (continued)

Source	$T_{ant} \cdot \tau$ (K km s^{-1})	$V_{\rm LSR}$ (km s^{-1})	Δv (km s^{-1})	τ	rms T_{mb} (K)	T_{ex} (K)	N_{tot} (10^{15} cm^{-2})
	1.97 ± 0.24	3.905 ± 0.070	2.599 ± 0.231	0.1	0.241	10.7	3.37 ± 0.50
C-MM6	3.99 ± 0.62	3.605 ± 0.035	0.557 ± 0.090	0.1	0.411	13.0	1.33 ± 0.30
	2.52 ± 0.40	3.702 ± 0.090	2.423 ± 0.242	0.1	0.411	13.0	3.64 ± 0.68
C-MM7	2.97 ± 0.36	3.772 ± 0.105	1.593 ± 0.208	0.1	0.607	12.0	2.92 ± 0.52
E-MM1	4.51 ± 0.61	3.764 ± 0.053	0.706 ± 0.165	0.1	0.505	15.0	1.83 ± 0.50
	2.57 ± 0.54	4.694 ± 0.106	0.681 ± 0.199	0.1	0.505	15.0	1.01 ± 0.36
E-MM2d	3.10 ± 0.27	3.823 ± 0.047	1.324 ± 0.136	0.1	0.322	13.6	2.41 ± 0.32
E-MM3	2.94 ± 0.27	3.449 ± 0.099	2.580 ± 0.308	0.1	0.907	15.0	4.37 ± 0.66
E-MM4	3.26 ± 0.20	3.604 ± 0.049	1.708 ± 0.128	0.1	0.301	15.0	3.21 ± 0.31
E-MM5	3.90 ± 0.30	3.882 ± 0.068	2.030 ± 0.191	0.1	0.859	15.0	4.56 ± 0.55
F-MM1	4.53 ± 0.19	3.717 ± 0.028	1.324 ± 0.070	0.1	0.252	15.3	3.44 ± 0.23
	3.20 ± 0.44	4.732 ± 0.017	0.222 ± 0.021	0.1	0.252	15.3	0.41 ± 0.07
F-MM2	4.10 ± 0.18	3.774 ± 0.030	1.517 ± 0.079	0.1	0.233	15.6	3.56 ± 0.24

Table A.7: Column density, deuterium fraction and CO-depletion factor

Source	$N_{tot}(N_2H^+)$ (10^{13} cm^{-2})	$N_{tot}(N_2D^+)$ (10^{12} cm^{-2})	R_D	$S_{850\mu m}$ (Jy beam^{-1})	T_k^a (K)	T_k ref.^{b}	$N(H_2)$ (10^{22} cm^{-2})	$N_{tot}(C^{17}O)$ (10^{15} cm^{-2})	f_d
A3-MM1	0.22 ± 0.02	<0.20	<0.09	262 ± 35	17.6 ± 0.7	P	1.00 ± 0.13	1.32 ± 0.24	0.66 ± 0.15
A-MM4	1.19 ± 0.28	<0.26	<0.02	541 ± 46	16.3 ± 0.5	P	2.34 ± 0.20	1.92 ± 0.20	1.06 ± 0.14
A-MM5	1.10 ± 0.06	<0.23	<0.02	1035 ± 59	18.6 ± 0.7	P	3.64 ± 0.21	2.37 ± 0.30	1.33 ± 0.18
VLA1623	1.60 ± 0.19	1.57 ± 0.13	0.10 ± 0.01	4887 ± 108	16.4 ± 0.5	P	20.89 ± 0.46	3.13 ± 0.13	5.80 ± 0.27
SM1N	4.21 ± 0.37	1.59 ± 0.08	0.038 ± 0.004	5760 ± 77	17.3 ± 0.6	P	22.63 ± 0.30	6.20 ± 0.31	3.17 ± 0.16
SM1	3.82 ± 0.30	2.56 ± 0.14	0.067 ± 0.006	8601 ± 84	17.2 ± 0.6	P	34.10 ± 0.33	6.86 ± 0.13	4.32 ± 0.09
A-MM6	0.51 ± 0.09	<0.26	<0.05	1864 ± 67	18.8 ± 0.8	P	6.44 ± 0.23	4.24 ± 0.23	1.32 ± 0.09
SM2	1.65 ± 0.15	0.97 ± 0.10	0.059 ± 0.008	3746 ± 45	18.5 ± 0.7	P	13.27 ± 0.16	4.28 ± 0.20	2.69 ± 0.13
A-MM8	1.19 ± 0.12	0.29 ± 0.08	0.024 ± 0.007	1065 ± 42	18.4 ± 0.7	P	3.80 ± 0.15		
A-S	0.11 ± 0.03	<0.25	<0.23	109 ± 40	20	M	0.34 ± 0.13		
B1-MM1	0.24 ± 0.06	0.93 ± 0.09	0.39 ± 0.10	131 ± 39	16.3 ± 1.9	F	0.57 ± 0.17	2.29 ± 0.12	0.22 ± 0.07
B1-MM3	1.92 ± 0.31	6.22 ± 1.62	0.32 ± 0.10	706 ± 20	12.2 ± 0.3	P	5.02 ± 0.14	2.25 ± 0.11	1.94 ± 0.11
B1-MM4	3.33 ± 0.47	4.15 ± 0.27	0.12 ± 0.02	528 ± 31	11.8 ± 0.2	P	3.99 ± 0.23	2.87 ± 0.24	1.21 ± 0.12
B1B2-MM1	0.51 ± 0.03	1.24 ± 0.08	0.24 ± 0.02	216 ± 47	13.3 ± 1.2	F	1.31 ± 0.28	2.09 ± 0.12	0.55 ± 0.12
B1B2-MM2	0.30 ± 0.09	<0.26	<0.09	107 ± 27	15.8 ± 0.5	P	0.49 ± 0.12	3.08 ± 0.13	0.14 ± 0.03
B2-MM1	0.87 ± 0.24	1.22 ± 0.09	0.14 ± 0.04	207 ± 39	14.1	F	1.14 ± 0.21	1.46 ± 0.15	0.68 ± 0.15
B2-MM2	1.21 ± 0.25	1.46 ± 0.15	0.12 ± 0.03	470 ± 40	11.4 ± 0.2	P	3.80 ± 0.32	1.08 ± 0.12	3.06 ± 0.43
B2-MM6	1.88 ± 0.43	3.34 ± 0.15	0.18 ± 0.04	1190 ± 35	11.3 ± 0.2	P	9.78 ± 0.28	1.23 ± 0.13	6.91 ± 0.76
B2-MM8	2.70 ± 0.28	1.85 ± 0.23	0.07 ± 0.01	1447 ± 34	13.5 ± 0.4	P	8.57 ± 0.20	1.87 ± 0.32	3.98 ± 0.69
B2-MM10	0.95 ± 0.09	<0.23	<0.02	1026 ± 41	15.8 ± 0.5	P	4.66 ± 0.19	2.02 ± 0.15	2.00 ± 0.17
B2-MM14	1.82 ± 0.53	1.67 ± 0.17	0.09 ± 0.03	1135 ± 29	10.7 ± 0.2	P	10.38 ± 0.27	1.35 ± 0.21	6.68 ± 1.05
B2-MM15	1.80 ± 0.38	0.61 ± 0.10	0.03 ± 0.01	834 ± 32	11.8 ± 0.3	P	6.31 ± 0.24	1.33 ± 0.20	4.12 ± 0.64
B2-MM16	1.54 ± 0.37	2.11 ± 0.11	0.14 ± 0.03	1001 ± 30	10.4 ± 0.2	P	9.69 ± 0.29	1.36 ± 0.08	6.19 ± 0.41
B2-MM17	1.36 ± 0.17	—	—	864 ± 30	13.4 ± 0.3	P	5.19 ± 0.18	2.00 ± 0.26	2.25 ± 0.30
C-We	0.48 ± 0.13	0.75 ± 0.07	0.16 ± 0.04	179 ± 34	12	M	1.31 ± 0.25	3.38 ± 0.09	0.34 ± 0.07
C-Ne	1.23 ± 0.15	5.25 ± 1.08	0.43 ± 0.10	412 ± 27	12	M	3.02 ± 0.20	3.21 ± 0.15	0.82 ± 0.07
C-MM3	1.67 ± 0.19	—	—	1224 ± 29	12.3 ± 0.3	P	8.57 ± 0.20	4.32 ± 0.23	1.72 ± 0.10
C-MM4	1.84 ± 0.56	—	—	1066 ± 32	10.4 ± 0.7	F	10.32 ± 0.31	4.48 ± 0.25	2.00 ± 0.13
C-MM5	2.29 ± 0.29	3.93 ± 1.29	0.17 ± 0.06	1176 ± 29	10.7 ± 0.8	F	10.75 ± 0.27	4.59 ± 0.49	2.04 ± 0.22
C-MM6	2.10 ± 0.28	—	—	976 ± 31	12.8 ± 0.4	P	6.18 ± 0.20	4.55 ± 0.22	1.18 ± 0.07

Table A.7 continued on the next page

[(a)] We assume gas and dust to have the same temperature. [(b)] Temperature taken from: P — Pattle et al. (2015), F — Friesen et al. (2009), M — Motte et al. (1998).

Table A.7 (continued)

Source	$N_{tot}(N_2H^+)$ (10^{13} cm^{-2})	$N_{tot}(N_2D^+)$ (10^{12} cm^{-2})	R_D	$S_{850\mu m}$ (Jy beam^{-1})	T_k^a (K)	T_k ref.^{b}	$N(H_2)$ (10^{22} cm^{-2})	$N_{tot}(C^{17}O)$ (10^{15} cm^{-2})	f_d
C-MM7	2.12 ± 0.33	—	—	450 ± 42	12	M	3.30 ± 0.30	3.77 ± 0.27	0.76 ± 0.09
E-MM1e	0.12 ± 0.01	<0.22	<0.18	34 ± 36	15	M	0.17 ± 0.18		
E-MM2d	0.59 ± 0.17	4.51 ± 1.30	0.42 ± 0.02	655 ± 36	13.6 ± 0.4	P	3.83 ± 0.21	3.05 ± 0.07	1.09 ± 0.07
E-MM3	—	—	—	217 ± 31	15	M	1.07 ± 0.15	4.19 ± 0.50	0.22 ± 0.04
E-MM4	0.29 ± 0.09	0.55 ± 0.07	0.19 ± 0.06	369 ± 53	15	M	1.83 ± 0.26	3.60 ± 0.13	0.44 ± 0.07
E-MM5	—	—	—	363 ± 41	15	M	1.79 ± 0.20	3.88 ± 0.30	0.40 ± 0.05
F-MM1	0.87 ± 0.14	<0.18	<0.02	741 ± 41	15.3 ± 0.5	P	3.55 ± 0.20	4.27 ± 0.23	0.72 ± 0.06
F-MM2	1.18 ± 0.15	1.54 ± 0.19	0.13 ± 0.02	760 ± 41	15.6 ± 0.5	P	3.52 ± 0.19	3.68 ± 0.22	0.83 ± 0.07
H-MM1	0.88 ± 0.09	3.76 ± 0.86	0.43 ± 0.11	614 ± 99	11 ± 0.2	P	5.32 ± 0.86	1.04 ± 0.15	4.44 ± 0.96
I-MM1	1.09 ± 0.13	3.40 ± 0.89	0.31 ± 0.09	392 ± 135	11		4.11 ± 1.41	0.49 ± 0.06	7.30 ± 2.66

$^{(a)}$We assume gas and dust to have the same temperature. $^{(b)}$Temperature taken from: P — Pattle et al. (2015), F — Friesen et al. (2009), M — Motte et al. (1998).

Appendix B

Hyperfine splitting and gradient analysis results for L1495

B.1 Line fitting

B.1.1 Comparison of hyperfine splitting and Gaussian fit results for the $H^{13}CO^{+}$(1–0) and DCO^{+}(2–1) transitions

Here we compare the line widths obtained by fitting the $H^{13}CO^{+}$(1–0) and DCO^{+}(2–1) line with single Gaussians and taking into account the hyperfine structure (hfs). We find that the Gaussian method gives systematically larger line widths than the hfs method. The hyperfine structure of the $H^{13}CO^{+}$ and DCO^{+} rotational transitions were previously studied by Schmid-Burgk et al. (2004) and Caselli & Dore (2005). However the impact of hyperfine splitting in the DCO^{+} transitions higher than the (1–0) transition and in $H^{13}CO^{+}$ was assumed negligible (e.g. Volgenau et al. 2006; Hirota & Yamamoto 2006). We implemented hfs fits of the $H^{13}CO^{+}$(1–0) and DCO^{+}(2–1) transitions in Pyspeckit. The line widths calculated with the hfs fits are systematically smaller than with the Gaussian fit. For this comparison, we use all of the spectra towards core 11 which have a SNR>5, produce fits that give uncertainties to the derived line width under 10%, and for which there is no sign of any asymmetry or multiple peaks. On average, the Gaussian line widths are 25% wider than the hfs derived line widths for $H^{13}CO^{+}$(1–0) and 22% wider for DCO^{+}(2–1) (see Fig. B.1).

B.1.2 Multiple velocity components and self-absorption

All spectra were fitted assuming one velocity component. To check the fit quality, we inspected by eye any spectrum where the residual after fitting divided by rms was less than 0.8 or more than 1.2. Ratio less than 0.8 implies an “overfit” when routine fit the noise features instead of the spectral line. A ratio higher than 1.2 implies the fit does not reproduce the line correctly. A significant difference between the data and the fit could

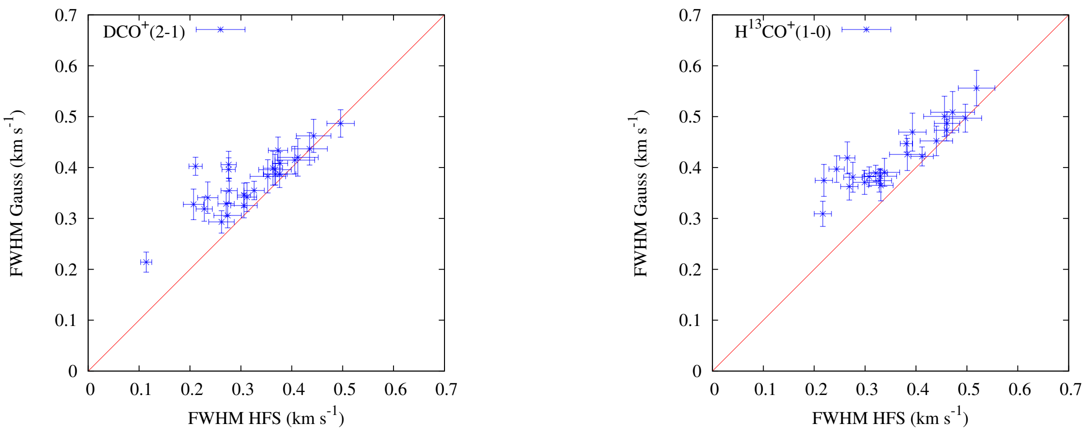

Figure B.1: Comparison of line widths (FWHM) obtained with Gaussian and hfs fits towards core 11 for DCO^+(2–1) (left) and for $H^{13}CO^+$(1–0) (right). The red lines show one-to-one correlation.

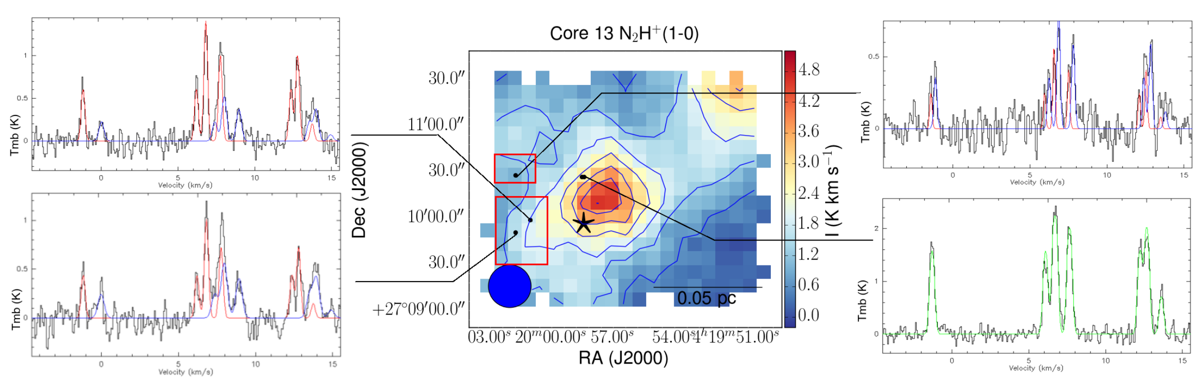

Figure B.2: The integrated intensity map of N_2H^+(1–0) towards core 13. The red boxes in the map show the areas where the additional velocity components are present. Left: the second velocity component (blue fit) is well separated (by $\simeq$1 km s^{-1}) from the main velocity component (red fit). Right top: the second velocity component (red fit) is partially blended with the main velocity component (blue fit, the separation is $\simeq$0.3 km s^{-1} which corresponds to a line width $\sigma = 0.13$ km s^{-1}). Right bottom: an example spectrum where only one velocity component is detected with the best fit shown as the green line.

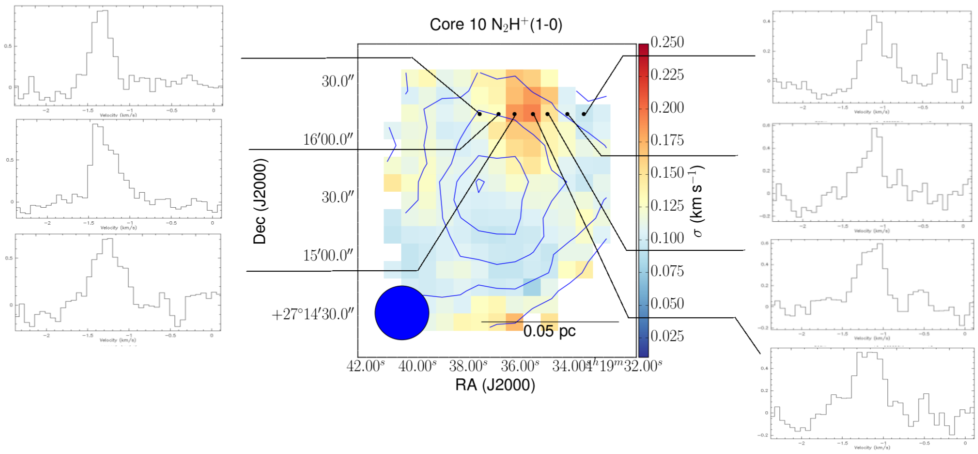

Figure B.3: The velocity dispersion map of N_2H^+(1–0) towards core 10 with a sample of the gas flow on the edge of the core connecting it to the envelope and the isolated components spectra.

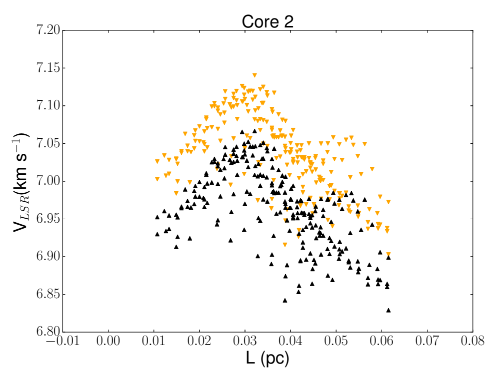

Figure B.4: Comparison of the centroid velocity ($V_{\rm LSR}$) of the DCO$^+$(2–1) line measured with Gaussian (yellow) and hfs (black) fits for core 2 plotted along the filament direction.

be due to the presence of a second line component, self-absorption of the line, asymmetric wings caused by gas flows or non-LTE effects. The N_2D^+(2–1) fits do not show significant differences between the fits and the data. The N_2H^+(1–0) and $H^{13}CO^+$(1–0) spectra show the presence of a second component towards cores 3, 8, 13, and 16 (see Fig. 2.2 and B.5). The DCO^+(2–1) spectra show double-peaked lines caused by either multiple velocity components or self-absorption towards all cores. Many N_2H^+(1–0) spectra also show non-LTE effects in the intensities of the hfs components, similar to those described in Caselli et al. (1995). Since the non-LTE effects do not affect the velocity dispersion and centroid velocity estimates, they are not taken into account in this work.

N_2H^+, DCO^+, and $H^{13}CO^+$ show the same line asymmetries, blue and red wings, towards cores 2, 6, 7, 10, 11, 13, and 19 (see Fig. B.5). The asymmetries also appear in the lines of the rare isotopologues $D^{13}CO^+$ and $HC^{18}O^+$ towards cores 2, 4, 7, 10, and 13 (see Fig. B.6). The wings cause an increase of the velocity dispersion. For example, on the north edge of core 10 the isolated component of the N_2H^+(1–0) hyperfine structure traces a gas flow which appears to connect the core and the envelope (see Fig. B.3). The other observed tracers also show an increase of the line width at the same place towards core 10 (see Fig. B.9).

DCO^+(2–1) and $H^{13}CO^+$(1–0) have no isolated components in their hyperfine structure. Because of the hyperfine components are close, it is not easy to find an unambiguous τ-unconstrained fit with the hfs fitting method, and the Gaussian fits do not properly fit the wings of the lines, thereby producing larger line widths. If the hfs structure makes the line asymmetric, the V_{LSR} of the Gaussian fit will also be altered from the correct value (see Fig. B.1 and B.4). Thus in the case of asymmetric or double-peaked lines in DCO^+ and $H^{13}CO^+$ we used a τ-constrained fit (τ=0.1) to gauge the centroid velocities. The velocity dispersions produced by the τ-constrained fit of the self-absorbed or blended lines are overestimated, as the fit considers one velocity component and the line is assumed to be optically thin (τ=1). We note that the assumption of the τ-constrained fit overestimates the majority of the velocity dispersion measurements for our DCO^+ data. We compared the velocity dispersion values obtained with τ-constrained and τ-unconstrained fits where the optical depth is defined with $\tau > 3\Delta\tau$. The τ-constrained fit produces a velocity dispersion 1–3.3 times larger than the τ-unconstrained fit, with an average dispersion 1.56 times larger.

Since DCO^+(2–1) and $H^{13}CO^+$(1–0) have no isolated components, it is not possible to distinguish between self-absorbed lines and blended second velocity components. However we control if the flux was lost due to self-absorption of the lines by observing transitions of the rare isotopologues $D^{13}CO^+$(2–1) and $HC^{18}O^+$(1–0) towards the DCO^+(2–1) emission peaks (which would suffer self-absorption more than $H^{13}CO^+$, because of its higher critical densities and because it is more abundant in dense, CO depleted gas) in nine cores. We compare the estimates of the column densities (N_{col}) of DCO^+ and HCO^+ obtained with the rearer isotopologues in Fig. B.7. To estimate the column densities, we assume that both lines are optically thin and the fractional abundances of O and C in the species are the same as the fractional abundances of the elements, $^{16}O/^{18}O = 560\pm25$, $^{12}C/^{13}C = 77\pm7$ (Wilson & Rood 1994). The comparison shows that both DCO^+(2–1) and $H^{13}CO^+$(1–0) do not suffer significant self-absorption. Thus the double-peaked lines are most likely two blended velocity components which trace different layers of an envelope and need better sensitivity and spectral resolution to be resolved.

We consider that a line has two velocity components if the components are separated by more than one line width (such as in core 13, see Fig. B.2). Multiple velocity components are only detected towards an area roughly the size of one to two beams towards core 13. The second components which are well separated from the main line (see Fig. B.1.2, left) were missed by the one-component fit procedure and were not taken into account in this work. We tried to avoid the blended components, however, in case they are close (see Fig. B.2, right top), they were fit as one velocity component which increased velocity dispersion in those points.

Table B.1: Results of a Gaussian fit of $D^{13}CO^+(2–1)$ towards the $DCO^+(2–1)$ emission peaks of the cores.

Core	I^a (K km s^{-1})	V_{LSR} (km s^{-1})	Δv (km s^{-1})	σ (km s^{-1})	I^b_{peak} (K)	Base rms (K)	Line rms (K)
*2	–	–	–	–	–	0.028	–
*3	–	–	–	–	–	0.039	–
4	0.061 ± 0.008	6.663 ± 0.021	0.329 ± 0.050	0.140 ± 0.021	0.173	0.045	0.028
6	0.060 ± 0.006	6.855 ± 0.017	0.385 ± 0.047	0.163 ± 0.020	0.146	0.029	0.021
7	0.062 ± 0.006	6.717 ± 0.019	0.353 ± 0.039	0.150 ± 0.017	0.164	0.037	0.035
10	0.035 ± 0.006	6.769 ± 0.030	0.324 ± 0.064	0.138 ± 0.027	0.102	0.039	0.020
11	0.031 ± 0.006	6.753 ± 0.064	0.592 ± 0.115	0.251 ± 0.049	0.050	0.029	0.025
13	0.244 ± 0.013	6.746 ± 0.014	0.531 ± 0.032	0.225 ± 0.014	0.431	0.059	0.078
19	0.034 ± 0.011	6.850 ± 0.050	0.376 ± 0.202	0.160 ± 0.086	0.086	0.037	0.027

Notes. * are non-detections; $^{(a)}$ Integrated intensity; $^{(b)}$ Peak intensity of the line.

Table B.2: Results of an hfs fit of $HC^{18}O^+$(1–0) towards the DCO^+(2–1) emission peaks of the cores.

Core	I^a (K km s^{-1})	V_{LSR} (km s^{-1})	Δv (km s^{-1})	σ (km s^{-1})	τ	Base rms (K)	Line rms (K)
2	0.118 ± 0.025	6.972 ± 0.020	0.196 ± 0.051	0.083 ± 0.022	0.1	0.027	0.002
3	0.119 ± 0.017	6.798 ± 0.024	0.375 ± 0.070	0.159 ± 0.030	0.1	0.024	0.020
4N	0.151 ± 0.019	6.654 ± 0.017	0.248 ± 0.032	0.105 ± 0.014	0.1	0.026	0.023
6S	0.160 ± 0.017	6.841 ± 0.021	0.364 ± 0.041	0.155 ± 0.017	0.1	0.028	0.015
7	0.284 ± 0.028	6.715 ± 0.014	0.281 ± 0.031	0.119 ± 0.013	0.1	0.039	0.027
10	0.207 ± 0.021	6.777 ± 0.013	0.275 ± 0.035	0.117 ± 0.015	0.1	0.026	0.015
11	0.229 ± 0.020	6.839 ± 0.031	0.468 ± 0.043	0.199 ± 0.018	2.5 ± 0.3	0.020	0.015
13	0.306 ± 0.025	6.687 ± 0.015	0.388 ± 0.041	0.165 ± 0.017	0.1	0.038	0.035
19	0.161 ± 0.020	6.835 ± 0.015	0.264 ± 0.039	0.112 ± 0.017	0.1	0.025	0.010

Notes. $^{(a)}$ Integrated intensity.

Table B.3: Characteristics of the N_2H^+(1–0), N_2D^+(2–1), $H^{13}CO^+$(1–0), and DCO^+(2–1) maps convolved to 27.8″, 27.8″, 29.9″, and 18″ beams, respectively.

Core	N_2H^+(1–0) rms in T_{mb} (K)	N_2D^+(2–1) rms in T_{mb} (K)	$H^{13}CO^+$(1–0) rms in T_{mb} (K)	DCO^+(2–1) rms in T_{mb} (K)
2	0.080	0.040	0.110	0.150
3	0.140	0.050	0.140	0.210
4	–	0.060	0.110	0.150
6	0.080	0.080	0.190	0.230
7	0.075	0.060	0.110	0.200
8	0.110	0.060	0.190	0.500
10	0.110	0.080	0.150	0.150
11	0.110	0.080	0.140	0.330
12	0.080	0.060	0.120	0.220
13	0.115	0.080	0.140	0.310
16	0.125	0.100	0.140	0.250
17	0.125	0.090	0.130	0.250
19	0.115	0.090	0.140	0.210

B.1.3 The results of hyperfine splitting fits

B.2 Results of velocity gradients and specific angular momentum calculations

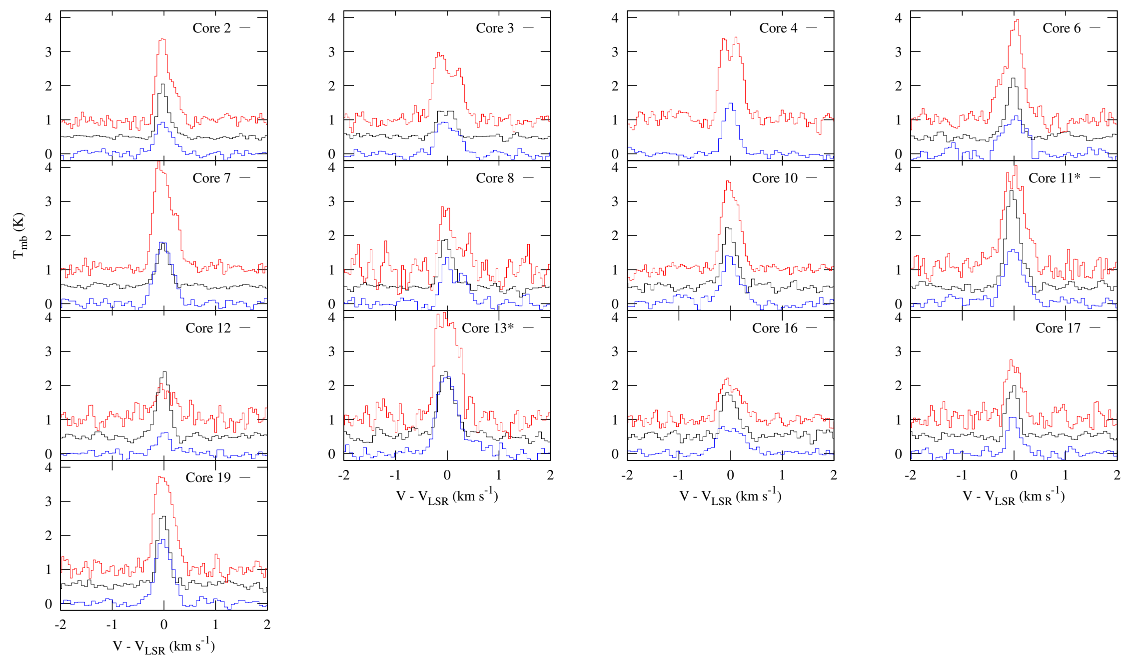

Figure B.5: Spectra of the isolated components of $N_2H^+(1\text{–}0)$ (black), $DCO^+(2\text{–}1)$ (red) and $H^{13}CO^+(1\text{–}0)$ (blue) towards the $N_2H^+(1\text{–}0)$ emission peaks. For convenient comparison, the $DCO^+(2\text{–}1)$ spectra are shifted up by 1 K and the $N_2H^+(1\text{–}0)$ spectra are shifted up by 0.5 K. The cores with an asterisk (*) near the title contain embedded protostrars.

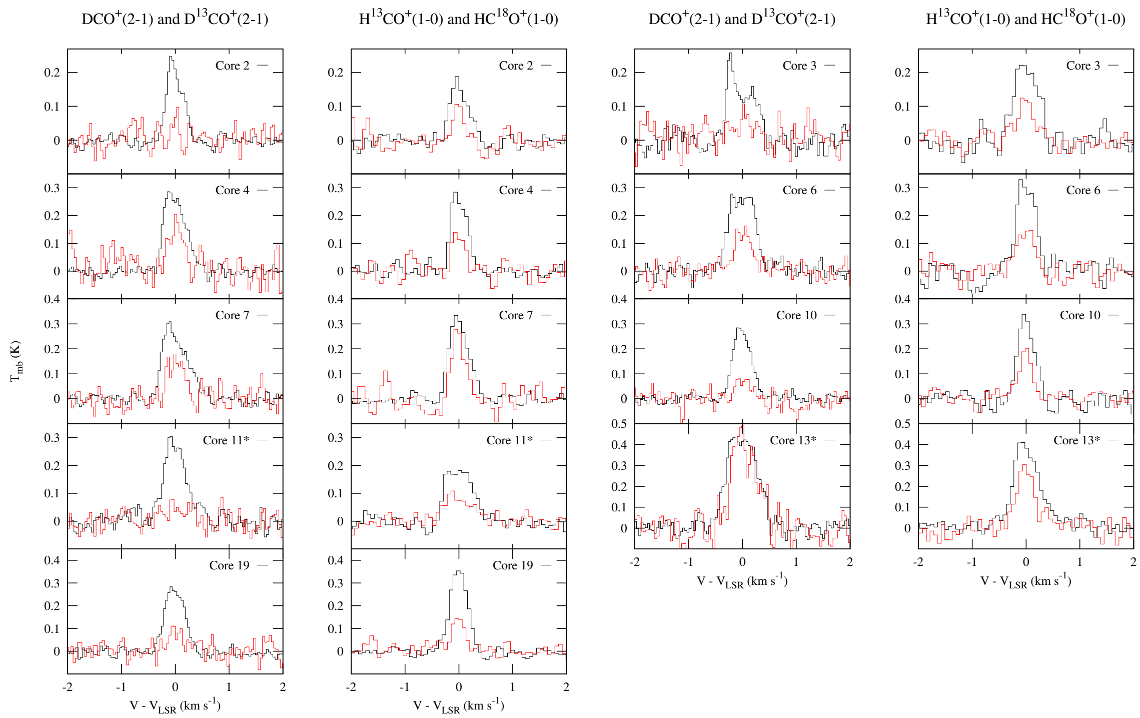

Figure B.6: Spectra of DCO^+(2–1) and $H^{13}CO^+$(1–0) (black) compared to $D^{13}CO^+$(2–1) and $HC^{18}O^+$(1–0) (red) respectively, towards the DCO^+(2–1) emission peaks. For convenient comparison the DCO^+(2–1) spectra are divided by 10 and the $H^{13}CO^+$(1–0) spectra are divided by 5. The cores with an asterisk (*) near the title contain embedded protostrars.

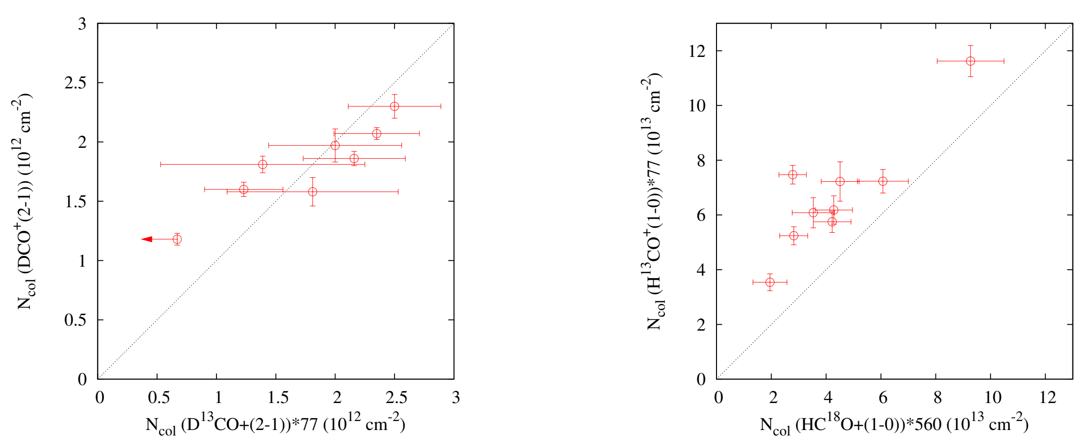

Figure B.7: Comparison of the column densities of DCO^+ (left) and HCO^+ (right) towards the DCO^+(2–1) emission peaks obtained with an assumption of optically thin lines. The dotted lines show one-to-one correlations.

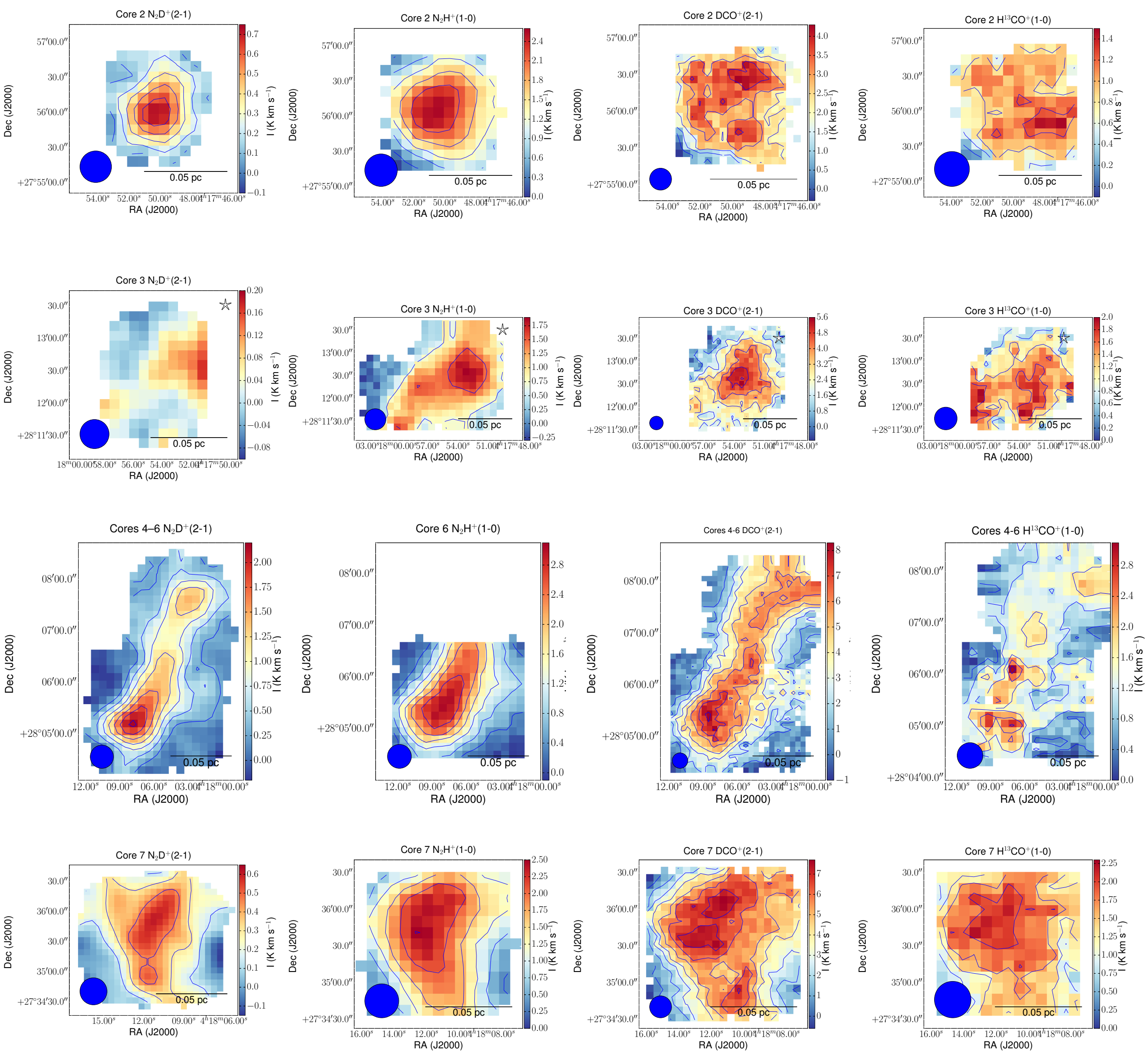

Figure B.8: Integrated intensities of the N_2D^+(2–1), N_2H^+(1–0), DCO^+(2–1), and $H^{13}CO^+$(1–0) lines across the cores. First contour is at the 5σ level and the contour step is 5σ. Stars show the positions of young stellar objects (YSOs) from Rebull et al. (2010): black stars are young, flat and class I objects, white stars are more evolved, class II and III objects.

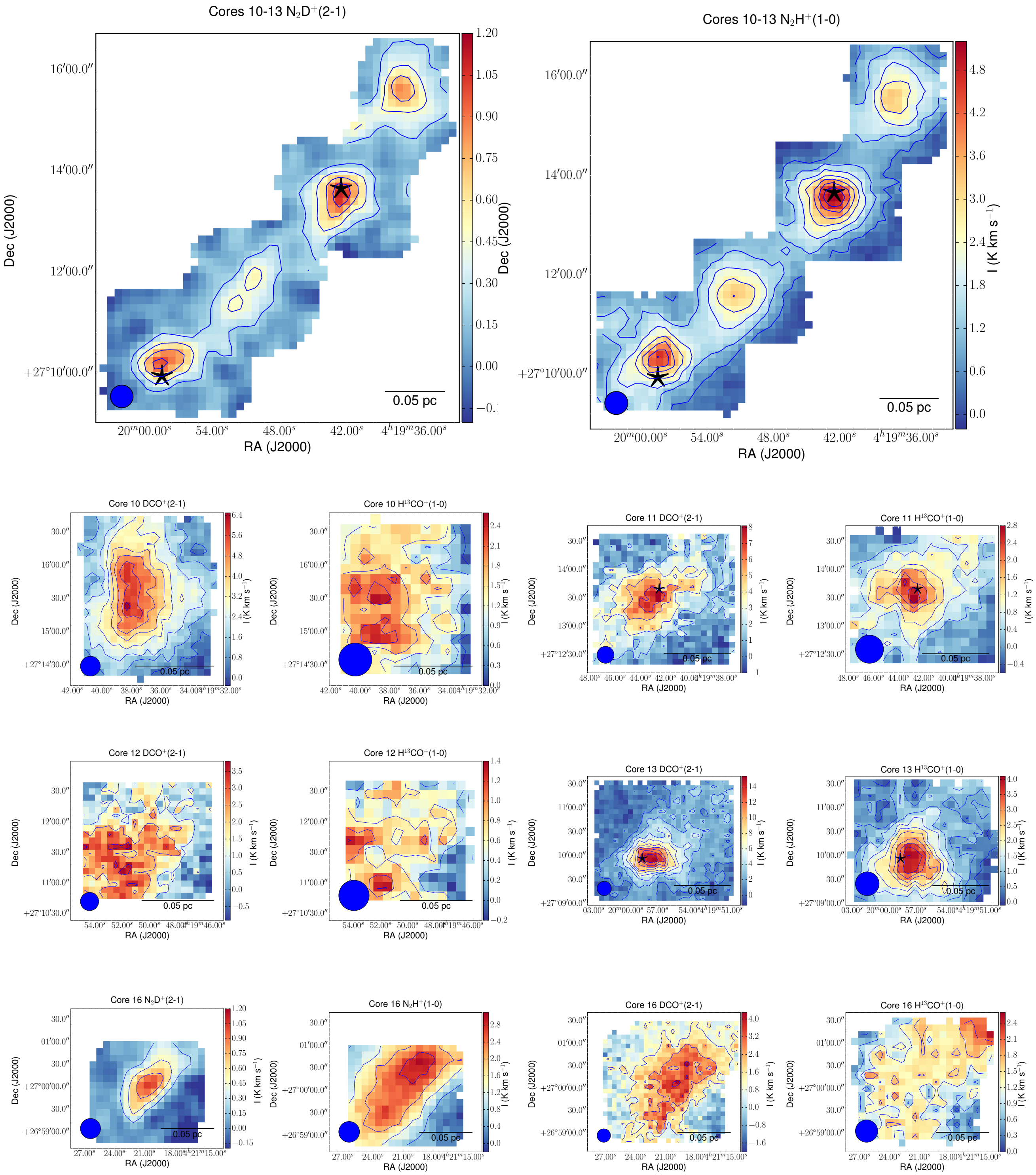

Figure B.8: continued.

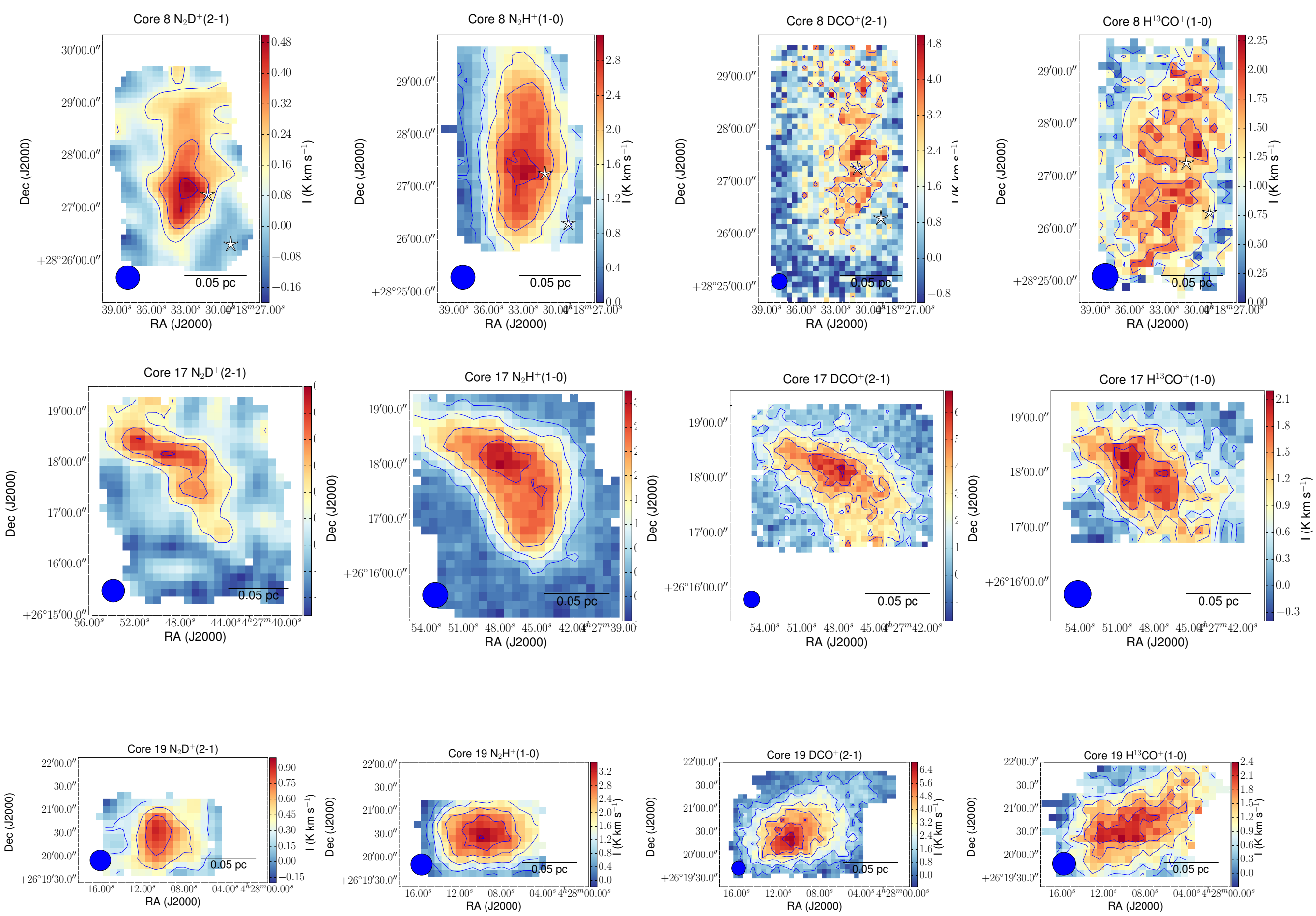

Figure B.8: continued.

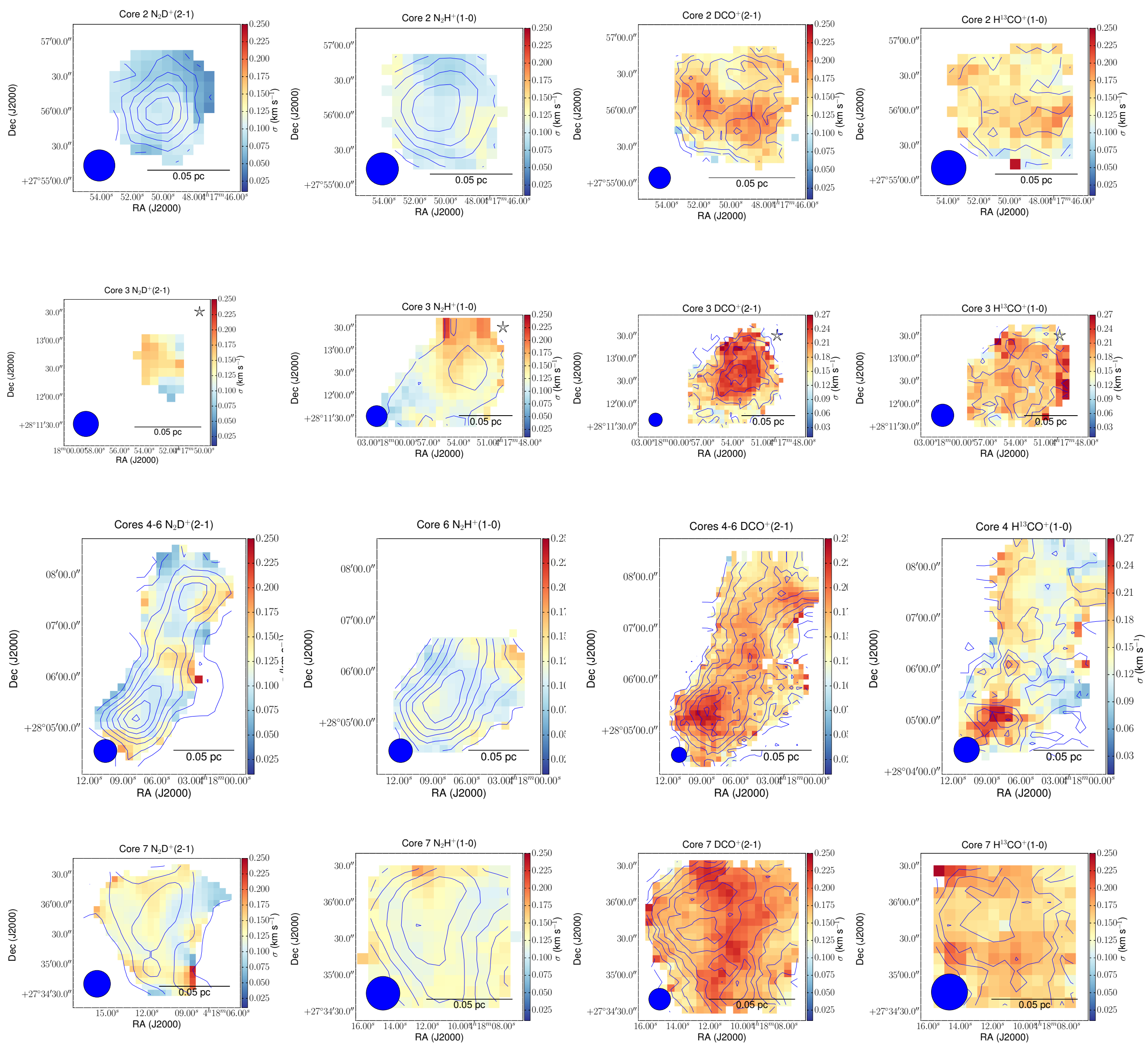

Figure B.9: Line widths (σ) of the N_2D^+(2–1), N_2H^+(1–0), DCO^+(2–1), and $H^{13}CO^+$(1–0) lines across the cores. Black contours show the integrated intensities of the corresponding species. First contour is at the 5σ level and the contour step is 5σ. Stars show the positions of young stellar objects (YSOs) from Rebull et al. (2010): black stars are young, flat and class I objects, white stars are more evolved, class II and III objects.

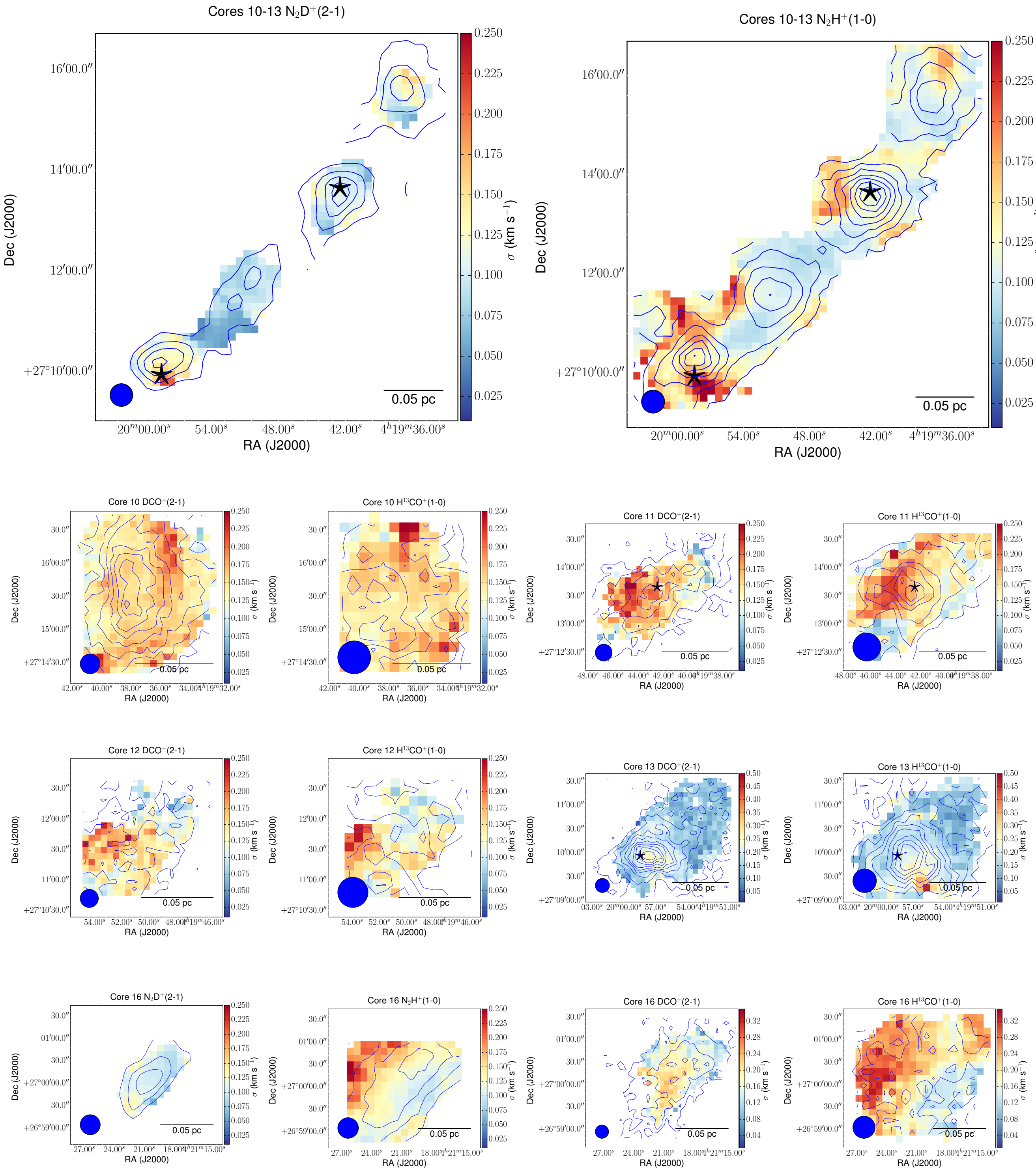

Figure B.9: continued.

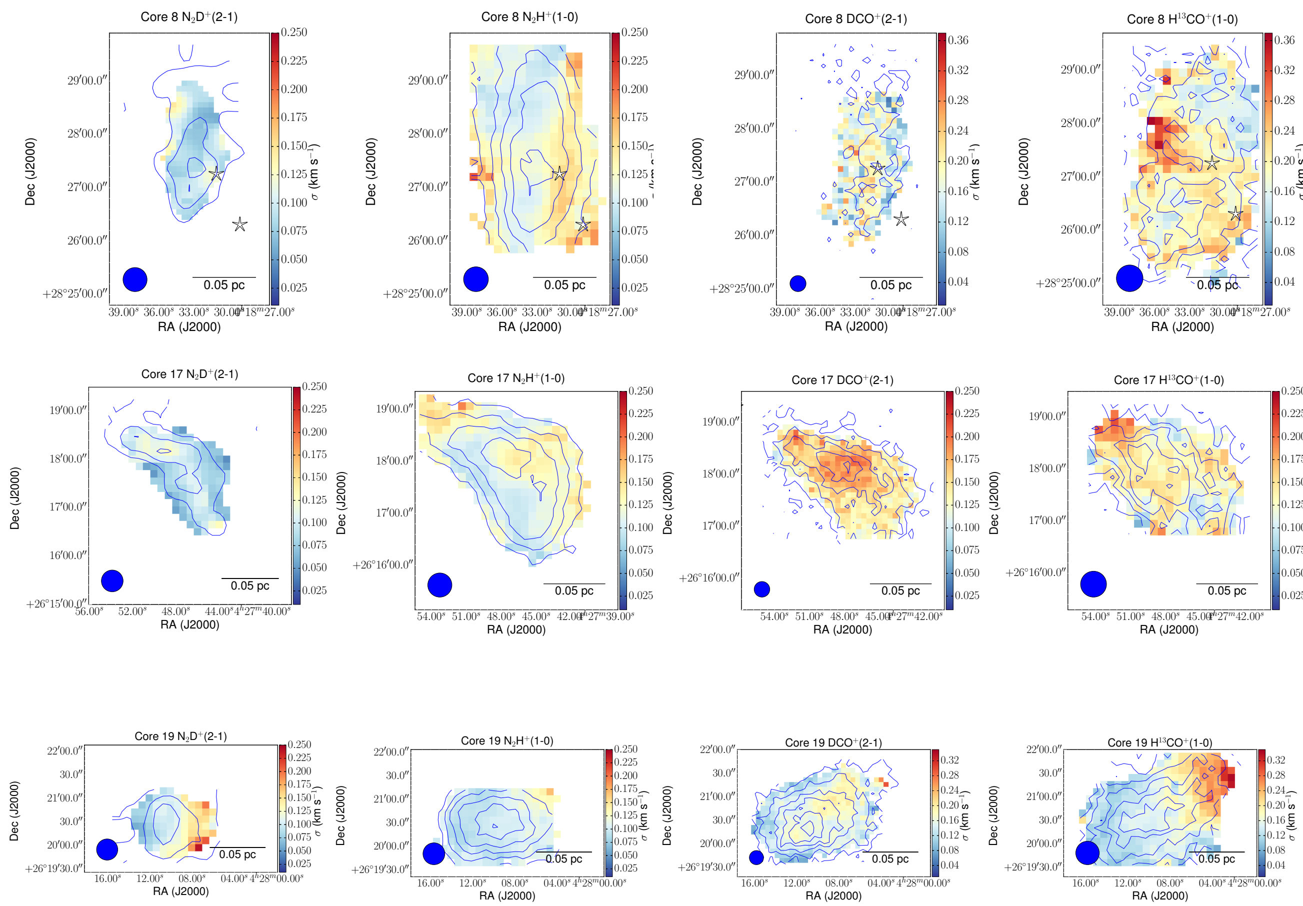

Figure B.9: continued.

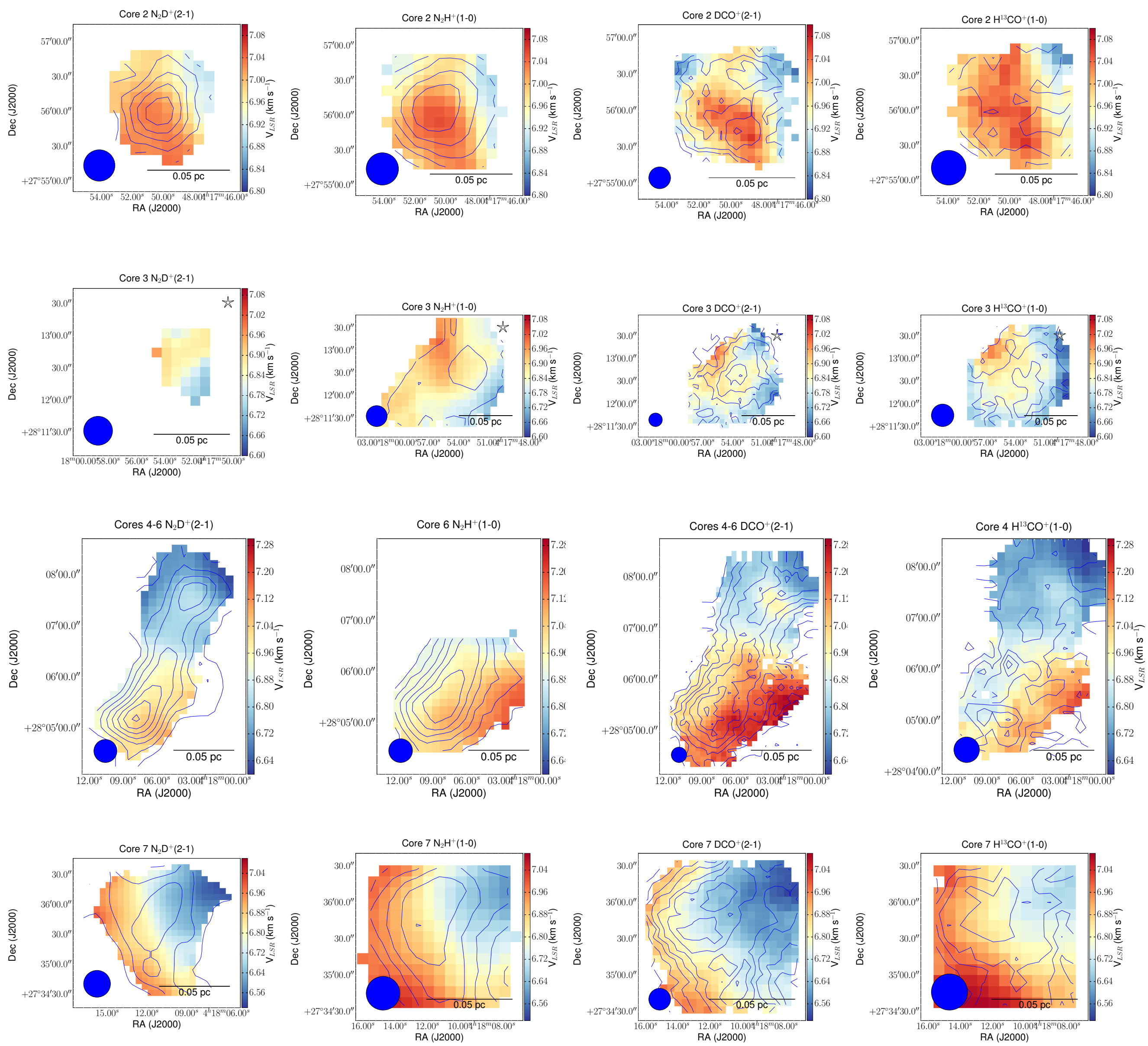

Figure B.10: Centroid velocities (V_{LSR}) of the N_2D^+(2–1), N_2H^+(1–0), DCO^+(2–1), and $H^{13}CO^+$(1–0) lines across the cores. Black contours show the integrated intensities of the corresponding species. First contour is at the 5σ level and the contour step is 5σ. Stars show the positions of young stellar objects (YSOs) from Rebull et al. (2010): black stars are young, flat and class I objects, white stars are more evolved, class II and III objects.

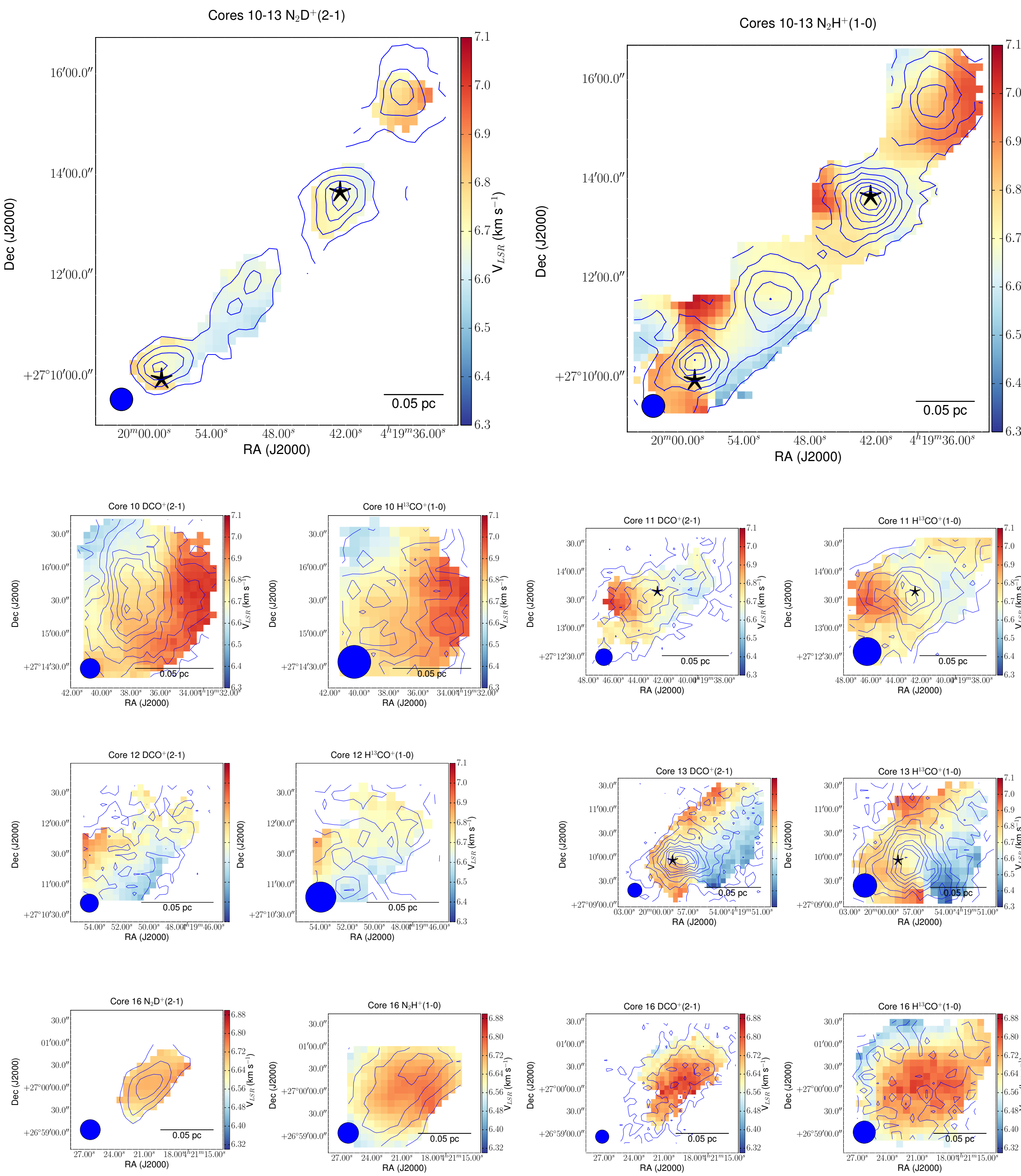

Figure B.10: continued.

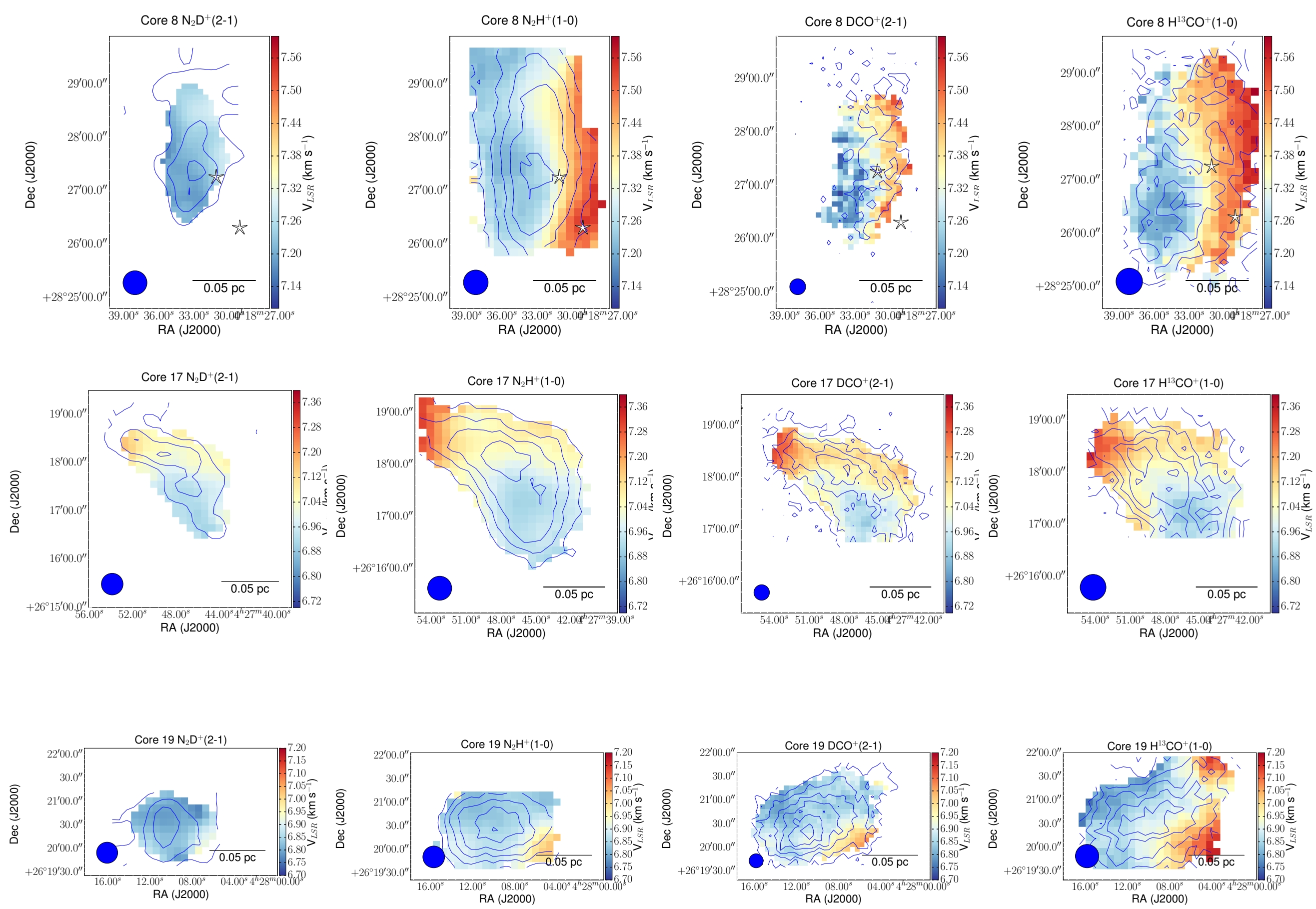

Figure B.10: continued.

Table B.4: Characteristics of the N_2H^+(1–0), N_2D^+(2–1), $H^{13}CO^+$(1–0), and DCO^+(2–1) maps convolved to a 29.9″ beam.

Core	N_2H^+(1–0) rms in T_{mb} (K)	N_2D^+(2–1) rms in T_{mb} (K)	$H^{13}CO^+$(1–0) rms in T_{mb} (K)	DCO^+(2–1) rms in T_{mb} (K)
2	0.070	0.040	0.120	0.070
3	0.120	0.040	0.150	0.100
4	–	0.050	0.110	0.070
6	0.080	0.050	0.205	0.085
7	0.065	0.050	0.110	0.080
8	0.090	0.055	0.210	0.150
10	0.090	0.070	0.155	0.050
11	0.090	0.070	0.140	0.120
12	0.075	0.050	0.120	0.080
13	0.090	0.070	0.150	0.115
16	0.100	0.085	0.150	0.090
17	0.100	0.080	0.140	0.100
19	0.090	0.080	0.130	0.080

Table B.5: Total velocity gradients G, position angles θ_G (measured west to north), equivalent radii[a] measured across the cores using all emitting areas of each species and corresponding specific angular momenta J/M.

Core	G (km s^{-1} pc^{-1})	θ_G (degrees)	R (pc)	J/M (10^{20} cm^2 s^{-1})	G (km s^{-1} pc^{-1})	θ_G (degrees)	R (pc)	J/M (10^{20} cm^2 s^{-1})
		N_2H^+(1–0)				N_2D^+(2–1)		
2	2.012± 0.010	-134.0 ± 0.3	0.036	3.19 ± 0.02	2.348 ± 0.055	-138.4 ± 1.5	0.031	2.75 ± 0.06
3	2.623 ± 0.017	129.7 ± 0.2	0.048	7.54 ± 0.05	5.135 ± 0.452	130.3 ± 5.7	0.019	2.18 ± 0.19
4	–	–	–	–	1.377 ± 0.032	-92.7 ± 2.2	0.039	2.58 ± 0.06
6	3.804 ± 0.010	-48.7 ± 0.1	0.049	11.43 ± 0.03	3.571 ± 0.047	-51.0 ± 0.5	0.039	6.75 ± 0.09
7	5.423 ± 0.001	-149.5 ± 0.1	0.044	13.20 ± 0.02	6.125 ± 0.054	-154.2 ± 0.5	0.040	11.94 ± 0.11
8	3.523 ± 0.008	1.9 ± 0.1	0.067	19.63 ± 0.05	1.789 ± 0.061	26.0 ± 1.4	0.051	5.72 ± 0.20
10	4.857 ± 0.015	-28.8 ± 0.1	0.045	12.18 ± 0.04	3.419 ± 0.180	-29.6 ± 2.9	0.022	2.11 ± 0.11
11	1.632 ± 0.012	-169.1 ± 0.5	0.048	4.59 ± 0.03	2.151 ± 0.100	-156.0 ± 3.5	0.026	1.86 ± 0.09
12	1.435 ± 0.009	92.9 ± 0.4	0.042	3.20 ± 0.02	1.795 ± 0.130	124.1 ± 2.7	0.029	1.92 ± 0.14
13	1.432 ± 0.007	-144.0 ± 0.5	0.056	5.48 ± 0.03	2.639 ± 0.123	158.7 ± 1.9	0.030	2.86 ± 0.13
16	1.069 ± 0.011	28.5 ± 1.0	0.050	3.34 ± 0.03	0.648 ± 0.075	51.7 ± 13.0	0.027	0.59 ± 0.07
17	2.048 ± 0.006	120.2 ± 0.3	0.058	8.47 ± 0.02	2.470 ± 0.045	85.8 ± 1.0	0.040	4.96 ± 0.09
19	1.809 ± 0.011	-66.8 ± 0.3	0.044	4.35 ± 0.03	1.284 ± 0.099	-87.6 ± 3.9	0.032	1.64 ± 0.13
		$H^{13}CO^+$(1–0)				DCO^+(2–1)		
2	1.616 ± 0.062	-144.1 ± 2.1	0.037	2.77 ± 0.11	1.616 ± 0.029	-112.5 ± 1.1	0.035	2.40 ± 0.04
3	1.670 ± 0.053	135.3 ± 1.4	0.047	4.48 ± 0.14	2.233 ± 0.036	150.6 ± 0.8	0.042	4.95 ± 0.08
4	2.336 ± 0.037	-99.2 ± 1.1	0.039	4.31 ± 0.07	2.370 ± 0.016	-103.4 ± 0.5	0.038	4.15 ± 0.03
6	4.144 ± 0.057	-38.6 ± 0.6	0.047	11.12 ± 0.15	4.495 ± 0.026	-45.8 ± 0.2	0.047	12.33 ± 0.07
7	4.764 ± 0.030	-134.7 ± 0.4	0.045	11.73 ± 0.07	4.672 ± 0.014	-144.9 ± 0.2	0.045	11.87 ± 0.04
8	4.091 ± 0.040	9.9 ± 0.4	0.064	20.99 ± 0.21	5.503 ± 0.089	6.0 ± 0.5	0.040	11.01 ± 0.18
10	4.497 ± 0.047	-26.0 ± 0.5	0.045	11.47 ± 0.12	5.548 ± 0.019	-31.5 ± 0.2	0.047	15.00 ± 0.05
11	2.633 ± 0.073	157.0 ± 1.1	0.043	6.14 ± 0.17	3.859 ± 0.066	159.6 ± 0.8	0.035	5.86 ± 0.10
12	2.515 ± 0.128	119.2 ± 1.8	0.034	3.61 ± 0.18	5.159 ± 0.071	128.1 ± 0.4	0.034	7.56 ± 0.10

Table B.5 continued on the next page

[a] Equivalent radius here is the radius of a circle which has the same area as the emitting area (see Subsect. 2.4.5).

Table B.5 (continued)

Core	G (km s^{-1} pc^{-1})	θ_G (degrees)	R (pc)	J/M (10^{20} cm^2 s^{-1})	G (km s^{-1} pc^{-1})	θ_G (degrees)	R (pc)	J/M (10^{20} cm^2 s^{-1})
	HCO^+(1–0)				DCO^+(2–1)			
13	4.714 ± 0.050	148.9 ± 0.5	0.052	15.76 ± 0.17	5.435 ± 0.045	144.9 ± 0.3	0.044	13.14 ± 0.11
16	1.602 ± 0.040	-48.3 ± 1.0	0.059	6.98 ± 0.17	2.624 ± 0.051	-60.7 ± 0.7	0.042	5.81 ± 0.11
17	2.906 ± 0.029	123.2 ± 0.8	0.052	9.67 ± 0.10	2.719 ± 0.027	103.9 ± 0.6	0.048	7.62 ± 0.08
19	2.838 ± 0.029	-37.2 ± 0.5	0.056	11.03 ± 0.11	2.214 ± 0.026	-56.3 ± 0.5	0.049	6.69 ± 0.08

Table B.6: Total velocity gradients G, position angles θ_G (measured west to north), equivalent radii[a], measured across the cores maps convolved to the largest beam of 29.9″ using the emitting area of N_2D^+(2–1), and corresponding specific angular momenta J/M.

Core	G (km s^{-1} pc^{-1})	θ_G (degrees)	R (pc)	J/M (10^{20} cm^2 s^{-1})	G (km s^{-1} pc^{-1})	θ_G (degrees)	R (pc)	J/M (10^{20} cm^2 s^{-1})
	N_2H^+(1–0)				N_2D^+(2–1)			
2	2.251 ± 0.017	-134.7 ± 0.5	0.032	2.91 ± 0.02	2.586 ± 0.073	-142.7 ± 1.9	0.032	3.35 ± 0.09
3	2.787 ± 0.100	161.3 ± 1.6	0.018	1.06 ± 0.04	2.689 ± 0.867	119.0 ± 18.8	0.018	1.02 ± 0.33
4	–	–		–	1.337 ± 0.055	-87.9 ± 3.4	0.038	2.44 ± 0.10
6	3.832 ± 0.016	-48.9 ± 0.2	0.040	7.44 ± 0.03	3.443 ± 0.075	-51.5 ± 0.8	0.040	6.68 ± 0.14
7	5.445 ± 0.012	-151.0 ± 0.1	0.040	10.77 ± 0.02	5.929 ± 0.070	-153.7 ± 0.7	0.041	12.18 ± 0.14
8	3.608 ± 0.017	7.3 ± 0.1	0.044	8.79 ± 0.04	1.687 ± 0.121	17.4 ± 2.1	0.044	4.11 ± 0.30
10	4.634 ± 0.035	-33.9 ± 0.3	0.027	4.06 ± 0.03	3.666 ± 0.248	-37.0 ± 3.6	0.027	3.21 ± 0.22
11	2.053 ± 0.018	-143.6 ± 0.8	0.031	2.42 ± 0.02	2.197 ± 0.134	-156.8 ± 4.5	0.031	2.59 ± 0.16
12	1.875 ± 0.018	109.3 ± 0.5	0.030	2.14 ± 0.02	1.629 ± 0.191	124.0 ± 4.7	0.030	1.86 ± 0.22
13	3.861 ± 0.042	150.6 ± 0.4	0.031	4.70 ± 0.05	2.741 ± 0.185	159.3 ± 3.0	0.031	3.34 ± 0.23
16	0.602 ± 0.044	-33.3 ± 2.2	0.029	0.64 ± 0.05	0.661 ± 0.115	34.8 ± 17.9	0.029	0.70 ± 0.12
17	2.049 ± 0.010	114.8 ± 0.5	0.038	3.59 ± 0.02	2.538 ± 0.080	84.1 ± 1.8	0.038	4.44 ± 0.14
19	1.523 ± 0.017	-72.8 ± 0.5	0.034	2.20 ± 0.03	1.224 ± 0.144	-89.1 ± 6.0	0.034	1.77 ± 0.21
	$H^{13}CO^+$(1–0)				DCO^+(2–1)			
2	2.577 ± 0.128	-149.7 ± 2.7	0.031	3.14 ± 0.16	2.392 ± 0.035	-132.0 ± 0.8	0.032	3.09 ± 0.05
3	7.354 ± 0.784	-164.0 ± 6.9	0.016	2.24 ± 0.24	3.732 ± 0.245	-156.4 ± 4.6	0.018	1.42 ± 0.09
4	2.410 ± 0.061	-97.9 ± 1.7	0.037	4.04 ± 0.10	2.150 ± 0.015	-103.9 ± 0.6	0.038	3.93 ± 0.03
6	4.274 ± 0.135	-40.1 ± 1.0	0.040	8.30 ± 0.26	4.638 ± 0.030	-43.5 ± 0.2	0.039	8.82 ± 0.06
7	4.964 ± 0.056	-136.3 ± 0.7	0.038	9.07 ± 0.10	4.623 ± 0.015	-146.5 ± 0.2	0.041	9.50 ± 0.03
8	4.779 ± 0.126	13.8 ± 0.8	0.044	11.64 ± 0.31	3.877 ± 0.093	7.1 ± 0.7	0.044	9.44 ± 0.23
10	3.998 ± 0.196	-25.5 ± 2.1	0.027	3.50 ± 0.17	4.904 ± 0.040	-37.1 ± 0.3	0.027	4.29 ± 0.04
11	3.300 ± 0.166	-178.4 ± 2.9	0.030	3.77 ± 0.19	4.325 ± 0.079	172.6 ± 0.9	0.031	5.10 ± 0.09

Table B.6 continued on the next page

[a] Equivalent radius here is the radius of a circle which has the same area as the emitting area (see Subsect. 2.4.5).

Table B.6 (continued)

Core	G (km s^{-1} pc^{-1})	θ_G (degrees)	R (pc)	J/M (10^{20} cm^2 s^{-1})	G (km s^{-1} pc^{-1})	θ_G (degrees)	R (pc)	J/M (10^{20} cm^2 s^{-1})
	HCO$^+$(1–0)				DCO$^+$(2–1)			
12	2.747 ± 0.300	120.8 ± 3.6	0.029	2.82 ± 0.31	3.924 ± 0.086	129.0 ± 0.7	0.030	4.48 ± 0.10
13	3.704 ± 0.152	157.6 ± 1.9	0.031	4.51 ± 0.19	3.681 ± 0.066	157.0 ± 0.8	0.031	4.48 ± 0.08
16	3.475 ± 0.185	-84.1 ± 2.8	0.029	3.70 ± 0.20	4.483 ± 0.098	-59.7 ± 0.8	0.029	4.78 ± 0.10
17	3.681 ± 0.112	96.3 ± 2.1	0.032	4.76 ± 0.15	3.160 ± 0.049	86.7 ± 0.8	0.037	5.41 ± 0.08
19	3.125 ± 0.080	-50.7 ± 1.3	0.034	4.52 ± 0.12	2.250 ± 0.036	-58.7 ± 0.8	0.034	3.25 ± 0.05

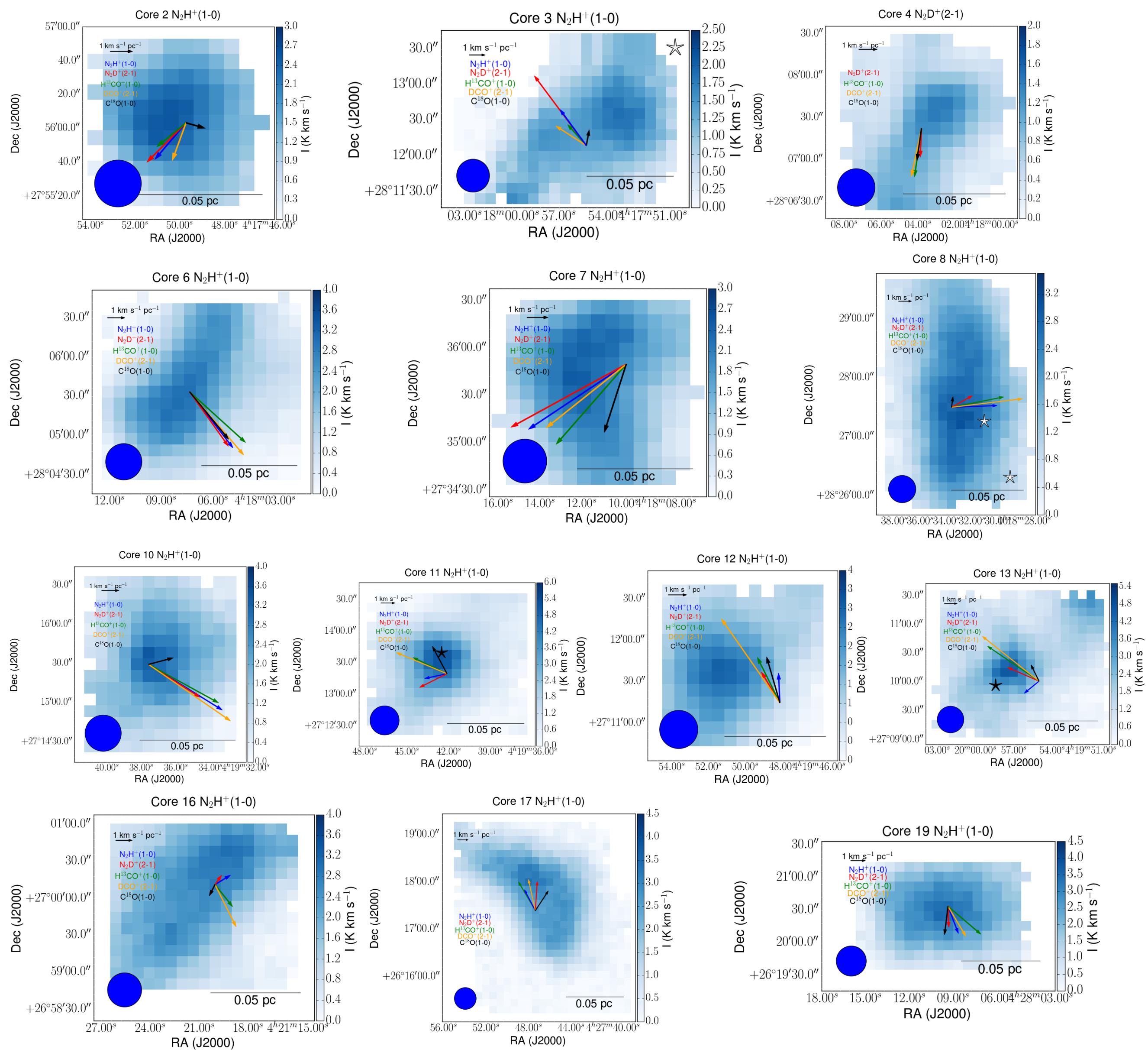

Figure B.11: Total velocity gradients of the N_2D^+(2–1) (red), N_2H^+(1–0) (blue), DCO^+(2–1) (orange), $H^{13}CO^+$(1–0) (green), and $C^{18}O$(1–0) (black) lines across the cores. The colorscale shows the integrated intensities of N_2H^+(1–0) across the cores except core 4, where the integrated intensity of N_2D^+(2–1) is shown. Stars show the positions of young stellar objects (YSOs) from Rebull et al. (2010): black stars are young, flat and class I objects, white stars are more evolved, class II and III objects.

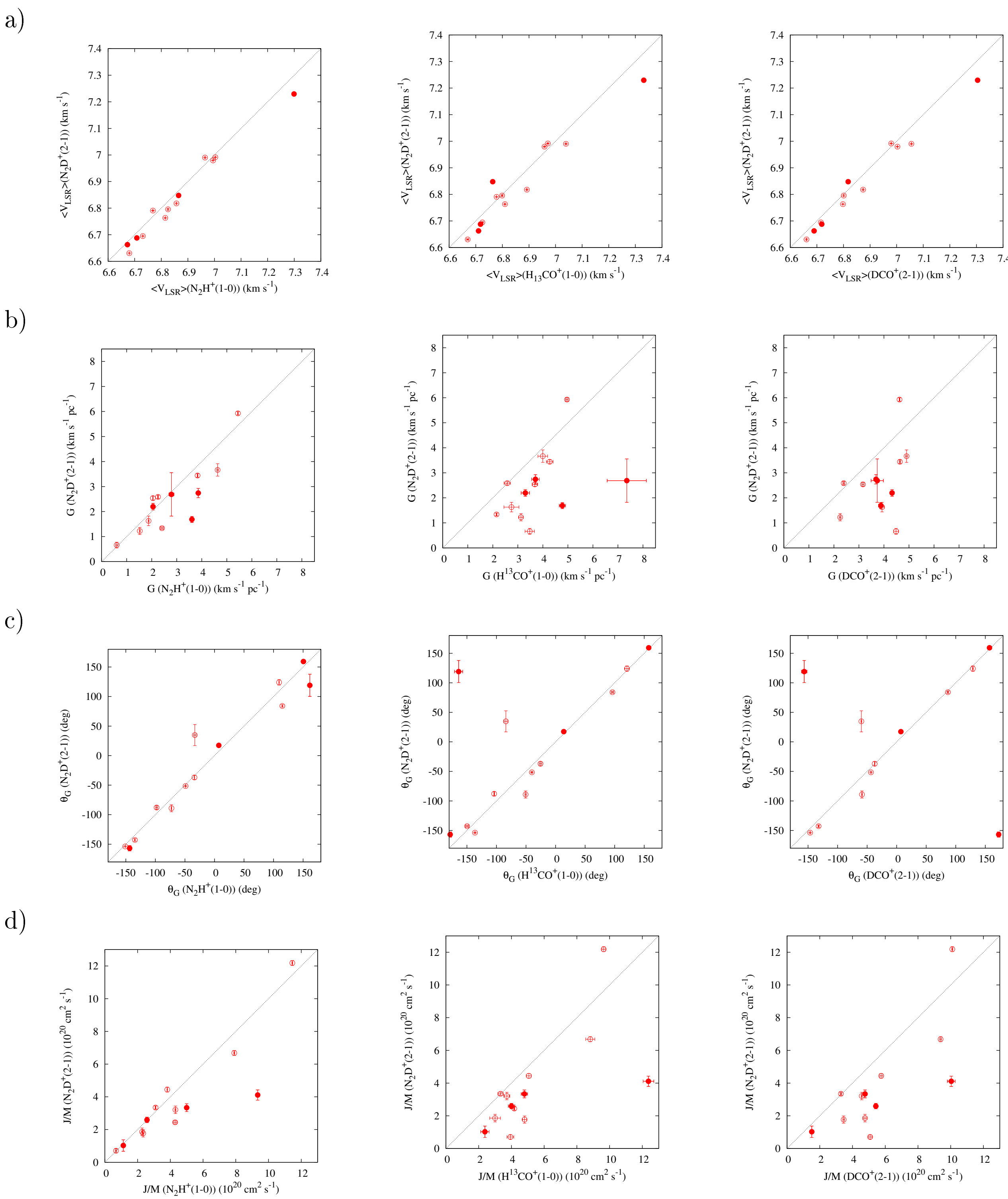

Figure B.12: N_2D^+(2–1) compared to N_2H^+(1–0), $H^{13}CO^+$(1–0) and DCO^+(2–1): a) average velocity across the core; b) total velocity gradient; c) position angle of the total velocity gradient; d) specific angular momentum. Open circles show starless cores and filled circles show protostellar cores. For the comparison, all maps are convolved to the largest beam of 29.9″ with Nyquist spacing and only the area which contains N_2D^+(2–1) emission is used.

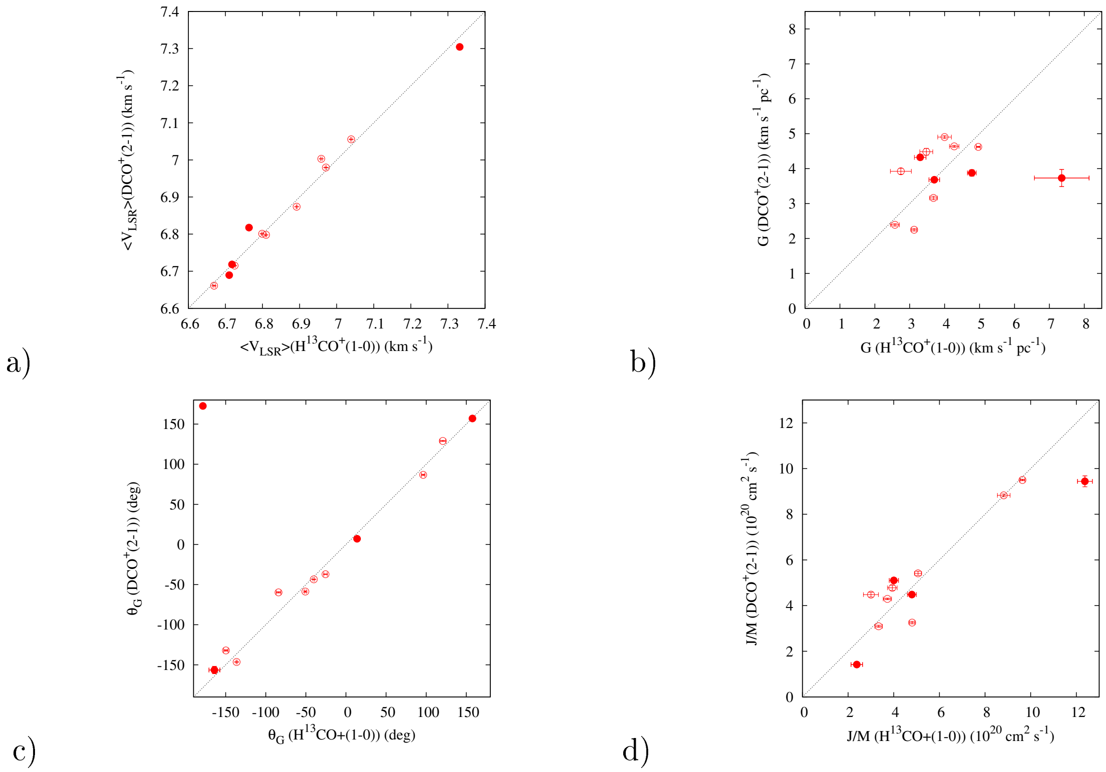

Figure B.13: DCO^+(2–1) compared to $H^{13}CO^+$(1–0): a) average velocity across the core; b) total velocity gradient; c) position angle of the total velocity gradient; d) specific angular momentum. Open circles show starless cores and filled circles show protostellar cores. For the comparison, all maps are convolved to the largest beam of 29.9″ with Nyquist spacing and only the area which containes both $H^{13}CO^+$(1–0) and DCO^+(2–1) emission is used.

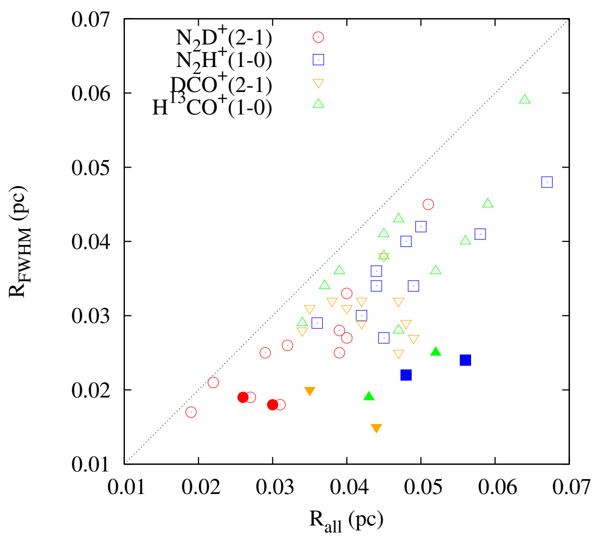

Figure B.14: Core radius at FWHM of maximum emission versus the radius of the total emitting area, measured with different species. Filled symbols show protostellar cores, and open symbols show starless cores. The dashed line shows a one-to-one correlation.

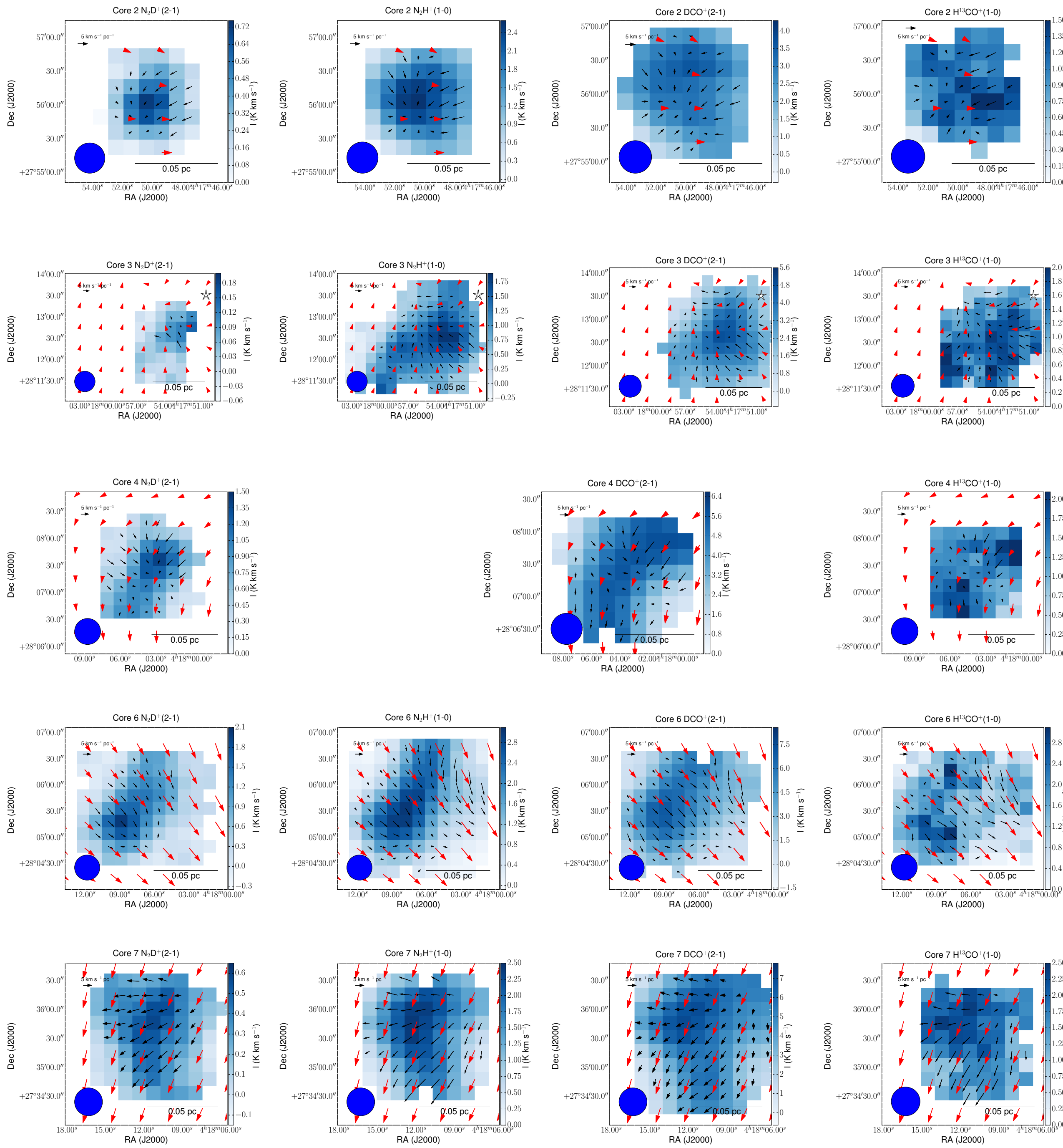

Figure B.15: V_{LSR} local gradients of the $N_2D^+(2–1)$, $N_2H^+(1–0)$, $DCO^+(2–1)$, and $H^{13}CO^+(1–0)$ lines across the cores (black arrows) and V_{LSR} local gradients of the $C^{18}O(1–0)$ line from Hacar et al. (2013) (red arrows). The scale of the $C^{18}O(1–0)$ gradients is 2.5 times larger then the scale indicated in the figures. Colorscale shows integrated intensities of corresponding species across the cores. Stars show the positions of young stellar objects (YSOs) from Rebull et al. (2010): black stars are young, flat and class I objects, white stars are more evolved, class II and III objects.

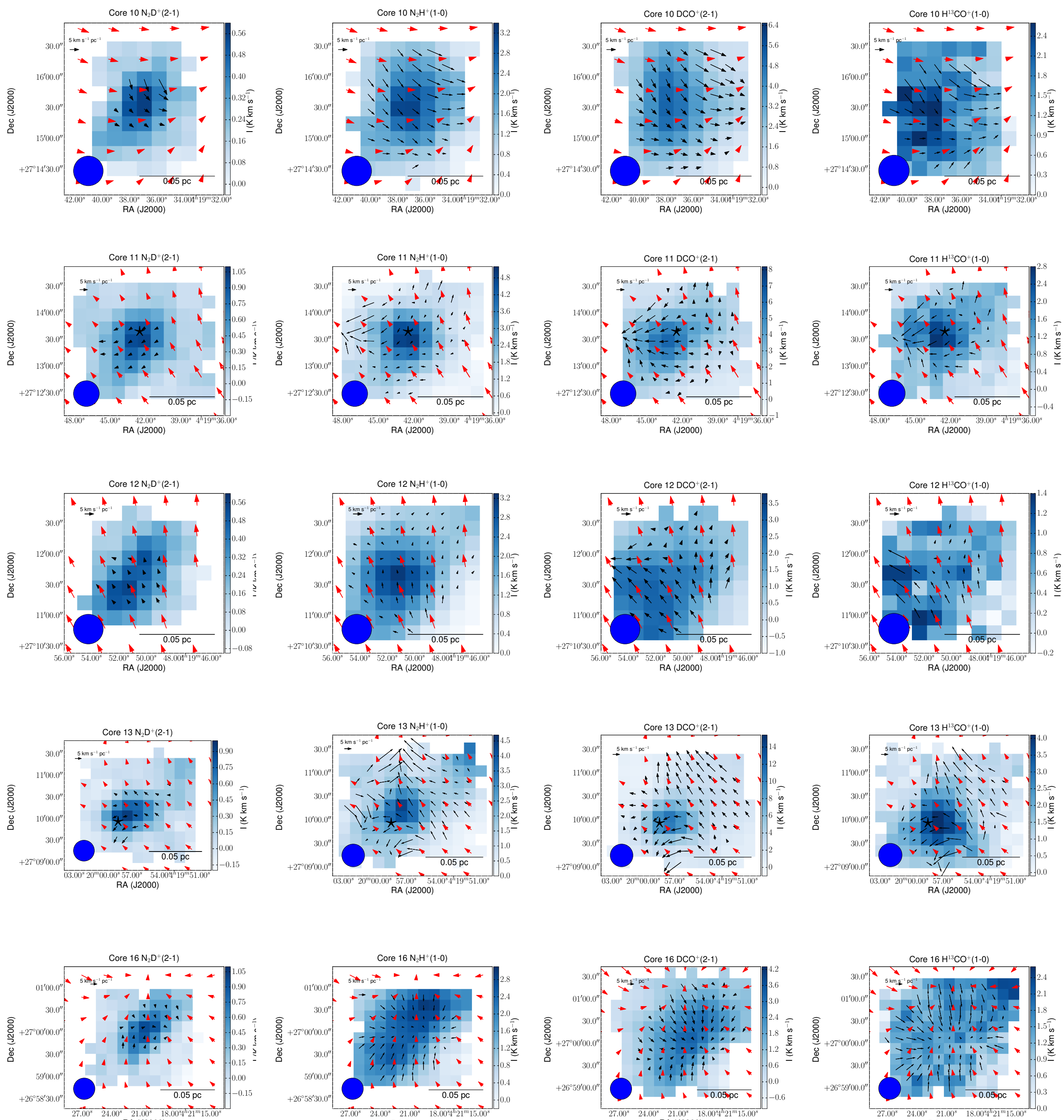

Figure B.15: continued.

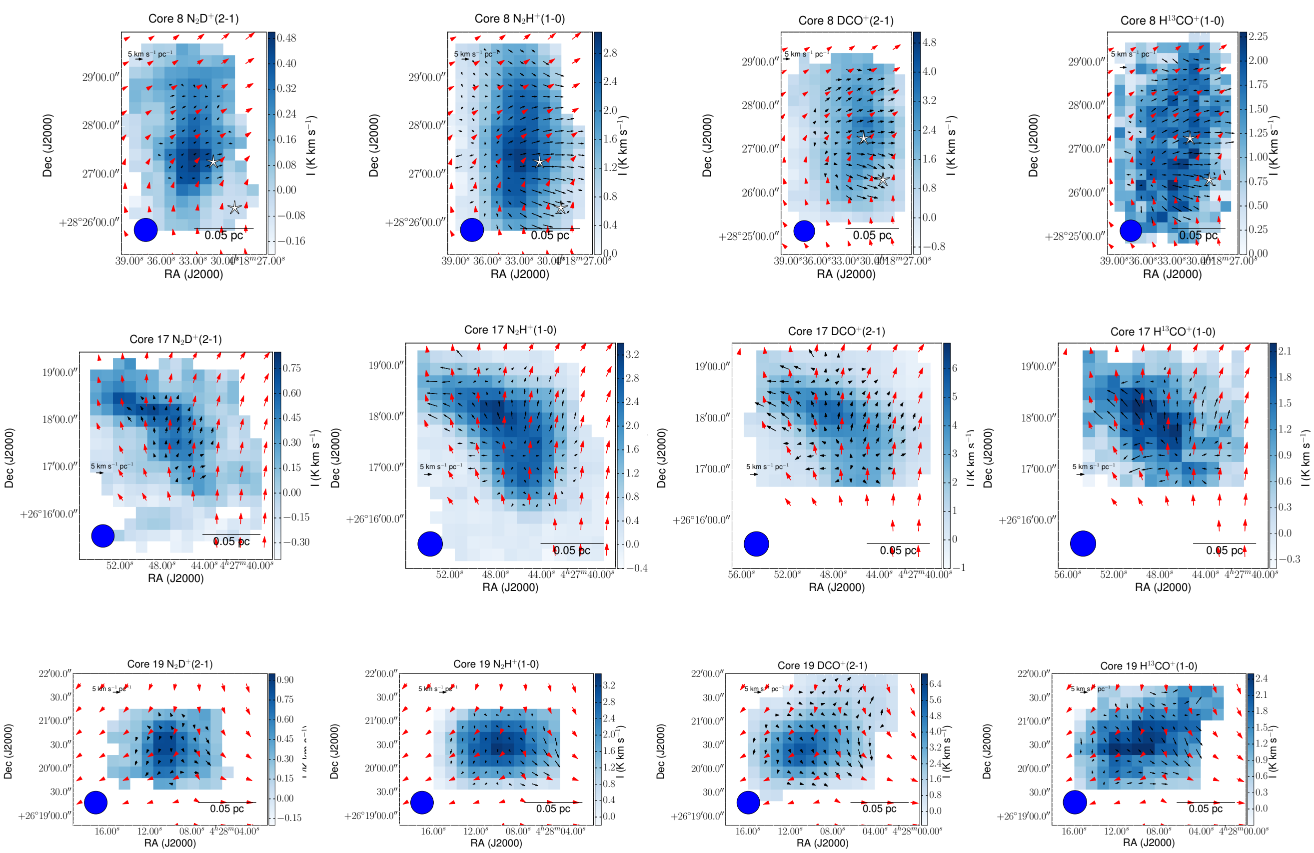

Figure B.15: continued.

Bibliography

André, P., Belloche, A., Motte, F., & Peretto, N. 2007, Astron. & Astrophys., 472, 519

André, P., Di Francesco, J., Ward-Thompson, D., et al. 2014, Protostars and Planets VI, 27

André, P., Men'shchikov, A., Bontemps, S., et al. 2010, Astron. & Astrophys., 518, L102

André, P., Ward-Thompson, D., & Barsony, M. 1993, Astrophys. J., 406, 122

Bacmann, A., Lefloch, B., Ceccarelli, C., et al. 2002, Astron. & Astrophys., 389, L6

Bailey, N. D. & Basu, S. 2012, Astrophys. J., 761, 67

Belloche, A. 2013, in EAS Publications Series, Vol. 62, EAS Publications Series, ed. P. Hennebelle & C. Charbonnel, 25–66

Benson, P. J. & Myers, P. C. 1989, Astrophys. J. Suppl., 71, 89

Bergin, E. A. & Tafalla, M. 2007, ARA&A, 45, 339

Bertin, M., Romanzin, C., Doronin, M., et al. 2016, Astrophys. J., 817, L12

Bizzocchi, L., Caselli, P., Spezzano, S., & Leonardo, E. 2014, Astron. & Astrophys., 569, A27

Bourke, T. L., Myers, P. C., Evans, II, N. J., et al. 2006, Astrophys. J., 649, L37

Brandner, W., Sheppard, S., Zinnecker, H., et al. 2000, Astron. & Astrophys., 364, L13

Cambrésy, L. 1999, Astron. & Astrophys., 345, 965

Caselli, P. 2011, in IAU Symposium, Vol. 280, IAU Symposium, ed. J. Cernicharo & R. Bachiller, 19–32

Caselli, P., Benson, P. J., Myers, P. C., & Tafalla, M. 2002a, Astrophys. J., 572, 238

Caselli, P. & Ceccarelli, C. 2012, Astron. & Astrophys. Rev., 20, 56

Caselli, P. & Dore, L. 2005, Astron. & Astrophys., 433, 1145

Caselli, P., Myers, P. C., & Thaddeus, P. 1995, Astrophys. J., 455, L77

Caselli, P., van der Tak, F. F. S., Ceccarelli, C., & Bacmann, A. 2003, Astron. & Astrophys., 403, L37

Caselli, P., Vastel, C., Ceccarelli, C., et al. 2008, Astron. & Astrophys., 492, 703

Caselli, P., Walmsley, C. M., Tafalla, M., Dore, L., & Myers, P. C. 1999, Astrophys. J., 523, L165

Caselli, P., Walmsley, C. M., Zucconi, A., et al. 2002b, Astrophys. J., 565, 331

Caselli, P., Walmsley, C. M., Zucconi, A., et al. 2002c, Astrophys. J., 565, 344

Chacón-Tanarro, A., Caselli, P., Bizzocchi, L., et al. 2017, ArXiv e-prints [arXiv:1707.00005]

Chapman, N. L., Goldsmith, P. F., Pineda, J. L., et al. 2011, Astrophys. J., 741, 21

Christie, H., Viti, S., Yates, J., et al. 2012, MNRAS, 422, 968

Crapsi, A., Caselli, P., Walmsley, C. M., et al. 2005, Astrophys. J., 619, 379

Crapsi, A., Caselli, P., Walmsley, C. M., et al. 2004, Astron. & Astrophys., 420, 957

Crapsi, A., Caselli, P., Walmsley, M. C., & Tafalla, M. 2007, Astron. & Astrophys., 470, 221

Cruz-Diaz, G. A., Martín-Doménech, R., Muñoz Caro, G. M., & Chen, Y.-J. 2016, Astron. & Astrophys., 592, A68

Dalgarno, A. & Lepp, S. 1984, Astrophys. J., 287, L47

de Zeeuw, P. T., Hoogerwerf, R., de Bruijne, J. H. J., Brown, A. G. A., & Blaauw, A. 1999, Astron. J., 117, 354

di Francesco, J., Evans, II, N. J., Caselli, P., et al. 2007, Protostars and Planets V, 17

Di Francesco, J., Johnstone, D., Kirk, H., MacKenzie, T., & Ledwosinska, E. 2008, Astrophys. J. Suppl., 175, 277

Draine, B. T. 1980, Astrophys. J., 241, 1021

Dunham, M. M., Allen, L. E., Evans, II, N. J., et al. 2015, Astrophys. J. Suppl., 220, 11

Duvert, G., Cernicharo, J., & Baudry, A. 1986, Astron. & Astrophys., 164, 349

Elias, J. H. 1978, Astrophys. J., 224, 857

Emprechtinger, M., Caselli, P., Volgenau, N. H., Stutzki, J., & Wiedner, M. C. 2009, Astron. & Astrophys., 493, 89

Flower, D. R., Pineau Des Forêts, G., & Walmsley, C. M. 2006, Astron. & Astrophys., 449, 621

Fontani, F., Giannetti, A., Beltrán, M. T., et al. 2012, MNRAS, 423, 2342

Fontani, F., Palau, A., Caselli, P., et al. 2011, Astron. & Astrophys., 529, L7

Fontani, F., Sakai, T., Furuya, K., et al. 2014, MNRAS, 440, 448

Frerking, M. A. & Langer, W. D. 1981, J. Chem. Phys., 74, 6990

Frerking, M. A., Langer, W. D., & Wilson, R. W. 1982, Astrophys. J., 262, 590

Friesen, R. K., Di Francesco, J., Bourke, T. L., et al. 2014, Astrophys. J., 797, 27

Friesen, R. K., Di Francesco, J., Myers, P. C., et al. 2010, Astrophys. J., 718, 666

Friesen, R. K., Di Francesco, J., Shirley, Y. L., & Myers, P. C. 2009, Astrophys. J., 697, 1457

Friesen, R. K., Kirk, H. M., & Shirley, Y. L. 2013, Astrophys. J., 765, 59

Friesen, R. K., Pineda, J. E., co-PIs, et al. 2017, Astrophys. J., 843, 63

Fuller, G. A. & Myers, P. C. 1992, Astrophys. J., 384, 523

Gagné, M., Skinner, S. L., & Daniel, K. J. 2004, Astrophys. J., 613, 393

Garrod, R. T. & Herbst, E. 2006, Astron. & Astrophys., 457, 927

Garrod, R. T., Wakelam, V., & Herbst, E. 2007, Astron. & Astrophys., 467, 1103

Gibb, E. L., Whittet, D. C. B., Schutte, W. A., et al. 2000, Astrophys. J., 536, 347

Ginsburg, A. & Mirocha, J. 2011, PySpecKit: Python Spectroscopic Toolkit, Astrophysics Source Code Library

Goldsmith, P. F. 2001, Astrophys. J., 557, 736

Goldsmith, P. F. & Langer, W. D. 1999, Astrophys. J., 517, 209

Gomez, M., Hartmann, L., Kenyon, S. J., & Hewett, R. 1993, Astron. J., 105, 1927

Goodman, A. A., Benson, P. J., Fuller, G. A., & Myers, P. C. 1993, Astrophys. J., 406, 528

Goodman, A. A., Jones, T. J., Lada, E. A., & Myers, P. C. 1992, Astrophys. J., 399, 108

Gordy, W. & Cook, R. L. 1970, Chemical applications of spectroscopy, Vol. 2, Microwave molecular spectra (New York u.a.: Interscience Publisher, 1970)

Gurney, M., Plume, R., & Johnstone, D. 2008, PASP, 120, 1193

Hacar, A., Tafalla, M., Kauffmann, J., & Kovács, A. 2013, Astron. & Astrophys., 554, A55

Harju, J., Daniel, F., Sipilä, O., et al. 2017, Astron. & Astrophys., 600, A61

Hasegawa, T. I., Herbst, E., & Leung, C. M. 1992, Astrophys. J. Suppl., 82, 167

Henning, T., Michel, B., & Stognienko, R. 1995, Planet. Space Sci., 43, 1333

Henshaw, J. D., Caselli, P., Fontani, F., Jiménez-Serra, I., & Tan, J. C. 2014, MNRAS, 440, 2860

Herbst, E. & Klemperer, W. 1973, Astrophys. J., 185, 505

Herbst, E. & van Dishoeck, E. F. 2009, ARA&A, 47, 427

Hernandez, A. K., Tan, J. C., Caselli, P., et al. 2011, Astrophys. J., 738, 11

Heyer, M. H., Vrba, F. J., Snell, R. L., et al. 1987, Astrophys. J., 321, 855

Hily-Blant, P., Walmsley, M., Pineau Des Forêts, G., & Flower, D. 2010, Astron. & Astrophys., 513, A41

Hirota, T. & Yamamoto, S. 2006, Astrophys. J., 646, 258

Jiménez-Serra, I., Vasyunin, A. I., Caselli, P., et al. 2016, Astrophys. J., 830, L6

Johnstone, D., Wilson, C. D., Moriarty-Schieven, G., et al. 2000, Astrophys. J., 545, 327

Kauffmann, J., Bertoldi, F., Bourke, T. L., Evans, II, N. J., & Lee, C. W. 2008, Astron. & Astrophys., 487, 993

Kennicutt, R. C. & Evans, N. J. 2012, ARA&A, 50, 531

Keto, E. & Caselli, P. 2008, Astrophys. J., 683, 238

Keto, E. & Caselli, P. 2010, MNRAS, 402, 1625

Keto, E., Caselli, P., & Rawlings, J. 2015, MNRAS, 446, 3731

Kong, S., Caselli, P., Tan, J. C., Wakelam, V., & Sipilä, O. 2015, Astrophys. J., 804, 98

Könyves, V., André, P., Palmeirim, P., et al. 2014, in Astrophysics and Space Science Proceedings, Vol. 36, The Labyrinth of Star Formation, ed. D. Stamatellos, S. Goodwin, & D. Ward-Thompson, 265

Kramer, C., Alves, J., Lada, C. J., et al. 1999, Astron. & Astrophys., 342, 257

Kramer, C., Peñalver, J., & Greve, A. 2013, Improvement of the IRAM 30m telescope beam pattern, Tech. rep.

Lacy, J. H., Knacke, R., Geballe, T. R., & Tokunaga, A. T. 1994, Astrophys. J., 428, L69

Lada, C. J., Lombardi, M., Roman-Zuniga, C., Forbrich, J., & Alves, J. F. 2013, Astrophys. J., 778, 133

Lada, C. J., Muench, A. A., Rathborne, J., Alves, J. F., & Lombardi, M. 2008, Astrophys. J., 672, 410

Lees, R. M. & Baker, J. G. 1968, The Journal of Chemical Physics, 48, 5299

Linsky, J. L., Draine, B. T., Moos, H. W., et al. 2006, Astrophys. J., 647, 1106

Liseau, R., Larsson, B., Lunttila, T., et al. 2015, Astron. & Astrophys., 578, A131

Liseau, R., White, G. J., Larsson, B., et al. 1999, Astron. & Astrophys., 344, 342

Lombardi, M., Lada, C. J., & Alves, J. 2008, Astron. & Astrophys., 480, 785

Lynds, B. T. 1962, Astrophys. J. Suppl., 7, 1

Machin, L. & Roueff, E. 2006, Astron. & Astrophys., 460, 953

Marsh, K. A., Griffin, M. J., Palmeirim, P., et al. 2014, MNRAS, 439, 3683

Men'shchikov, A., André, P., Didelon, P., et al. 2010, Astron. & Astrophys., 518, L103

Miettinen, O., Harju, J., Haikala, L. K., & Juvela, M. 2012, Astron. & Astrophys., 538, A137

Millar, T. J., Bennett, A., & Herbst, E. 1989, Astrophys. J., 340, 906

Miotello, A., Bruderer, S., & van Dishoeck, E. F. 2014, Astron. & Astrophys., 572, A96

Motte, F., Andre, P., & Neri, R. 1998, Astron. & Astrophys., 336, 150

Myers, P. C., Ladd, E. F., & Fuller, G. A. 1991, Astrophys. J., 372, L95

Nakamura, F., Kamada, Y., Kamazaki, T., et al. 2011, Astrophys. J., 726, 46

Onishi, T., Mizuno, A., Kawamura, A., Tachihara, K., & Fukui, Y. 2002, Astrophys. J., 575, 950

Pagani, L., Bacmann, A., Cabrit, S., & Vastel, C. 2007, Astron. & Astrophys., 467, 179

Pagani, L., Daniel, F., & Dubernet, M.-L. 2009, Astron. & Astrophys., 494, 719

Pagani, L., Lesaffre, P., Jorfi, M., et al. 2013, Astron. & Astrophys., 551, A38

Pagani, L., Salez, M., & Wannier, P. G. 1992, Astron. & Astrophys., 258, 479

Palmeirim, P., André, P., Kirk, J., et al. 2013, Astron. & Astrophys., 550, A38

Parise, B., Belloche, A., Du, F., Güsten, R., & Menten, K. M. 2011, Astron. & Astrophys., 526, A31

Parise, B., Castets, A., Herbst, E., et al. 2004, Astron. & Astrophys., 416, 159

Pattle, K., Ward-Thompson, D., Kirk, J. M., et al. 2015, MNRAS, 450, 1094

Phillips, J. P. 1999, Astron. & Astrophys. Suppl., 134, 241

Pineda, J. E., Goodman, A. A., Arce, H. G., et al. 2010, Astrophys. J., 712, L116

Pineda, J. E., Goodman, A. A., Arce, H. G., et al. 2011, Astrophys. J., 739, L2

Pon, A., Johnstone, D., Kaufman, M. J., Caselli, P., & Plume, R. 2014, MNRAS, 445, 1508

Pon, A., Plume, R., Friesen, R. K., et al. 2009, Astrophys. J., 698, 1914

Punanova, A., Caselli, P., Pon, A., Belloche, A., & André, P. 2016, Astron. & Astrophys., 587, A118

Rebull, L. M., Padgett, D. L., McCabe, C.-E., et al. 2010, Astrophys. J. Suppl., 186, 259

Santiago-García, J., Tafalla, M., Johnstone, D., & Bachiller, R. 2009, Astron. & Astrophys., 495, 169

Schmalzl, M., Kainulainen, J., Quanz, S. P., et al. 2010, Astrophys. J., 725, 1327

Schmid-Burgk, J., Muders, D., Müller, H. S. P., & Brupbacher-Gatehouse, B. 2004, Astron. & Astrophys., 419, 949

Schöier, F. L., Jørgensen, J. K., van Dishoeck, E. F., & Blake, G. A. 2002, Astron. & Astrophys., 390, 1001

Schöier, F. L., van der Tak, F. F. S., van Dishoeck, E. F., & Black, J. H. 2005, Astron. & Astrophys., 432, 369

Seo, Y. M., Shirley, Y. L., Goldsmith, P., et al. 2015, Astrophys. J., 805, 185

Shannon, R. J., Caravan, R. L., Blitz, M. A., & Heard, D. E. 2014, Physical Chemistry Chemical Physics (Incorporating Faraday Transactions), 16, 3466

Simpson, R. J., Nutter, D., & Ward-Thompson, D. 2008, MNRAS, 391, 205

Sipilä, O., Caselli, P., & Harju, J. 2013, Astron. & Astrophys., 554, A92

Sipilä, O., Caselli, P., & Taquet, V. 2016, Astron. & Astrophys., 591, A9

Sipilä, O., Harju, J., Caselli, P., & Schlemmer, S. 2015, Astron. & Astrophys., 581, A122

Spezzano, S., Bizzocchi, L., Caselli, P., Harju, J., & Brünken, S. 2016, Astron. & Astrophys., 592, L11

Spezzano, S., Caselli, P., Bizzocchi, L., Giuliano, B. M., & Lattanzi, V. 2017, ArXiv e-prints [arXiv:1707.06015]

Stahler, S. W. & Palla, F. 2005, The Formation of Stars, 865

Tafalla, M. & Hacar, A. 2015, Astron. & Astrophys., 574, A104

Tafalla, M., Myers, P. C., Caselli, P., & Walmsley, C. M. 2004, Astron. & Astrophys., 416, 191

Tafalla, M., Santiago-García, J., Myers, P. C., et al. 2006, Astron. & Astrophys., 455, 577

Tielens, A. G. G. M. & Hagen, W. 1982, Astron. & Astrophys., 114, 245

van den Ancker, M. E., The, P. S., Tjin A Djie, H. R. E., et al. 1997, Astron. & Astrophys., 324, L33

Vastel, C., Caselli, P., Ceccarelli, C., et al. 2006, Astrophys. J., 645, 1198

Vastel, C., Ceccarelli, C., Lefloch, B., & Bachiller, R. 2014, Astrophys. J., 795, L2

Vasyunin, A. I., Caselli, P., Dulieu, F., & Jiménez-Serra, I. 2017, Astrophys. J., 842, 33

Vasyunin, A. I. & Herbst, E. 2013, Astrophys. J., 769, 34

Volgenau, N. H., Mundy, L. G., Looney, L. W., & Welch, W. J. 2006, Astrophys. J., 651, 301

Wang, L.-Y., Shang, H., Su, Y.-N., et al. 2014, Astrophys. J., 780, 49

Wannier, P. G. 1980, ARA&A, 18, 399

Ward-Thompson, D., Motte, F., & Andre, P. 1999, MNRAS, 305, 143

Watanabe, N. & Kouchi, A. 2002, Astrophys. J., 571, L173

Watson, W. D. 1976, Reviews of Modern Physics, 48, 513

Wilson, T. L. & Rood, R. 1994, ARA&A, 32, 191

Wouterloot, J. G. A., Brand, J., & Henkel, C. 2005, Astron. & Astrophys., 430, 549

Xu, L.-H. & Lovas, F. J. 1997, Journal of Physical and Chemical Reference Data, 26, 17

Acknowledgements

I thank Paola Caselli for introducing me to the world of Astrochemistry and world-level science, and being the best supervisor. I thank my co-supervisor Andy Pon for all help in writing the papers and proposals (especially in the last minutes before the deadlines), correcting my English grammar, and proof-reading of the thesis. I thank my co-supervisor Jaime Pineda for forcing me to use modern data analysis tools and all help and advice in the data reduction. I thank my co-authors Luca Bizzocchi, Arnaud Belloche, Jorma Harju, Mario Tafalla, and Alvaro Hacar for fruitful and interesting discussions and help in preparation of my papers and observing scripts. I thank Anika Schmiedeke for translation of the thesis abstract to German.

I thank Anton Vasyunin for faithful support during the four years of my PhD. This work would not be possible without you.

I would like to thank Tom Hartquist, the professors and the PhD students of the Astrophysics Group at the School of Physics and Astronomy of the University of Leeds for a warm welcome and very friendly atmosphere in my first year of PhD.

I would like to thank the IRAM 30 m and NOEMA teams, especially Carsten Kramer, Claudia Marka, Juan Peñalver, Joaquín Santiago-Garcia, Nicolas Billot, Roberto Neri, Frédéric Damour, Enrique Lobato, Víctor Peula, Manuel Ruiz, Ignacio Ruiz, Walter Brunswig, Manuel González, and Cinthya Herrera, who helped me during observations, spent long observing runs and periods of bad weather in interesting chats with me, answered numerous questions about observing scripts and data reduction, taught during the 30 m summer school in 2015, and took care of me when I got sick at the 30m observatory.

I would like to thank the administrative staff in all organisations I worked with, especially Angelika Langer (CAS@MPE), Faith Bonner (School of Physics and Astronomy of the University of Leeds), and Catherine Berhaud (IRAM). Your help and advice made my PhD life much easier.

I thank Ekaterina Avvakumova for answering all my questions about LaTeX, Vlas Sokolov for answering all my questions about Pyspeckit and watering my plants when I was away, Ana Chacón-Tanarro for chats, discussions and numerous figures of dust in L1544, and Ashley Barnes for doing the pool observations at the 30 m for my project. Vlas and Ana, you are the best office mates. I thank Felipe Alves and Nichol Cunningham for teaching and helping us to observe and survive at the GBT. I thank all CAS group for just beeng nice, for time spent in the bar queezes, beergartens, and for wonderful homemade ice-cream. I thank my friends from Russia, especially Taisya Kopytova and Marina

Sivkova, for believing in me, and Kseniya Chaiko for staying with me in the last two weeks of the thesis preparation. I thank my brothers for their support and my parents for being patient while I was away from home. I am very grateful to Dima Semenov for cheering me up with tons of delicious food, alcohol, and journeys around Germany. I thank the IMPRS for student parties and for giving me an opportunity to train my skills of giving talks.

And the last, but not the least, I would like to acknowledge the financial support of the European Research Council (ERC; project PALs 320620) and of the School of Physics and Astronomy of the University of Leeds.

Curriculum Vitae

Anna Punanova

Date and place of birth	September 05, 1989, Ilyinsko-Podomskoye, USSR (now Russia)
School education	
1995 – 2000	Klyuchiki School, Russia
2000 – 2006	Krasnoufimsk School 9, Russia 2006 graduated with distinction – silver medal for excellent study
University education	
2006 – 2010	A. M. Gorky Ural State University, Yekaterinburg, Russia Physics department, chair of Astronomy and Geodesy Bachelor degree in technique and technology Bachelor thesis "Building a 3D model of the body of irregular geometric shape" Supervisors – Dr. Nataliya Frolova, Dmitriy Krutikov
2010 – 2012	Ural Federal University (former A. M. Gorky Ural State University), Yekaterinburg, Russia Physics department, chair of Astronomy and Geodesy Master degree in technique and technology Master thesis "Search for variable stars in open clusters NGC 7142 and NGC 2281 with MASTER-II-Ural telescope at Kourovskaya astronomical observatory" Supervisors – Dr. Aleksander Loktin, Vadim Krushinsky
2013 – 2014	University of Leeds, Leeds, UK School of Physics and Astronomy, PhD research student PhD project "Deuterium fractionation in low-mass star-forming regions" Supervisors – Prof. Dr. Paola Caselli, Prof. Dr. Tom Hartquist
2015 – present time	Ludwig-Maximilians-Universität München, Munich, Germany, Fakultät für Physik, PhD student research project "Chemistry and kinematics in low-mass star-forming regions" Supervisor – Prof. Dr. Paola Caselli

Employment

Jan 2011 – Sep 2013	Kourovskaya Astronomical Observatory of the Ural Federal University, researcher
Since Jul 2014	Max-Planck-Institut für extraterrestrische Physik, doctorate student

Successful observing proposals

IRAM 30m, 2014	Deuterium fraction in the Taurus molecular cloud complex, PI – A. Punanova
APEX, 2014	Deuterium fraction along the Ophiuchus filament, PI – A. Punanova
IRAM 30m, 2014	Kinematics and structure of the high density gas within filaments in the Taurus molecular cloud, PI – A. Punanova
GBT, 2014	The Green Bank Ammonia Survey (GAS, large program), PIs – R. Friesen and J. Pineda
VLA, 2015	Where does star formation start? Ammonia mapping of the Oph A star-forming ridge, PI – M. van der Wiel
APEX, 2015	Nuclear spin ratios of deuterated ammonia, PI – J. Harju
IRAM 30m, 2015	Deuterium fraction in the Ophiuchus molecular cloud, PI – A. Punanova
NOEMA, 2015	Seeds of Life in Space, (SOLIS, large program), PIs – C. Ceccarelli and P. Caselli
NOEMA, 2015	Kinematics and a search for hierarchical structures within the B213-10 dense core, PI – A. Punanova
VLA, 2016	Grain growth in the star-forming cluster rho Oph A, PI – A. Coutens
APEX, 2016	Deuteration of ammonia in starless cores, PI – J. Harju
IRAM 30m, 2016	Distribution of deuterium fraction in starless cores, PI – A. Punanova
ALMA, 2016	Nuclear spin ratios as clues to the origin of deuterated ammonia, PI – J. Harju
APEX, 2017	Direct observational constraints on turbulent dissipation within a star-forming clump: the Ophiuchus E-MM2d core, PI – J. Pineda
JCMT, 2017	Tracing the heart of a prestellar core in H_2D^+, PI – A. Pon
IRAM 30m, 2017	Constraining astrochemical models with the spin ratios of NH_2D in starless cores, PI – J. Harju
ALMA, 2017	Are dense cores formed through shocks? An observational test in Ophiuchus, PI – J. Pineda
ALMA, 2017	Highly deuterated starless cores with low CO freeze out: a chemical puzzle, PI – A. Punanova

Observing experience

IRAM 30m	in-situ observations – 161 hours, remote observations – 58 hours
GBT	in-situ training observations – 2 hours
APEX	observing scripts preparation
	Optical observations with high resolution echelle spectrographs: 6m telescope BTA at SAO RAS, 2m telescope at Terskol observatory of INASAN, 1.2m telescope of Kourovka observatory UrFU Optical photometric observations with MASTER-II-Ural

Talks

May 2011	VRI CCD Photometry of the Old Open Cluster NGC7142, Young Scientists' Conference on Astronomy and Space Physics, Kyiv, Ukraine
Feb 2012	Investigation of the fiber-linked echelle spectrograph at the 1.2-meter telescope at Kourovskaya astronomical observatory, 41th Winter Workshop Physics of Space, Yekaterinburg, Russia
Oct 2012	The fiber-fed echelle spectrograph at the 1.2-meter telescope at Kourovskaya astronomical observatory, Observable manifestations of stellar evolution, Nizhnij Arkhyz, Russia
Jul 2016	Deuterium fraction and kinematics in low-mass star-forming regions: environmental effects, Symposium 9 of EWASS-2016, Athens, Greece
Oct 2016	Deuterium fractionation and kinematics in the Taurus molecular cloud, Fractionation of isotopes: from Solar System to galaxies, Florence, Italy
Feb 2017	L1544: overview of the status, the third SOLIS meeting, Universite de Cergy-Pontoise, France
Jun 2017	Kinematics of dense gas in the L1495 filament, CAS retreat, Ringberg castle, Germany

Publications list

Publications in refereed journals:

1. Friesen, R. K.; Pineda, J. E.; Rosolowsky, E. et al. The Green Bank Ammonia Survey (GAS): First Results of NH3 mapping the Gould Belt, ApJ 843, 63, 2017

2. Harju, J.; Daniel, F.; Sipilä, O.; et al. Deuteration of ammonia in the starless core Ophiuchus/ H-MM1, A&A 600, A61, 2017

3. Punanova, A.; Caselli, P.; Pon, A.; et al. Deuterium fractionation in the Ophiuchus molecular cloud, A&A 587, A118, 2016

4. Daniel, F.; Coudert, L. H.; Punanova, A.; et al. The NH_2D hyperfine structure revealed by astrophysical observations, A&A 586, L4, 2016

5. Krushinsky, V. V.; Popov, A. A.; Punanova, A. F. Upgrade of the fiber-fed spectrograph of the Kourovka Astronomical Observatory, AstBu 69–4, 497–505, 2014

6. Gorbovskoy, E. S.; Lipunov, V. M.; Kornilov, V. G.; et al. The MASTER-II network of robotic optical telescopes. First results, ARep 57–4, 233–286, 2013

7. Ugolnikov, O. S.; Punanova, A. F.; Krushinsky, V. V. Trajectory retrieval and component investigations of the southern polar stratosphere based on high-resolution spectroscopy of the totally eclipsed moon surface, JQSRT 116, 67–74, 2013